N°Ordre……./Faculté des sciences/UMBB/2024

REPUBLIQUE ALGERIENNE DEMOCRATIQUE ET POPULAIRE

MINISTERE DE L'ENSEIGNEMENT SUPERIEUR ET DE LA RECHERCHE SCIENTIFIQUE

UNIVERSITE M'HAMED BOUGARA-BOUMERDES

Faculté des Sciences

Thèse de Doctorat

Présenté par :

NECIB Nihal

En vue de l'obtention du diplôme de **DOCTORAT 3eme cycle** en :

Filière : Physique

Option : Dynamique des Fluides et Energétique

Étude numérique du transfert de chaleur par convection laminaire de nanofluide hybride entre deux cylindres concentriques horizontaux en présence de chauffage uniforme

Devant le jury composé de :

Mr	ABAIDIA	Seddik ELhak	Pr	UMBB	Président
Mr	BENKHEDDA	Mohammed	MCA	UMBB	Rapporteur
Mr	ZAMOUM	Mohammed	Pr	UMBB	Examinateur
Mr	ALLALOU	Nabil	Pr	USTHB	Examinateur
Mr	LASBET	Yahia	Pr	U DJELFA	Examinateur
Mr	KEZRANE	Cheikh	Pr	U DJELFA	Invité

Année Universitaire 2023/2024

N° of order……./Faculty of Sciences/UMBB/2024

DEMOCRATIC AND POPULAR REPUBLIC OF ALGERIA

MINISTRY OF HIGH EDUCATION AND SCIENTIFIC RESEARCH

UNIVERSITY OF M'HAMED BOUGARA-BOUMERDES

Faculty of Sciences

Doctoral thesis

Presented by:

NECIB Nihal

With a view to obtaining the degree of **DOCTORATE 3rd cycle** in:

Major: Physics

Option: Fluid Dynamics and Energetic

Numerical study of laminar convective heat transfer of hybrid nanofluid between two horizontal concentric cylinders under uniform heating

In front of the jury composed of:

Mr	ABAIDIA	Seddik ELhak	Pr	UMBB	President
Mr	BENKHEDDA	Mohammed	MCA	UMBB	Supervisor
Mr	ZAMOUM	Mohammed	Pr	UMBB	Examiner
Mr	ALLALOU	Nabil	Pr	USTHB	Examiner
Mr	LASBET	Yahia	Pr	U DJELFA	Examiner
Mr	KEZRANE	Cheikh	Pr	U DJELFA	Invited

Academic year 2023/2024

Acknowledgement

I thank the Merciful God for giving me the strength, courage, willpower, and guidance to overcome all difficulties and complete this work.

First and foremost, I would like to express my most sincere thanks and deep gratitude to my supervisor Dr. Benkhedda Mohammed, Associate Professor from University of Boumerdes, for his advice, guiding, availability, motivation, and great patience. This thesis could never have been successfully completed without his precious supervision, and words of encouragement.

I want to thank Professor Engin Gedik at the University of Karabuk for accepting me through an internship within their research team. Your confidence in my abilities, warm welcome, and valuable advice have been essential for the continuation and deepening of my research work. Additionally, I thank Dr. Cuneyt, Associate Professor at the University of Karabuk for his help and support.

I extend my sincere thanks to Professor Abaidia Sedik Elhak at the University of Boumerdes, for the great honour of accepting to chair the jury for this thesis.

I wish also to extend my profound thanks to the jury members, Professor Zamoum Mohammed from the University of Boumerdes, Professor Allalou Nabil from the University of Science and Technology Houari Boumediene, Professor Lasbet Yahia, and Professor Kezrane Cheikh from the University of Djelfa, who kindly agreed to read this thesis and provide pertinent critiques.

I am grateful to all the teachers in the Department of Physics at the University of Boumerdes, especially Ms. Abdellahoum and Ms. Baaziz.

Finally, my heartfelt thanks go to all those who have contributed, directly or indirectly, to the completion of this work.

Dedication

To my beloved parents, Khadra Salhi and Louardi Necib, your sacrifices, love, and endless support have been the greatest gift in my life. You have always believed in me, even when I doubted myself, and your encouragement has been my greatest source of strength. Without you, I could never have reached where I am today. Your guidance, wisdom, and prayers have been instrumental in my journey, and for that, I am eternally grateful; you deserve the most considerable dedication in the world, honouring the extraordinary parents you are. Thank you for everything.

To my wonderful aunt Sabah, for her constant support and encouragement. Your kindness and generosity have meant the world to me.

To my beloved siblings, Safoua, Amani, and Islam, for their unconditional love and support.

To my uncle Karim, who has always been there to help me.

To my uncles Kamel and Liamine.

To my cousins, Ranim and Tesnim.

Necib Nihal

Contents

List of Figures

List of Tables

Nomenclature

General Introduction ***1***

Chapter I: Generalities and Literature Review

I.1. Introduction 4

I.2. Description of nanofluids 4

I.2.1. Synthesis of Nanofluids 6

I.2.2. Applications 7

I.2.3. Thermophysical properties 9

I.2.4. CFD approaches 12

I.3. Porous media 14

I.3.1. Characteristics of the porous medium 14

I.3.2. Momentum equation 14

I.3.3. Energy equation 16

I.4. Introduction to Magnetohydrodynamic (MHD) 17

I.4.1. Definition 17

I.4.2. Fundamental principles 17

I.4.3. Applications of MHD 18

I.5. Literature review 18

Chapter II: Mathematical Modelling

II.1. Introduction 35

II.2. Physical Model 35

II.2.1. First Application 35
II.2.2. Second Application 36
II.3. Governing equations 38
II.3.1. First configuration 41
II.3.2. Second configuration 42
II.4. Nusselt number 46
II.5. Skin friction coefficient 47
II.6. Pressure drop 47
II.7. Entropy generation 47

Chapter III: Numerical resolution

III.1. Introduction 49
III.2. Resolution methods 49
III.3. Numerical methods 50
III.4. Finite volume method procedure 50
III.4.1. Domain discretization 50
III.4.2. Discretization of the energy transport 53
III.4.3. Discretization of the governing equations 55
III.4.4. Discretization of the boundary conditions 66
III.4.5. Solution algorithm 69
III.4.6. Solution of the discretized equations 69
III.5. Computational fluid dynamics software 74
III.5.1. Discretization scheme 74
III.5.2. Solution algorithm 75
III.5.3. Boundary condition 75
III.5.4. Under relaxation factor 76
III.5.5. Convergence criteria 76

III.5.6. Computational domain and mesh generation 77
III.5.7. Code validation 78

Chapter IV: Results and discussions

IV.1. Introduction 81
IV.2. First application 81
IV.2.1 Hydrodynamic field 81
IV.2.2 Thermal field 95
IV.2.3 Secondary flow 98
IV.2.4 Nusselt number 101
IV.2.5 Skin friction coefficient 103
IV.2.6. Pressure drop 105
IV.2.7. Entropy generation 107
IV.3 Second application 112
IV.3.1 Hydrodynamic field 112
IV.3.2 Thermal field 119
IV.3.3 Nusselt number 123
IV.3.4 Skin friction coefficient 127
IV.3.5. Pressure drop 130
IV.3.6. Entropy generation 133

General conclusion ***……143***

References ***……...145***

List of Figures

Chapter I: Generalities and literature review

Figure I.1. Thermal conductivity of various material at 300K [3]. 5

Figure I.2. Sketch of the geometry studied [19]. 19

Figure I.3. Schematic of the geometry [20]. 20

Figure I.4. Schematic of the geometry [23]. 20

Figure I.5. Geometry of the problem studied [24]. 21

Figure I.6. Schematic of the geometry [25]. 22

Figure I.7. Sketch of the geometry studied [27]. 23

Figure I.8. The geometry of the study [30]. 23

Figure I.9. Sketch of the geometry with: (a) negative and (b) positive magnetic field gradient, and (c) mesh used [31]. 24

Figure I.10. Geometry of the problem [32]. 24

Figure I.11. Sketch of the problem [33]. 25

Figure I.12. Sketch of the geometry [34]. 26

Figure I.13. Schematic of the problem studied [35]. 27

Figure I.14. Sketch of the geometry [36]. 27

Figure I.15. Schematic of the experiment [37]. 28

Figure I.16. Sketch of the problem studied [38]. 29

Figure I.17. Sketch of the problem studied [39]. 30

Figure I.18. Sketch of the problem studied [40]. 30

Figure I.19. Sketch of the geometry [41]. 31

Figure I.20. Schematic of the geometry studied [42]. 32

Figure I.21. The geometry studied [43]. 32

Figure I.22. Geometry studied [44]. 33

Figure I.23. Sketch of the problem studied [47]. 34

Figure I.24. Sketch of the problem studied [48]. 34

Chapter II: Mathematical modelling

Figure II. 1. First configuration schematic. 36

Figure II. 2. Second configuration schematic 37

Figure II. 3. Schematic illustrating different scenarios of magnetic field application. 38

Chapter III : Numerical resolution

Figure III. 1. Control volume. 51

Figure III. 2. Projection of the finite volume along a: (r,θ) plane, b: (r,z) plane, and c: (θ,z) plane. 53

Figure III. 3. Projection of the shifted mesh in the radial direction along a: (r*,z*) plane and b: (r*,θ) plane. 58

Figure III. 4. Projection of the shifted mesh in the angular direction along a: (θ,z*) plane and b: (r*,θ) plane. 61

Figure III. 5. Projection of the shifted mesh in the angular direction along a: (θ,z*) plane and b: (r*,z*) plane. 64

Figure III. 6. Generated mesh: (a) 3D view and (b) front view. 71

Figure III. 7. Grid test. 72

Figure III. 8. Local Nusselt number along the tube. 73

Figure III. 9. Comparison of the wall temperature profile at Re=1275. 74

Figure III. 10. Mesh tests at Re=800, and Pr=6.2. 78

Figure III. 11. Comparison of Axial Nusselt number through a straight duct. 80

Figure III. 12. Comparison of the axial velocity along radial direction. 80

Chapter IV: Results and discussion

Figure IV. 1. Angular velocity contours at various locations using (TiO_2-CNT-Graphene/kerosene)..... 82

Figure IV.2. Axial velocity contours at various locations using (TiO_2-CNT-Graphene/kerosene)..... 83

Figure IV. 3. Effect of Da on angular velocity contours for: a (TiO_2-CNT-Graphene/ kerosene), b (TiO_2-CNT/kerosene), c (TiO_2-Graphene/kerosene). 85

Figure IV. 4. Effect of Hartmann number on angular velocity contours at ψ=0°, for: a (TiO_2-CNT-Graphene/kerosene), b (TiO_2-CNT/kerosene), c (TiO_2-Graphene/kerosene)..... 87

Figure IV. 5. Effect of Hartmann number on angular velocity contours at ψ=90° using (TiO_2-CNT-Graphene/kerosene). 88

Figure IV. 6. Non-dimensional axial velocity profiles at the duct's outlet across different Da number for: a (TiO_2,CNT,Graphene/kerosene), b (TiO_2,CNT/kerosene), and c (TiO_2,Graphene/kerosene)..... 90

Figure IV. 7. Influence of Hartmann number on non-dimensional axial velocity contours at the outlet for ψ=0°: a (TiO_2-CNT-Graphene/ kerosene), b (TiO_2-CNT/ kerosene), c (TiO_2-Graphene/ kerosene)..... 91

Figure IV. 8. Effect of Hartmann number on non-dimensional axial velocity contours at the outlet for ψ=90°, Gr=10^6, and ϕ= 5% using TiO_2-CNT-Graphene/ kerosene. 92

Figure IV. 9. Non dimensional axial velocity ratio along the radial direction for different Darcy numbers and Ha=0 by utilizing (TiO_2-CNT-Graphene/kerosene). 93

Figure IV. 10. Non-dimensional velocity ratio along the radial direction for different Hartmann numbers at Da=0.01 using (TiO_2-CNT/kerosene): a ψ=0°, b ψ=90°..... 94

Figure IV. 11. 3D temperature contours for various Da numbers at Ha=0: (a) TiO_2,CNT,Graphene/kerosene, (b) TiO_2,CNT/kerosene, (c) TiO_2,Graphene/kerosene. 96

Figure IV. 12. 3D isotherm contours versus Ha numbers at Da=0.01, and ψ=0°: (a) TiO_2,CNT,Graphene/kerosene, (b) TiO_2,CNT/kerosene, and (c) TiO_2, Graphene/kerosene... 97

Figure IV. 13. 3D isotherm contours for various Ha numbers at ψ=90°, and Da=0.01, using (TiO_2-CNT-Graphene/kerosene). 98

Figure IV. 14. Development of secondary flow along the annulus duct for Gr=2.5 x 10^6, Ha=0, Da=0, and ϕ=5%. 99

Figure IV. 15. Secondary flow at the outlet of the annular duct for different Gr numbers at Da=0.01, Ha=0, and ϕ=5%..... 99

Figure IV. 16. Secondary flow at the outlet of the annular duct for different Darcy numbers at Gr=10^6, Ha=0, and ϕ=5%..... 100

Figure IV. 17. Secondary flow at the outlet of the annular duct for different Ha number and magnetic field inclination at Gr=106, Da=0.01, and ϕ=5%. 100

Figure IV. 18. Average Nusselt number for different: (a) Da number, (b) Ha number at ψ=0°, (c) Ha number at ψ=90°. 103

Figure IV. 19. Average skin friction coefficient for various: (a) Da number at Ha=0, (b) Ha number at Da=0.01, and ψ=0°..... 105

Figure IV. 20. Pressure drop for various: (a) Dar number at Ha=0, (b) Ha number at Da=0.01, and ψ=0°..... 106

Figure IV. 21. Entropy generation for various Darcy number at Ha=0: (a) thermal entropy, (b) frictional entropy, (c) Bejan number. 109

Figure IV. 22. Entropy generation for various Hartmann number at Da=0.01 and ψ =0°: (a) Thermal entropy, (b) Frictional entropy, (c) Magnetic entropy, (d) Bejan number..... 111

Figure IV. 23. Axial velocity contours using (TiO_2-CNT-Graphene/water) at Re=800, Da=0.01, and ϕ=5 for (a) straight duct, and (b) wavy duct. 113

Figure IV. 24. Axial velocity contours for different amplitude at Re=800, Da=0.01, L=2.452, and ϕ=5%: (a) TiO_2-CNT/water, (b) TiO_2-Graphene/water, and (c) TiO_2-CNT-Graphene/water. 114

Figure IV. 25. Axial velocity contours using (TiO_2-CNT-Graphene/water) for different amplitude wave at Re=800, Da=0.01, L=2.452, and ϕ=5%: (a) A=0.1, (b) A=0.2, and (c) A=0.3. 115

Figure IV. 26. Axial velocity contours for two different wave lengths using (TiO_2-CNT-Graphene/water) ternary hybrid nanofluid at Re=800, Da=0.01, A=0.2, and ϕ=5%. 116

Figure IV. 27. Effect of Hartmann number on axial velocity contours at the duct's outlet for: (a) TiO_2-CNT/water, (b) TiO_2-Graphene/water, and (c) TiO_2-CNT-Graphene/water. 117

Figure IV. 28. Effect of different partial magnetic field scenarios on axial velocity contours at (r,z) plane. 118

Figure IV. 29. 3D isotherms contours using (TiO_2-CNT-Graphene/water) at Re=800, Da=0.01, and ϕ=5%: (a) straight duct, (b) wavy duct. 119

Figure IV. 30. 3D isotherms contours for different amplitude at Re=800, Da=0.01, L=2.452, and ϕ=5%: (a) TiO_2-CNT/water, (b) TiO_2-Graphene/water, and (c) TiO_2-CNT-Graphene/water. 120

Figure IV. 31. 3D isotherms contours using (TiO_2-CNT-Graphene/water) for different wavelengths at Re=800, Da=0.01, A=0.2, and ϕ=5%. 121

Figure IV. 32. Hartmann number effect on temperature contours for different hybrid nanofluids. 122

Figure IV. 33. The effect of different partial magnetic field scenarios on temperature contours using ternary hybrid nanofluid. 123

Figure IV. 34. Average Nusselt number using three different hybrid nanofluids for (a) effect of wave amplitude, (b) effect of wavelength. 125

Figure IV. 35. Average Nusselt number versus Hartmann number (a) for different hybrid nanofluid using full magnetic field, (b) comparison of full and partial magnetic field scenarios. 127

Figure IV. 36. Average skin friction coefficient using three different hybrid nanofluids for (a) wave amplitude, (b) wavelength. 128

Figure IV. 37. Average skin friction coefficient versus Hartmann number (a) for different hybrid nanofluid using full magnetic field, (b) comparison of full and partial magnetic field scenarios. 130

Figure IV. 38. Pressure drop using three different hybrid nanofluids for (a) effect of wave amplitude, (b) effect of wavelength. 131

Figure IV. 39. Pressure drop versus Hartmann number (a) for different hybrid nanofluid using full magnetic field, (b) comparison of full and partial magnetic field scenarios. 133

Figure IV. 40. Entropy generation and Bejan number for different hybrid nanofluids and wave amplitude at L=2.452. 135

Figure IV. 41. Entropy generation and Bejan number for different hybrid nanofluids and wavelengths at A=0.2. 137

Figure IV. 42. Entropy generation and Bejan number for different hybrid nanofluids and Hartmann number using full magnetic field. 140

Figure IV. 43. Entropy generation and Bejan number for different Hartmann number and different magnetic field scenarios using Ternary hybrid nanofluid at A=0.2, and L=2.452.. 142

List of Tables

Table II. 1. The thermophysical properties of the solid nanoparticles and the base fluid [10,32,49]. 44

Table III. 1. The mesh test on the average Nusselt number. 71

Table III. 2. The numerical schemes used. 75

Table III. 3. The boundary conditions. 76

Table III. 4. Under-relaxation factor. 76

Table IV. 1. Location of the maximum angular velocity for various Darcy number. 84

Table IV. 2. Location of the maximum angular velocity for various orientations and Hartmann number. 86

Nomenclature

Symboles

a	Amplitude	(mm)
A	Dimensionless amplitude (a/D_o-D_i)	-
B	Magnetic field intensity	(T)
C_{fo}	Skin friction coefficient	-
C_p	Heat capacity	(J/Kg K)
Da	Darcy number	-
D_h	Hydraulic diameter	(m)
D_i	inner diameter	(m)
D_o	outer diameter	(m)
E	electric field	(V/m)
Ha	Hartmann number	-
J	Current density	(A/m^2)
K	Permeability	(m^2)
L	Length of the annulus	(m)
Pr	Prandtl number	-
q	Uniform heat flux	(W/m^2)
r	Radial coordinate	(m)
Re	Reynolds number	-
S	Entropy	(J/K s)
T	Temperature	(K)
T_0	Inlet temperature	(K)

u	Radial velocity	(m/s)
v	Axial velocity	(m/s)
w	Angular velocity	(m/s)
z	Axial coordinate	(m)

Greek symbols:

ε	porosity	%
θ	Angular coordinate	(rad)
λ	wavelength	(mm)
μ	Dynamic viscosity	(kg/m s)
μ_0	Magnetic permeability	(H/m)
ν	Kinematic viscosity	(m^2/s)
ρ	density	(kg/m^3)
σ	Electrical conductivity	(s/m)
τ	shear stress	(Pa)
ϕ	volume concentration	(%)

Subscripts:

*	non-dimensional parameters
av	Average
b	Bulk
f	base fluid
fr	frictional
hnf	hybrid nanofluid
thnf	ternary hybrid nanofluid
i	inlet
M	magnetic
nf	nanofluid
o	outlet
p	nanoparticle
th	thermal

General Introduction

Improvement in heat transfer is vital in many of industrial and engineering applications such as energy systems, electronics cooling and biomedical devices. An adequately managed thermal system can increase the system's performance and reliability and save energy when integrated seamlessly into the environment they were designed to be used in. In this context, a deep study has been paid great attention to convective heat transfer mechanisms with the advent of innovative techniques.

The engineered colloidal suspensions of nanoparticles in a base fluid, known as nanofluids, offer the potential to improve thermal properties. They have better thermal conductivity than the traditional fluids, which is why they are used in different heat transfer systems. Hybrid nanofluids, composed of more than two kinds of solid nanoparticles, find a way to further enhance the net heat transfer via synergistic effects.

The porous media also enhances heat transfer. It is a material with an interconnected void that could be saturated with fluid. High surface areas, with complex internal structures, can improve thermal efficiency in many different applications.

Another method that has received excellent attention is the use of magnetic fields to enhance heat transfer systems. Magnetohydrodynamics (MHD) is a branch of physics that deals with electrically conducting fluids in a magnetic field. Fluid motion can be affected by the Lorentz force acting on the charged particles of the fluid when a magnetic field is present. This technique could ensure flow patterns, work out enhanced mixing, and achieve practical heat transfer efficiencies.

Even though there is a large amount of work done on nanofluid research, there is still an extensively unexplored domain when it comes to the use of nanofluids for complex geometries and under varying external conditions. In particular, behaviour of hybrid nanofluids in confined geometries such as concentric cylinders, porous media, and magnetic fields are still lacking.

This thesis aims to fill this knowledge gap by investigating the laminar convective heat transfer of binary and ternary hybrid nanofluids in two concentric cylinders filled with a porous medium and subjected to a magnetic field.

The study focuses on two applications:

- 3D mixed convection in a straight annulus duct exposed to uniform heat flux and magnetic field.
- 3D forced convection in a wavy annulus duct exposed to a uniform heat flux and non-uniform magnetic field.

The main objectives are:

- ✓ Analyzing the magneto-hydrothermal performance of ternary and binary hybrid nanofluids in concentric cylindrical geometries saturated with porous media.
- ✓ Evaluate the influence of porous media on heat transfer and fluid flow.
- ✓ Examine the influence of uniform and non-uniform magnetic fields through different scenarios on the convective heat transfer.

The thesis consists of four chapters: the first chapter lays out the theoretical background, concepts, and most of the existing relevant literature on the topic. It begins with a description of nanofluids, types of nanofluids, synthesis methodologies, and applications. The chapter also explores the nanofluid's thermophysical properties, which are important in heat transfer enhancement. After this, it reviews Computational Fluid Dynamics (CFD) approaches used for simulating nanofluids. Additionally, generalities about porous media and Magnetohydrodynamics (MHD) are explored to understand the following chapters. The chapter closes with a thorough literature review, outlining the main findings and missing pieces from existing research.

The second chapter presents the mathematical framework used to analyze the heat transfer characteristics of the systems under study. It includes the governing equations that describe fluid flow and heat transfer within the concentric cylinders filled with porous media. The description of the physical model outlines assumptions and simplifications made for facilitating the mathematical formulation.

The third chapter focuses on the numerical resolution of the equations derived in the previous chapter. Computational techniques and algorithms were discussed to obtain solutions from this complex set of equations describing the system. The resolution method is the finite volume technique, which ensures accurate and reliable numerical solutions. The chapter explains

discretization methods, boundary conditions, and numerical schemes to obtain accurate and reliable solutions.

The detailed results of the numerical simulations are discussed in chapter four. The findings are reported in velocity contours, 3D isotherm contours, Nusselt number, skin friction coefficient, pressure drop, and entropy generation analysis. It interprets data in the context of heat transfer enhancement with the effects of binary and ternary hybrid nanofluids, porous media, and magnetic fields on the convective heat transfer process. A comparative performance analysis is conducted between different configurations and conditions. The discussion also leads toward the implication of results for practical application and suggests possible areas for future research.

Finally, in the conclusion, we summarize the significant findings of the present work, discuss the impact of the results on practical cases, and propose potential areas for future research.

Chapter I: Generalities and Literature Review

I.1. Introduction

This chapter comprehensively overviews the fundamental concepts and existing research on heat transfer related to nanofluids, porous media, entropy generation, and magneto-hydrothermal for laminar flow forced or mixed convection. It begins with a description of nanofluids, types of nanofluids, synthesis methodologies, and applications. The chapter also explores nanofluids' thermophysical properties, essential in transfer enhancement. After this, it reviews Computational Fluid Dynamics (CFD) approaches for simulating nanofluids. Additionally, generalities about porous media and magnetohydrodynamics (MHD) are explored to understand better the following chapters. The chapter closes with a thorough literature review, outlining the main findings and missing pieces from existing research.

I.2. Description of nanofluids

Numerous studies have focused on improving the thermal properties of liquids. The first analytical study by Maxwell [1] demonstrated that adding micrometric-sized particles could enhance thermal conductivity. However, these particles caused issues like agglomeration and pressure drops. These problems have been addressed using stably suspended nanometric-sized solid particles through conventional liquids.

In the last decade, nanometric size nanoparticle production technology has improved, and the small quantity of solid nanoparticles in a liquid mixture known as nanofluids was introduced first by Choi [2] in 1995 at the US National Laboratory of Argonne. Heat transfer in nanofluids: a new term represents the new class of heat transfer using nanotechnology fluids with better thermophysical properties than their base fluids. Nanofluids are engineered colloidal suspensions consisting of nanoparticles ranging from 1-100 nm in size in a base fluid formulated to improve the thermal characteristics.

Nanoparticles can be metals, oxide metals, or carbon-based materials. **Figure I.1** illustrates the thermal conductivities of various materials. For example, metallic nanoparticles like gold (Au), silver (Ag), and copper (Cu) demonstrate excellent thermal conductivity, with values around 318 W/mK, 429 W/mK, and 400 W/mK, respectively. Oxide nanoparticles, such as aluminium oxide (Al_2O_3), and titanium dioxide (TiO_2) also significantly enhance thermal performance, although their conductivities are generally lower, approximately 30 W/mK for Al_2O_3 and 8.95 W/mK for TiO_2. Carbon-based nanoparticles, including carbon nanotubes (CNTs) and

graphene, exhibit exceptional thermal conductivities of up to 3000 W/mK and 5000 W/mK due to their unique molecular structures.

The base fluids used in nanofluids, such as water, ethylene glycol, and various oils, are crucial in determining overall thermal performance. Water, with a thermal conductivity of around 0.6 W/mK, is often used due to its high specific heat capacity and availability. Ethylene glycol, commonly used in antifreeze solutions, has a lower thermal conductivity of about 0.25 W/mK but offers a lower freezing point. Oils, including mineral and silicone oils, provide good thermal stability with moderate thermal conductivities ranging from 0.15 to 0.2 W/mK.

In addition to single-component nanofluids, hybrid nanofluids, which combine two or three different nanoparticles, have emerged as a promising research area. These hybrid nanofluids leverage the synergistic effects of different nanoparticles to enhance thermal conductivity and stability further. For example, combinations like Cu-Al_2O_3 or Ag-TiO_2 blend the high thermal conductivity of metals with the thermal stability of oxides, optimizing the fluid's overall performance. The hybrid approach tailors the thermal and physical properties to meet specific requirements, resulting in even more effective heat transfer fluids. The combination of nanoparticles and base fluids in nanofluids, including hybrid nanofluids, enhances heat transfer capabilities through mechanisms like Brownian motion and thermophoresis, contributing to the superior thermal performance of nanofluids in various industrial and scientific applications.

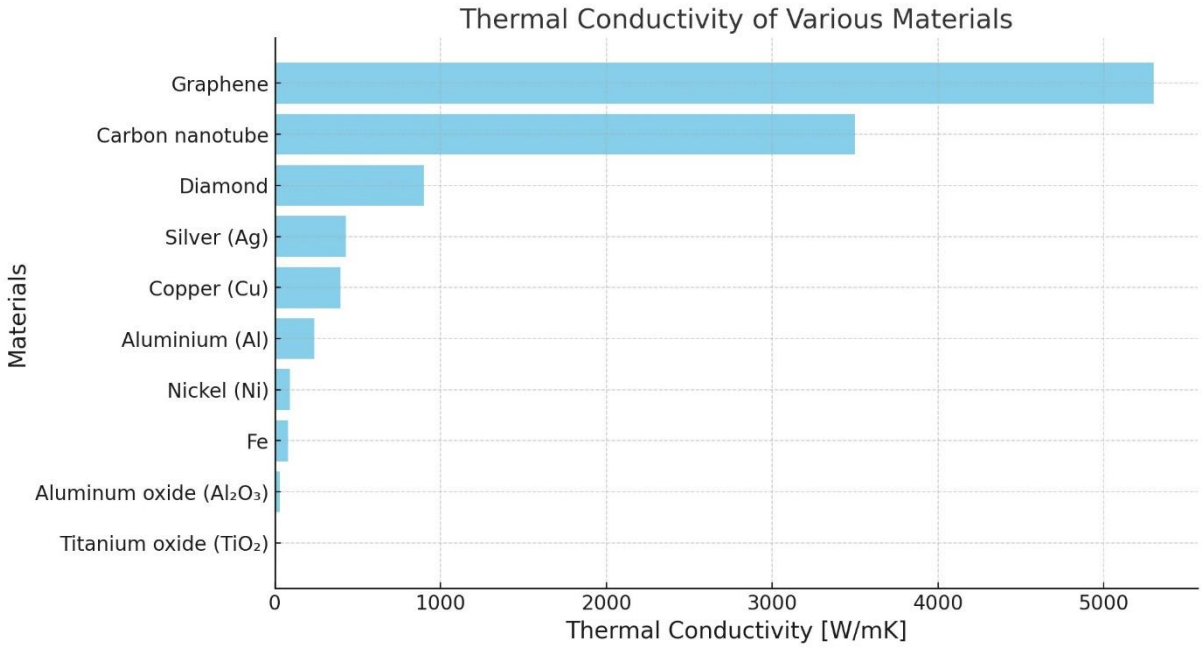

Figure I.1. Thermal conductivity of various material at 300K [3].

I.2.1. Synthesis of Nanofluids

Nanofluids are synthesized by dispersing stable suspensions of nanoparticles into a base fluid. The most common methods are one- and two-step, each with its characteristics and advantages.

- **One-step approach**

The nanoparticles are made and dispersed into the base fluid simultaneously. This method provides the benefits of simplicity and efficiency as it eliminates the need for separate nanoparticle synthesis and dispersion steps to reduce the agglomeration of the nanoparticles. The techniques used in this method are laser ablation, chemical vapor condensation, flame, etc. One-step methods are particularly suitable for producing high-quality nanofluids with uniform nanoparticle distribution. However, the one-step approach is often costly and cannot be manufactured in large quantities.

- **Two-step approach**

This two-step method first prepares nanoparticles by using techniques such as sol-gel, co-precipitation, or hydrothermal methods. These nanoparticles are dispersed in the base fluid after being synthesized. The two-step approach offers advantages in terms of flexibility and optimization, as researchers can optimize each stage of nanoparticle synthesis and dispersion independently. It is the most economical method in the large-scale production of nanofluids. When producing nanofluids using this method, nanoparticles tend to agglomerate; therefore, to avoid this problem, surface modification techniques can also be integrated to enhance nanoparticle stability. This method is commonly used when precise control over nanoparticle characteristics and dispersion is critical for achieving desired heat transfer enhancement properties in the nanofluid.

An experimental study was carried out by Chandrasekar et al. [4] to synthesize Al_2O_3 nanoparticles using a microwave assisted chemical precipitation technique. Their research concluded that increasing the concentration of nanoparticles in nanofluids results in higher thermal conductivity and viscosity. Gupta et al. [5] prepared Cu–CNT/water using a two-phase technique. Their study demonstrated a 75.57% increase in thermal conductivity for a 0.1 wt% Cu–CNT binary hybrid nanofluid in comparison to the base fluid. Said et al. [6] prepared (rGO-Fe_3O_4-TiO_2/EG) ternary hybrid nanofluid through the sol-gel technique. They tested the density and the rheological behavior experimentally by varying temperatures from 25 °C to 50°C and

concentrations from 0.01 wt% to 0.25 wt%. Their findings suggested that these nanofluids are well-suited for applications demanding long-term stability and enhanced heat transfer performance.

I.2.2. Applications

Nanofluids can be applied in various thermal systems where efficient heat transfer is crucial. Among these applications, we can mention:

- **Solar Thermal collectors**

Solar thermal collectors harness sunlight to generate heat, and nanofluids play an essential role in augmenting the efficiency of these collectors. The high thermal conductivity of nanoparticles enables more efficient heat transfer from the absorber surface (where sunlight is converted to heat) to the base fluid in the collector. This improved heat transfer minimizes thermal losses and maximizes solar energy utilization for heating applications. Ekiciler et al. [7] showed an improvement in the efficiency of the parabolic trough collector (PTC) by utilizing (Ag-MgO/Syltherm 800) binary hybrid nanofluid with 4% nanoparticle volume concentration.

- **Cooling electronic devises**

Nanofluids are used in electronic devices and computer systems to enhance heat dissipation and prevent overheating. By circulating nanofluids through cooling channels or heat sinks, electronics can operate at optimal temperatures, improving reliability and performance. Vishnuprasad Selvaraj and Haribabu Krishnan [8] synthesized, graphene nanoplatelets encased alumina nanocomposite for the cooling of an electronic system. They showed that the core temperature was reduced by 11.38% when using 0.2% volume concentration.

- **Vehicle engine cooling system**

Nanofluids are integrated into automotive cooling systems to improve engine cooling efficiency and reduce fuel consumption. They enable more effective heat transfer within the engine, leading to improved performance and durability. Abbas et al. [9] synthesized a (Fe_3O_4-TiO_2/ water) binary hybrid nanofluid to improve heat transfer efficiency in automotive radiators. They found that using 0.009% volume concentration significantly enhances heat transfer rates and Nusselt numbers by 26.7% and 21%, respectively. Sahoo [10] investigated the thermohydraulic characteristics of a ternary hybrid nanofluid used as a radiator coolant, utilizing nanoparticles

with various forms: cylindrical (CNT), spherical (Al_2O_3), and platelet (Graphene). The research demonstrated that nanoparticle form has a substantial impact on the performance of an automotive cooling system.

- **Nuclear reactor**

Nanofluids have potential applications in nuclear reactor cooling systems, where they can improve heat transfer and safety margins. They can enhance the performance of coolant fluids in reactor cores, contributing to more efficient and reliable nuclear power generation.

- **Medical application**

Nanofluids have potential applications in medical devices such as hyperthermia treatment systems, where a therapeutic technique involves heating specific body tissues to induce localized cell damage or enhance the effectiveness of other treatments (such as chemotherapy or radiation therapy). Nanofluids can be injected into target tissues or organs, where nanoparticles absorb electromagnetic waves (e.g., radiofrequency or microwave) and convert them into heat. This localized heating can selectively target cancer cells while minimizing damage to healthy tissues.

- **Energy storage**

Some nanofluids exhibit phase-change properties, undergoing reversible phase transitions (such as solid-liquid or liquid-vapor) with latent heat absorption/release. These phase-change nanofluids can be utilized for thermal energy storage in solar thermal systems, allowing for efficient energy capture during sunny periods and release of stored heat when needed, even during periods of low sunlight or at night. Alrowaili et al. [11] performed an experimental study using CuO-Cu/water binary hybrid nanofluid to boost the performance of solar thermal energy storage systems. Their results indicated that the hybrid nanofluid significantly enhances both the thermal-optical efficiency and the overall effectiveness of the solar thermal energy storage systems.

- **HVAC systems**

Nanofluids are used in heating, ventilation, and air conditioning (HVAC) systems to improve energy efficiency and indoor thermal comfort. They enable more efficient heat exchange in HVAC equipment, leading to reduced energy consumption and operating costs.

I.2.3. Thermophysical properties

I.2.3.1. Density

Density is a fundamental physical property that quantitatively describes how much mass is packed into a given volume of a substance. In simpler terms, it measures how heavy or dense a material is relative to its size. A substance's density is denoted by ρ and expressed in kilograms per cubic meter (kg/m³).

$$\rho = \frac{m}{v} \qquad (I.1)$$

The following equation gives the density of a mixture:

$$\rho = \frac{m_f + m_s}{v_f + v_s} \qquad (I.2)$$

The volume concentration of the nanoparticles is given as:

$$\phi = \frac{solid\ volume}{total\ nanofluid\ volume} = \frac{v_s}{v_f + v_s} \qquad (I.3)$$

Pak and Cho [12] have pioneered an innovative equation for determining the density of nanofluids, which has been validated against experimental data. The equation (I.4) they have established is as follows:

$$\rho_{nf} = \phi\rho_{np} + (1 - \phi)\rho_{bf} \qquad (I.4)$$

In the equation (I.4), ρ_{nf} symbolizes the density of nanofluids, ρ_{np} signifies the density of nanoparticles, ρ_f denotes the base fluid density, and ϕ represents the volume concentration of nanoparticles within the nanofluid.

Takabi et Salehi [13] later introduced an equation (I.5) tailored for determining the density of hybrid nanofluids, encompassing multiple nanoparticle types.

$$\rho_{hnf} = \phi_{np1}\rho_{np1} + \phi_{np2}\rho_{np2} + \left(1 - \phi_{np1} - \phi_{np2}\right)\rho_f \qquad (I.5)$$

ρ_{np1}, and ρ_{np2} represent the densities of the respective types of nanoparticles, ϕ_{np1} and ϕ_{np2} denote the volume fractions of each nanoparticles within the base fluid.

I.2.3.2. Heat capacity

Pak and Cho have also pioneered an equation (I.6) to calculate the heat capacity of nanofluids as follows:

$$(\rho C_p)_{nf} = \phi_{np}(\rho C_p)_{np} + +\left(1-\phi_{np}\right)\left(\rho C_p\right)_f \qquad (I.6)$$

Takabi et Salehi [13] later established an equation (I.7) to calculate the heat capacity of hybrid nanofluids as follows:

$$(\rho C_p)_{hnf} = \phi_{np1}(\rho C_p)_{np1} + \phi_{np2}(\rho C_p)_{np2} + \left(1-\phi_{np1}-\phi_{np2}\right)\left(\rho C_p\right)_f \qquad (I.7)$$

I.2.3.3. Thermal expansion

The thermal expansion of nanofluids refers to the change in volume or dimensions of a nanofluid in response to temperature change. When nanofluids are heated or cooled, their particles, including the base fluid and nanoparticles, may undergo thermal expansion or contraction, leading to changes in their overall volume or size. It is typically expressed in units per degree Celsius (or per Kelvin). It is a crucial property to consider in various applications, including thermal management systems, heat transfer processes, and materials science. Khanafer and Vefai [14] expressed the thermal expansion of nanofluids as follows:

$$(\rho\beta)_{nf} = \phi_{np}(\rho\beta)_{np} + +\left(1-\phi_{np}\right)(\rho\beta)_f \qquad (I.8)$$

Later, many studies introduced the thermal expansion of hybrid nanofluids as follows:

$$(\rho\beta)_{hnf} = \phi_{np1}(\rho\beta)_{np1} + \phi_{np2}(\rho\beta)_{np2} + \left(1-\phi_{np1}-\phi_{np2}\right)(\rho\beta)_f \qquad (I.9)$$

I.2.3.4. Dynamic viscosity

The dispersion of nanoparticles into the base fluid can alter its viscosity, leading to changes in its flow behaviour and rheological properties. Numerous studies explored the characteristics of nanofluids. Einstein was the first to establish a model that calculates the effective viscosity of nanofluids with sphere nanoparticles form:

$$\mu_{nf} = (1+2.5\phi)\mu_f \qquad (I.10)$$

Based on Einstein's model, Brinkman has extended Einstein's model to cover a large volume concentration. It is given as follows:

$$\mu_{nf} = \frac{\mu_f}{(1-\phi)^{2.5}} \quad (I.11)$$

While these models provide estimates, the actual dynamic viscosity of a specific nanofluid is best determined experimentally. Factors such as nanoparticle aggregation, surface coatings, and the specific chemistry of the base fluid can significantly affect the results. Among several experimental studies, Timofeeva et al. [15] conducted an experiment to determine the effective viscosity of different nanofluids with various nanoparticle shapes. Their correlations are given as follows:

Spherical shape:

$$\mu_{nf}/\mu_f = 1 + 2.5\phi + 6.2\phi^2 \quad (I.12)$$

Cylindrical shape:

$$\mu_{nf}/\mu_f = 1 + 13.5\phi + 904.4\phi^2 \quad (I.13)$$

Platelet shape:

$$\mu_{nf}/\mu_f = 1 + 37.1\phi + 612.6\phi^2 \quad (I.14)$$

Blade shape:

$$\mu_{nf}/\mu_f = 1 + 14.6\phi + 123.3\phi^2 \quad (I.15)$$

Brick shape:

$$\mu_{nf}/\mu_f = 1 + 1.9\phi + 471.4\phi^2 \quad (I.16)$$

I.2.3.5. Thermal conductivity

Thermal conductivity is a crucial property of nanofluids, known for their enhanced thermal conductivity compared to the base fluid alone. This enhancement arises from the elevated thermal conductivity of nanoparticles, which facilitate efficient heat transfer within the fluid. It depends on several factors, including the type, size, and concentration of nanoparticles, as well as the temperature and properties of the base fluid. Several researchers explored theoretical and experimental correlations to model thermal conductivity.

Maxwell [16] introduced a model to calculate thermal conductivity for spherical suspensions. His model is given in equation (I.17) as follows:

$$\frac{k_{nf}}{k_f} = \frac{k_p + 2k_f + 2\phi(k_p - k_f)}{k_p + 2k_f + 2\phi(k_p + k_f)} \quad (I.17)$$

Afterwards, Hamilton-Crosser [17] developed a new model valuable for different nanoparticle shapes given as follows:

$$\frac{k_{nf}}{k_f} = \frac{k_p + (n-1)k_f + (n-1)\phi(k_p - k_f)}{k_p + (n-1)k_f - \phi(k_p - k_f)} \quad (I.18)$$

Some researchers developed models that take into consideration the Brownian motion; among these models, we mention the Koo and Kleinstreuer model [18]:

$$\frac{k_{nf}}{k_f} = \frac{(k_p + 2k_f) - 2\phi(k_f - k_p)}{(k_p + 2k_f) - 2(k_f - k_p)} + 5 \times 10^4 \beta\phi\rho_f C_{pf}\sqrt{\frac{k_B T}{\rho_p d_p}} f(t,\phi) \quad (I.19)$$

$$f(t,\phi) = (-134.63 + 1722.3\phi) + 0.4705 - 6.04\phi)(T/T_0) \quad (I.20)$$

$$\beta = \begin{cases} 0.0137(100\phi)^{-0.8229}, \phi < 0.01 \\ 0.0111(100\phi)^{-0.7272}, \phi > 0.01 \end{cases} \quad (I.21)$$

I.2.3.6. Electric conductivity

The electric conductivity of nanofluids was established by Maxwell [16] as follows:

$$\frac{\sigma_{nf}}{\sigma_f} = 1 + \frac{3(\sigma_p/\sigma_f - 1)\phi}{(\sigma_p/\sigma_f + 2) - (\sigma_p/\sigma_f - 1)\phi} \quad (I.22)$$

I.2.4. CFD approaches

I.2.4.1. Single-phase approach:

The single-phase method is commonly used to simplify the computation by treating the nanofluid as a homogenous mixture without considering the slip between the nanoparticles and the fluid; the nanoparticles and the base fluid could be considered in thermal equilibrium with zero relative velocity and at the same temperature. Several models have been developed within this approach to capture different aspects of heat transfer and fluid dynamics.

- **Homogenous model**

The Homogeneous Model presumes that the nanofluid is uniform, with nanoparticles evenly dispersed throughout the base fluid without settling or clustering. The primary assumption is that the thermal conductivity and viscosity of the nanofluid can be predicted based on the volume concentration and properties of the nanoparticles and the base fluid. This straightforward and computationally less intensive model makes it popular for analyses. However, it might not accurately reflect scenarios where nanoparticle concentration gradients or thermal conductivity variations are significant.

- **Thermal dispersion model**

The Thermal dispersion model includes the increased thermal conductivity due to the random motion of nanoparticles within the base fluid. This model accounts for additional thermal energy transport by the dispersed nanoparticles, which is not captured by the simple mixture theory used in the homogeneous model. In this model, the thermal conductivity is modified to include a dispersion coefficient that considers kinetic effects associated with the motion of nanoparticles that enhance the overall energy transfer. This model is applicable in situations where the thermal effects due to the Brownian motion of the nanoparticles dominate the thermal conductivity.

- **Buongiorno model**

The Buongiorno model is an extension of the single-phase model; it includes two critical phenomena: Brownian motion and thermophoresis.

I.2.4.2. Two phase approach

In this approach, nanoparticles and the base fluid are regarded as discreet phases due to the influence of various factors such as Brownian force, thermophoresis, and gravity. While the two-phase approach is effective in capturing realistic phenomena, it requires much more computational resources and tends to be more complex to implement and analyze. The most used models in this approach are Lagrangian-Eulerian and Eulerian-Eulerian models.

I.2.4.3. Lattice Boltzmann approach

The Lattice Boltzmann method (LBM) is a particle-based method for modelling fluid flows. The fluid is represented by fictitious particles carrying the particle distribution functions on a

discrete lattice, which is a micro-scale model with spreading and collision rules. It is a novel way of attacking the problem, providing a handling of the fluid dynamics simple enough to model complex interactions by treating the flowing material as a collection of particles that only interact at a local level.

I.3. Porous media

Porous media is material or substance that contains interconnected pores. Such pores can be filled with air, water, or other fluids. Because of their interconnected nature, fluids can flow through the material, making porous media of interest in numerous scientific and engineering fields. Porous media can be found in natural materials like soil, rocks, and biological tissues, as well as in manufactured materials like sponges, filters, and some ceramics. The voids or pores in the porous medium promote convective heat transfer due to the interconnected channels. Fluid flowing through these voids is brought into intimate contact with solid surfaces, enabling heat transfer, and usually, this is translated into higher heat transfer coefficients than non-porous materials.

I.3.1. Characteristics of the porous medium

I.3.1.1 Porosity

Porosity is the ratio of void volume to total volume (Eq I.23). It indicates a porous material's total volume of empty spaces or voids. A higher porosity means more open space within the material, and a lower porosity indicates fewer open spaces and more solid material.

$$\epsilon = \frac{void\ volume}{total\ volume} \qquad (I.23)$$

I.3.1.2. Permeability

Permeability measures a porous medium's ability to permit fluids to pass through it under a given pressure gradient. Permeability affects the flow rate; highly permeable materials allow rapid flow, while low permeability restricts flow.

I.3.2. Momentum equation

The models for modelling the fluid flow through porous media are outlined below.

I.3.2.1. Darcy model

The first model used to describe fluid flow through porous media was pioneered by Darcy and is represented by equation (I.24) as follows:

$$V = -\frac{K}{\mu}\frac{\partial P}{\partial x} \qquad (I.24)$$

K is the permeability of the medium, μ stands for the dynamic viscosity of the fluid, and $\partial P/\partial x$ is the pressure gradient through the flow direction.

I.3.2.2. Frochheimer model

Forchheimer's Law is an extension of Darcy's model that includes a quadratic drag term ($C_F K^{-1/2}|V|V$) to model non-linear flow behaviour in porous media at higher flow velocities.

$$\nabla P = -\frac{\mu}{K}\vec{V} - C_F K^{-\frac{1}{2}}\left|\vec{V}\right|\vec{V} \qquad (I.25)$$

The Forchheimer coefficient C_F can be determined experimentally or through empirical correlations based on experimental data.

I.3.2.3. Brinkman model

Brinkman's equation extends Darcy's Law by incorporating additional terms for viscous effects and inertial forces in fluid flow through porous media.

$$\nabla P = -\frac{\mu}{K}\vec{V} + \mu_e \nabla^2 \vec{V} \qquad (I.26)$$

μ_e: Effective dynamic viscosity

I.3.2.4. Darcy-Frochheimer-Brinkman model

It takes into consideration all the previous effects as follows:

$$\nabla P = -\frac{\mu}{K}\vec{V} - C_F K^{-\frac{1}{2}}\left|\vec{V}\right|\vec{V} + \mu_e \nabla^2 \vec{V} \qquad (I.27)$$

I.3.3. Energy equation

Understanding the energy equation subject to porous media involves a combination of heat transfer modes within the porous material, how fluid flow and heat transfer can interact with each other, and the influence of porosity, permeability, and thermal properties of the porosity medium. There are two different ways to describe it: local thermal equilibrium and local thermal non-equilibrium.

I.3.3.1. Local thermal equilibrium approach

The local thermal equilibrium model (LTE) assumes that within a small region of the medium, the solid phase and the fluid phase are in thermal equilibrium, which means that at a given location and instant in time, the temperatures of the solid matrix and the fluid are considered equal. Mathematically, this assumption is expressed as $T_f=T_s=T$.

Where:

T_s: Temperature of the solid phase (solid matrix).

T_f: Temperature of the fluid phase (fluid flowing through the porous medium).

$$\left(\rho C_p\right)\frac{\partial T}{\partial t}+\left(\rho C_p\right)_f V.\nabla T=\nabla.\left(k_{eff}\nabla T\right) \qquad (I.28)$$

Where

$$k_{eff}=\varepsilon k_f+(1-\varepsilon)k_s \qquad (I.29)$$

The LTE assumption is frequently applied in simplified heat transfer models in porous media, especially in scenarios where the temperature gradient within the solid and fluid phases is relatively minor or when the heat transfer rate between the phases is slow compared to other processes.

I.3.3.2. Local thermal non-equilibrium approach

When considering non-equilibrium effects, where the solid matrix and fluid phase can have different temperature fields and are not assumed to be in thermal equilibrium, the energy equation becomes more complex.

I.4. Introduction to Magnetohydrodynamic (MHD)

I.4.1. Definition

Magnetohydrodynamics (MHD) is a branch of physics and fluid dynamics that studies the behaviour of electrically conductive fluids (such as plasmas, liquid metals, and electrolytes) in the existence of magnetic fields and electric currents. It combines principles from electromagnetism and fluid mechanics to describe the interactions between magnetic fields and flowing fluids. In MHD, the motion of the fluid generates electric currents, which in turn interact with the magnetic field to fabricate electromagnetic forces that influence the fluid's behaviour.

I.4.2. Fundamental principles

The magnetohydrodynamics of conducting fluids are governed by the Navier-Stokes equations from fluid dynamics and Maxwell's equations from electromagnetism. These equations describe how the fluid velocity field couples to magnetic fields.

An essential process whereby magnetic fields affect fluid motion is the Lorentz force. The Lorentz force is the force exerted on a charged particle moving through a magnetic field, and the equation gives it:

$$F = q(E + v \times B) \qquad (I.30)$$

Where:

F: Lorentz force

q: Electric charge of a particle

E: Electric field

V: Velocity of the particle

B: Magnetic field

In MHD, the Lorentz force is applied to the entire fluid, not individual particles. This force arises from the interaction between the magnetic field and the electric currents in the fluid, and it couples the Navier-Stocks and Maxwell's equations together, leading to a term J×B in the momentum equation, where J is the current density.

Another mechanism involved in MHD phenomena is Joule heating. This occurs when an electric current passes through a conducting fluid, producing heat due to the fluid's resistance.

I.4.3. Applications of MHD

In Fluid Mechanics

MHD has broader applications in industry, particularly in mechanical engineering, where it can be used to derive the flow of conducting fluids without mechanical parts, such as in marine propulsion. This application uses a magnetic field to derive the seawater flow and generate a push. It offers more efficient and manoeuvrable propulsion for naval and commercial vessels.

In Heat Transfer

MHD is important in heat transfer applications, especially in nuclear reactor cooling, where conventional convection modes are insufficient. Traditional cooling methods generally use water as a coolant, but advanced reactors use liquid metals due to their higher thermal conductivities and specific heat capacities. Based on the magnetic field subjected, the coolant is circulated between the reactor core and the heat exchanger in MHD-based cooling reactors.

In Biomedical

MHD has significant applications in the biomedical field, particularly in developing advanced medical devices and treatment methods. Researchers have developed ways to introduce magnetic nanoparticles containing drugs into the body and use magnetic fields to guide them to locations within the body, such as tumours.

I.5. Literature review

Several researchers have conducted analytical, numerical, and experimental analyses of heat transfer phenomena related to porous media, entropy generation, Joule heating, and magneto-hydrothermal effects using nanofluids, binary hybrid nanofluids, or ternary hybrid nanofluids. The following section, a literature review of these studies is provided to identify the existing gaps.

Motallebzadeh et al. [19] investigated laminar mixed convection heat transfer of (Al_2O_3/water) nanofluid inside a concentric annulus duct. The inner wall was subjected to a constant heat flux, while the outer wall was insulated. The system of equations was discretized using the control

volume technique, and the SIMPLEC procedure was introduced for the velocity-pressure coupling. They employed a two-phase mixture model to study the impacts of different nanoparticle volume concentrations on the fluid's hydrodynamic and thermal behaviours. The simulation was carried out for various values of Azimuthe angle (0°,90°,180°), Rayleigh number Ra (8×10^6, $2.5\ 10^7$, 1.5×10^7) and volume fraction from 0% to 5%. Their findings revealed that increasing the nanoparticle volume concentrations increased secondary flow strength, and the highest temperature appeared at the top of the annuli.

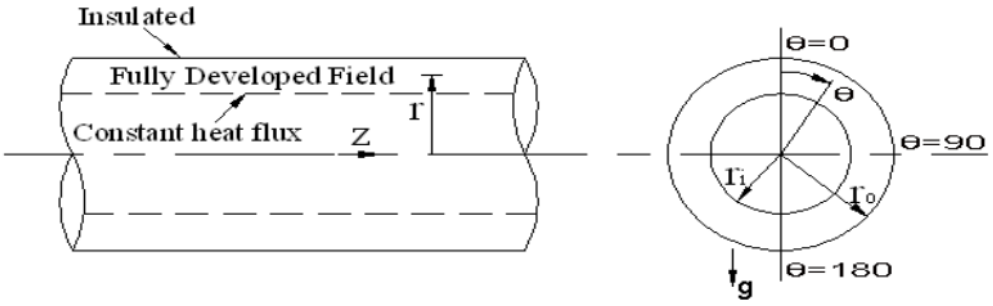

Figure I.2. Sketch of the geometry studied [19].

Benkhedda et al. [20] numerically studied mixed convection heat transfer using (TiO_2/Water) nanofluid and (Ag-TiO_2/Water) binary hybrid nanofluid in a horizontal concentric cylinder with a uniform heat flux condition on the outer cylinder, while the inner cylinder was adiabatic. The governing equations were discretized using Finite volume method. Their result was validated by the results of Takabi et al.[21] and Shah et al. [22]. The control parameters are the nanoparticle's volume fraction ($0\% \leq \phi \leq 8\%$) and Grachof number ($10^5 \leq Gr \leq 10^6$). These parameters indicated that no significant change exists in the axial velocity of nanofluid and hybrid nanofluid along the radial direction, whilst the axial velocity along the cylinder changed because of the buoyancy force. In addition, they have developed two correlations of Nusselt number (Eq I.31) and (Eq I.32) for (TiO_2/water) nanofluid and Ag-TiO_2/water hybrid nanofluid, respectively.

$$Nu = 0.3824 Gr^{0.2088} Pr^{0.4092} (1+\phi)^{2.0153} \qquad (I.31)$$

$$Nu = 0.6765 Gr^{0.21} Pr^{0.1162} (1+\phi)^{1.621} \qquad (I.32)$$

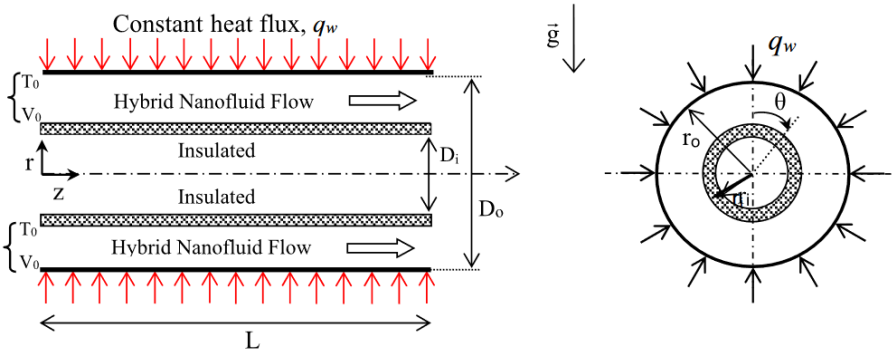

Figure I.3. Schematic of the geometry [20].

Benkhedda et al. [23] numerically studied nanoparticle shape's effect on laminar forced convection utilizing (Ag-TiO_2/Water) binary hybrid nanofluid in a horizontal pipe heated by a uniform heat flux. The 3D equations are solved using the Finite volume technique. The results obtained for different nanoparticle shapes (spherical, cylindrical, blade, platelet), a volume fraction varying from (0-8%), and several Re varying from (750-1775) revealed that:

- Nusselt number rises with rising the volume fraction and Reynolds number for all nanoparticle forms.
- The rise in Nusselt number is most notable for hybrid nanofluids containing nanoparticles with blade form, followed by those with platelet, cylindrical, and spherical nanoparticles.
- The friction factor rises with rising nanoparticle volume concentrations and reduces with rising Reynolds number. Moreover, hybrid nanofluids with blade shapes present high friction factor values.

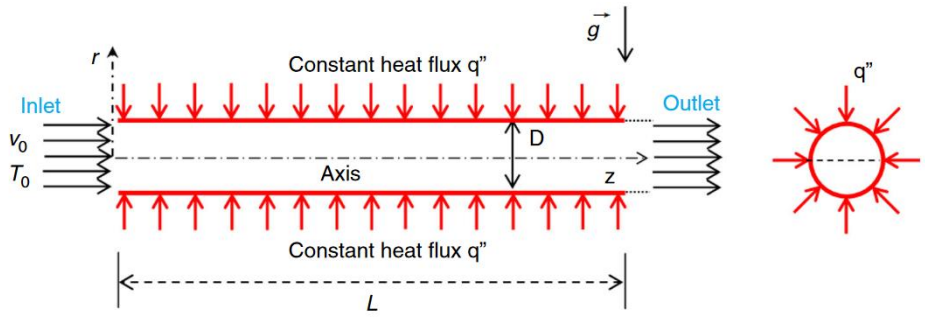

Figure I.4. Schematic of the geometry [23].

Benkhedda et al. [24] reported a parametric investigation on the thermal performance of forced convection laminar flow using three nanoparticles types (TiO_2, Al_2O_3, Cu) through a horizontal annular pipe. The outer cylinder was exposed to a constant heat flux while the inner cylinder was adiabatic. Finite volume technique was used to solve the partial equations using FORTRAN code. The simulation was carried out with ($800<Re<1200$), ($0<\varphi<6$). They found that

- Bulk temperature and wall temperature rises with rising volume concentration and reduces with increasing Reynolds number.
- The Nusselt numbers have increased as the volume concentration and Reynolds number rise and show the highest value with Cu nanoparticles.

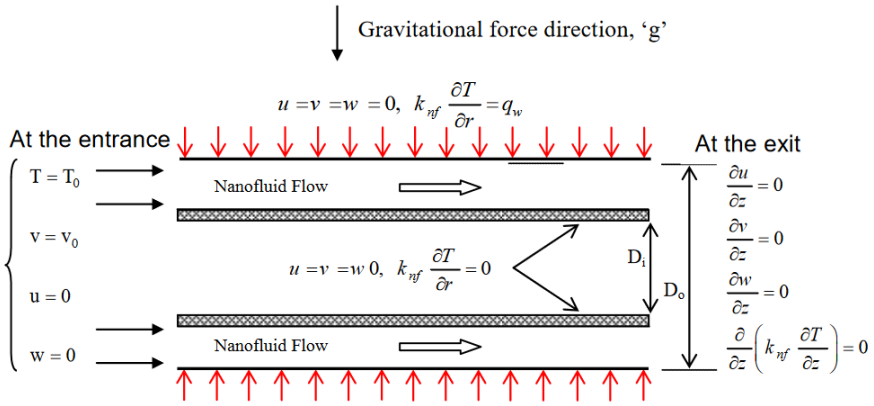

Figure I.5. Geometry of the problem studied [24].

Albeshri et al. [25] performed a numerical simulation of laminar mixed convection flow through a horizontal annulus entrance region by utilizing Ag-TiO_2/Water hybrid nanofluid. The interior cylinder has a uniform heat flux, while the exterior cylinder is adiabatic. They reported that the secondary flow was important in the upper part of the annulus and influenced the development of axial flow and temperature field. In addition, the secondary flow decelerates the axial velocity in the upper part of the annulus and accelerates it in the lower part.

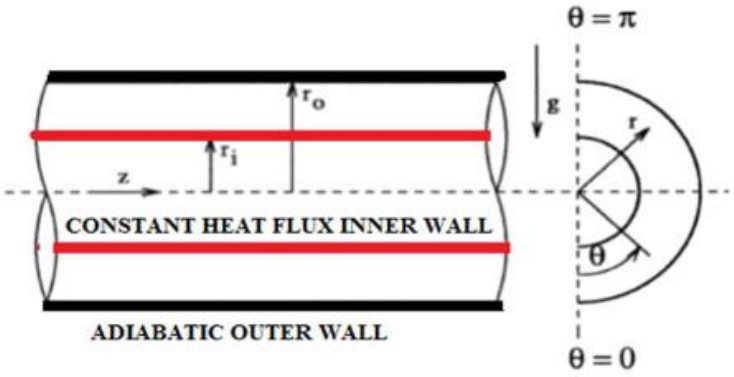

Figure I.6. Schematic of the geometry [25].

Abedini et al. [26] investigated numerically mixed convection using a water-based fluid with aluminium oxide, titanium oxide, silver and copper nanoparticles through a horizontal annular duct. The inner and outer cylinders have constant temperatures and rotate at a constant angular velocity in both directions. Finite volume method was used to solve the system of equations. The simulation was carried out for various values of Rayleigh ($10^3 \leq Ra \leq 10^5$), Richardson, Reynolds ($\leq Re \leq 200$), and the volume fraction ($0 \leq \varphi \leq 5$). Their findings revealed that the heat transfer was increased as Rayleigh and Richardson increased, while it was reduced as the Reynolds number increased.

Gorjaei et al. [27] studied laminar forced convection of (Al_2O_3/Water)nanofluid inside a horizontal concentric annulus with a constant wall temperature using a two-phase method. Their results were verified by Mirmasoumi and Behzadmehr. [28] and the experimental work of [29]. They noticed that heat transfer and thermal entropy rates enhanced with the augmentation of Reynolds number or volume fraction. They also found the dominance of thermal entropy generation during all the studies.

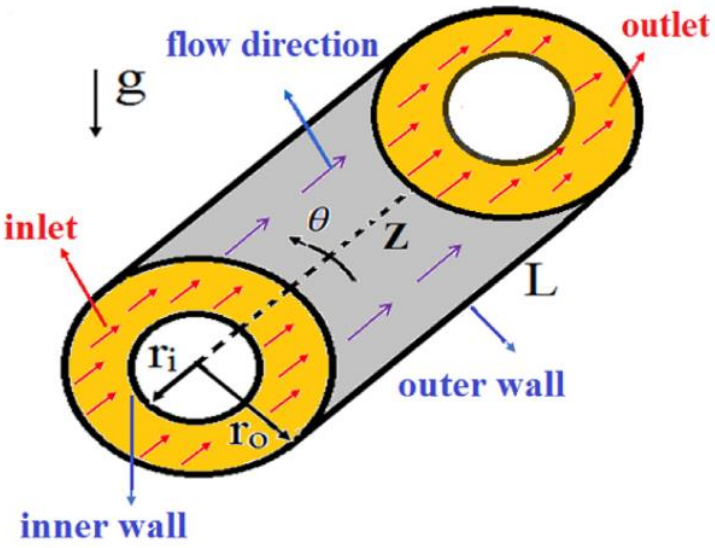

Figure I.7. Sketch of the geometry studied [27].

Bahiraei et al. [30] studied mixed convection and entropy generation using CuO-Water nanofluid through an inclined annulus. The interior and exterior cylinders have a uniform heat flux. They reported that the total entropy generation and heat transfer rate rise with the rise of Richardson number. Furthermore, raising the inclination angle from 0° to 75° leads to a rise in heat transfer and a reduction in total entropy generation.

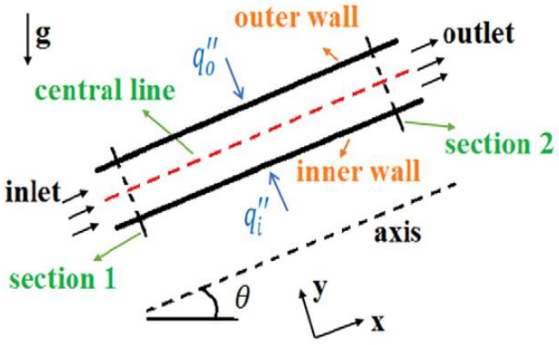

Figure I.8. The geometry of the study [30].

In the presence of a magnetic field, the fluid flow is exposed to two-volume forces: the buoyancy and Lorentz forces. The latter can induce magnetohydrodynamics (MHD). Aminfar et al. [31] simulated a three dimensional mixed convection heat transfer of (Fe_3O_4-kerosene) magnetic nanofluid through a circular pipe under the influence of a non uniform magnetic field. The governing equations were discretized using the control volume technique. The simulation was carried out for two magnetic field gradients and found that a magnetic field with a negative

gradient behaves like buoyancy force and increases the Nusselt number. In contrast, a magnetic field with a positive gradient reduces it.

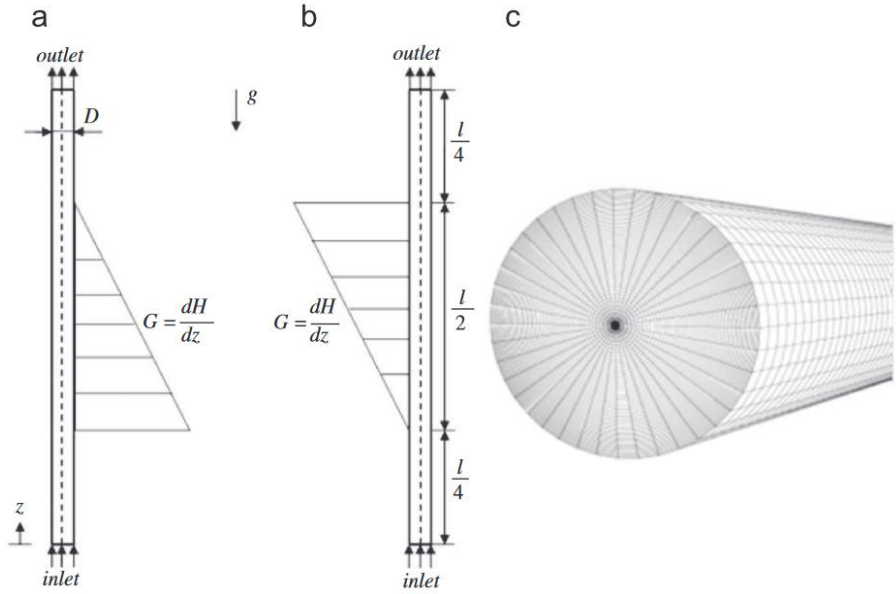

Figure I.9. Sketch of the geometry with: (a) negative and (b) positive magnetic field gradient, and (c) mesh used [31].

Alsaedi et al. [32] investigated a numerical study of GO-Cu/kerosene hybrid nanofluid between two coaxial cylinders under a magnetic field along the radial direction. The inner cylinder was fixed, while the outer cylinder displayed a rotation. They found that a strong magnetic field increases the temperature, fluid pressure, and skin friction while it decreases the velocity and the Nusselt number.

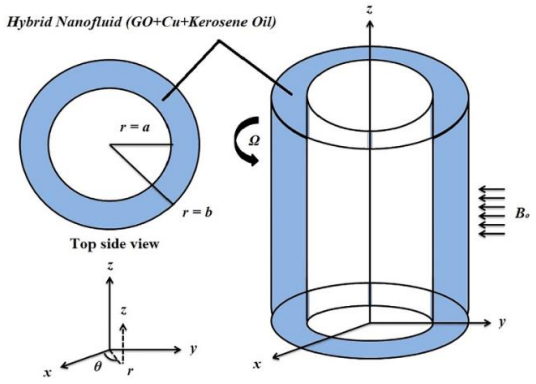

Figure I.10. Geometry of the problem [32].

Barnoon et al. [33] analyzed entropy generation and heat transfer of various nanofluids (Al_2O_3/water, TiO_2/water, ZnO/water, and SiO_2/water) through an annular pipe under the influence of a magnetic field. The system of equations was solved by the Finite volume technique using single-phase and two-phase models. Their investigation was carried out for different Reynolds numbers ($500 \leq Re \leq 1500$) and ($0 \leq Ha \leq 20$). They found that:

- Nusselt number was higher in the two-phase model than in the single-phase model. Also, by boosting the nanoparticle diameter, entropy generation increased.
- Nusselt number increases slightly with the Hartmann number increasing.

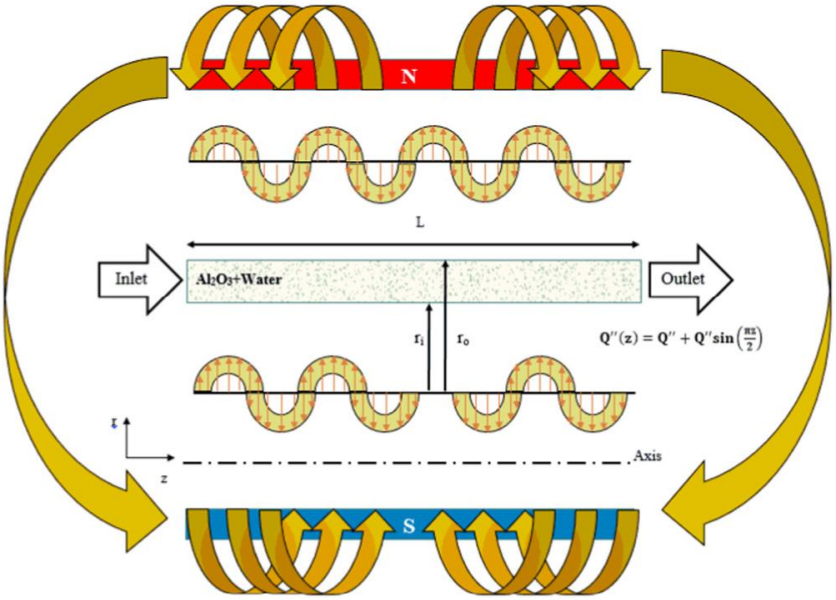

Figure I.11. Sketch of the problem [33].

Goharkhah et al. [34] simulated the impact of a non-uniform magnetic field on forced convection heat transfer of magnetic nanofluid through a horizontal pipe. Their objective is to highlight the importance of the magnetic field's location and to explore the potential for enhancing heat transfer by identifying the optimal placement of the magnetic field source. The simulation was carried out in two cases. In the first case, the emplacement of the magnetic dipole varied vertically and horizontally; in the second case, multiple magnetic sources were tested. The two-dimensional equations were solved using the Finite volume method. Their results showed that:

- Positioning a magnetic field at any location near the channel does not improve convective heat transfer.
- The influence of magnetic field position on heat transfer depends entirely on thermal boundary conditions.
- Using a Genetic Algorithm (GA), an optimal configuration for a set of 8 magnetic field source locations was obtained, leading to a 27% improvement in heat transfer compared to the absence of a magnetic field.

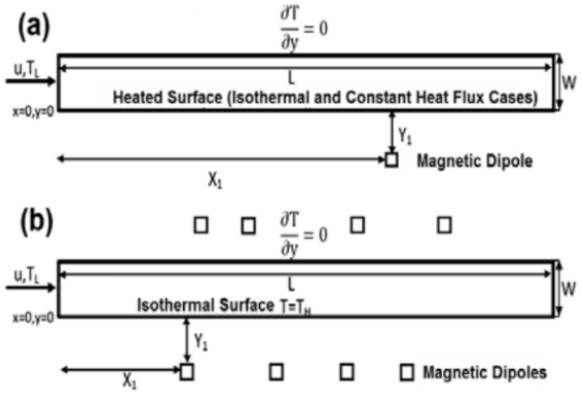

Figure I.12. Sketch of the geometry [34].

Servati et al. [35] investigated forced convection heat transfer (Al_2O_3–water) nanofluid through a pipe partially filled with porous media and exposed to a constant magnetic field. Lattice Boltzmann technique was used to solve the system of equations. They examined the effect of various values of Hartmann number ($0 \leq Ha \leq 15$) and volume fraction ($0\% \leq \phi \leq 7\%$) on the rate of heat transfer, and they revealed that:

- Increasing Hartmann number causes a slow improvement in the Nusselt number.
- There is no significant effect of Hartmann number in the porous zone.

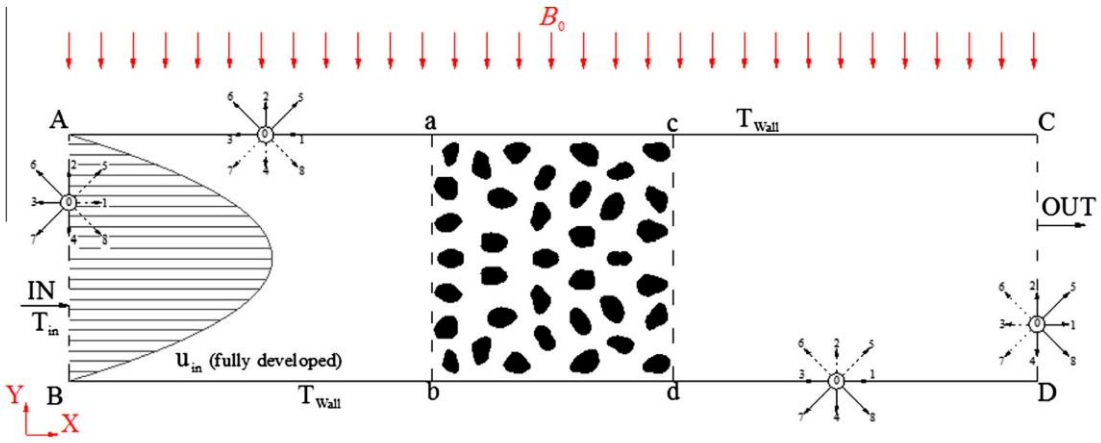

Figure I.13. Schematic of the problem studied [35].

Mohsenian et al. [36] studied analytically convective heat transfer within an annular channel influenced by a horizontal magnetic field. They studied the impacts of Reynolds number ($0 < Re < 4$), Hartmann number ($0 < Ha < 8$), Eckert number ($0 < Ec < 0.4$), radiation parameter ($0 < Rd < 10$), and the aspect ratio ($0.5 \leq r_1/r_2 \leq 0.8$). They revealed that increasing the Hartmann number for a given Reynolds number improves the heat transfer.

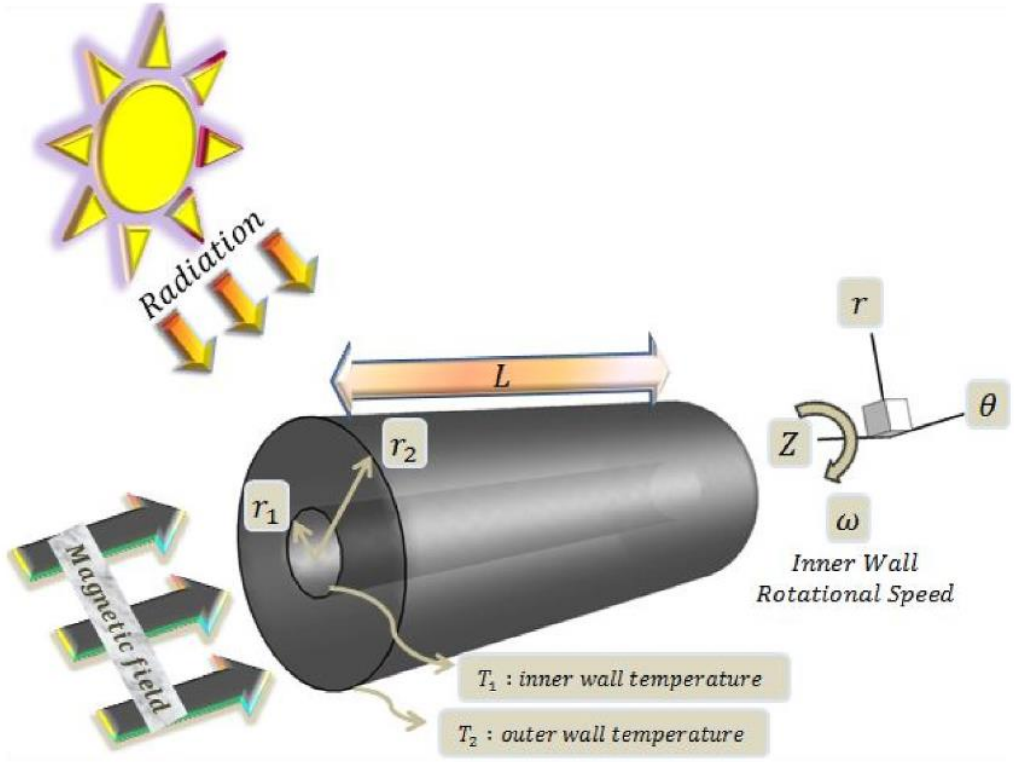

Figure I.14. Sketch of the geometry [36].

Hatami et al [37] studied experimentally forced convection heat transfer of Fe_3O_4–water nanofluid through a uniform heated horizontal tube. They studied the effect of Hartmann number ($33.4 \times 10^{-4} \leq Ha \leq 136.6 \times 10^{-4}$) and nanoparticle concentrations ($0\% \leq \phi \leq 1\%$) on heat transfer characteristics. They found that boosting the Hartmann number reduces the Nusselt number by 25%.

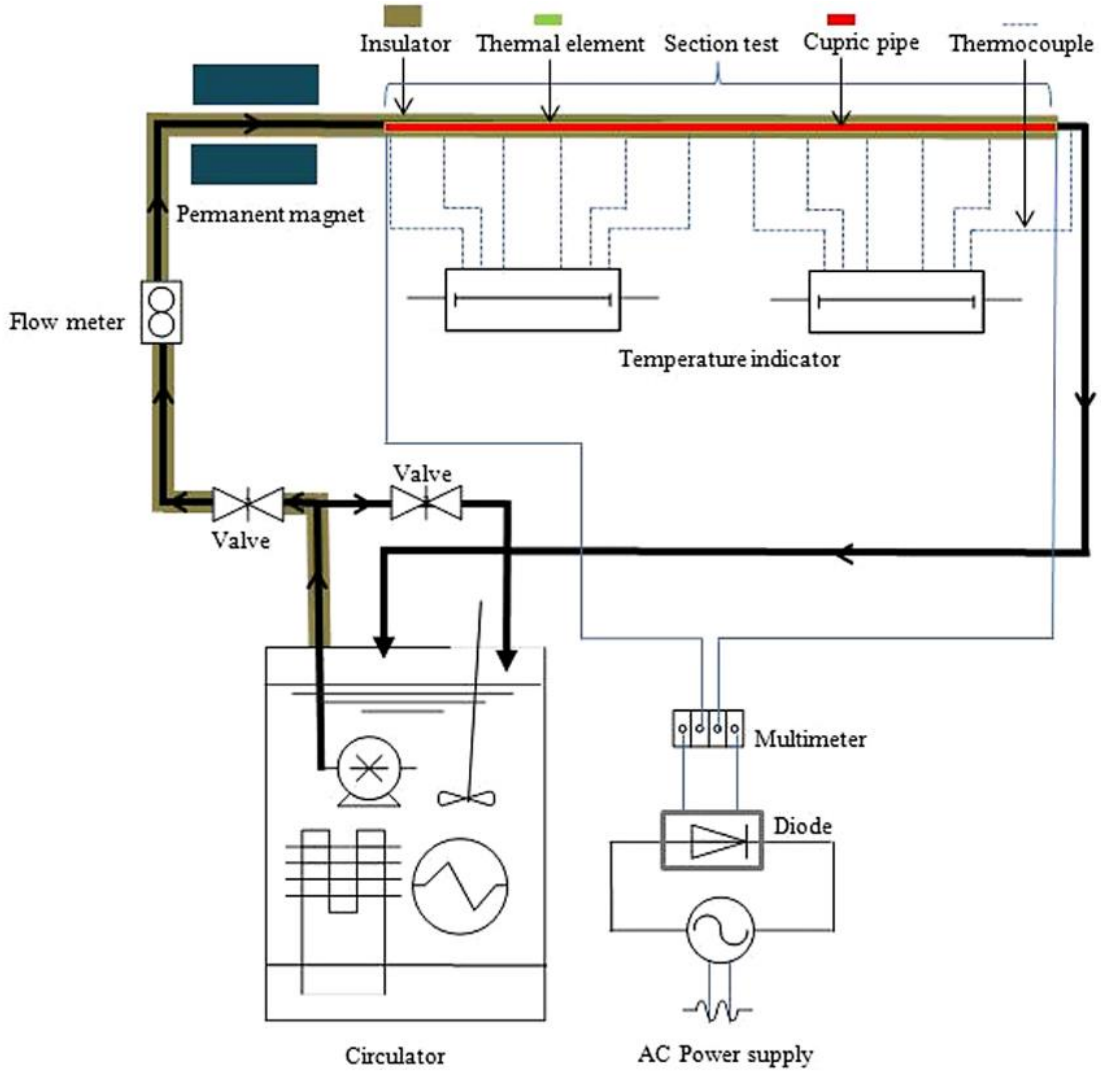

Figure I.15. Schematic of the experiment [37].

Liu et al. [38] conducted a numerical study on laminar forced convection of a (Cu/water) nanofluid within two coaxial cylinders. Both the outer and inner walls were subjected to a constant heat flux, with a porous grid applied to these walls. Finite volume method was used to solve the system of equations. The simulation explored two different geometries, where in the second geometry, the porous grid extended radially. The study varied the Reynolds number

from (10≤Re≤100), volume fraction from (0% ≤ϕ≤ 5%), and porosity at 0.5 and 0.9. Their results found that:

- The highest value of Nusselt number was attained with the second geometry and a porosity of 0.9, compared to 0.5.
- Increasing the volume fraction at high Reynolds numbers did not significantly enhance heat transfer.

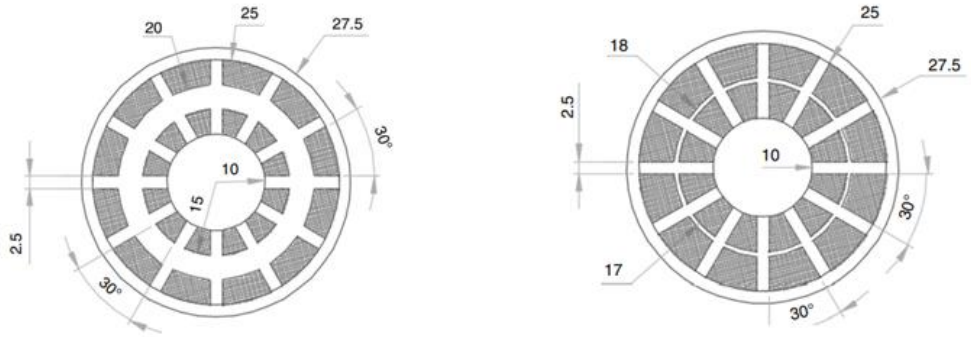

Figure I.16. Sketch of the problem studied [38].

Moghadasi et al. [39] studied numerically laminar forced convection enhancement of (Al_2O_3-CuO/water) hybrid nanofluid through a U-shape pipe embedded in a porous medium exposed to a constant heat flux. Ansys Fluent software was used to solve the system of equations. The nanofluid flow was treated as a two-phase flow, and the Darcy-Brinkman-Forchheimer model was utilized to model the fluid movement within a porous medium. They evaluated the effect of volume fraction (0%≤ϕ≤5%), Darcy number (10^{-4}≤Da≤10^{-1}), and porous thickness ratio (0≤r_p≤1) on average Nusselt number, pressure drop, and performance evaluation criteria PEC. Their findings revealed that the highest PEC was achievable with permeable porous media (Da = 0.1 and r_p = 0.8). Furthermore, among the other nanoparticles tested, CuO provided the greatest enhancement.

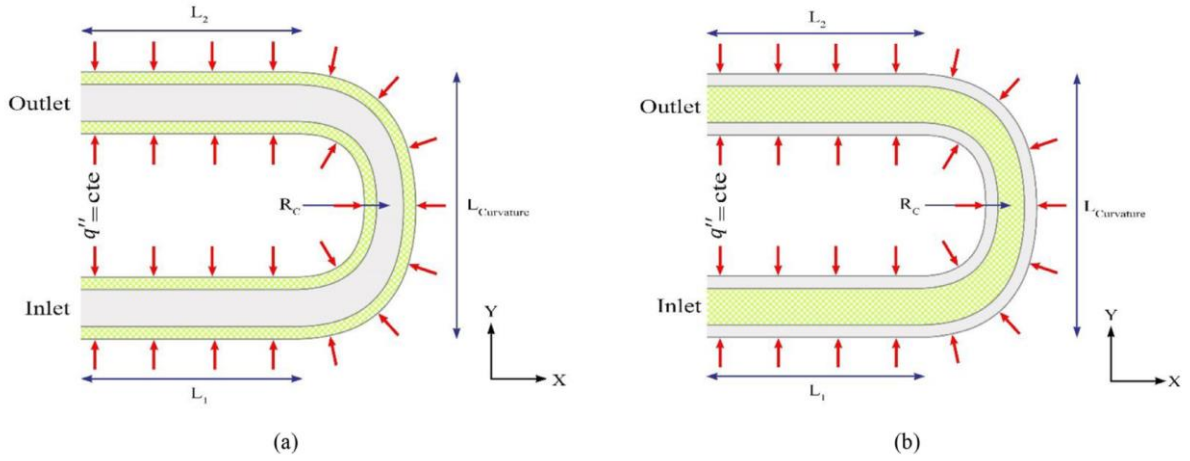

Figure I.17. Sketch of the problem studied [39].

Siavashi et al. [40] investigated forced convection heat transfer of (alumina/water) nanofluid inside an annulus using porous ribs to improve the heat transfer. The annulus's inner and outer walls were subjected to a uniform heat flux. The emplacement of the porous ribs was evaluated in two cases: they are attached to the inner wall of the annulus in the first case, whereas they are attached to the outer wall in the second case. The simulation was conducted using Ansys fluent 16 software, based on Finite volume method for different volume fraction values varying from 0 to 5%, and two values Darcy number Da 0.1, 0.0001. They found that the emplacement of the porous ribs on the inner wall enhances the performance number (the ratio of heat transfer enhancement over pressure increment, PN) rather than using theme at the outer wall, which increases unity less.

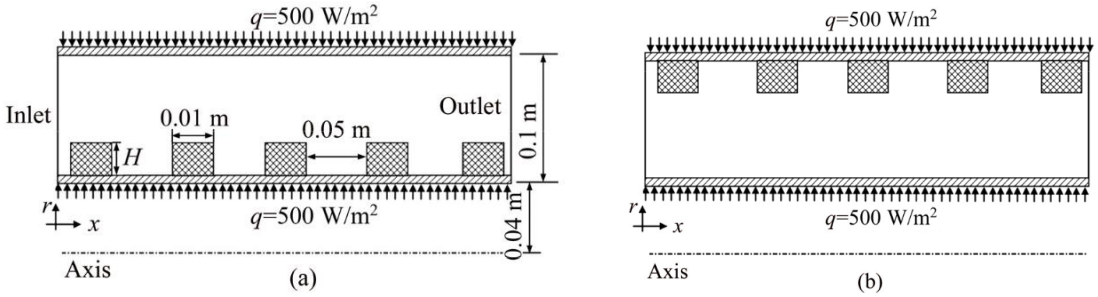

Figure I.18. Sketch of the problem studied [40].

Talesh Bahrami and Safikhani [41] numerically studied the improvement of mixed convection heat transfer through an eccentric annulus by placing a porous layer on the inner rotating wall. The inner cylinder was cooler than the outer one. The simulation was carried out using ANSYS FLUENT 15.0 software for various value of Richardson number, Rayleigh number, Darcy number, the eccentricity, and the inner wall peripheral location. Their results showed that as the Rayleigh number increases, the effect of the porous media insert becomes very significant. Furthermore, the heat transfer was enhanced with a high value of Darcy number.

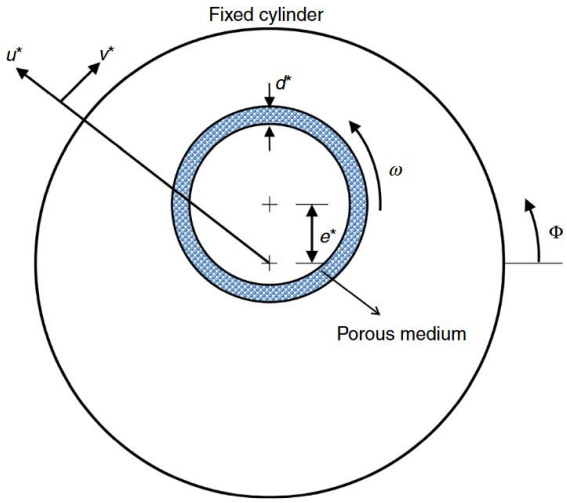

Figure I.19. Sketch of the geometry [41].

Nejad et al. [42] performed a numerical investigation on the heat transfer of Al_2O_3–Cu/water hybrid nanofluid through a copper metal foam subjected to a constant heat flux. They studied the effect of Reynolds number, nanofluid concentration, porosity, number of pores per inch PPI, and Prandtl number. The simulation used a single-phase approach to model the nanofluid flow. They found that the increase in Reynolds number, volume fraction, PPI, and Pr increases the Nusselt number, while the increase in porosity decreases it. Furthermore, new correlations were proposed for fixed and variable porosity.

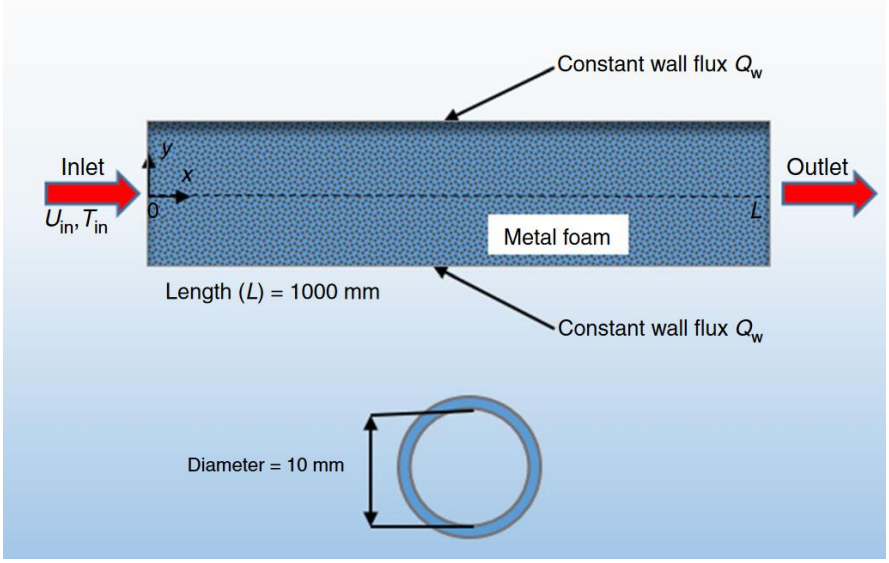

Figure I.20. Schematic of the geometry studied [42].

Kuharat and Bég [43] simulated the convective heat transfer of different nanofluid types, CuO, TiO_2, and Al_2O_3, through an annular solar collector. The inner tube includes pure water, while the annulus region includes nanofluid. The simulation was carried out using Ansys Fluent software. The radiative heat transfer was included using the Rosseland radiative model. Their analysis has shown that the highest temperature was achieved for copper oxide nanofluid, followed by titanium oxide, and the lowest temperature was achieved for aluminium oxide.

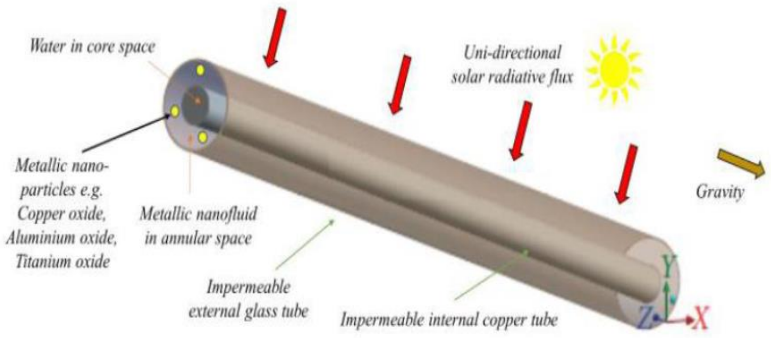

Figure I.21. The geometry studied [43].

Peng et al. [44] simulated nanofluid flow in an axial magnetic field considering radiation impact and viscous dissipation in a horizontal concentric pipe. The fourth order solved the basic equations of the Rang Kuta scheme, and the Rosseland model was used to model the radiative heat transfer. They studied the impact of the Reynold number, Hartman number, radiation parameter, and aspect ratio. Their results were validated by Aberkane et al [45]. They found

that increasing the radiation parameter and Hartman number reduces the velocity and temperature boundary layer thicknesses. Conversely, rising Eckert and Reynolds numbers cause an augmentation in the thicknesses of the velocity and temperature boundary layers.

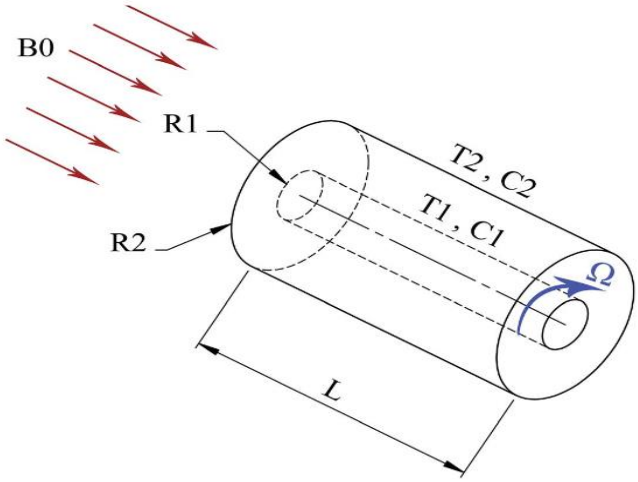

Figure I.22. Geometry studied [44].

Ahmed Faiq Al-Alawy [46] performed numerical analysis of forced convection heat transfer using Cu/Engine oil nanofluid through an annular duct. The upper and lower surfaces were subjected to a uniform temperatures T_h and T_c, respectively. The simulation was performed using COMSOL 3.5 software. They reported that both temperature and velocity profile decrease with the rise of nanoparticles volume concentration due to increased viscosity. In contrast, the heat transfer coefficient increases due to the enhanced thermal conductivity that overcome the reduction in gradient.

Siavashi Majid and Jamali Mohammad [47] studied heat transfer and entropy generation of (Al_2O_3/water) through an annulus duct subjected to a uniform heat flux. Their goal was to determine the optimum radius ratio that maximizes the heat transfer and minimizes the entropy generation. The simulation was conducted for different volume concentrations, Reynolds numbers, and thermal boundaries. Two different approaches were used to model the entropy. Their results found that the optimal radius ratio for increasing the Nusselt number while decreasing entropy generation is influenced by the thermal boundary conditions, Reynolds number, and nanoparticle volume fraction.

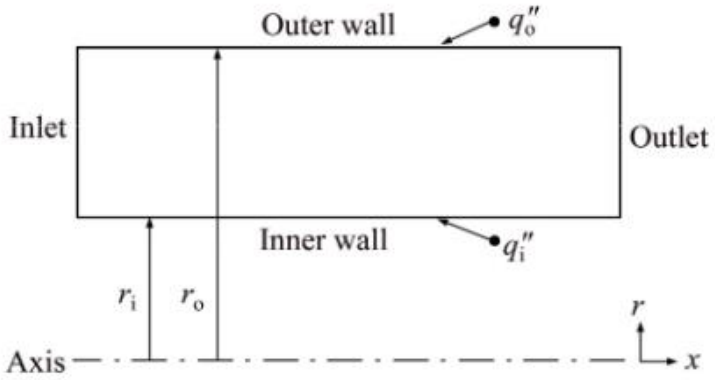

Figure I.23. Sketch of the problem studied [47].

Shahsavar et al. [48] studied heat transfer and entropy generation of (CNT-Fe_3O_4/Water) inside a 2D annulus pipe exposed to a uniform heat flux on both walls. Their investigation was to find the optimum cases which give high heat transfer coefficients and low entropy generation by varying the radius ratio 0.2<r*<0.8 and the volume concentration of (0.5< Fe3O4 < 0.9), and (0.1 <CNT< 1.1). The simulation was carried out using the Finite volume approach, and the neural network method that used a genetics algorithm to find the optimum case. They found that the optimum case was achieved for phi1=0.8, = 1.1 and r*= 0.2.

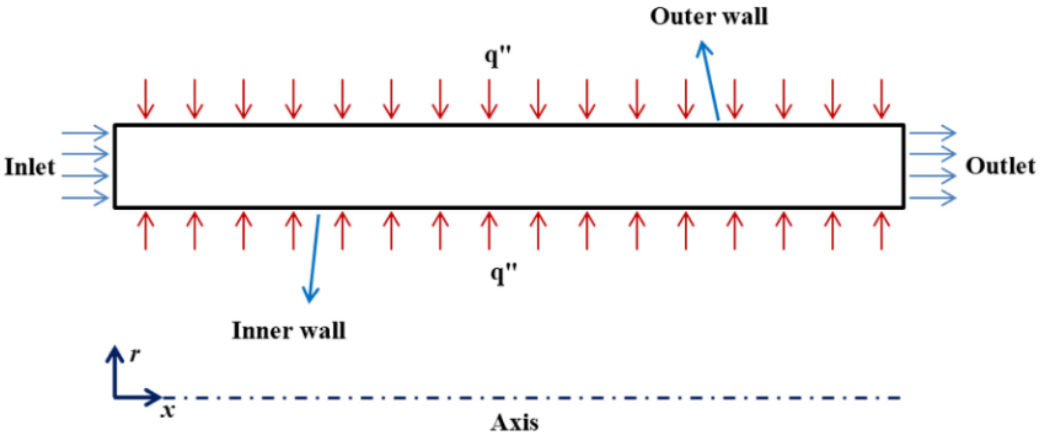

Figure I.24. Sketch of the problem studied [48].

Chapter II: Mathematical Modelling

II.1. Introduction

This chapter will present two applications outlined below, providing detailed insights into each configuration's physical models, governing equations, boundary conditions, and hypotheses.

- The first application involves a three dimensional investigation of mixed convection and entropy generation using binary and ternary hybrid nanofluids. This investigation will be conducted through a straight annulus duct exposed to a uniform heat flux and magnetic field utilizing the FORTRAN code.
- The second application focuses on a three dimensional investigation of forced convection heat transfer and entropy generation of binary and ternary hybrid nanofluid. This analysis will be carried out through a wavy annulus duct exposed to a uniform heat flux and a non-uniform magnetic field utilizing Ansys-Fluent software.

Additionally, we will establish dimensionless parameters to transform the equation system into a dimensionless form.

II.2. Physical Model

II.2.1. First Application

In this configuration, mixed convection heat transfer and entropy generation through a permeable annulus exposed to both uniform heat flux and magnetic field are studied. The geometry sketch is illustrated in **Figure II.1**; it includes two horizontal concentric cylinders; the inner cylinder diameter D_i=5 mm, while the outer cylinder diameter D_o=10 mm, thus resulting in a radius ratio of r_o/r_i=2. The exterior wall is exposed to a constant heat flux, while the inner wall remains adiabatic. The nanofluid enters at constant velocity and temperature v_0 and T_0. A FORTRAN code based on finite volume technique is used to solve the system of equations. The control parameters are Re=800, ($0 \leq Ha \leq 50$), ($10^{-4} \leq Da \leq 10^{-1}$), ($7.5\times10^{5} \leq Gr \leq 10^{6}$), and ($0\% \leq \phi \leq 5\%$).

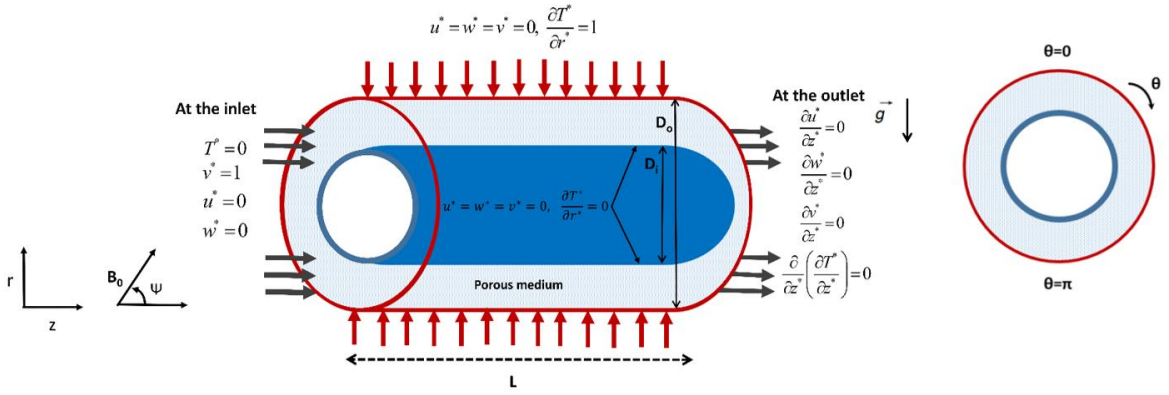

Figure II. 1. First configuration schematic.

The hypotheses forming the basis of this configuration are as follows:

Single-Phase Approach: The system is approached from a single-phase perspective, neglecting multiphase complexities.

Unsteady State in 3D Cylindrical Coordinates: The problem is conceptualized as an unsteady state scenario, accounting for three-dimensional cylindrical coordinates to capture the system's temporal and spatial variations.

Porous Media Characteristics: The porous media within the annulus are treated as saturated, homogeneous, and isotropic, streamlining the analysis of fluid flow and heat transfer.

Neglect of Viscous Dissipation and Joule Heating: This study disregarded the influence of viscous dissipation and Joule heating, focusing primarily on convective heat transfer and magnetic field interactions.

II.2.2. Second Application

In this configuration, forced convection and entropy generation through a wavy porous annulus exposed to a uniform heat flux and a non-uniform magnetic field is studied. The geometry used in this investigation is shown in **Figure II.2**, which includes two concentric wavy cylinders. The exterior cylinder is exposed to a constant heat flux, while the inner cylinder is adiabatic. At the inlet to the annulus channel, the hybrid nanofluids are assumed to have a constant temperature T_0 and velocity v_0. Joule heating and viscous dissipation are considered. A single-phase approach and thermal equilibrium are assumed. A non-uniform magnetic field is enacted on the outer heated wall in the radial direction, with variations in its application across four

scenarios depicted in **Figure II.3**. In the scenario of full magnetic field application (FMF), it permeates the entire outer wall throughout the domain. Conversely, for partial magnetic field application (PMF), the domain is divided into four distinct sections. In the first scenario, the magnetic field is applied to two zones: one at the initial section and the other at the midsection. In the second scenario, it is solely applied at the midpoint of the duct. Finally, in the third scenario, it is applied to a midsection and a section close to the outlet. A computational fluid dynamics (CFD) solver based on Finite volume technique is used.

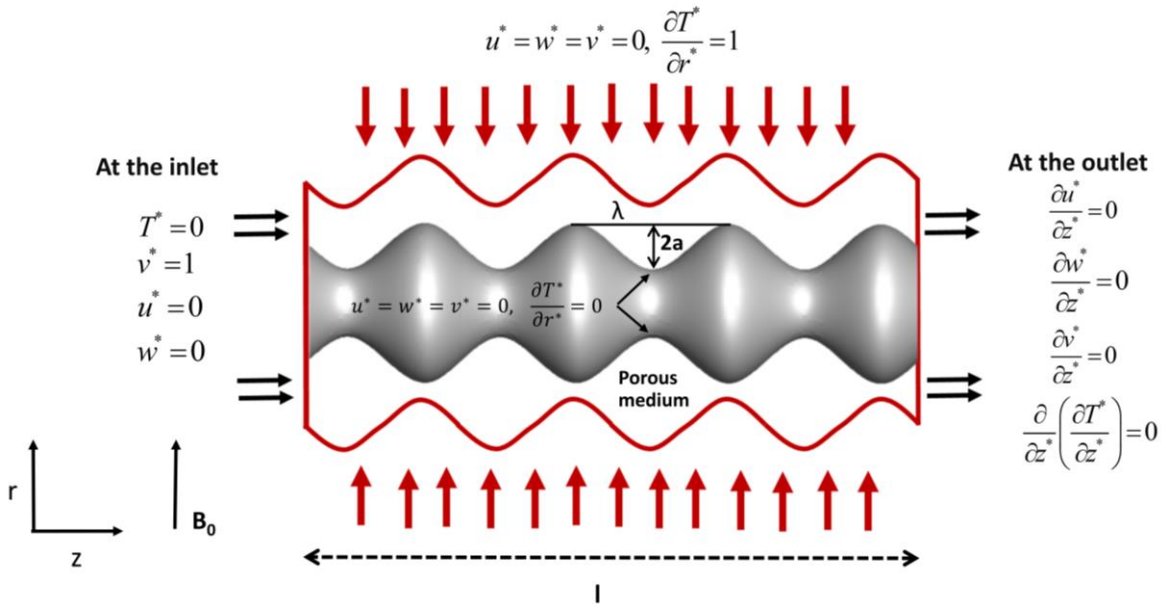

Figure II. 2. Second configuration schematic

Full magnetic field (FMF) Partial magnetic field (PMF): scenario 1

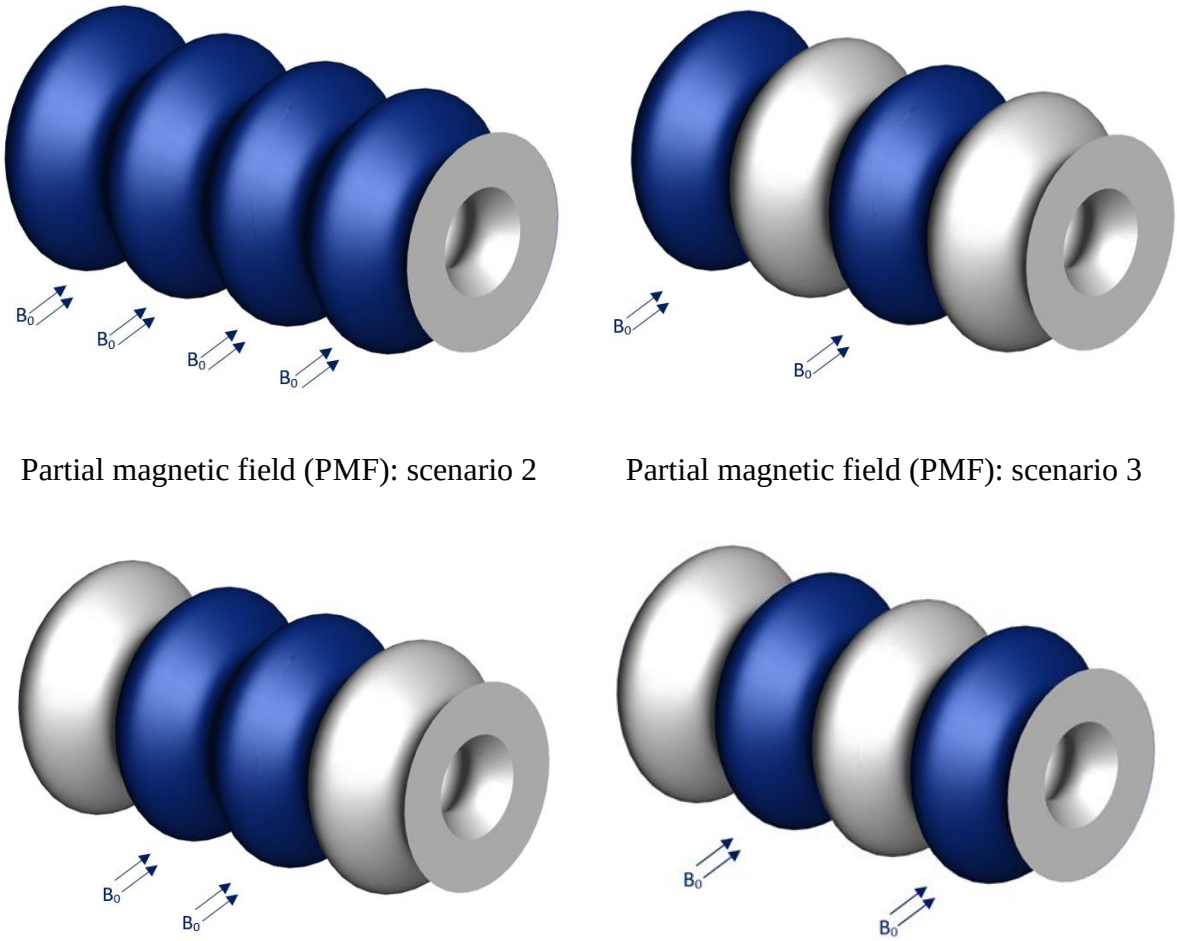

Partial magnetic field (PMF): scenario 2 Partial magnetic field (PMF): scenario 3

Figure II. 3. Schematic illustrating different scenarios of magnetic field application.

II.3. Governing equations

The convection phenomena coupled with the magneto-hydrodynamics are governed by the general equations of mass, momentum, and energy conservation, with Ohm's law and Maxwell equations for magnetic field application.

- **Conservation of mass,**

$$\frac{\partial \rho}{\partial t} + \frac{1}{r}\frac{\partial (\rho r u)}{\partial r} + \frac{1}{r}\frac{\partial (\rho w)}{\partial \theta} + \frac{\partial (\rho v)}{\partial z} = 0 \qquad (II.1)$$

- **Conservation of momentum in radial direction,**

$$\rho\left(\frac{\partial u}{\partial t}+\frac{1}{r}\frac{\partial}{\partial r}(ruu)+\frac{1}{r}\frac{\partial}{\partial \theta}(uw)+\frac{\partial}{\partial z}(uv)-\frac{w^2}{r}\right) = -\frac{\partial p}{\partial r}+\mu\left[\frac{1}{r}\frac{\partial}{\partial r}\left(r\frac{\partial u}{\partial r}\right)+\frac{1}{r^2}\frac{\partial}{\partial \theta}\left(\frac{\partial u}{\partial \theta}\right)+\frac{\partial}{\partial z}\left(\frac{\partial u}{\partial z}\right)-\frac{u}{r^2}-\frac{2}{r^2}\frac{\partial w}{\partial \theta}\right]+\rho g_r - \frac{\mu}{\mathrm{K}}u+F_r \qquad (II.2)$$

- **Conservation of momentum in angular direction,**

$$\rho\left(\frac{\partial w}{\partial t}+\frac{1}{r}\frac{\partial}{\partial r}(ruw)+\frac{1}{r}\frac{\partial}{\partial \theta}(ww)+\frac{\partial}{\partial z}(vw)+\frac{uw}{r}\right) = -\frac{\partial p}{\partial \theta}+\mu\left[\frac{1}{r}\frac{\partial}{\partial r}\left(r\frac{\partial w}{\partial r}\right)+\frac{1}{r^2}\frac{\partial}{\partial \theta}\left(\frac{\partial w}{\partial \theta}\right)+\frac{\partial}{\partial z}\left(\frac{\partial w}{\partial z}\right)-\frac{w}{r^2}+\frac{2}{r^2}\frac{\partial u}{\partial \theta}\right]+\rho g_\theta - \frac{\mu}{\mathrm{K}}w+F_\theta \qquad (II.3)$$

- **Conservation of momentum in axial direction,**

$$\rho\left(\frac{\partial v}{\partial t}+\frac{1}{r}\frac{\partial}{\partial r}(ruv)+\frac{1}{r}\frac{\partial}{\partial \theta}(wv)+\frac{\partial}{\partial z}(vv)\right) = -\frac{\partial p}{\partial z}+\mu\left[\frac{1}{r}\frac{\partial}{\partial r}\left(r\frac{\partial v}{\partial r}\right)+\frac{1}{r^2}\frac{\partial}{\partial \theta}\left(\frac{\partial v}{\partial \theta}\right)+\frac{\partial}{\partial z}\left(\frac{\partial w}{\partial z}\right)\right]-\frac{\mu}{\mathrm{K}}v + F_z \qquad (II.4)$$

Where F represent the Lorentz force which is given as follows:

$$\vec{F}=\vec{J}\times\vec{B} \qquad (II.5)$$

$$\vec{J}=\sigma_{thnf}\left(\vec{E}+\vec{V}\times\vec{B}\right) \qquad (II.6)$$

$$\left(\vec{V}.\nabla\right)\vec{B}=\frac{1}{\mu_0\sigma_{thnf}}\nabla^2\vec{B}+\left(\vec{B}.\nabla\right)\vec{V} \qquad (II.7)$$

- **Energy equation,**

The energy equation considering the viscous dissipation and joule heating is given as follows:

$$\frac{\partial T}{\partial t}+\frac{1}{r}\frac{\partial}{\partial r}(ruT)+\frac{1}{r}\frac{\partial}{\partial \theta}(wT)+\frac{\partial}{\partial z}(vT) = \frac{k}{\rho C_p}\left[\frac{1}{r}\frac{\partial}{\partial r}\left(r\frac{\partial T}{\partial r}\right)+\frac{1}{r^2}\frac{\partial}{\partial \theta}\left(\frac{\partial T}{\partial \theta}\right)+\frac{\partial}{\partial z}\left(\frac{\partial T}{\partial z}\right)\right]+\emptyset + \frac{J^2}{\sigma} \quad (II.8)$$

Where $\emptyset$ represents the viscous dissipation term;

$$\emptyset = 2\mu\left[\left(\frac{\partial u}{\partial r}\right)^2+\left(\frac{1}{r}\frac{\partial w}{\partial \theta}+\frac{u}{r}\right)^2+\left(\frac{\partial v}{\partial z}\right)^2\right]+\mu\left(r\frac{\partial}{\partial r}\left(\frac{w}{r}\right)+\frac{1}{r}\frac{\partial u}{\partial \theta}\right)^2+\mu\left(\frac{1}{r}\frac{\partial v}{\partial \theta}+\frac{\partial w}{\partial z}\right)^2 + \mu\left(\frac{\partial u}{\partial z}+\frac{\partial v}{\partial r}\right)^2 \quad (II.9)$$

- **The boundary conditions**

At the duct's inlet:

$$z=0, r_i \le r \le r_o, 0 \le \theta \le 2\pi : u=w=0, v=v_0, T=T_0 \quad (II.10)$$

At duct's outlet

$$z=L, r_i \le r \le r_o, 0 \le \theta \le 2\pi : \frac{\partial u}{\partial z}=\frac{\partial w}{\partial z}=\frac{\partial v}{\partial z}=\frac{\partial}{\partial z}\left(\frac{\partial T}{\partial z}\right)=0 \quad (II.11)$$

At the outer wall

$$r=r_o, 0 \le \theta \le 2\pi, 0 \le z \le L : u=w=v=0, q_w=k_s\frac{\partial T}{\partial r} \quad (II.12)$$

At the inner wall

$$r=r_o, 0 \le \theta \le 2\pi, 0 \le z \le L : u=w=v=k_s\frac{\partial T}{\partial r}=0 \quad (II.13)$$

The systems of equations using in this study is transformed into the dimensionless form using the following parameters:

$$r^*=r/D_h, z^*=z/D_h,\ u^*=u/v_0,\ w^*=w/v_0, v^*=v/v_0, t^*=v_0 t/D_h,$$

$$p^*=\frac{P}{\rho_{hnf} v_0}, T^*=\frac{(T-T_0)}{q_w D_h/k_{hnf}}, Re=\frac{\rho_f v_0 D_h}{\mu_f}, Gr=\frac{g\beta_f q_w D_h^4}{k_f \nu_f^2}, Pr=\frac{\mu_f Cp_f}{k_f},$$

$$Ha=B_0 D_h\sqrt{\frac{\sigma_f}{\mu_f}},\ Da=\frac{K}{D_h^2} \quad (II.14)$$

II.3.1. First configuration

The systems of equations used in the first configuration is given as follows:

Conservation of mass,

$$\frac{1}{r^*}\frac{\partial(r^*u^*)}{\partial r^*}+\frac{1}{r^*}\frac{\partial w^*}{\partial\theta}+\frac{\partial v^*}{\partial z^*}=0 \qquad (II.15)$$

Conservation of momentum in radial direction,

$$\begin{aligned}\frac{\partial u^*}{\partial t^*}+\frac{1}{r^*}\frac{\partial}{\partial r^*}(r^*u^*u^*)+\frac{1}{r^*}\frac{\partial}{\partial\theta}(u^*w^*)+\frac{\partial}{\partial z^*}(u^*v^*)-\frac{w^{*2}}{r^*}\\ =-\frac{\partial p^*}{\partial r^*}+\frac{(\rho\beta)_{hnf}}{\rho_{hnf}}\frac{\mathrm{Gr}}{\mathrm{Re}^2}\cos\theta T^*+\frac{\sigma_{hnf}/\sigma_f}{\rho_{hnf}/\rho_f}\frac{\mathrm{Ha}^2}{\mathrm{Re}}(v^*\sin\psi\cos\psi-u^*\cos^2\psi)\\ -\frac{1}{\mathrm{Re\,Da}}u^*\\ +\frac{\mu_{hnf}/\mu_f}{\rho_{hnf}/\rho_f}\frac{1}{\mathrm{Re}}\left[\frac{1}{r^*}\frac{\partial}{\partial r^*}\left(r^*\frac{\partial u^*}{\partial r^*}\right)+\frac{1}{r^{*2}}\frac{\partial}{\partial\theta}\left(\frac{\partial u^*}{\partial\theta}\right)+\frac{\partial}{\partial z^*}\left(\frac{\partial u^*}{\partial z^*}\right)-\frac{u^*}{r^{*2}}\right.\\ \left.-\frac{2}{r^{*2}}\frac{\partial w^*}{\partial\theta}\right]\end{aligned} \qquad (II.16)$$

Conservation of momentum in angular direction,

$$\begin{aligned}\frac{\partial w^*}{\partial t^*}+\frac{1}{r^*}\frac{\partial}{\partial r^*}(r^*u^*w^*)+\frac{1}{r^*}\frac{\partial}{\partial\theta}(w^*w^*)+\frac{\partial}{\partial z^*}(v^*w^*)-\frac{u^*w^*}{r^*}\\ =-\frac{1}{r^*}\frac{\partial p^*}{\partial\theta}+\frac{\sigma_{hnf}/\sigma_f}{\rho_{hnf}/\rho_f}\frac{\mathrm{Ha}^2}{\mathrm{Re}}(w^*\cos^2\psi+w^*\sin^2\psi)-\frac{1}{\mathrm{Re\,Da}}w^*\\ -\frac{(\rho\beta)_{hnf}}{\rho_{hnf}}\frac{\mathrm{Gr}}{\mathrm{Re}^2}\sin\theta T^*\\ +\frac{\mu_{hnf}/\mu_f}{\rho_{hnf}/\rho_f}\frac{1}{\mathrm{Re}}\left[\frac{1}{r^*}\frac{\partial}{\partial r^*}\left(r^*\frac{\partial w^*}{\partial r^*}\right)+\frac{1}{r^{*2}}\frac{\partial}{\partial\theta}\left(\frac{\partial w^*}{\partial\theta}\right)+\frac{\partial}{\partial z^*}\left(\frac{\partial w^*}{\partial z^*}\right)-\frac{w^*}{r^{*2}}\right.\\ \left.-\frac{2}{r^{*2}}\frac{\partial u^*}{\partial\theta}\right]\end{aligned} \qquad (II.17)$$

Conservation of momentum in axial direction,

$$\frac{\partial v^*}{\partial t^*} + \frac{1}{r^*}\frac{\partial}{\partial r^*}(r^* u^* v^*) + \frac{1}{r^*}\frac{\partial}{\partial \theta}(v^* w^*) + \frac{\partial}{\partial z^*}(v^* v^*) = -\frac{\partial p^*}{\partial z^*} + \frac{\sigma_{hnf}/\sigma_f}{\rho_{hnf}/\rho_f}\frac{\mathrm{Ha}^2}{\mathrm{Re}}(u^* \sin\psi \cos\psi - v^* \sin^2\psi) - \frac{1}{\mathrm{Re\ Da}}v^* + \frac{\mu_{hnf}/\mu_f}{\rho_{hnf}/\rho_f}\frac{1}{\mathrm{Re}}\left[\frac{1}{r^*}\frac{\partial}{\partial r^*}\left(r^*\frac{\partial v^*}{\partial r^*}\right) + \frac{1}{r^{*2}}\frac{\partial}{\partial \theta}\left(\frac{\partial v^*}{\partial \theta}\right) + \frac{\partial}{\partial z^*}\left(\frac{\partial v^*}{\partial z^*}\right)\right] \quad (II.18)$$

Conservation of energy,

$$\frac{\partial T^*}{\partial t^*} + \frac{1}{r^*}\frac{\partial}{\partial r^*}(r^* u^* T^*) + \frac{1}{r^*}\frac{\partial}{\partial \theta}(w^* T^*) + \frac{\partial}{\partial z^*}(v^* T^*) = \frac{k_{hnf}/k_f}{(\rho Cp)_{hnf}/(\rho Cp)_f}\frac{1}{\mathrm{Re\ Pr}}\left[\frac{1}{r^*}\frac{\partial}{\partial r^*}\left(r^*\frac{\partial T^*}{\partial r^*}\right) + \frac{1}{r^{*2}}\frac{\partial}{\partial \theta}\left(\frac{\partial T^*}{\partial \theta}\right) + \frac{\partial}{\partial z^*}\left(\frac{\partial T^*}{\partial z^*}\right)\right] \quad (II.19)$$

The initial and boundary conditions are follows:

$$t^* = 0, u^* = w^* = v^* = T^* = 0 \quad (II.20)$$

$t^* > 0$:

$$z^* = 0, u^* = w^* = T^* = 0, v^* = 1 \quad (II.21)$$

$$z^* = 100, \frac{\partial u^*}{\partial z^*} = \frac{\partial w^*}{\partial z^*} = \frac{\partial v^*}{\partial z^*} = \frac{\partial}{\partial z^*}\left(\frac{\partial T^*}{\partial z^*}\right) = 0 \quad (II.22)$$

$$r_0^* = 0.5, u^* = w^* = v^* = 0, \frac{\partial T^*}{\partial r^*} = 0 \quad (II.23)$$

$$r_0^* = 1, u^* = w^* = v^* = 0, \frac{\partial T^*}{\partial r^*} = 1 \quad (II.24)$$

II.3.2. Second configuration

The system of equations used in the second configuration is given as follows:

Conservation of mass,

$$\frac{1}{r^*}\frac{\partial (r^* u^*)}{\partial r^*} + \frac{1}{r^*}\frac{\partial w^*}{\partial \theta} + \frac{\partial v^*}{\partial z^*} = 0 \quad (II.25)$$

Conservation of momentum in radial direction,

$$\frac{1}{r^*}\frac{\partial}{\partial r^*}(r^*u^*u^*)+\frac{1}{r^*}\frac{\partial}{\partial \theta}(u^*w^*)+\frac{\partial}{\partial z^*}(u^*v^*)-\frac{w^{*2}}{r^*}$$
$$=-\frac{\partial p^*}{\partial r^*}+\frac{(\rho\beta)_{hnf}}{\rho_{hnf}}\frac{\mathrm{Gr}}{\mathrm{Re}^2}\cos\theta T^*$$
$$+\frac{\mu_{hnf}/\mu_f}{\rho_{hnf}/\rho_f}\frac{1}{\mathrm{Re}}\left[\frac{1}{r^*}\frac{\partial}{\partial r^*}\left(r^*\frac{\partial u^*}{\partial r^*}\right)+\frac{1}{r^{*2}}\frac{\partial}{\partial \theta}\left(\frac{\partial u^*}{\partial \theta}\right)+\frac{\partial}{\partial z^*}\left(\frac{\partial u^*}{\partial z^*}\right)-\frac{u^*}{r^{*2}}\right.$$
$$\left.-\frac{2}{r^{*2}}\frac{\partial w^*}{\partial \theta}\right]-\frac{1}{\mathrm{Re\,Da}}u^*+\frac{\sigma_{hnf}/\sigma_f}{\rho_{hnf}/\rho_f}\frac{\mathrm{Ha}^2}{\mathrm{Re}}(J^*\times B^*) \qquad (II.26)$$

Conservation of momentum in angular direction,

$$\frac{1}{r^*}\frac{\partial}{\partial r^*}(r^*u^*w^*)+\frac{1}{r^*}\frac{\partial}{\partial \theta}(w^*w^*)+\frac{\partial}{\partial z^*}(v^*w^*)-\frac{u^*w^*}{r^*}$$
$$=-\frac{1}{r^*}\frac{\partial p^*}{\partial \theta}-\frac{(\rho\beta)_{hnf}}{\rho_{hnf}}\frac{\mathrm{Gr}}{\mathrm{Re}^2}\sin\theta T^*$$
$$+\frac{\mu_{hnf}/\mu_f}{\rho_{hnf}/\rho_f}\frac{1}{\mathrm{Re}}\left[\frac{1}{r^*}\frac{\partial}{\partial r^*}\left(r^*\frac{\partial w^*}{\partial r^*}\right)+\frac{1}{r^{*2}}\frac{\partial}{\partial \theta}\left(\frac{\partial w^*}{\partial \theta}\right)+\frac{\partial}{\partial z^*}\left(\frac{\partial w^*}{\partial z^*}\right)-\frac{w^*}{r^{*2}}\right.$$
$$\left.-\frac{2}{r^{*2}}\frac{\partial u^*}{\partial \theta}\right]-\frac{1}{\mathrm{Re\,Da}}w^*+\frac{\sigma_{hnf}/\sigma_f}{\rho_{hnf}/\rho_f}\frac{\mathrm{Ha}^2}{\mathrm{Re}}(J^*\times B^*) \qquad (II.27)$$

Conservation of momentum in axial direction,

$$\frac{\partial v^*}{\partial t^*}+\frac{1}{r^*}\frac{\partial}{\partial r^*}(r^*u^*v^*)+\frac{1}{r^*}\frac{\partial}{\partial \theta}(v^*w^*)+\frac{\partial}{\partial z^*}(v^*v^*)$$
$$=-\frac{\partial p^*}{\partial z^*}+\frac{\mu_{hnf}/\mu_f}{\rho_{hnf}/\rho_f}\frac{1}{\mathrm{Re}}\left[\frac{1}{r^*}\frac{\partial}{\partial r^*}\left(r^*\frac{\partial v^*}{\partial r^*}\right)+\frac{1}{r^{*2}}\frac{\partial}{\partial \theta}\left(\frac{\partial v^*}{\partial \theta}\right)+\frac{\partial}{\partial z^*}\left(\frac{\partial v^*}{\partial z^*}\right)\right]$$
$$-\frac{1}{\mathrm{Re\,Da}}v^*+\frac{\sigma_{hnf}/\sigma_f}{\rho_{hnf}/\rho_f}\frac{\mathrm{Ha}^2}{\mathrm{Re}}(J^*\times B^*) \qquad (II.28)$$

Conservation of energy,

$$\frac{\partial T^*}{\partial t^*}+\frac{1}{r^*}\frac{\partial}{\partial r^*}(r^*u^*T^*)+\frac{1}{r^*}\frac{\partial}{\partial \theta}(w^*T^*)+\frac{\partial}{\partial z^*}(v^*T^*)=$$

$$\frac{k_{hnf}/k_f}{(\rho Cp)_{hnf}/(\rho Cp)_f}\frac{1}{\mathrm{Re\,Pr}}\left[\frac{1}{r^*}\frac{\partial}{\partial r^*}\left(r^*\frac{\partial T^*}{\partial r^*}\right)+\frac{1}{r^{*2}}\frac{\partial}{\partial \theta}\left(\frac{\partial T^*}{\partial \theta}\right)+\frac{\partial}{\partial z^*}\left(\frac{\partial T^*}{\partial z^*}\right)\right]$$

$$+\frac{\mu_{hnf}/\mu_f}{(\rho Cp)_{hnf}/(\rho Cp)_f}\frac{\mathrm{Br}}{\mathrm{Re\,Pr}}\left[2\left(\left(\frac{\partial u^*}{\partial r^*}\right)^2+\left(\frac{1}{r^*}\frac{\partial w^*}{\partial \theta}+\frac{u^*}{r^*}\right)^2+\left(\frac{\partial v^*}{\partial z^*}\right)^2\right)\right.$$

$$\left.+\left(r^*\frac{\partial}{\partial r^*}\left(\frac{w^*}{r^*}\right)+\frac{1}{r}\frac{\partial u^*}{\partial \theta}\right)^2+\left(\frac{1}{r^*}\frac{\partial v^*}{\partial \theta}+\frac{\partial w^*}{\partial z^*}\right)^2+\left(\frac{\partial u^*}{\partial z^*}+\frac{\partial v^*}{\partial r^*}\right)^2\right]$$

$$+\frac{\sigma_{hnf}/\sigma_f}{(\rho Cp)_{hnf}/(\rho Cp)_f}\frac{Br\,\mathrm{Ha}^2}{\mathrm{Re\,Pr}}(V^*\times B^*) \qquad (II.29)$$

The initial and boundary conditions are follows:

$$u^*=w^*=v^*=T^*=0 \qquad (II.30)$$

$$z^*=0, u^*=w^*=T^*=0, v^*=1 \qquad (II.31)$$

$$z^*=100, \frac{\partial u^*}{\partial z^*}=\frac{\partial w^*}{\partial z^*}=\frac{\partial v^*}{\partial z^*}=\frac{\partial}{\partial z^*}\left(\frac{\partial T^*}{\partial z^*}\right)=0 \qquad (II.32)$$

$$r_0^*=0.5, u^*=w^*=v^*=0, \frac{\partial T^*}{\partial r^*}=0 \qquad (II.33)$$

$$r_0^*=1, u^*=w^*=v^*=0, \frac{\partial T^*}{\partial r^*}=1 \qquad (II.34)$$

Thermophysical properties

The thermophysical properties of the base fluids and nanoparticles used in this study are illustrated in Table II.1

Table II. 1. The thermophysical properties of the solid nanoparticles and the base fluid [10,32,49].

Properties	**Water**	**Kerosene**	**TiO_2**	**CNT**	**Graphene**
$\rho(kg/m^3)$	997.1	783	4250	2100	2200
C_p (j/kg K)	4179	2090	686.2	410	790
$\beta(K^{-1})\times10^{-5}$	21	99	2	9	-0.8
k (W/m K)	0.613	0.145	8.9538	3007.4	5000
σ(s/m)	0.05	6×10^{-6}	2.6×10^{-6}	5×10^{6}	10^{7}
μ (kg/m s)	0.000855	0.0024	-	-	-
Shape	-	-	Spherical	Cylindrical	Platelet

The density, heat capacity, and thermal expansion of the binary and ternary hybrid nanofluids are established as follows:

$$\begin{cases} \rho_{hnf} = (\phi_{TiO_2}\rho_{TiO_2} + \phi_{CNT}\rho_{CNT})/\phi \\ \rho_{thnf} = \phi_{TiO_2}\rho_{TiO_2} + \phi_{CNT}\rho_{CNT} + \phi_{Graphene}\rho_{Graphene} + (1-\phi)\rho_f \end{cases} \quad (II.35)$$

$$\begin{cases} (\rho C_p)_{hnf} = (\phi_{TiO_2}(\rho C_p)_{TiO_2} + \phi_{CNT}(\rho C_p)_{CNT})/\phi \\ (\rho C_p)_{thnf} = \phi_{TiO_2}(\rho C_p)_{TiO_2} + \phi_{CNT}(\rho C_p)_{CNT} + \phi_{Graphene}(\rho C_p)_{Graphene} + (1-\phi)\rho \end{cases} \quad (II.36)$$

$$\begin{cases} (\rho\beta)_{hnf} = (\phi_{TiO_2}(\rho\beta)_{TiO_2} + \phi_{CNT}(\rho\beta)_{CNT})/\phi \\ (\rho\beta)_{thnf} = \phi_{TiO_2}(\rho\beta)_{TiO_2} + \phi_{CNT}(\rho\beta)_{CNT} + \phi_{Graphene}(\rho\beta)_{Graphene} + (1-\phi)\rho_f \end{cases} \quad (II.37)$$

The Dynamic viscosity of the nanofluid is determined using Timofeeva et al model [15]:

$$\mu_{nf}/\mu_f = 1 + A\phi + B\phi^2 \quad (II.38)$$

Spherical shape:

$$\mu_{nf1}/\mu_f = 1 + 2.5\phi + 6.2\phi^2 \quad (II.39)$$

Cylindrical shape:

$$\mu_{nf2}/\mu_f = 1 + 13.5\phi + 904.4\phi^2 \quad (II.40)$$

Platelet shape:

$$\mu_{nf3}/\mu_f = 1 + 37.1\phi + 612.6\phi^2 \quad (II.41)$$

The dynamic viscosity of binary and ternary hybrid nanofluids are calculated as outlined below:

$$\begin{cases} \mu_{hnf} = (\phi_{TiO_2}\mu_{nf1} + \phi_{CNT}\mu_{nf2})/\phi \\ \mu_{thnf} = (\phi_{TiO_2}\mu_{nf1} + \phi_{CNT}\mu_{nf2} + \phi_{Graphene}\mu_{nf3})/\phi \end{cases} \quad (II.42)$$

The thermal conductivity of nanoparticle shapes is provided by the Hamilton-Crosser model [17] :

$$\frac{k_{nf}}{k_f} = \frac{k_p + (n-1)k_f + (n-1)\phi(k_p - k_f)}{k_p + (n-1)k_f - \phi(k_p - k_f)} \quad (II.43)$$

Spherical nanoparticle shape :

$$\frac{k_{nf1}}{k_f} = \frac{k_{TiO_2} + 2k_f + 2(k_{TiO_2} - k_f)}{k_{TiO_2} + 2k_f - \phi(k_{TiO_2} - k_f)} \quad (II.44)$$

Cylindrical nanoparticle shape:

$$\frac{k_{nf2}}{k_f} = \frac{k_{CNT} + 3.9k_f + 3.9(k_{CNT} - k_f)}{k_{CNT} + 3.9k_f - \phi(k_{CNT} - k_f)} \quad (II.45)$$

Platelet nanoparticle shape:

$$\frac{k_{nf3}}{k_f} = \frac{k_{Graphene} + 4.7k_f + 4.7(k_{Graphene} - k_f)}{k_{Graphene} + 4.7k_f - \phi(k_{Graphene} - k_f)} \quad (II.46)$$

The thermal conductivity of binary and ternary hybrid nanofluids with different nanoparticle forms are computed in the following manner:

$$\begin{cases} k_{hnf} = (\phi_{TiO_2} k_{nf1} + \phi_{CNT} k_{nf2})/\phi \\ k_{thnf} = (\phi_{TiO_2} k_{nf1} + \phi_{CNT} k_{nf2} + \phi_{Graphene} k_{nf3})/\phi \end{cases} \quad (II.47)$$

The electric conductivity is computed by utilizing Maxwell model [16]

$$\frac{\sigma_{nf}}{\sigma_f} = 1 + \frac{3(\sigma_p/\sigma_f - 1)\phi}{(\sigma_p/\sigma_f + 2) - (\sigma_p/\sigma_f - 1)\phi} \quad (II.48)$$

The electric conductivity using distinct nanoparticle forms is determined as outlined below:

$$\begin{cases} \sigma_{hnf} = (\phi_{TiO_2} \sigma_{nf1} + \phi_{CNT} \sigma_{nf2})/\phi \\ \sigma_{thnf} = (\phi_{TiO_2} \sigma_{nf1} + \phi_{CNT} \sigma_{nf2} + \phi_{Graphene} \sigma_{nf3})/\phi \end{cases} \quad (II.49)$$

σ_{nf1}, σ_{nf2}, and σ_{nf3} refer to the electric conductivity of the nanofluid with spherical, cylindrical, and platelet nanoparticles, respectively.

The total volume fraction is given as follows:

$\phi = \phi_{TiO_2} + \phi_{CNT} + \phi_{Graphene}$.

II.4. Nusselt number

The axial Nusselt number is calculated according to the following equation [23]:

$$Nu(\theta, z) = \frac{k_{hnf}}{k_f} \frac{\left(\frac{\partial T^*}{\partial r^*}\right)_{r^* = r_0^*}}{(T^*(1, \theta, z^*) - T_b^*(z^*))} \quad (II.50)$$

Where the bulk temperature is given as follows:

$$T_b^*(z^*) = \frac{\int_{0.5}^{1} \int_0^{2\pi} v^*(r^*, \theta, z^*) T^*(r^*, \theta, z^*) r^* \, dr^* d\theta}{\int_{0.5}^{1} \int_0^{2\pi} v^*(r^*, \theta, z^*) r^* \, dr^* d\theta} \quad (II.51)$$

The average Nusselt number is calculated as follows:

$$Nu_{av} = \frac{1}{2\pi L}\int_0^L \int_0^{2\pi} Nu(\theta, z^*) d\theta dz^* \qquad (II.52)$$

II.5. Skin friction coefficient

$$C_{fo} = \frac{\tau_w}{\frac{1}{2}\rho_{hnf} v_0^2} \qquad (II.53)$$

II.6. Pressure drop

$$\Delta p = p_{av}|_{z_1} - p_{av}|_{z_2} \qquad (II.54)$$

The position of z_1 and z_2 is selected near the inlet and the outlet of the duct, respectively.

II.7. Entropy generation

The total entropy generation is computed as [50]:

$$S'''_{tot} = S'''_{th} + S'''_{fr} + S'''_M \qquad (II.55)$$

$$S'''_{th} = \frac{k_{hnf}}{T^2}\left[\left(\frac{\partial T}{\partial r}\right)^2 + \left(\frac{1}{r}\frac{\partial T}{\partial \theta}\right)^2 + \left(\frac{\partial T}{\partial z}\right)^2\right] \qquad (II.56)$$

$$S'''_{fr} = \frac{\mu_{hnf}}{T}\left\{2\left[\left(\frac{\partial u}{\partial r}\right)^2 + \left(\frac{1}{r}\frac{\partial w}{\partial \theta} + \frac{u}{r}\right)^2 + \left(\frac{\partial v}{\partial z}\right)^2\right] + \left(r\frac{\partial}{\partial r}\left(\frac{w}{r}\right) + \frac{1}{r}\frac{\partial u}{\partial \theta}\right)^2 + \left(\frac{1}{r}\frac{\partial v}{\partial \theta} + \frac{\partial w}{\partial z}\right)^2 + \left(\frac{\partial u}{\partial z} + \frac{\partial v}{\partial r}\right)^2 + \frac{1}{K}(u^2 + w^2 + v^2)\right\} \qquad (II.57)$$

$$S'''_M = \frac{\sigma_{hnf} B_0^2}{T}(w^2 + (u\cos\psi + v\sin\psi)^2) \qquad (II.58)$$

$$S_{tot} = \int S'''_{tot}\, dV \qquad (II.59)$$

The non-dimensional entropy generation is computed as:

$$S^{*'''}_{th} = \frac{k_{hnf}}{k_f}\left[\left(\frac{\partial T^*}{\partial r^*}\right)^2 + \left(\frac{1}{r^*}\frac{\partial T^*}{\partial \theta}\right)^2 + \left(\frac{\partial T^*}{\partial z^*}\right)^2\right] \qquad (II.60)$$

$$S_{fr}^{*'''} = \chi \frac{\mu_{hnf}}{\mu_f} \left\{ 2 \left[\left(\frac{\partial u^*}{\partial r^*} \right)^2 + \left(\frac{1}{r^*} \frac{\partial w^*}{\partial \theta} + \frac{u}{r} \right)^2 + \left(\frac{\partial v^*}{\partial z^*} \right)^2 \right] + \left(r^* \frac{\partial}{\partial r^*} \left(\frac{w^*}{r^*} \right) + \frac{1}{r^*} \frac{\partial u^*}{\partial \theta} \right)^2 + \left(\frac{1}{r^*} \frac{\partial v^*}{\partial \theta} + \frac{\partial w^*}{\partial z^*} \right)^2 + \left(\frac{\partial u^*}{\partial z^*} + \frac{\partial v^*}{\partial r^*} \right)^2 + \frac{1}{\mathrm{Da}} (u^{*2} + w^{*2} + v^{*2}) \right\} \qquad (II.61)$$

$$S_M^{*'''} = \chi \frac{\sigma_{hnf} \mathrm{Ha}^2}{\sigma_f} (w^{*2} + (u^* cos\psi + v^* sin\psi)^2) \qquad (II.62)$$

Chapter III: Numerical resolution

III.1. Introduction

In this chapter, we explore the numerical methods employed to solve the final form of the mathematical models, which are derived from the specified physical models. These models are represented as a set of nonlinear partial differential equations. Such complex equations require numerical techniques for their resolution, as analytical methods are not feasible. The primary numerical method discussed is the finite volume method.

- The first application uses FORTRAN code to solve the discretized equations. The detailed procedure starts with the description of the mesh, and all conservation equations are integrated into a single general transport equation that is then discretized. The mesh test and the code validation are discussed to assure the validity and accuracy of the results.
- ANSYS-Fluent software is employed in the second application, and the methodological steps are similarly detailed.

III.2. Resolution methods

In tackling the complexities of fluid behavior, three different methods have been used to solve fluid dynamics problems: analytical, experimental, and numerical. Analytical methods involve deriving mathematical equations to describe fluid behavior, experimental methods employ physical experiments for observation and measurement, while numerical methods utilize computer algorithms for simulation and analysis. In the following diagram, the advantages and disadvantages of these methods are described:

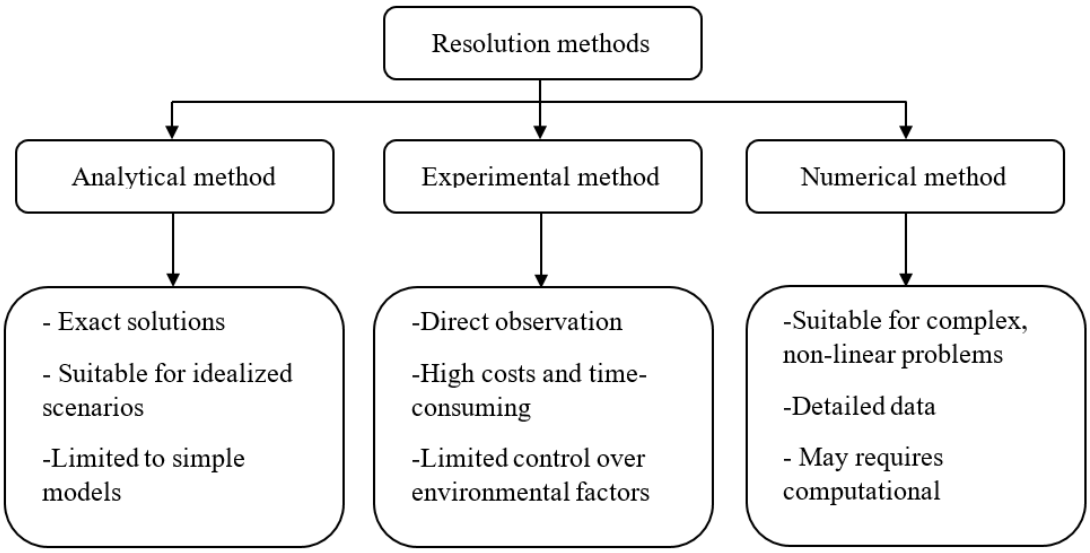

III.3. Numerical methods

Numerical methods in fluid dynamics encompass a range of techniques used to solve the governing equations of fluid motion. Three different methods have been widely used in fluid dynamics: the finite element technique, the finite difference technique, and the finite volume technique. The numerical approach used is determined by several factors, such as the problem's complexity, boundary conditions, required accuracy, computational resources, and the specific objectives of the analysis or simulation.

- **Finite element method (FEM)**

FEM discretizes the domain into finite elements connected by nodes. It approximates the solution within each element using basis functions and solves for nodal values.

- **Finite difference method (FDM)**

FDM approximates derivatives in the governing equations using discrete differences. It divides the domain into a grid and computes the values of variables at grid points.

- **Finite volume method (FVM)**

In our current study, we have chosen the finite volume method. FVM was created by Patankar [51]. It discretizes the governing equations by integrating them over control volumes. This method offers conservation of mass, momentum, and energy within each control volume. In the first application, FORTRAN code based on the finite volume method was used, and in the second application, ANSYS-Fluent software was used.

III.4. Finite volume method procedure

Discretizing the transport equation using the finite volume method (FVM) involves several steps to convert the continuous differential equation into a set of algebraic equations that can be solved numerically.

III.4.1. Domain discretization

The computational domain, defined by ($r_i/D_h \leq r^* \leq r_o/D_h$), ($0 \leq \theta \leq 2\pi$), and ($0 \leq z^* \leq L/D_h$) along the radial, angular, and axial direction, respectively, is divided into a set of finite volumes. Each volume has dimensions given by $\Delta V = r\Delta r\Delta\theta\Delta z$. **Figure III.1** shows the 3D numerical domain; the center is associated with node P and is bounded by six faces: the north and south radial

centers N and S, respectively. The east and west angular centers with E and W, respectively, and the top and bottom axial centers with T and B, respectively. Scalar quantities such as pressure and temperature are stored at the centers of the control volumes, whereas vector quantities like velocity are stored on the faces.

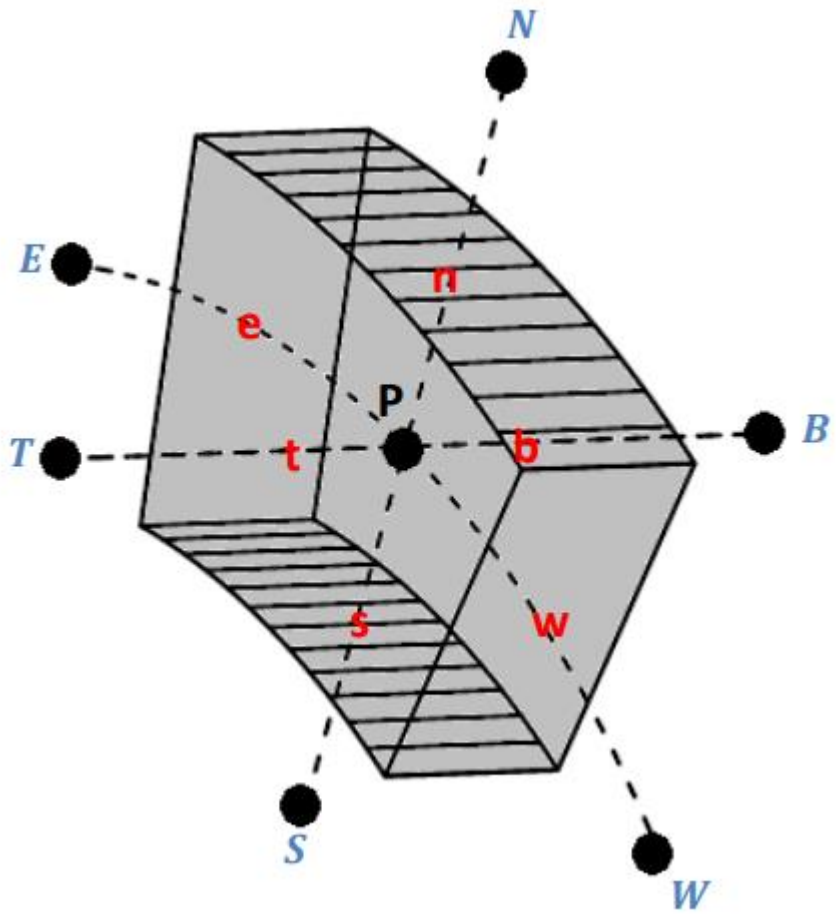

Figure III. 1. Control volume.

(a)

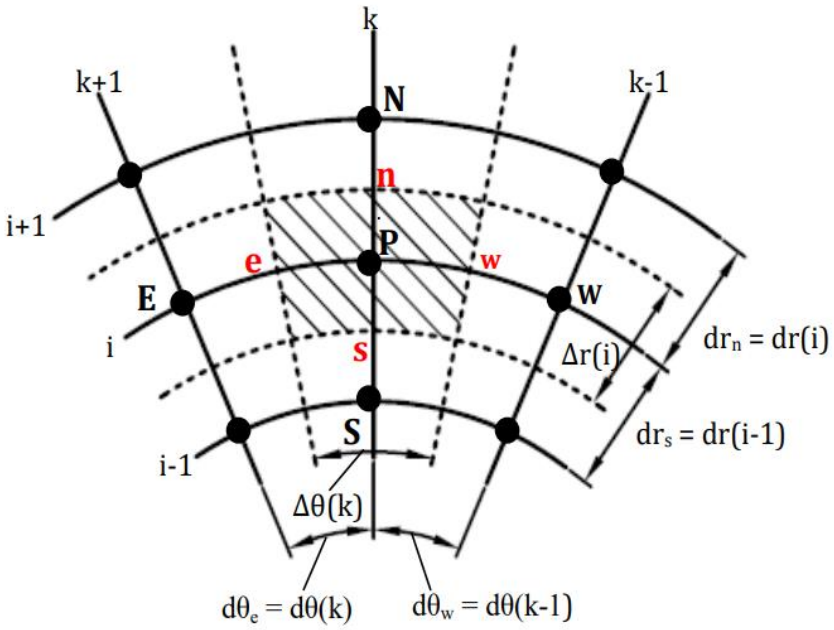
k
k+1
k-1
N
n
i+1
P
e
w
E
W
i
s
Δr(i)
drn = dr(i)
S
drs = dr(i-1)
i-1
Δθ(k)
dθe = dθ(k)
dθw = dθ(k-1)

(b)

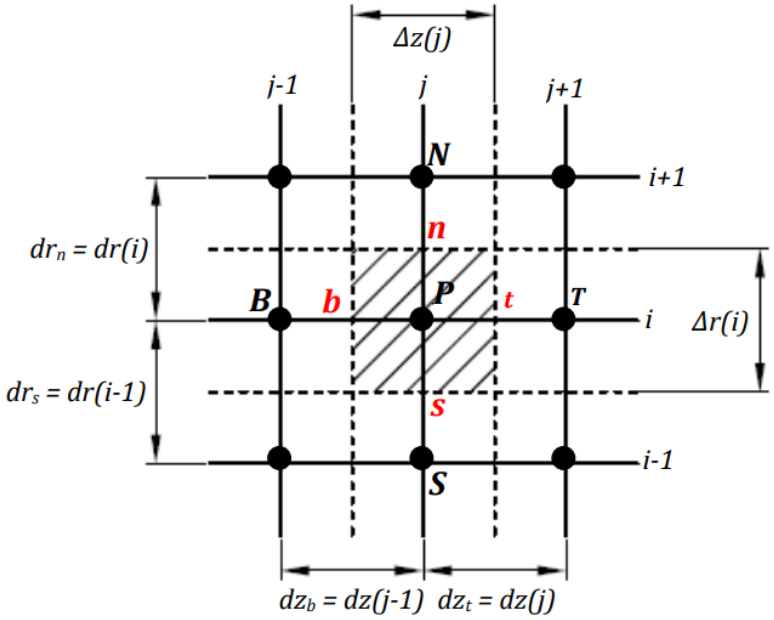
Δz(j)
j-1
j
j+1
N
i+1
drn = dr(i)
n
B
b
P
t
T
i
Δr(i)
drs = dr(i-1)
s
i-1
S
dzb = dz(j-1)
dzt = dz(j)

(c)

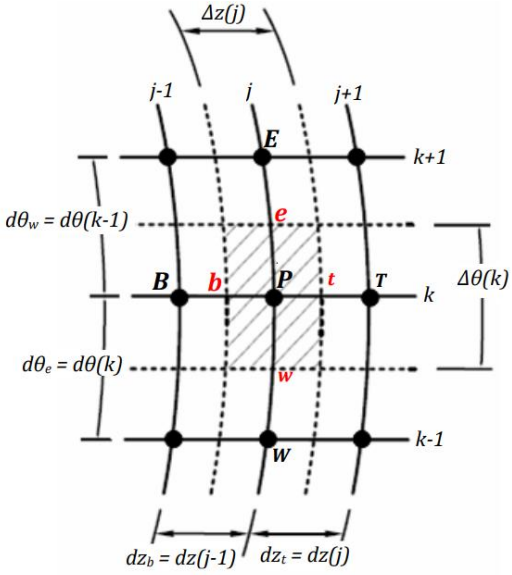

Figure III. 2. Projection of the finite volume along a: (r,θ) plane, b: (r,z) plane, and c: (θ,z) plane.

III.4.2. Discretization of the energy transport

The transport equation, commonly called the convection-diffusion equation, is a fundamental partial differential equation (PDE) in fluid dynamics and heat transfer. It describes how mass, energy, or momentum is transported in a flow field due to convection and diffusion processes. The general form of the transport equation for a scalar quantity φ (which could represent temperature, concentration, etc.) in a fluid is given by:

$$\frac{\partial(\rho\varphi)}{\partial t} + \nabla.(\rho V\varphi) = \nabla.(\mathrm{L}^{\varphi}\nabla\varphi) + Q^{\varphi} \qquad (III.1)$$

Where:

ρ : Fluid density

φ: Transported scalar quantity

V: Velocity field vector

L: Diffusion coefficient

Q: Source term

On the left side of the transport equation, the initial term signifies the transient variation of φ, and the following term indicates the convective transport of φ. On the right side, the initial term pertains to the diffusion component. The subsequent term represents the source term that accounts for the generation or removal of φ.

III.4.2.1 Temporal discretization

The discretization of the unsteady terms in the momentum and energy equations follows a second-order scheme to ensure our results are accurate. The discretization is based on the second-order Taylor series expansion, as illustrated in the following equations:

$$\varphi^{t} = \varphi^{t+\Delta t} - \frac{\Delta t}{1!}\frac{\partial \varphi}{\partial t}\bigg|^{t+\Delta t} + \frac{(\Delta t)^2}{2!}\frac{\partial^2 \varphi}{\partial t^2}\bigg|^{t+\Delta t} + 0(\Delta t)^2 \qquad (III.2)$$

$$\varphi^{t-\Delta t} = \varphi^{t+\Delta t} - \frac{(2\Delta t)}{1!}\frac{\partial \varphi}{\partial t}\bigg|^{t+\Delta t} + \frac{(2\Delta t)^2}{2!}\frac{\partial^2 \varphi}{\partial t^2}\bigg|^{t+\Delta t} + 0(\Delta t)^2 \qquad (III.3)$$

By multiplying equation (III.2) by 4 and subtracting the product with the equation (III.3), we found:

$$\frac{\partial \varphi}{\partial t}\bigg|^{t+\Delta t} = \frac{3\varphi^{t+\Delta t} - 4\varphi^{t} + \varphi^{t-\Delta t}}{2\Delta t} \qquad (III.4)$$

The thermal buoyancy force in momentum equations is discretized by the Adams-Bashforth method. We multiply equation (III.1) by 2, then subtract it from the product equation (III.2) to obtain:

$$\varphi^{t+\Delta t} = 2\varphi^{t} - \varphi^{t-\Delta t} \qquad (III.5)$$

III.4.2.2. Spatial discretization

The central differencing scheme with second order precision is used for spatial discretization terms.

By using Taylor series expansion along a given direction, such as radial, we found:

$$\frac{\partial \varphi}{\partial r}\bigg|_{n} = \frac{\varphi_N - \varphi_P}{dr_n} \qquad (III.6)$$

III.4.3. Discretization of the governing equations

III.4.3.1. Continuity equation

$$\int_w^e \int_s^n \int_b^t \left[\frac{1}{r^*}\frac{(r^*u^*)}{\partial r^*} + \frac{1}{r^*}\frac{\partial w^*}{\partial \theta} + \frac{\partial v^*}{\partial z^*}\right] r^* dr^* d\theta dz^* = 0 \qquad (III.7)$$

$$\int_w^e \int_s^n \int_b^t \frac{1}{r^*}\frac{(r^*u^*)}{\partial r^*} r^* dr^* d\theta dz^* = (r_n^* u_n^* - r_s^* u_s^*)\Delta\theta_p \Delta z^*_p \qquad (III.8)$$

$$\int_w^e \int_s^n \int_b^t \frac{1}{r^*}\frac{\partial w^*}{\partial \theta} r^* dr^* d\theta dz^* = (w_e^* - w_w^*)\Delta r_p^* \Delta z_p^* \qquad (III.9)$$

$$\int_w^e \int_s^n \int_b^t \frac{\partial v^*}{\partial z^*} r^* dr^* d\theta dz^* = (v_t^* - v_b^*) r_p^* \Delta r_p^* \Delta\theta_p \qquad (III.10)$$

The final equation is derived as follows:

$$(r_n^* u_n^* - r_s^* u_s^*)\Delta\theta_p \Delta z^*_p + (w_e^* - w_w^*)\Delta r_p^* \Delta z_p^* + (v_t^* - v_b^*) r_p^* \Delta r_p^* \Delta\theta_p = 0 \qquad (III.11)$$

III.4.3.2. Momentum equation along the radial direction

The radial momentum equation (II.16) is integrated into the control volume shifted in the radial direction (**Figure III.3**) as follows:

Transient term

$$\int_w^e \int_s^n \int_b^t \frac{\partial u^*}{\partial t^*} r^* dr^* d\theta dz^* = \int_w^e \int_s^n \int_b^t \left(\frac{3u_{pu}^* - 4u_{pu}^{*1} + u_{pu}^{*0}}{2\Delta t}\right) r^* dr^* d\theta dz^* \qquad (III.12)$$

Advective term

$$\int_w^e \int_s^n \int_b^t \frac{1}{r^*}\frac{\partial}{\partial r^*}(r^*u^*u^*) r^* dr^* d\theta dz^*$$

$$= \int_w^e \int_s^n \int_b^t \left(\frac{2}{r}(r^*u^*u^*)\Big|^1 - \frac{1}{r}(r^*u^*u^*)\Big|^0\right) r^* dr^* d\theta dz^* \qquad (III.13)$$

$$= [(2r_{nu}^*(u_{nu}^{*2})^1 - 2r_{su}^*(u_{su}^{*2})^1) - (r_{nu}^*(u_{nu}^{*2})^0 - r_{su}^*(u_{su}^{*2})^0)]\Delta\theta\Delta z_p^*$$

$$\int_w^e \int_s^n \int_b^t \frac{1}{r^*}\frac{\partial}{\partial\theta}(u^*w^*)r^*dr^*d\theta dz^*$$

$$= \int_w^e \int_s^n \int_b^t \left(\frac{2}{r}(r^*u^*w^*)\Big|^1 - \frac{1}{r}(r^*u^*w^*)\Big|^0\right) r^*dr^*d\theta dz^* \qquad (III.14)$$

$$= [(2(u^*_{eu}w^*_{eu})^1 - 2(u^*_{wu}w^*_{wu})^1) - ((u^*_{eu}w^*_{eu})^0 - (u^*_{wu}w^*_{wu})^0)]dr^*_n\Delta z^*_p$$

$$\int_w^e \int_s^n \int_b^t \frac{1}{r^*}\frac{\partial}{\partial z^*}(u^*v^*)r^*dr^*d\theta dz^* \qquad (III.15)$$

$$= \left[(2(u^*_{tu}v^*_{tu})^1 - 2(u^*_{bu}v^*_{bu})^1) - \left(((u^*_{tu}v^*_{tu})^0 - (u^*_{bu}v^*_{bu})^0)\right)\right]r^*_n dr^*_n \Delta\theta_P$$

$$\int_w^e \int_{su}^{nu} \int_b^t \frac{w^{*2}}{r^*} r^*dr^*d\theta dz^* = \frac{w^*_{pu}}{r^*_n}\, dr^*_n\, \Delta\theta_P \Delta z^*_p \qquad (III.16)$$

Pressure term

$$\int_w^e \int_s^n \int_b^t -\frac{\partial p^*}{\partial r^*} r^*dr^*d\theta dz^* = (p^*_P - p^*_N)r^*_n\Delta\theta_P\Delta z^*_P \qquad (III.17)$$

Diffusive term

$$\int_w^e \int_{su}^{nu} \int_b^t \frac{1}{r^*}\frac{\partial}{\partial r^*}(r^*\frac{\partial u^*}{\partial r^*})r^*dr^*d\theta dz^* = \left(r^*_{nu}\frac{u^*_{Nu} - u^*_{Pu}}{dr^*_{nu}} - r^*_{su}\frac{u^*_{Pv} - u^*_{Su}}{dr^*_{su}}\right)\Delta\theta_P\Delta z^*_P \qquad (III.18)$$

$$\int_{wu}^{eu} \int_s^n \int_b^t \frac{1}{r^*}\frac{\partial}{\partial\theta}(\frac{1}{r^*}\frac{\partial u^*}{\partial\theta})r^*dr^*d\theta dz^* = \left(\frac{1}{r^*_{ev}}\frac{u^*_{Eu} - u^*_{Pu}}{d\theta_{eu}} - \frac{1}{r^*_{wu}}\frac{u^*_{Pu} - u^*_{Wu}}{d\theta_{wu}}\right)\Delta r^*_P\Delta z^*_P \qquad (III.19)$$

$$\int_w^e \int_s^n \int_{bu}^{tu} \frac{\partial}{\partial z^*}(\frac{\partial u^*}{\partial z^*})r^*dr^*d\theta dz^* = \left(\frac{u^*_{Tu} - u^*_{Pu}}{dz^*_{tu}} - \frac{u^*_{Pu} - u^*_{Bu}}{dz^*_{bu}}\right)r^*_n dr^*_n\Delta\theta_P \qquad (III.20)$$

$$\int_w^e \int_s^n \int_b^t -\frac{u^*}{r^{*2}} r^*dr^*d\theta dz^* = -\frac{u^*_{Pu}}{r^*_n} dr^*_n\Delta\theta_P\Delta z^*_p \qquad (III.21)$$

$$\int_{w}^{e}\int_{su}^{nu}\int_{b}^{t} -\frac{2}{r^{*2}}\frac{\partial w^{*}}{\partial \theta} r^{*} dr^{*} d\theta dz^{*}$$

$$= -\int_{w}^{e}\int_{su}^{nu}\int_{b}^{t}\left(2\left(\frac{2}{r^{*2}}\frac{\partial w^{*}}{\partial \theta}\right)\Big|^{1} - \left(\frac{2}{r^{*2}}\frac{\partial w^{*}}{\partial \theta}\right)\Big|^{0}\right) r^{*} dr^{*} d\theta dz^{*} \qquad (III.22)$$

Buoyancy term

$$\int_{w}^{e}\int_{s}^{n}\int_{b}^{t}\left(\frac{Gr_f}{Re_f^2}\frac{\beta_{nf}}{\beta_{nf}} cos\theta\right) T^{*} r^{*} dr^{*} d\theta dz^{*}$$

$$= \left(\frac{Gr_f}{Re_f^2}\frac{\beta_{nf}}{\beta_{nf}} cos\theta\right)(2T_P^{*1} - T_P^{*0}) r_n^{*} dr_n^{*} \Delta\theta_P \Delta z_P^{*} \qquad (III.23)$$

Porous medium term

$$\int_{w}^{e}\int_{s}^{n}\int_{b}^{t} \frac{1}{Re\ Da} u^{*}\, r^{*} dr^{*} d\theta dz^{*} = \frac{1}{Re\ Da}\, u_{pu}^{*} r_n^{*} dr_n^{*}\, \Delta\theta_P \Delta z_p^{*} \qquad (III.24)$$

Magnetic force term

$$\int_{w}^{e}\int_{s}^{n}\int_{b}^{t} \frac{\sigma_{hnf}/\sigma_f}{\rho_{hnf}/\rho_f}\frac{\mathrm{Ha}^2}{\mathrm{Re}} u^{*}\, r^{*} dr^{*} d\theta dz^{*} = \frac{\sigma_{hnf}/\sigma_f}{\rho_{hnf}/\rho_f}\frac{\mathrm{Ha}^2}{\mathrm{Re}} u_{pu}^{*} r_n^{*} dr_n^{*}\, \Delta\theta_P \Delta z_p^{*} \qquad (III.25)$$

(a)

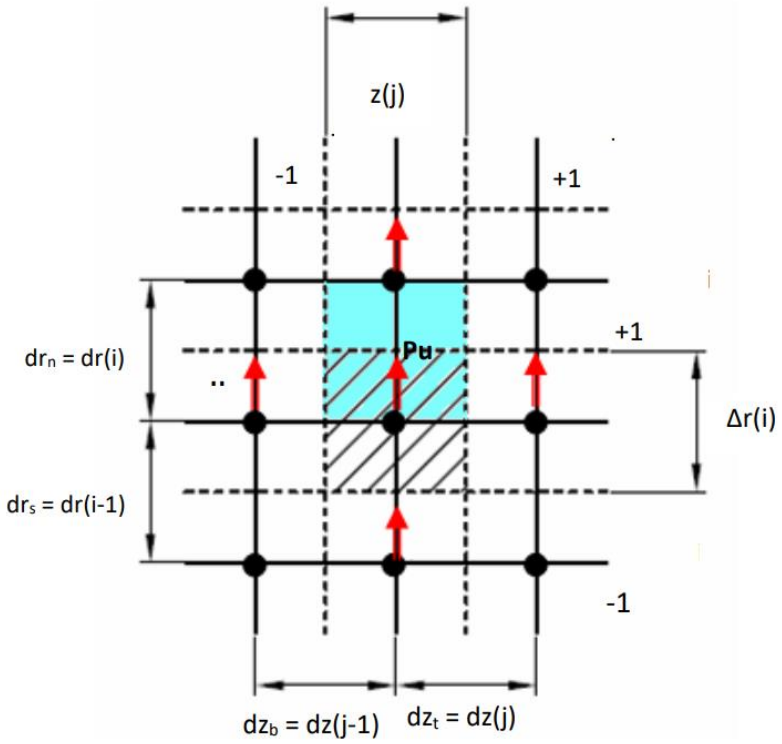

(b)

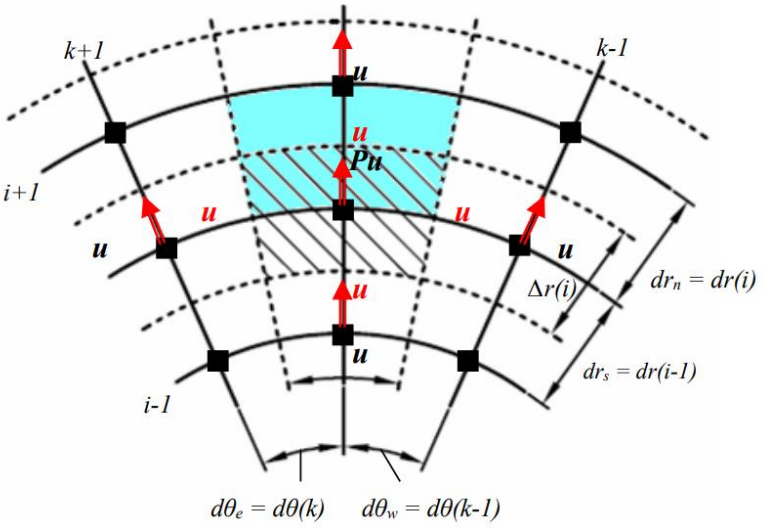

Figure III. 3. Projection of the shifted mesh in the radial direction along a: (r*,z*) plane and b: (r*,θ) plane.

III.4.3.3. Momentum equation along the angular direction

The angular momentum equation (II.17) is integrated in the control volume shifted in the radial direction (**Figure III.4**) as follows:

Transient term

$$\int_{ww}^{ew}\int_{s}^{n}\int_{b}^{t}\frac{\partial w^*}{\partial t^*}r^*dr^*d\theta dz^* = \int_{w}^{e}\int_{s}^{n}\int_{b}^{t}\left(\frac{3w_{pw}^* - 4w_{pw}^{*1} + w_{pw}^{*0}}{2\Delta t}\right)r^*dr^*d\theta dz^* \qquad (III.26)$$

$$= \frac{3w_{pw}^* - 4w_{pw}^{*1} + w_{pw}^{*0}}{2\Delta t}r_P^*\Delta r_p^*\Delta\theta_e\Delta z_p^*$$

Advective term

$$\int_{w}^{e}\int_{s}^{n}\int_{b}^{t}\frac{1}{r^*}\frac{\partial}{\partial r^*}(r^*u^*u^*)r^*dr^*d\theta dz^*$$

$$= \int_{w}^{e}\int_{s}^{n}\int_{b}^{t}\left(\frac{2}{r}(r^*u^*u^*)\Big|^{1} - \frac{1}{r}(r^*u^*u^*)\Big|^{0}\right)r^*dr^*d\theta dz^* \qquad (III.27)$$

$$= \begin{bmatrix}(2r_{nw}^*(u_{nw}^*w_{nw}^*)^1 - 2r_{sw}^*(u_{sw}^*w_{sw}^*)^1)\\ -(r_{nw}^*(u_{nw}^*w_{nw}^*)^0 - r_{sw}^*(u_{sw}^*w_{sw}^*)^0)\end{bmatrix}d\theta_e\Delta z_p^*$$

$$\int_{w}^{e}\int_{s}^{n}\int_{b}^{t}\frac{1}{r^*}\frac{\partial}{\partial\theta}(w^*w^*)r^*dr^*d\theta dz^* \qquad (III.28)$$

$$= [(2(w_{ew}^*w_{ew}^*)^1 - 2(w_{wu}^*w_{ww}^*)^1) - ((w_{eu}^*w_{eu}^*)^0 - (w_{ww}^*w_{ww}^*)^0)]\Delta r_p^*\Delta z_p^*$$

$$\int_{w}^{e}\int_{s}^{n}\int_{b}^{t}\frac{1}{r^*}\frac{\partial}{\partial z^*}(u^*w)r^*dr^*d\theta dz^* \qquad (III.29)$$

$$= [(2(v_{tw}^*w_{tw}^*)^1 - 2(v_{bw}^*w_{bw}^*)^1) - \left(((v_{tw}^*w_{tw}^*)^0 - (w_{bw}^*w_{bw}^*)^O)\right)]r_p^*\Delta r_p^*d\theta_e$$

Pressure term

$$\int_{w}^{e}\int_{s}^{n}\int_{b}^{t}-\frac{\partial p^*}{\partial\theta^*}r^*dr^*d\theta dz^* = (p_P^* - p_E^*)r_n^*\Delta r_P^*\Delta z_P^* \qquad (III.30)$$

Diffusive term

$$\int_w^e \int_s^n \int_b^t \left(\frac{Gr_f}{Re_f^2}\frac{\beta_{nf}}{\beta_{nf}} sin\theta\right) T^* r^* dr^* d\theta dz^*$$

$$= \left(\frac{Gr_f}{Re_f^2}\frac{\beta_{nf}}{\beta_{nf}} sin\theta\right)(2T_P^{*1} - T_P^{*0}) r_P^* dr_P^* \Delta\theta_e \Delta z_P^* \qquad (III.31)$$

$$\int_w^e \int_{su}^{nu} \int_b^t \frac{1}{r^*}\frac{\partial}{\partial r^*}(r^*\frac{\partial w^*}{\partial r^*}) r^* dr^* d\theta dz^*$$

$$= \left(r_{nw}^* \frac{w_{Nw}^* - w_{Pw}^*}{dr_{nw}^*} - r_{sw}^* \frac{w_{Pw}^* - u_{Sw}^*}{dr_{sw}^*}\right) d\theta_P \Delta z_P^* \qquad (III.32)$$

$$\int_{wu}^{eu} \int_s^n \int_b^t \frac{1}{r^*}\frac{\partial}{\partial\theta}(\frac{1}{r^*}\frac{\partial w^*}{\partial\theta}) r^* dr^* d\theta dz^*$$

$$= \left(\frac{1}{r_{ew}^*}\frac{w_{Ew}^* - w_{Pw}^*}{d\theta_{ew}} - \frac{1}{r_{ww}^*}\frac{w_{Pw}^* - w_{Ww}^*}{d\theta_{ww}}\right) \Delta r_P^* \Delta z_P^* \qquad (III.33)$$

$$\int_w^e \int_s^n \int_{bu}^{tu} \frac{\partial}{\partial z^*}(\frac{\partial w^*}{\partial z^*}) r^* dr^* d\theta dz^* = \left(\frac{w_{Tw}^* - u_{Pw}^*}{dz_{tw}^*} - \frac{w_{Pw}^* - w_{Bw}^*}{dz_{bw}^*}\right) r_p^* \Delta r_p^* \Delta z_P \qquad (III.34)$$

Porous term

$$\int_w^e \int_s^n \int_b^t \frac{1}{Re\ Da} w^*\ r^* dr^* d\theta dz^* = \frac{1}{Re\ Da}\ w_{pw}^* r_p^* \Delta r_p^*\ d\theta_e \Delta z_p^* \qquad (III.35)$$

Magnetic force term

$$\int_w^e \int_s^n \int_b^t \frac{\sigma_{hnf}/\sigma_f}{\rho_{hnf}/\rho_f}\frac{\mathrm{Ha}^2}{\mathrm{Re}} w^*\ r^* dr^* d\theta dz^* = \frac{\sigma_{hnf}/\sigma_f}{\rho_{hnf}/\rho_f}\frac{\mathrm{Ha}^2}{\mathrm{Re}} w_{pw}^* r_p^* \Delta r_p^*\ d\theta_e \Delta z_p^* \qquad (III.36)$$

(a)

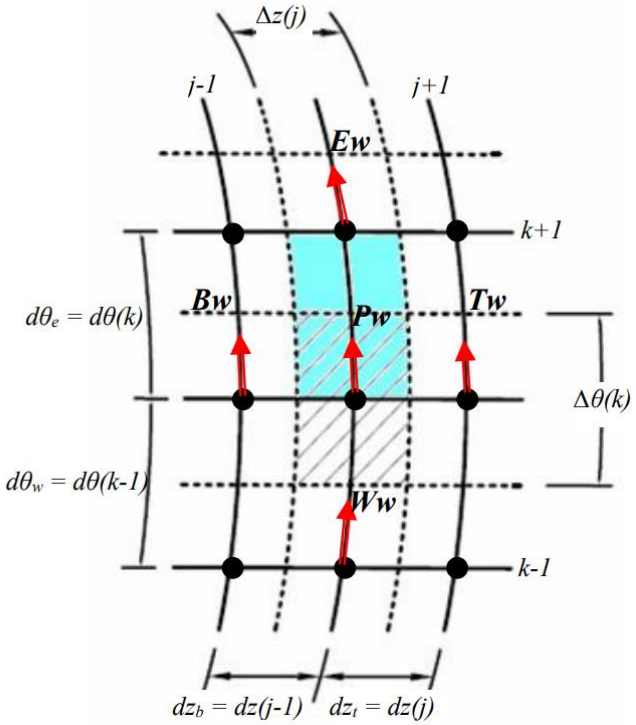

(b)

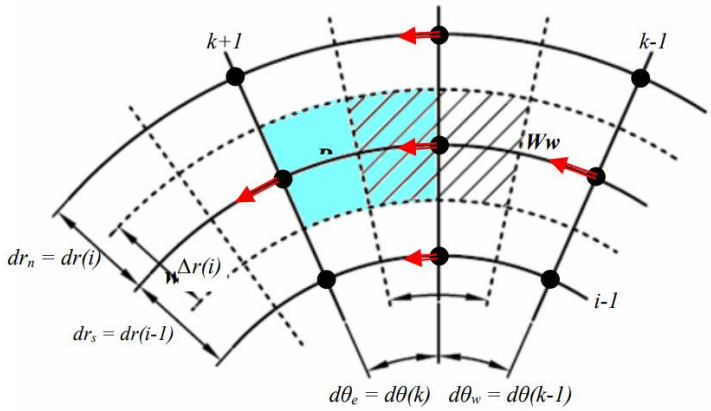

Figure III. 4. Projection of the shifted mesh in the angular direction along a: (θ,z*) plane and b: (r*,θ) plane.

III.4.3.4. Momentum equation along the axial direction

The axial momentum equation (II.18) is integrated in the control volume shifted in the radial direction (**Figure III.5**) as follows:

Transient term

$$\int_w^e \int_s^n \int_{bv}^{tv} \frac{\partial v^*}{\partial t^*} r^* dr^* d\theta dz^*$$

$$= \int_w^e \int_s^n \int_{bv}^{tv} \left(\frac{3v_{pv}^* - 4v_{pv}^{*1} + v_{pv}^{*0}}{2\Delta t} \right) r^* dr^* d\theta dz^* \qquad (III.37)$$

$$= \frac{3v_{pv}^* - 4v_{pv}^{*1} + v_{pv}^{*0}}{2\Delta t} r_P^* \Delta r_p^* \Delta\theta_p \Delta z_t^*$$

Advective term

$$\int_w^e \int_s^n \int_b^t \frac{1}{r^*} \frac{\partial}{\partial r^*} (r^* u^* v^*) r^* dr^* d\theta dz^* = \int_w^e \int_s^n \int_b^t \left(\frac{2}{r} (r^* u^* v^*) \Big|^1 - \frac{1}{r} (r^* u^* v^*) \Big|^0 \right) r^* dr^* d\theta dz^*$$

$$= [(2r_{nv}^* (u_{nv}^* v_{nv}^*)^1 - 2r_{sv}^* (u_{sv}^* v_{sv}^*)^1) - (r_{nv}^* (u_{nv}^* v_{nv}^*)^0 - r_{sv}^* (u_{sv}^* w_{sv}^*)^0)] \Delta\theta_p dz_t^*$$

$$\int_w^e \int_s^n \int_b^t \frac{1}{r^*} \frac{\partial}{\partial \theta} (w^* v^*) r^* dr^* d\theta dz^* =$$

$$= [(2(w_{ev}^* v_{ev}^*)^1 - 2(w_{wv}^* v_{wv}^*)^1) - ((w_{ev}^* v_{ev}^*)^0 - (w_{wv}^* v_{wv}^*)^0)] \Delta r_p^* dz_t^*$$

$$\int_w^e \int_s^n \int_b^t \frac{1}{r^*} \frac{\partial}{\partial z^*} (v^* v^*) r^* dr^* d\theta dz^* =$$

$$= [(2(v_{tv}^* v_{tv}^*)^1 - 2(v_{bv}^* v_{bv}^*)^1) - \left(((v_{tv}^* v_{tv}^*)^0 - (v_{bv}^* v_{bv}^*)^O)\right)] \Delta r_p^* \Delta\theta_P$$

Pressure term

$$\int_w^e \int_s^n \int_b^t -\frac{\partial p^*}{\partial z^*} r^* dr^* d\theta dz^* = (p_P^* - p_T^*) r_n^* \Delta r_P^* \Delta\theta_P \qquad (III.41)$$

Diffusive term

$$\int_{w}^{e}\int_{s}^{n}\int_{bv}^{tv}\frac{1}{r^*}\frac{\partial}{\partial r^*}\left(r^*\frac{\partial v^*}{\partial r^*}\right)r^*dr^*d\theta dz^* = \left(r_{nv}^*\frac{v_{Nv}^*-v_{Pv}^*}{dr_{nv}^*}-r_{sv}^*\frac{v_{Pv}^*-v_{Sv}^*}{dr_{sv}^*}\right)\Delta\theta_P\Delta z_P^* \qquad (III.42)$$

$$\int_{w}^{e}\int_{s}^{n}\int_{bv}^{tv}\frac{1}{r^*}\frac{\partial}{\partial\theta}\left(\frac{1}{r^*}\frac{\partial v^*}{\partial\theta}\right)r^*dr^*d\theta dz^* = \left(\frac{1}{r_{ev}^*}\frac{v_{Ev}^*-v_{Pv}^*}{d\theta_{ev}}-\frac{1}{r_{wv}^*}\frac{v_{Pv}^*-v_{Wv}^*}{d\theta_{wv}}\right)\Delta r_P^*\Delta z_P^* \qquad (III.43)$$

$$\int_{w}^{e}\int_{s}^{n}\int_{bv}^{tv}\frac{\partial}{\partial z^*}\left(\frac{\partial v^*}{\partial z^*}\right)r^*dr^*d\theta dz^* = \left(\frac{v_{Tv}^*-v_{Pv}^*}{dr_{tv}^*}-\frac{v_{Pv}^*-v_{Bv}^*}{dr_{bv}^*}\right)r_P^*\Delta r_P^*\Delta\theta_P \qquad (III.44)$$

Porous term

$$\int_{w}^{e}\int_{s}^{n}\int_{b}^{t}\frac{1}{Re\,Da}v^*\,r^*dr^*d\theta dz^* = \frac{1}{Re\,Da}\,v_{pv}^*r_p^*\Delta r_p^*\,\Delta\theta_e dz^* \qquad (III.45)$$

(a)

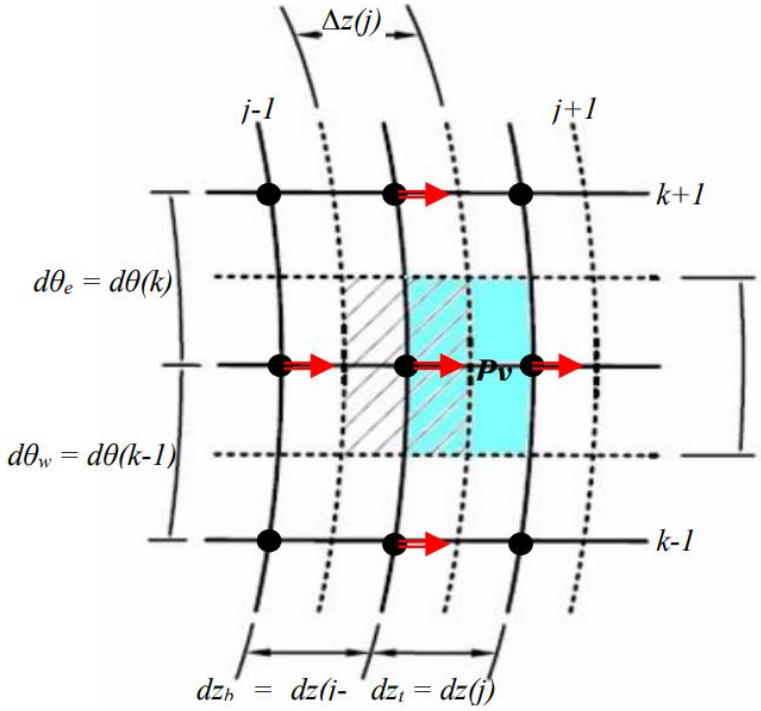

(b)

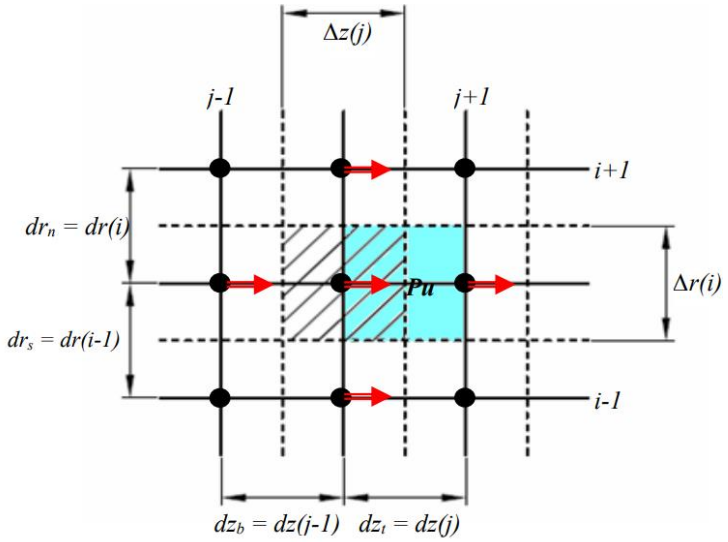

Figure III. 5. Projection of the shifted mesh in the angular direction along a: (θ,z*) plane and b: (r*,z*) plane.

III.4.3.5. Energy equation

The energy equation (II.19) is integrated in the control volume (**Figure III.2**) as follows:

Transient term

$$\int_w^e \int_s^n \int_b^t \frac{\partial v^*}{\partial t^*} r^* dr^* d\theta dz^* = \frac{3T_P^* - 4T_P^{*1} + T_P^{*0}}{2\Delta t^*} r_P^* \Delta r_p^* \Delta\theta_e \Delta z_p^* \qquad (III.46)$$

Advective term

$$\int_w^e \int_s^n \int_b^t \frac{1}{r^*}\frac{\partial}{\partial r^*}(r^* u^* T^*) r^* dr^* d\theta dz^*$$

$$= \int_w^e \int_s^n \int_b^t \left(\frac{2}{r^*}\frac{\partial}{\partial r^*}(r^* u^* T^*)\Big|^1 - \frac{1}{r^*}\frac{\partial}{\partial r^*}(r^* u^* T^*)\Big|^0 \right) r^* dr^* d\theta dz^* \qquad (III.47)$$

$$\int_w^e \int_s^n \int_b^t \frac{1}{r^*}\frac{\partial}{\partial r^*}(r^* w^* T^*) r^* dr^* d\theta dz^*$$

$$= \int_w^e \int_s^n \int_b^t \left(\frac{2}{r^*}\frac{\partial}{\partial \theta}(r^* w^* T^*)\Big|^1 - \frac{1}{r^*}\frac{\partial}{\partial \theta}(r^* w^* T^*)\Big|^0 \right) r^* dr^* d\theta dz^* \qquad (III.48)$$

$$\int_w^e \int_s^n \int_b^t \frac{1}{r^*}\frac{\partial}{\partial r^*}(r^* v^* T^*) r^* dr^* d\theta dz^*$$

$$= \int_w^e \int_s^n \int_b^t \left(\frac{2}{r^*}\frac{\partial}{\partial z^*}(r^* v^* T^*)\Big|^1 - \frac{1}{r^*}\frac{\partial}{\partial z^*}(r^* v^* T^*)\Big|^0 \right) r^* dr^* d\theta dz^* \qquad (III.49)$$

Diffusive term

$$\int_w^e \int_s^n \int_b^t \frac{1}{r^*}\frac{\partial}{\partial r^*}\left(r^* \frac{\partial T^*}{\partial r^*}\right) r^* dr^* d\theta dz^* = \left(r_n^* \frac{T_N^* - T_P^*}{dr_n^*} - r_s^* \frac{T_P^* - T_S^*}{dr_s^*} \right) \Delta\theta_P \Delta z_P^* \qquad (III.50)$$

$$\int_w^e \int_s^n \int_b^t \frac{1}{r^*}\frac{\partial}{\partial \theta}\left(\frac{1}{r^*}\frac{\partial T^*}{\partial \theta}\right) r^* dr^* d\theta dz^* = \left(\frac{1}{r_e^*}\frac{T_E^* - T_P^*}{d\theta_e} - \frac{1}{r_w^*}\frac{T_P^* - T_W^*}{d\theta_w} \right) \Delta r_P^* \Delta z_P^* \qquad (III.51)$$

$$\int_w^e \int_s^n \int_b^t \frac{\partial}{\partial z^*}\left(\frac{\partial T^*}{\partial z^*}\right) r^* dr^* d\theta dz^* = \left(\frac{T_T^* - T_P^*}{dr_t^*} - \frac{T_P^* - T_B^*}{dr_b^*}\right) r_P^* \Delta r_P^* \Delta\theta_P \qquad (III.52)$$

III.4.4. Discretization of the boundary conditions

All the boundary conditions on the velocity, temperature, and heat flux are transformed to a discrete form according to the grid.

III.4.4.1. At the inlet of the annular duct

The numerical domain at the inlet: $j = 1, 1 \le i \le IL, 1 \le k \le KL$

- Axial velocity: $v^*(r^*, \theta, 0, t^*) = 1$

The general form of the equation is given as follows:

$$\begin{aligned} A_P(i,j,k)v^*(i,j,k) &= A_N(i,j,k)v^*(i+1,j,k) + A_S(i,j,k)v^*(i-1,j,k) \\ &+ A_E(i,j,k)v^*(i,j,k+1) + A_W(i,j,k)v^*(i,j,k-1) \\ &+ A_T(i,j,k)v^*(i,j+1,k) + A_B(i,j,k)v^*(i,j-1,k) + S_v(i,j,k) \end{aligned} \qquad (III.53)$$

Which should be written as:

$$\begin{aligned} 1v^*(i,j,k) &= 0v^*(i+1,j,k) + 0v^*(i-1,j,k) + 0v^*(i,j,k+1) + 0v^*(i,j,k-1) \\ &+ 0v^*(i,j+1,k) + 0v^*(i,j-1,k) + 1 \end{aligned} \qquad (III.54)$$

- Radial and angular velocity: $u^*(r^*, \theta, 0, t^*) = w^*(r^*, \theta, 0, t^*) = 0$

$$\begin{aligned} 1u^*(i,j,k) &= 0u^*(i+1,j,k) + 0u^*(i-1,j,k) + 0u^*(i,j,k+1) + 0u^*(i,j,k-1) \\ &+ 0u^*(i,j+1,k) + 0u^*(i,j-1,k) + 0 \end{aligned} \qquad (III.55)$$

$$\begin{aligned} 1w^*(i,j,k) &= 0w^*(i+1,j,k) + 0w^*(i-1,j,k) + 0w^*(i,j,k+1) + 0w^*(i,j,k-1) \\ &+ 0w^*(i,j+1,k) + 0w^*(i,j-1,k) + 0 \end{aligned} \qquad (III.56)$$

- Temperature condition: T*=0

$$\begin{aligned} 1T^*(i,j,k) &= 0T^*(i+1,j,k) + 0T^*(i-1,j,k) + 0T^*(i,j,k+1) + 0T^*(i,j,k-1) \\ &+ 0T^*(i,j+1,k) + 0T^*(i,j-1,k) + 0 \end{aligned} \qquad (III.57)$$

III.4.4.2. At the outlet of the annular duct

The numerical domain: $j = JL, 1 \leq i \leq IL, 1 \leq k \leq KL$

- Radial, axial, and angular velocities: $\left.\frac{\partial u^*}{\partial z^*}\right|_{z^*=100} = \left.\frac{\partial v^*}{\partial z^*}\right|_{z^*=100} = \left.\frac{\partial w^*}{\partial z^*}\right|_{z^*=100} = 0$

Velocity is discretized using first-order backward finite difference scheme:

$$\frac{u^*(i,JL,k) - u^*(i,JL-1,k)}{dz^*(JL-1)} = 0 \Longrightarrow u^*(i,JL,k) = u^*(i,JL-1,k)$$

$$\frac{v^*(i,JL,k) - v^*(i,JL-1,k)}{dz^*(JL-1)} = 0 \Longrightarrow v^*(i,JL,k) = v^*(i,JL-1,k)$$

$$\frac{w^*(i,JL,k) - w^*(i,JL-1,k)}{dz^*(JL-1)} = 0 \Longrightarrow w^*(i,JL,k) = w^*(i,JL-1,k)$$

Where the coefficients are given as:

$$A_P(i,j,k) = 0 \qquad A_B(i,JL,k) = 1$$

$$A_N(i,JL,k) = A_S(i,JL,k) = A_E(i,JL,k) = A_W(i,JL,k) = A_T(i,JL,k) = A_B(i,JL,k) = 0$$

$$S(i,JL,k) = 0 \qquad (III.58)$$

- Temperature condition: $\frac{\partial}{\partial z^*}\left(\frac{\partial T^*}{\partial z^*}\right)\Big|_{z^*=100} = 0$

It is discretized using first-order backward finite difference scheme:

$$\frac{T^*(i,JL,k) - T^*(i,JL-1,k)}{dz^*(JL-1)} - \frac{T^*(i,JL-1,k) - T^*(i,JL-2,k)}{dz^*(JL-2)} = 0$$

The coefficients are given as:

$$A_P(i,j,k) = 1 \qquad A_B(i,JL,k) = 1$$

$$A_N(i,JL,k) = A_S(i,JL,k) = A_E(i,JL,k) = A_W(i,JL,k) = A_T(i,JL,k) = A_B(i,JL,k) = 0$$

$$S(i,JL,k) = T^*(i,JL-1,k) - T^*(i,JL-2,k) \qquad (III.59)$$

III.4.4.3. At the interior cylinder

The numerical domain is: $i = 1, 1 \leq j \leq JL, 1 \leq k \leq KL$

- Radial, angular, and axial velocities, only the coefficients A_P are equal to 1
- Adiabatic cylinder $\left(\frac{\partial T^*(r,\theta,z,t}{\partial r^*}\right)\Big|_{r=r_i} = 0$

It is discretized using first-order backward finite difference scheme:

$$\frac{T^*(1,j,k) - T^*(2,j,k)}{dr^*(IL)} = 0 \Rightarrow T^*(1,j,k) = T^*(2,j,k)$$

The coefficients are written as:

$A_P(1,j,k) = 1 \qquad A_S(1,j,k) = 1$

$A_E(1,j,k) = A_W(1,j,k) = A_T(1,j,k) = A_B(1,j,k) = 0$

$S(1,j,k) = 0 \qquad (III.60)$

III.4.4.3. At the exterior cylinder

The numerical domain is: $i = IL, 1 \leq j \leq JL, 1 \leq k \leq KL$

- Radial, angular, and axial velocities: only the coefficients A_P are equal to 1
- Heat flux $\left(\frac{\partial T^*(r,\theta,z,t}{\partial r^*}\right)\Big|_{r=r_o} = 1$

It is discretized using first-order backward finite difference scheme:

$$\frac{T^*(IL,j,k) - T^*(IL-2,j,k)}{dr^*(IL)} = 1 \Rightarrow T^*(IL,j,k) = T^*(IL-2,j,k) + dr^*(IL)$$

The coefficients are written as:

$A_P(IL,j,k) = 1 \qquad A_S(IL,j,k) = 1$

$A_E(IL,j,k) = A_W(IL,j,k) = A_T(IL,j,k) = A_B(IL,j,k) = 0$

$S(IL,j,k) = dr^*(IL) \qquad (III.61)$

III.4.5. Solution algorithm

Patankar's SIMPLER technique (Semi Implicit Pressure Linked Equation Revised) [51] is used to solve the discretized equation systems for velocity, pressure, and temperature fields.

The key steps involved in the SIMPLER algorithm are:

1. Guess an initial pressure field P* and velocity fields u*, w*, v*.
2. Solve discretized momentum equation with assumed pressures and generate pseudo-velocity fields u^, w^, v^.
3. Calculate mass source terms from the pseudo-velocities and use them in the corrected equation of pressure.
4. Solve the new equation to calculate the corrected pressure P'.
5. Modify the pressure and velocity fields using the new corrected equation.
6. Solve the discretized energy/temperature equation using the updated velocities.
7. Treat the updated pressure and velocities as new guesses P*, u*, v*, w* and repeat from step 2 until convergence.

III.4.6. Solution of the discretized equations

The resolution of the algebraic equations is achieved using an iterative approach along radial, angular and axial directions.

III.4.6.1 Thomas Algorithm

The Thomas algorithm, also known as the tridiagonal matrix algorithm (TDMA), is a simplified form of Gaussian elimination used to solve tridiagonal systems of linear equations.

The tridiagonal system has the form:

$$a_i x_{i-1} + b_i x_i + c_i x_{i+1} = d_i \qquad \text{for i} = 1, \text{IL} \qquad \text{(III. 62)}$$

Where a_i, b_i, c_i, and d_i are known coefficients:

$$a_i = A_P(i, j, k)$$

$$b_i = A_N(i,j,k)$$

$$c_i = A_S(i,j,k)$$

$$d_i = A_T(i,j,k)\,\varphi(i,j+1,k) + A_B(i,j,k)\,\varphi(i,j-1,k) + A_E(i,j,k)\,\varphi(i,j,k+1) + A_W(i,j,k)\,\varphi(i,j,k-1) + S_\varphi(i,j,k) \qquad (III.63)$$

III.4.6.2. Mesh test

It is essential to perform mesh independence tests in CFD simulations to guarantee that our results are not significantly influenced by the grid resolution and to determine the optimal mesh density that balances accuracy and computational cost. For our study, a uniform hexahedral mesh was employed in each of the cylindrical coordinate directions (radial, angular, and axial), as illustrated in **Figure III.6**. Three different mesh resolutions were tested to assess the effects of grid size and obtain accurate results: 32 × 34 × 162, 42 × 44 × 142, and 42 × 44 × 152. The simulations were performed for kerosene fluid, with Re= 800 Gr= 7.5×10^5. **Table II.1** presents the effect of the mesh resolution on the average Nusselt number, and **Figure III.7** displays the local Nusselt number along the axial direction for the three mesh resolutions.

The results showed that the last two meshes (42 × 44 × 142 and 42 × 44 × 152) in the radial, angular, and axial direction, respectively, produced qualitatively and quantitatively similar results, with the average Nusselt numbers being 16.33751 and 16.33945, respectively.

This results indicate that further refinement of the mesh beyond 42 × 44 × 152 would not significantly improve the accuracy of the results. Among the three meshes tested, the grid with 42 × 44 × 152 nodes was chosen as the optimum mesh resolution, as it provided accurate results and better visualization of the flow field and heat transfer features.

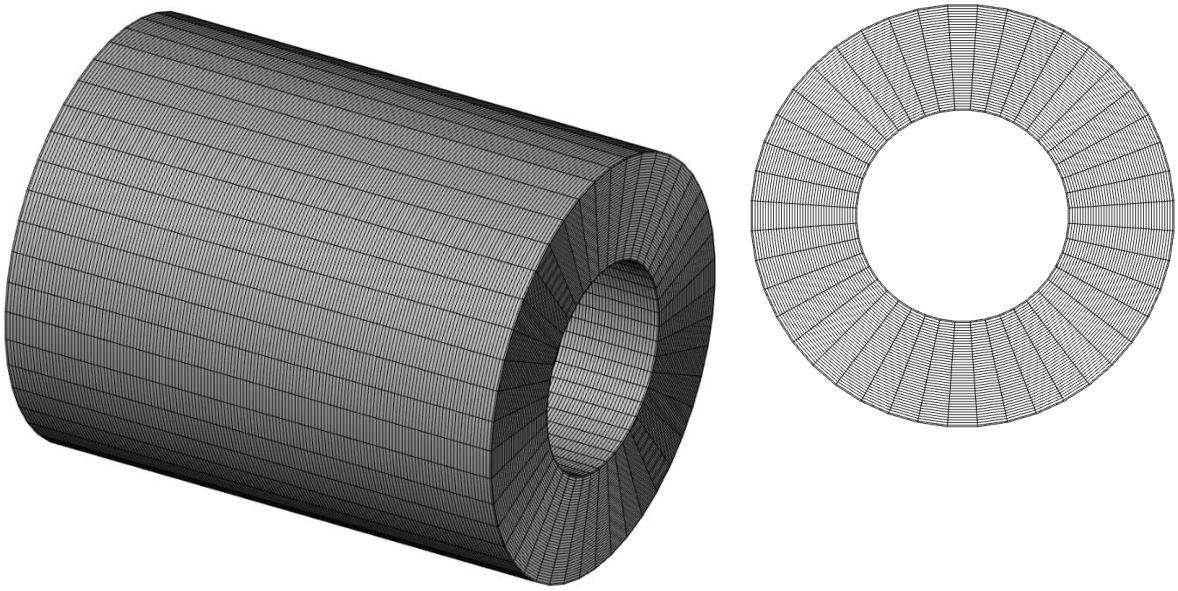

(a) (b)

Figure III. 6. Generated mesh: (a) 3D view and (b) front view.

Table III. 1. The mesh test on the average Nusselt number.

Mesh (r,θ,z)	**32×34×162**	**42×44×142**	**42×44×152**
Nu_{ave}	16.67938	16.33751	16.33945

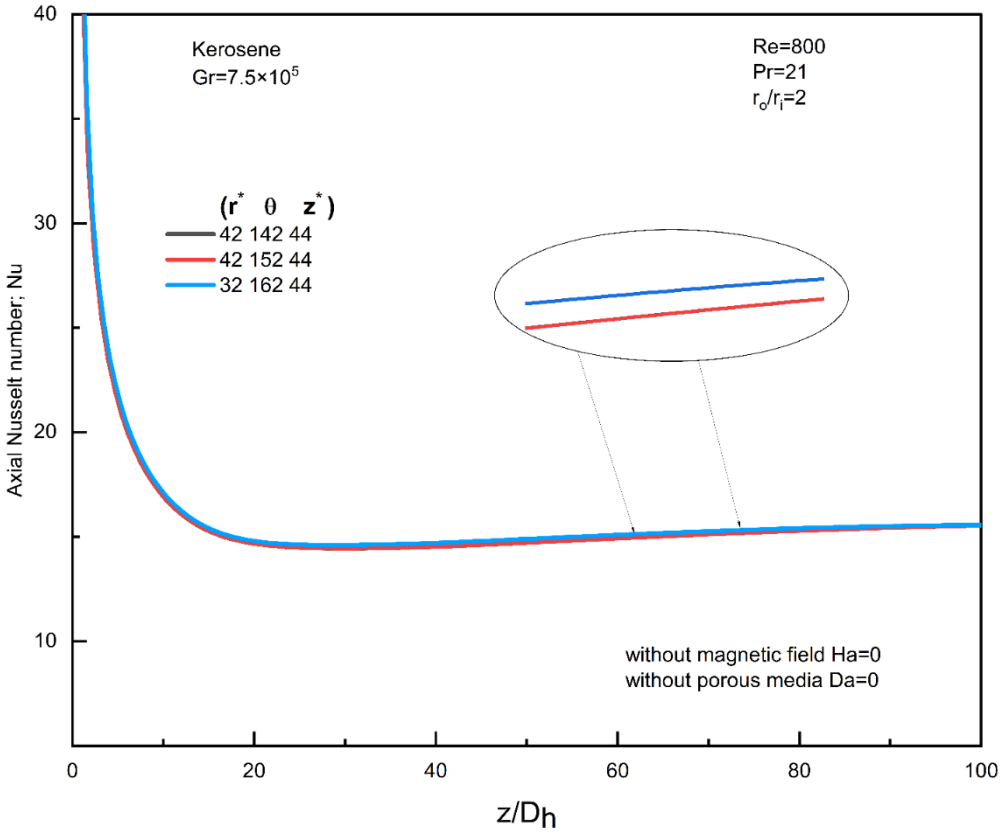

Figure III. 7. Grid test.

III.4.6.3. Code validation

The validation process is crucial because it ensures that the numerical model accurately captures the physical phenomena under investigation and provides confidence in the results obtained from the simulations. In this case, the validation process involves comparing the axial Nusselt number and wall temperature profiles obtained from the CFD simulations with published experimental and numerical results, as well as analytical correlations.

Firstly, we focused on validating the axial Nusselt number; **Figure III.8** presents a comparison of our local Nusselt number with the experimental results of Kim et al. [52], the numerical results of Bayat and Nikseresht [53], and the analytical correlation of Shah and London [22] equation (III.64) using water as base fluid. This comparison shows that the current results correspond well with the experimental, numerical, and analytical results. This agreement validates the accuracy of the numerical model and the implemented computational methodology.

In addition to the axial Nusselt number, the temperature profile of the wall is also validated. **Figure III.9** compares the wall temperature profile obtained from the current simulations and the results reported by Takabi et al. [54] using (Al_2O_3/water) nanofluid at ϕ=2% and Re=1257. The excellent agreement among both data further confirms the reliability of our numerical simulations.

$$\begin{cases} Nu = 1.953\left(\mathrm{Re}\,\mathrm{Pr}\frac{\mathrm{D}}{\mathrm{z}}\right)^{1/3} & for\ \mathrm{Re}\,\mathrm{Pr}\frac{\mathrm{D}}{\mathrm{z}} \geq 33.33 \\ Nu = 4.364 + 0.0722\left(\mathrm{Re}\,\mathrm{Pr}\frac{\mathrm{D}}{\mathrm{z}}\right) & for\ \mathrm{Re}\,\mathrm{Pr}\frac{\mathrm{D}}{\mathrm{z}} \leq 33.33 \end{cases} \quad \text{(III.64)}$$

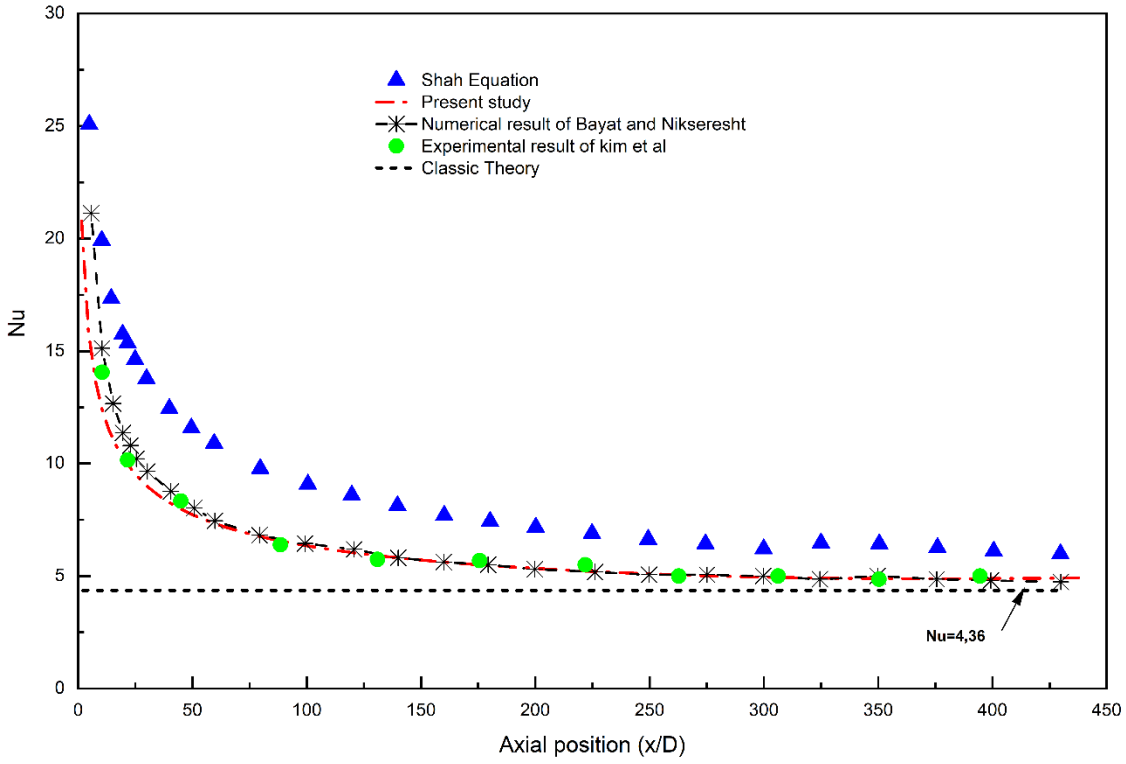

Figure III. 8. Local Nusselt number along the tube.

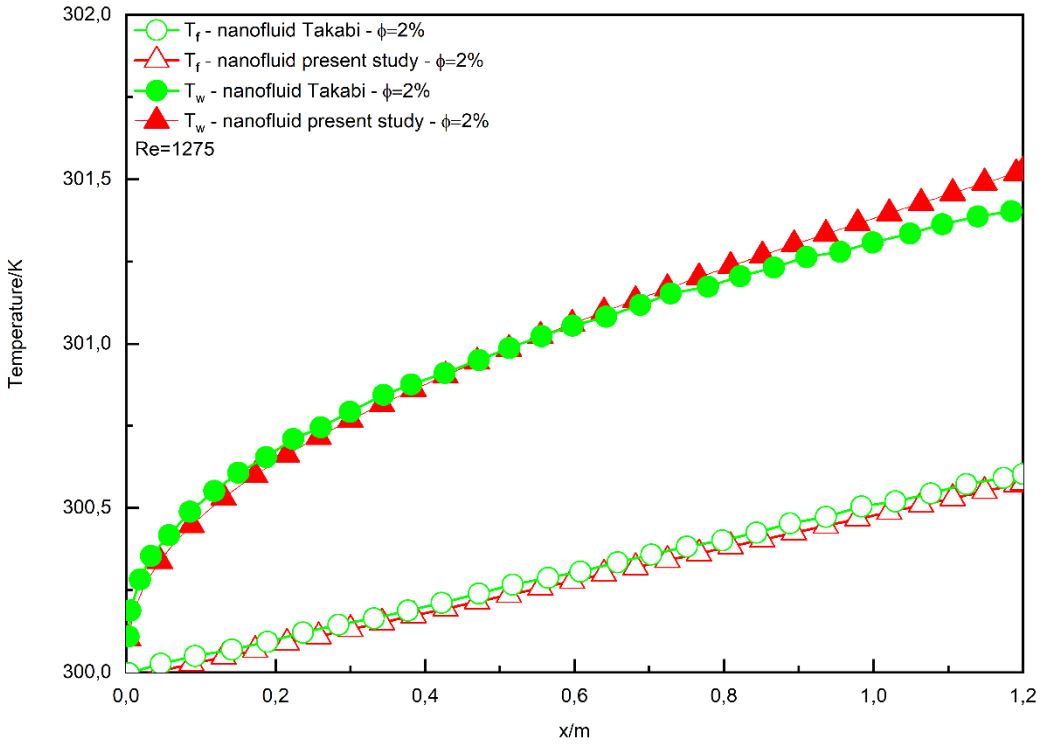

Figure III. 9. Comparison of the wall temperature profile at Re=1275.

III.5. Computational fluid dynamics software

The second application uses ANSYS-Fluent (CFD) software based on a finite volume approach. It involves pre-processing (mesh generation), solving (numerical simulation), and post-processing (data analysis) stages. ANSYS-Fluent offers advanced simulation capabilities, robust pre-processing tools, efficient solver technology, and comprehensive post-processing capabilities, making it a preferred choice for complex fluid dynamics simulations across various industries.

III.5.1. Discretization scheme

In ANSYS Fluent, the system of equations are discretized using Finite volume technique. The discretization schemes used in the current study are summarized in **Table III.2**. Each equation in the governing set has been discretized using an appropriate scheme to ensure the best possible results.

Table III. 2. The numerical schemes used.

Equation	**Scheme**
Gradient	Green-Gauss cell based
Pressure	Second order Upwind
Momentum	Second order Upwind
Energy	Second order Upwind
Magnetic induction	First order Upwind

III.5.2. Solution algorithm

The SIMPLE (Semi-Implicit Method for Pressure-Linked Equations) algorithm was utilized to solve the velocity-pressure coupling. It is a widely adopted approach to solving the Navier-Stokes equations in incompressible flow simulations.

III.5.3. Boundary condition

The boundary conditions applied for our numerical simulations are essential for defining how the fluid interacts with the surfaces of the domain and how heat transfer is managed. **Table III.3** outlines these conditions, detailing the hydrodynamic and thermal conditions at various boundaries of the simulation domain:

- **Inlet:** The hydrodynamic condition specifies a uniform velocity $v=v_0$, while the thermal condition sets the uniform temperature $T=T_0$, denoting that the fluid enters the domain at a constant temperature.
- **Outlet**: The outlet boundary is defined as a pressure outlet.
- **Inner wall:** The inner wall comes under non-slip conditions, ensuring no fluid slips along the wall surface. Thermally, it is assumed to be adiabatic: no heat is transferred across this boundary.
- **Outer wall**: For the hydrodynamic condition, a non-slip condition is considered, and for the thermal condition, it is exposed to a constant heat flux.

Table III. 3. The boundary conditions.

Boundary	**Hydrodynamic condition**	**Thermal condition**
Inlet	$V=v_0$	$T=T_0$
Outlet	Pressure outlet	
Inner wall	Non-slip condition	Adiabatic
Outer wall	Non-slip condition	Uniform heat flux q_w

III.5.4. Under relaxation factor

The under-relaxation factors help control the updates of the respective variables during the iterative solution process, preventing divergence and ensuring stable convergence toward the final solution. **Table III.4** presents the under-relaxation factors employed in ANSYS Fluent to enhance the stability and convergence of the numerical solution.

Table III. 4. Under-relaxation factor.

Variables	**Under-relaxation factors**
Pressure	0.3
Density	1
Body forces	1
Momentum	0.7
Energy	0.9
Magnetic induction	0.9

III.5.5. Convergence criteria

The numerical solution's convergence was tracked via the residuals of the governing equations. The residuals represent the imbalances in the conservation equations for momentum, mass, energy, etc.

In ANSYS Fluent, they are described based on a discretized form of the conservation equation for a general variable φ as follows:

$$R_{\varphi} = \sum_{cells\ p} \left| \sum_{i} a_i \varphi_i + b - a_p \varphi_p \right| \qquad (III.65)$$

In the present study, the simulations were considered converged when the residuals for the equations are as shown below:

Continuity and Momentum: 10^{-4}

Energy: 10^{-8}

User-defined scalars (UDS): 10^{-3}

These converged criteria ensure that the numerical solution has been converged properly, and doing more iterations won't change the final results.

III.5.6. Computational domain and mesh generation

In ANSYS computational fluid dynamics (CFD) simulations, the accuracy and reliability of the numerical results are heavily influenced by the quality of the computational mesh. To ensure the convergence of the solution and minimize numerical errors, a grid test investigation was performed by evaluating the simulation results on six different meshes. A uniform hexahedral mesh was employed across all directions (radial, angular, and axial) to discretize the computational domain. **Figure III.10** illustrates the effect of mesh size on the average Nusselt number, a dimensionless parameter that quantifies the convective heat transfer. The simulations were performed for a water-based fluid, with a fixed Reynolds number of Re = 800, without considering magnetohydrodynamic (MHD) effects (Ha = 0), and without the presence of porous media (Da = 0). The results depicted in **Figure III.10** show that the last three mesh resolutions (768,000, 883,000, and 968,000 cells) yielded similar results for the average Nusselt number, indicating that further mesh refinement beyond 768,000 cells would not significantly improve the accuracy of the solution. Based on this observation, the mesh comprising 768,000 cells was selected as the optimal mesh resolution, striking a balance between computational accuracy and simulation time.

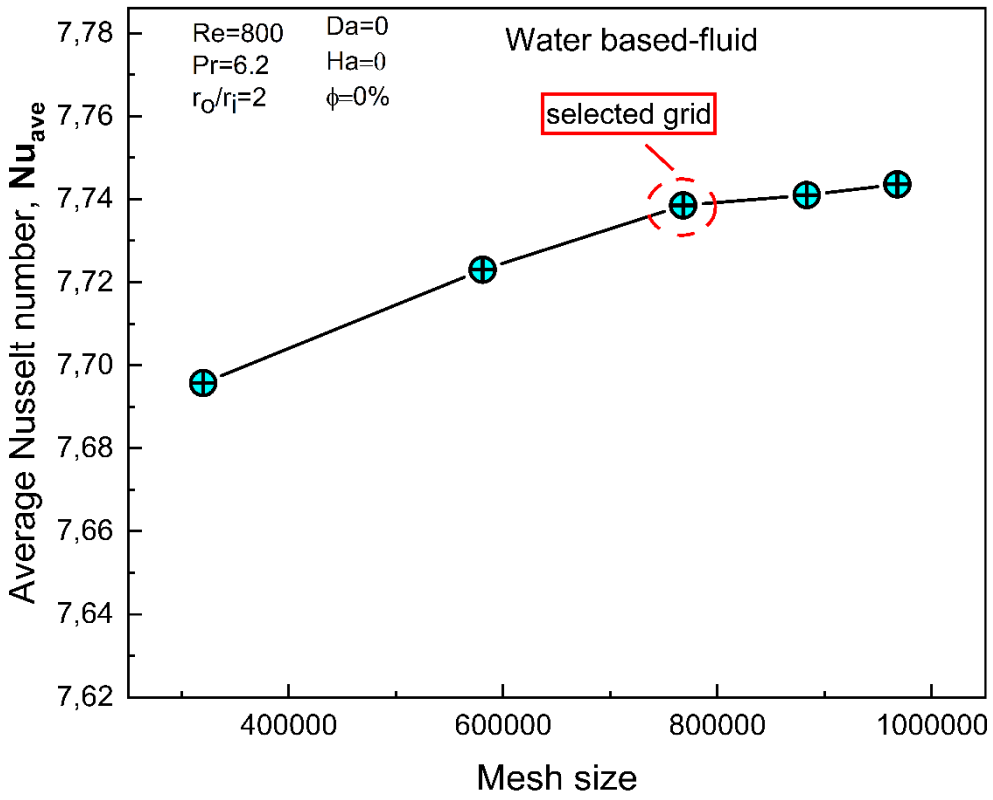

Figure III. 10. Mesh tests at Re=800, and Pr=6.2.

III.5.7. Code validation

To ensure the credibility of our results, we conducted an extensive series of validations by comparing our results with analytical solutions, numerical studies, and experimental data.

The first validation was obtained using the axial Nusselt number, which quantifies the convective heat transfer along the length of the duct or channel. **Figure III.11a** compares the axial Nusselt number distribution within a straight duct. Our numerical results were benchmarked against two well-established references:

- Analytical solution by Shah and London [22]: This widely accepted analytical correlation accurately estimates the Nusselt number in ducts and pipes.
- Numerical results by Benkhedda et al. [23]: These authors conducted numerical simulations for a similar flow configuration and reported their results for the Nusselt number distribution.

The comparison was performed for a Reynolds number of Re = 1275 and water fluid. Our results exhibited excellent agreement with both the analytical solution and the numerical results, validating the accuracy of our computational model for predicting heat transfer in straight ducts.

To further validate the numerical model's capability in simulating fluid flow and heat transfer through porous media, **Figure III.11b** compares our results and experimental data obtained by Pavel and Mohamad [55]. The comparison was made for Re = 100, Da = 0.001, and a porosity ratio of Rp = 1, using water as the base fluid. The strong consistency of our numerical and experimental results verifies our computational model's ability to accurately capture the physics of flow and heat transport in porous media.

Additionally, to validate the impact of an applied magnetic field on forced convection, **Figure III.12** compares the axial velocity profile in the radial direction obtained from our simulations with the numerical results reported by Aminian et al. [56]. The comparison was made for the specific parameters of Da = 0.1 (Darcy number) and Ha = 40 (Hartmann number). The good agreement between our results and the reference numerical study further confirms the accuracy of our computational model in simulating magnetohydrodynamic (MHD) flows.

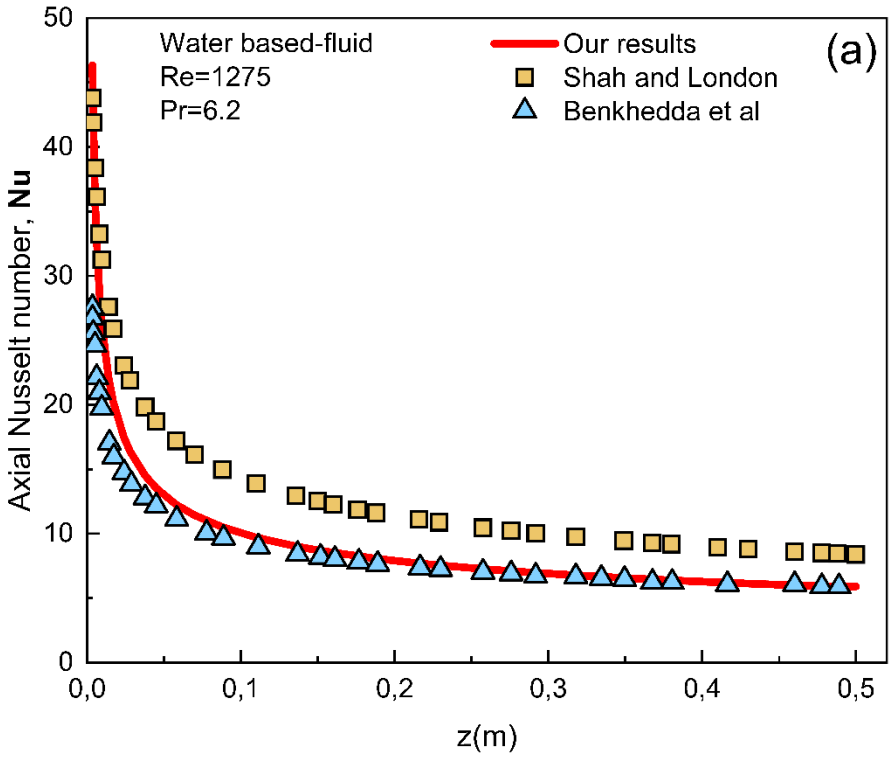

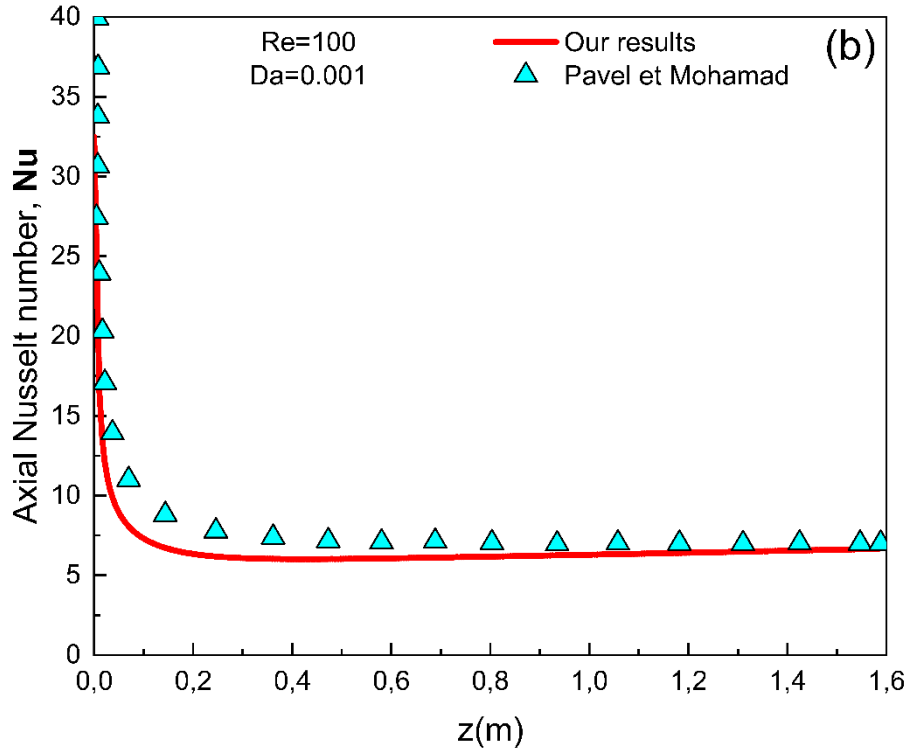

Figure III. 11. Comparison of Axial Nusselt number through a straight duct.

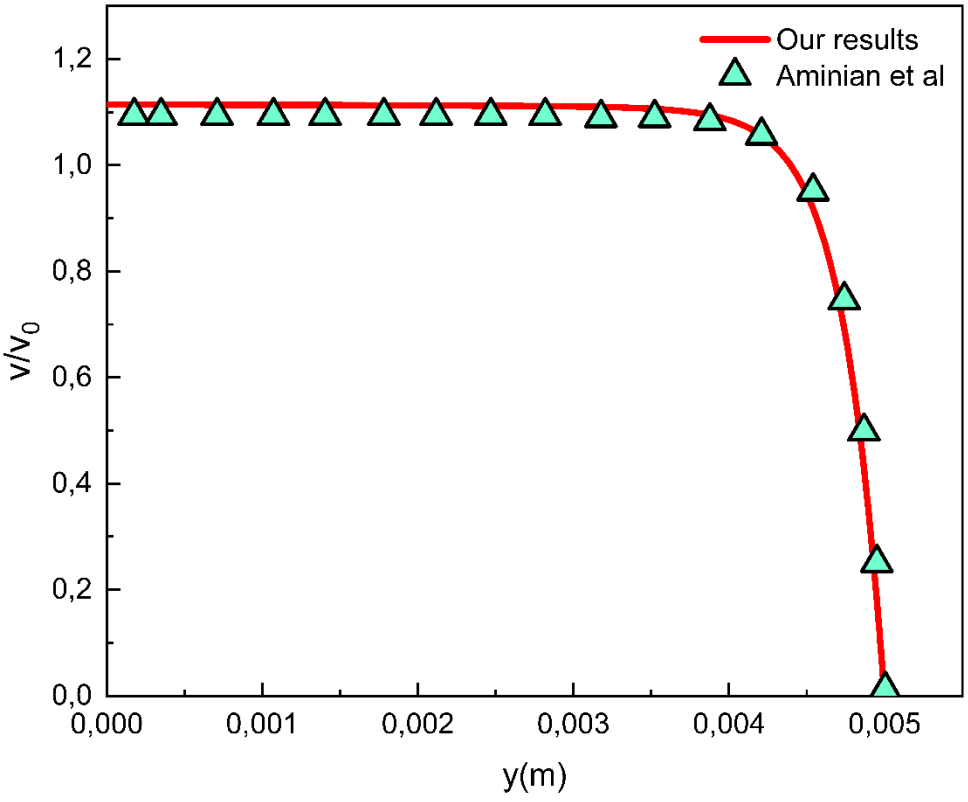

Figure III. 12. Comparison of the axial velocity along radial direction.

Chapter IV: Results and discussions

IV.1. Introduction

The current chapter presents the obtained results from the numerical simulations and provides a thorough discussion of the findings. Results are displayed as velocity contours, 3D isotherm contours, Nusselt number, skin friction coefficient, pressure drop, and entropy analysis. It interprets the data in the context of heat transfer enhancement, examining the effects of binary and ternary hybrid nanofluids, porous media, and magnetic fields on the convective heat transfer process. Comparative analyses are conducted to evaluate the performance of different configurations and conditions.

IV.2. First application

In this application, the numerical investigation focuses on mixed convection heat transfer involving two different binary hybrid nanofluids and one ternary hybrid nanofluid flowing via annular duct filled with permeable medium under a uniform magnetic field. The hybrid nanofluids consist of various nanoparticles types and forms dispersed in kerosene. The first binary hybrid nanofluid consisted of TiO_2 in a spherical form, and CNT in a cylindrical form, whilst the second binary hybrid nanofluid comprised TiO_2 with a spherical form, and Graphene with a platelet form mixed in equal proportions 50% TiO_2, and 50% CNT, 50% TiO_2, and 50% Graphene. The Ternary hybrid nanofluid, however, included TiO_2, CNT, and Graphene nanoparticles in a mixture ratio of 50% TiO_2, 25% CNT, and 25% Graphene. The simulation was conducted for various Hartmann numbers ($0 \leq Ha \leq 50$), Darcy numbers ($10^{-4} \leq Da \leq 10^{-1}$), and magnetic field inclination ($0° \leq \psi \leq 90°$) at a fixed Grashof number $Gr=10^6$, $\phi=5\%$, and $Re=800$. This section examines and discusses the effects of these parameters on the hydrodynamic and thermal fields. Additionally, it presents the average Nusselt number, pressure drop, average skin friction coefficient, and entropy generation.

IV.2.1 Hydrodynamic field

In **Figures IV.1** and **IV.2**, the dimensionless angular and axial velocity contours are provided at different locations in the annular duct using (TiO_2-CNT-Graphene/kerosene) for Da=0, Ha=0, $Gr=10^6$, and $\phi=5\%$. A vertical symmetry line at the plane has been indicated, which passes through the duct's midpoint. **Figure IV.1** shows that in the region close to the inlet $z^*=0.33$, irregularities in the angular velocity are observed, with it dropping and rising. The perturbation zone develops due to the application of buoyancy-driven phenomena and it is a

result of the varied fluid densities caused by hot and cold fluids. Subsequently, as the flow develops along the pipes, the angular velocity stabilizes, maintaining a qualitative similarity until the exit. The angular velocity occurs in the form of two counter-rotating cells: one near the interior wall, which is adiabatic, and the other one near the outer wall. These flows are essentially buoyancy-driven, whereby hot, less dense fluids rise while the cold, denser fluid drops. Further, the maximum angular velocity along the pipe length increases at z* = 27. This is because the buoyancy force is maximum in this region, and there exists a substantial temperature difference. Beyond z* = 27, the angular velocity diminishes towards the outlet mainly due to the decrease in the buoyancy force; the ternary hybrid nanofluid temperature approaches the temperature of the annulus wall. As a result, the maximum velocity in the annular ducts is situated at the perturbation zone (r*=0.931, θ=π, z*=0.33).

(a) z^*=0.33 (b) z^*=27 (c) z^*=100

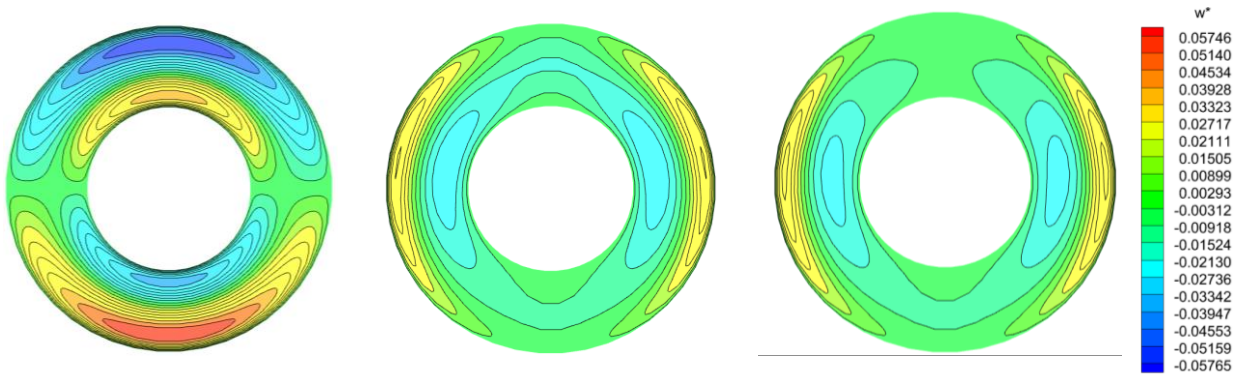

Figure IV. 1. Angular velocity contours at various locations using (TiO_2-CNT-Graphene/kerosene).

In **Figure IV.2**, at a location extremely near the inlet (z*=0.33), the axial velocity remains nearly uniform with slight variations near both the outer and inner walls. As we progress to z*=6.33, the velocity contours take the form of concentric circles, with the maximum velocity located at the center of the annular duct. Upon reaching z*=27, an angular distortion becomes noticeable, resulting in the maximum velocity shifting towards the central and lower region within the duct. At the duct outlet for z*=100, we observe the emergence of two distinct cells, each exhibiting maximum velocity at their midpoint.

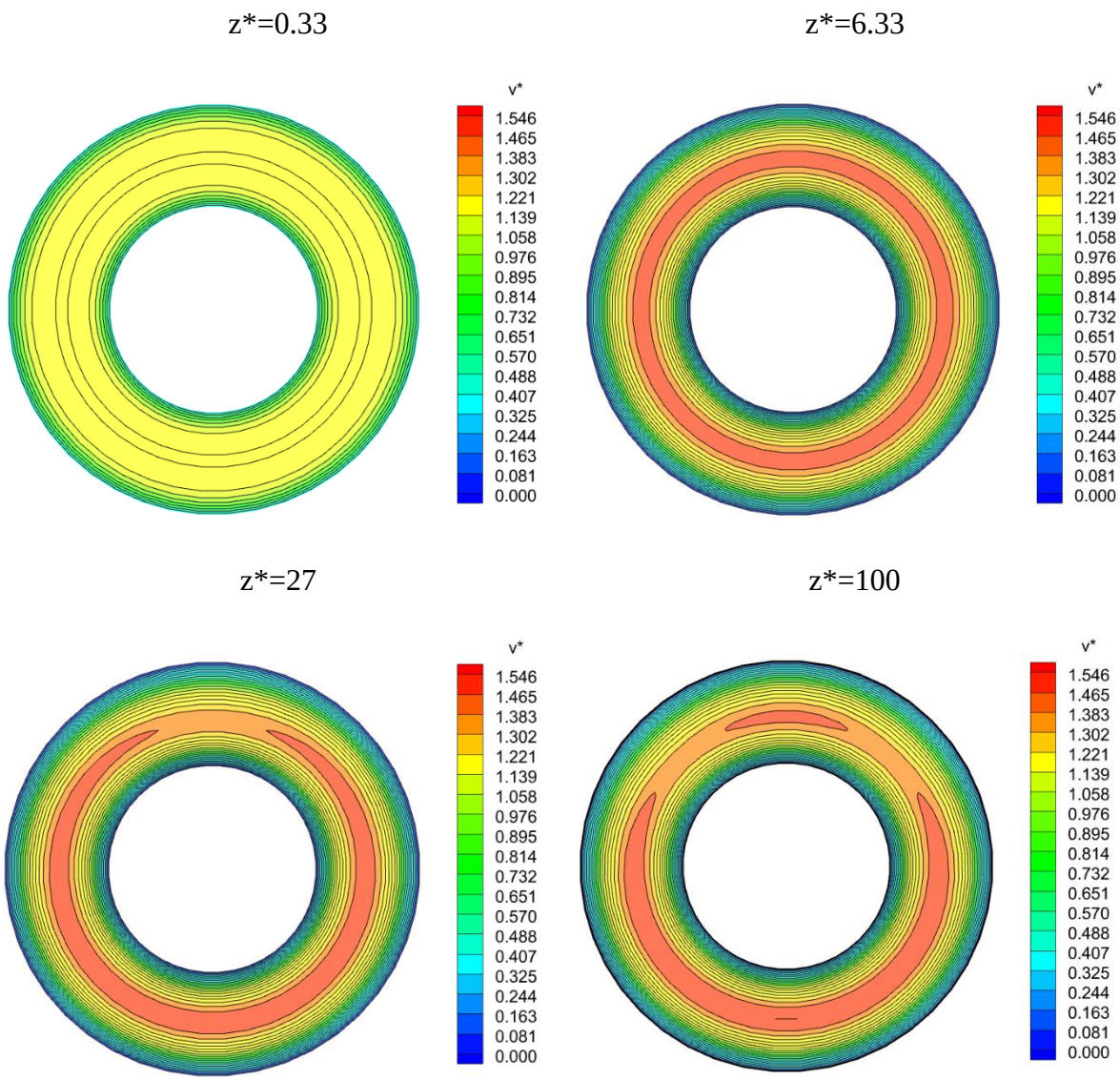

Figure IV.2. Axial velocity contours at various locations using (TiO_2-CNT-Graphene/kerosene).

Figure IV.3 illustrates the effect of Darcy numbers on the non-dimensional angular velocity contours using (TiO_2,CNT,Graphene/kerosene) ternary hybrid nanofluid, (TiO_2,CNT,kerosene), and (TiO_2,Graphene,kerosene) binary hybrid nanofluids at the absence of the magnetic field. Because of the symmetrical characteristics, just half of the annulus velocity contours are shown. At $Da=10^{-4}$, the strength of vortices is less pronounced compared to higher Darcy numbers regardless the hybrid nanofluids examined. As Darcy number increases, the strength of the counter rotating cells becomes increasingly evident. The ternary hybrid nanofluid has a lower maximum angular velocity than the binary hybrid nanofluids (TiO_2,CNT/kerosene) and (TiO_2,Graphene/kerosene). This is because the mixing of three different nanoparticles with various forms boosts the viscosity of the ternary hybrid nanofluid.

The increased viscosity restricts the fluid's capacity to carry angular momentum, leading to a reduced dimensionless angular velocity. The location of the maximum angular velocity is given in **Table IV.1**.

Table IV. 1. Location of the maximum angular velocity for various Darcy number.

Darcy number	**Radial location**	**Angular location**	**Axial location**
10^{-4}	0.543	0°	0.3
10^{-3}	0.931	180°	0.33
10^{-1}	0.931	180°	0.33

Da=0.0001 Da=0.001 Da=0.1

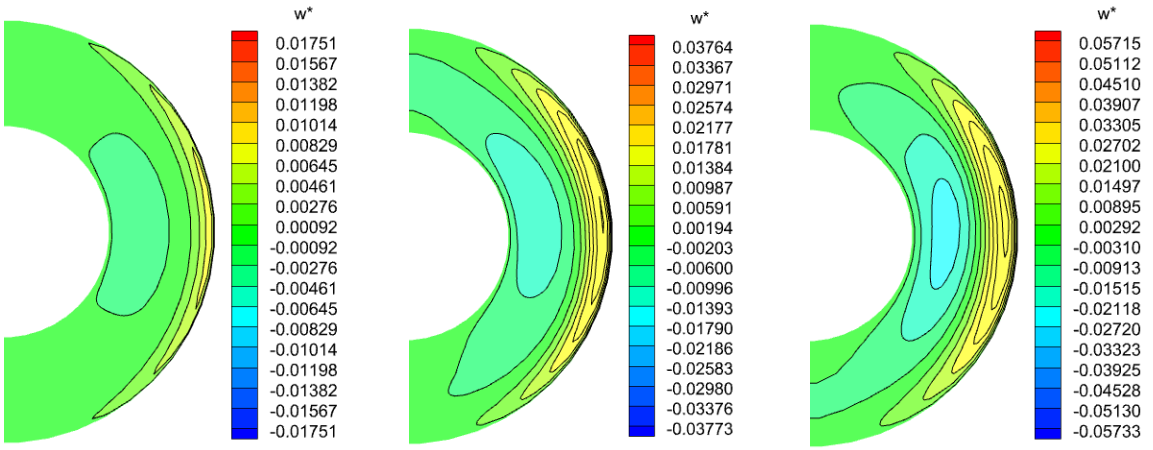

(a)TiO_2-CNT-Graphene/kerosene

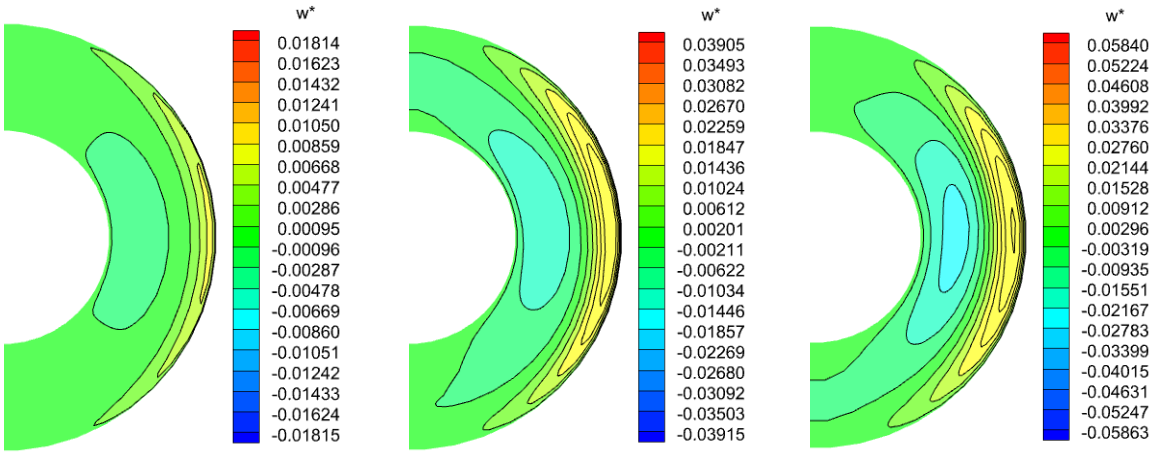

(b) TiO_2-CNT/kerosene

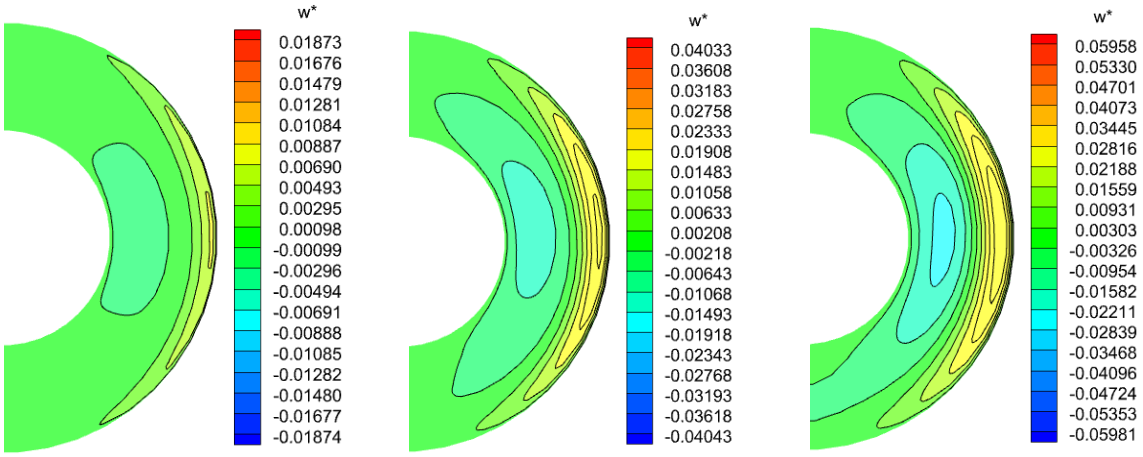

(c) TiO_2-Graphene/kerosene

Figure IV. 3. Effect of Da on angular velocity contours for: a (TiO_2-CNT-Graphene/ kerosene), b (TiO_2-CNT/kerosene), c (TiO_2-Graphene/kerosene).

The impact of the magnetic field on the non-dimensional angular velocity at various orientations of the magnetic field is illustrated in **Figures IV.4** and **IV.5**. The cases are considered with the Grashof number (Gr) of 10^6. The Darcy number is equal to 0.01, and the volume concentration is 5%. In **Figure IV.4**, (ψ=0°) the case is simulated with three different hybrid nanofluids: (TiO_2-CNT-Graphene/kerosene), (TiO_2-CNT/ kerosene), and (TiO_2-Graphene/ kerosene). In the considered cases with the increased values of the Hartmann number, the angular velocity values decrease for all of the hybrid nanofluids tested; they also depict the intense counter rotating cells. The decreased angular velocity can be explained due to the magnetic field influence on the fluid dynamics. The increased Hartmann number triggers the stronger magnetic field, and, in its turn, this field operates on a breaking influence on the fluid motion resulting in the diminished angular velocities. Whereas, the intense counter-rotating cells can be explained through the increased influence of the buoyancy force; in other words, the magnetic field increase raises the buoyancy force influence on the flow dynamics. The results of the analysis indicate that the TiO_2-Graphene/kerosene binary hybrid nanofluid possesses the highest velocity, but only for the low Hartmann number. Conversely, the TiO_2-CNT/kerosene binary hybrid nanofluid possesses the maximum velocity at higher Hartmann number (Ha=50).

Figure IV.5 reflects the angular velocity at the tube exit for the TiO_2-CNT-Graphene/kerosene ternary hybrid nanofluid, at (ψ=90°) and various Hartmann numbers. As the results

demonstrate, there are no unremarkable alternations in angular velocity values. The location of the maximum angular velocity for various inclination angles and Hartmann number are presented in **Table IV.2**. It is observed that, the maximum velocity occurs in the perturbation zone near the inlet of the duct, except when ψ=0° and Ha=50, where the maximum velocity shifts to the area near the outlet of the duct.

Table IV. 2. Location of the maximum angular velocity for various orientations and Hartmann number.

Orientation	**Hartmann number**	**Radial location**	**Angular location**	**Axial location**
ψ=0°	10	0.906	180°	0.33
	30	0.906	180°	0.33
	50	0.943	90°	85
ψ=90°	10	0.906	180°	0.33
	30	0.906	180°	0.33
	50	0.906	180°	0.33

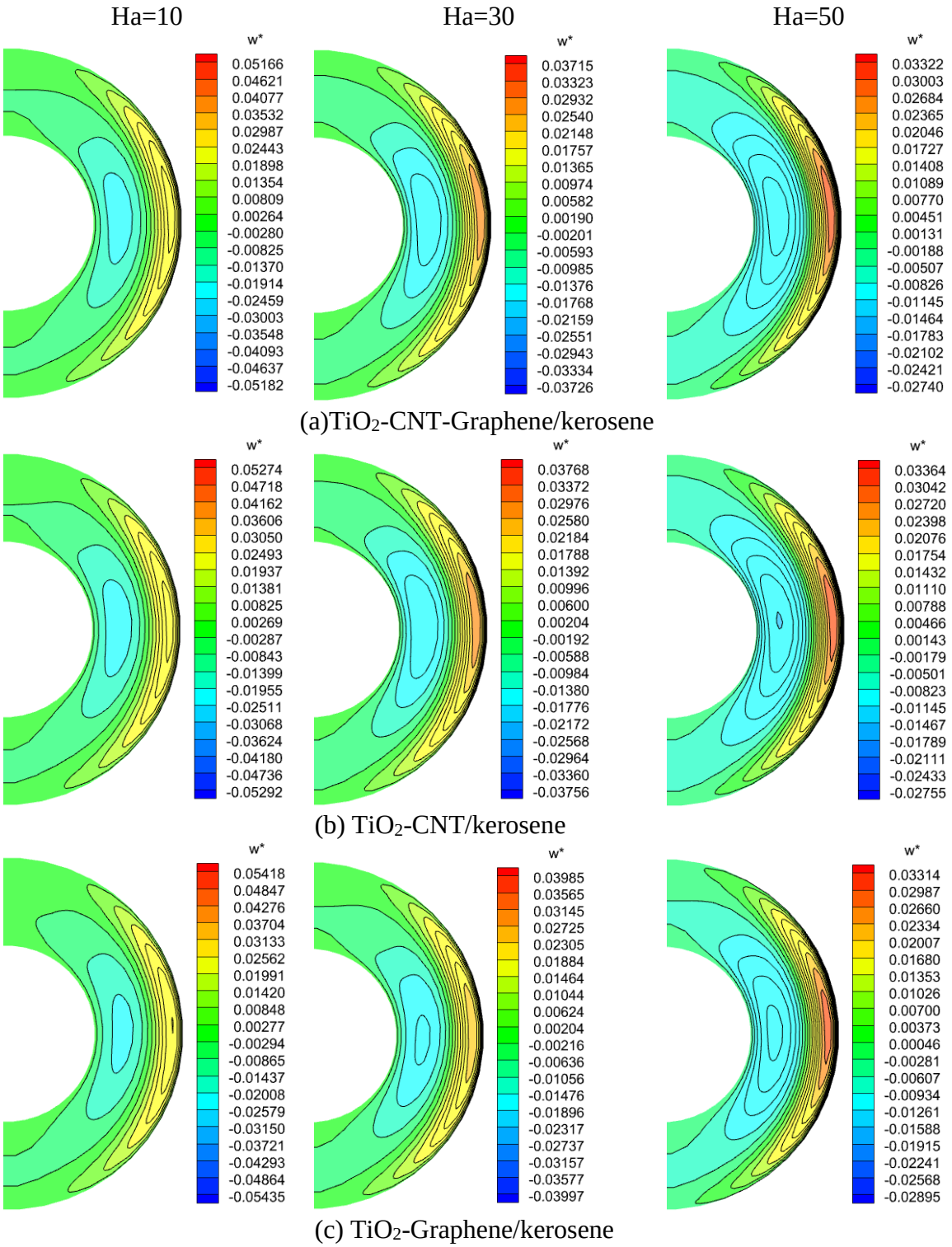

Figure IV. 4. Effect of Hartmann number on angular velocity contours at ψ=0°, for: a (TiO_2-CNT-Graphene/kerosene), b (TiO_2-CNT/kerosene), c (TiO_2-Graphene/kerosene).

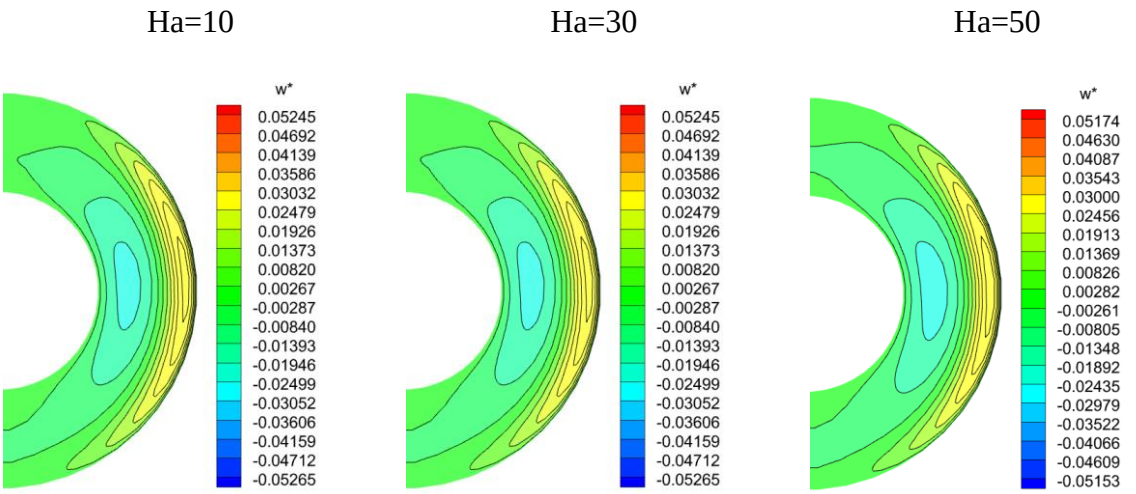

Figure IV. 5. Effect of Hartmann number on angular velocity contours at ψ=90° using (TiO_2-CNT-Graphene/kerosene).

Figure IV.6 presents the non-dimensional axial velocity profiles for three different hybrid nanofluids across various Da numbers. At low Darcy numbers ($Da=10^{-4}$), the velocity is uniformly low across the duct, indicating minimal fluid movement. As the Darcy number boosts ($Da=10^{-3}$), the cells in vicinity of the walls start to divide indicating variation in the velocity, and the highest velocity value increases. The axial velocity shows a structure of circular cells, maintaining consistent value within the annulus duct except in the vicinity of the channel's wall. For ($Da=10^{-2}$), the concentric circle cells in the center undergo angular deformation with the ternary hybrid nanofluid, while they remain circular for the other binary hybrid nanofluids. At ($Da=10^{-1}$), the formation of distinct flow cells within the annulus becomes evident due to the impact of buoyancy forces. In particular, for the ternary hybrid nanofluid composed of TiO_2, CNT, and Graphene dispersed in kerosene, two distinct cells form in the middle of the annulus. This behavior can be attributed to the combined effects of buoyancy forces and the enhanced thermal properties of the ternary hybrid nanofluid, which promote more vigorous fluid movement and the formation of convective cells. Similarly, the TiO_2-CNT/kerosene binary hybrid nanofluid also exhibits the formation of two cells in the middle of the annulus at $Da=10^{-1}$. The buoyancy force, resulting from the temperature gradient and the enhanced thermal conductivity of the hybrid nanofluid, leads to this noticeable convective pattern. The presence of CNTs (Carbon Nanotubes) likely contributes significantly to the fluid's thermal conductivity, thereby intensifying the convective currents and resulting in the formation of these cells. In contrast, for the TiO_2-Graphene/kerosene binary hybrid nanofluid,

the behavior differs slightly. While there is a notable convective cell in the middle of the annulus, it remains a single cell with only slight deformation observed at the top middle region.

The Darcy number reflects the permeability of the porous medium. A higher Da number indicates higher permeability, allowing for greater fluid flow. While, a lower Da number indicates higher viscous forces, reducing the fluid motion velocity. In addition, at higher Darcy numbers, the increased permeability of the medium allows these buoyancy-driven flows to become more pronounced, leading to the formation of distinct convective cells.

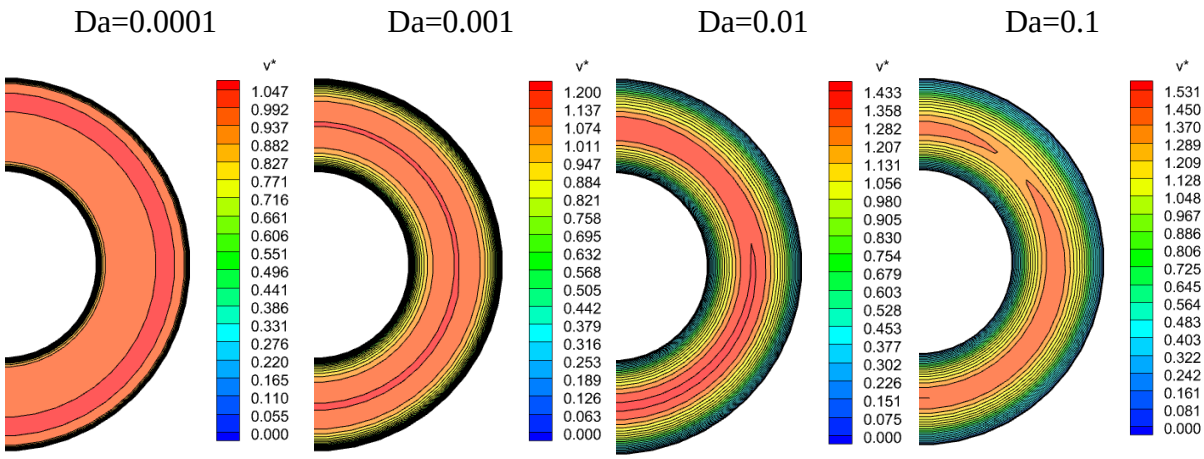

(a)TiO_2-CNT-Graphene/kerosene

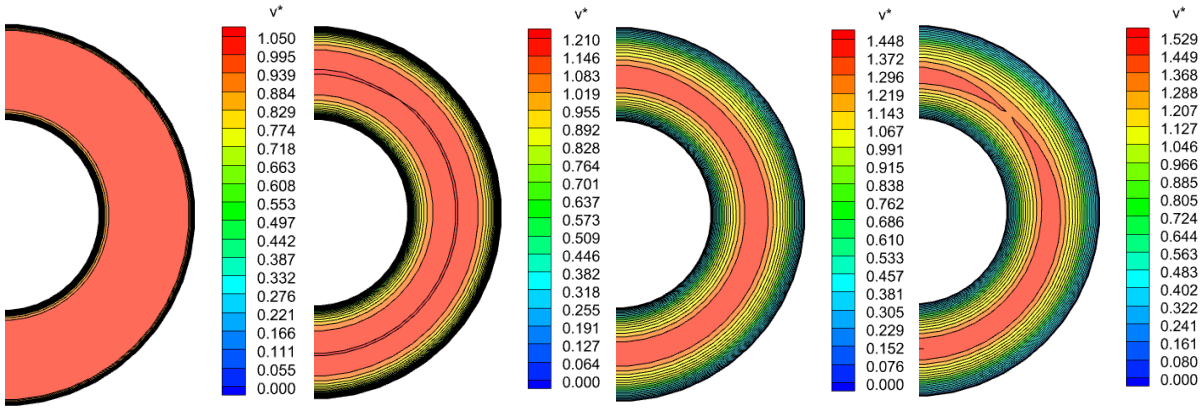

(b) TiO_2-CNT/kerosene

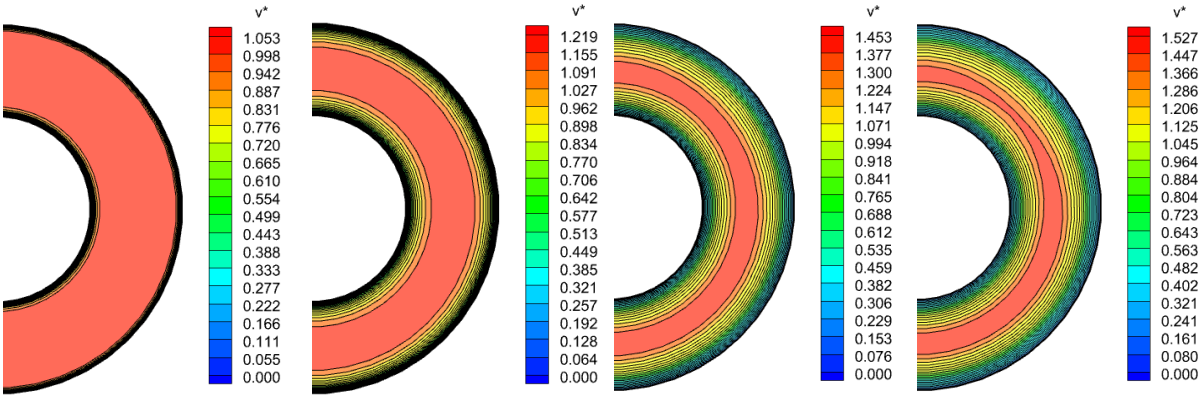

(c) TiO_2-Graphene/kerosene

Figure IV. 6. Non-dimensional axial velocity profiles at the duct's outlet across different Da number for: a (TiO_2,CNT,Graphene/kerosene), b (TiO_2,CNT/kerosene), and c (TiO_2,Graphene/kerosene).

Figures IV.7 and **IV.8** illustrate the non-dimensional axial velocity at the outlet of the duct with distincts Hartmann number and magnetic field orientations. **Figure IV.7** shows the effect of Hartmann number at ψ=0°. At Ha=10, the axial velocity of the (TiO_2-CNT-Graphene/ kerosene) ternary hybrid nanofluid and the (TiO_2-CNT/ kerosene) binary hybrid nanofluid takes the form of concentric circle cells, with the maximum velocity centered in the center of the duct. The (TiO_2-Graphene/kerosene) binary hybrid nanofluid has a cell with the highest velocity in the center and lower half of the duct. As the Hartmann number increases Ha=30 and Ha=50, the cells in the center of the duct with the highest velocity stretch to both its inner and outer walls, reducing the thickness of the boundary layer. Furthermore, utilizing the ternary hybrid nanofluid and the TiO_2-CNT/kerosene binary hybrid nanofluid resulted in lower axial velocity than using the TiO_2-Graphene/kerosene binary hybrid nanofluid. **Figure IV.8** shows that when the magnetic field is perpendicular to the flow (ψ=90°), the Hartmann number has no effect on axial velocity. As a result, it does not obstruct fluid flow.

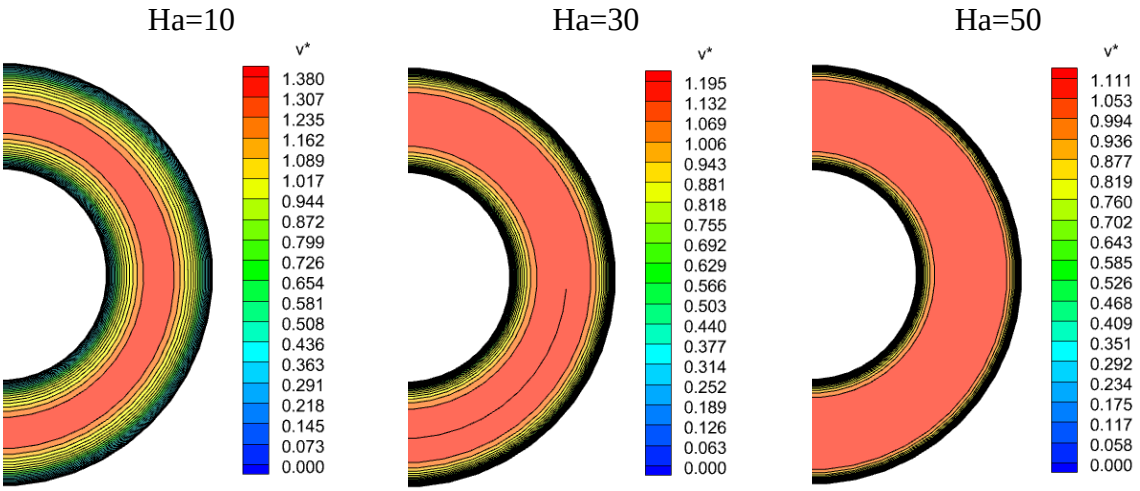

(a)TiO_2-CNT-Graphene/kerosene

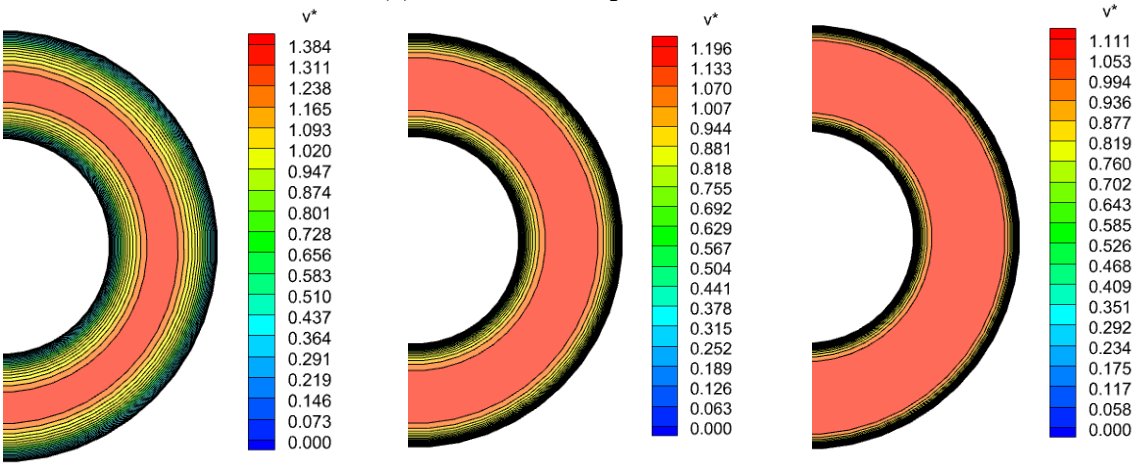

(b) TiO_2-CNT/kerosene

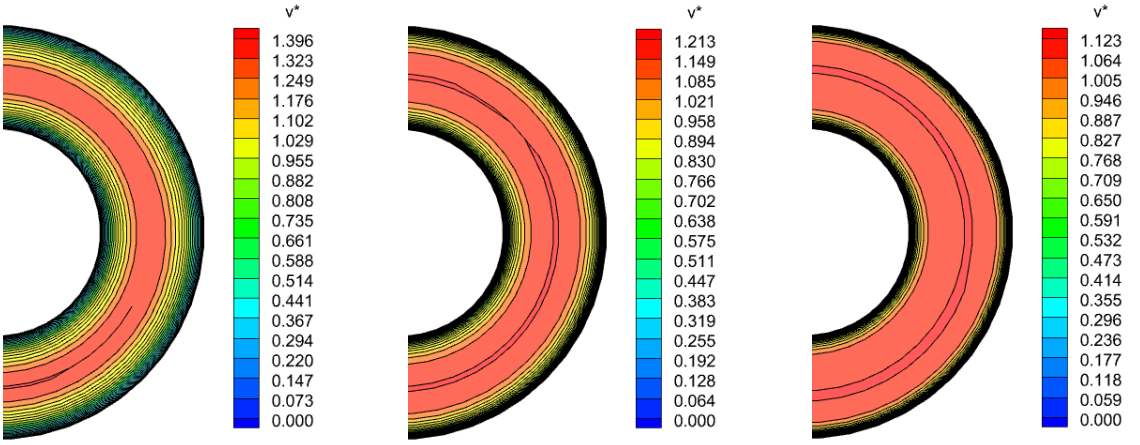

(c) TiO_2-Graphene/kerosene

Figure IV. 7. Influence of Hartmann number on non-dimensional axial velocity contours at the outlet for ψ=0°: a (TiO_2-CNT-Graphene/ kerosene), b (TiO_2-CNT/ kerosene), c (TiO_2-Graphene/ kerosene).

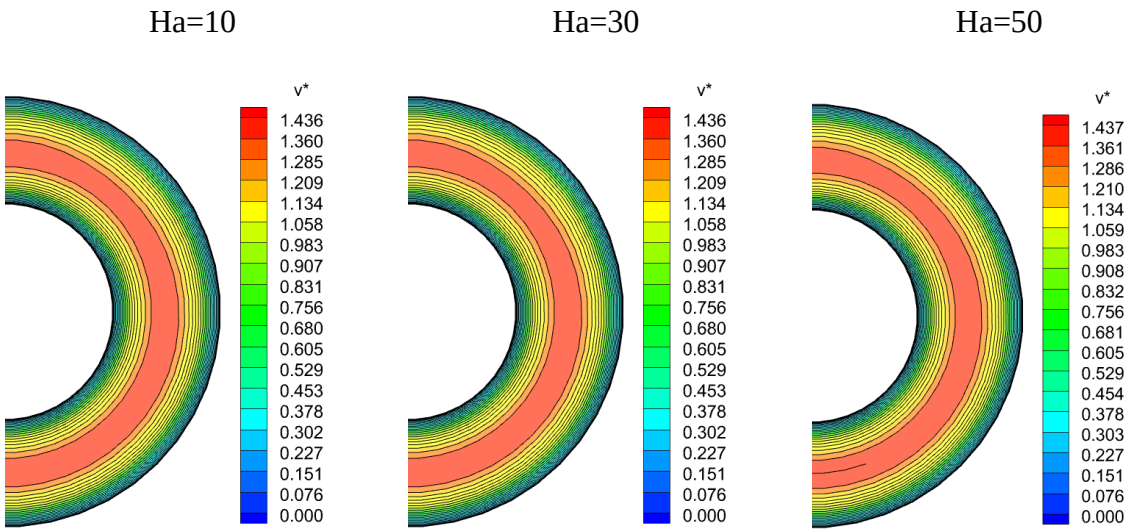

Figure IV. 8. Effect of Hartmann number on non-dimensional axial velocity contours at the outlet for ψ=90°, Gr=10^6, and ϕ= 5% using TiO_2-CNT-Graphene/ kerosene.

Figures IV.9 and **IV.10** illustrate the dimensionless axial velocity along the radial direction for distinct Darcy number, Hartmann number, and magnetic field orientation by utilizing TiO_2-CNT-Graphene/kerosene. It is clear form **Figure IV.9** that for low Darcy the highest velocity drops and flattens. Lowering the Darcy number reduces the permeability of porous medium. The velocity decreases due to the porous structure's resistance to flow. In conclusion, the drop in velocity is directly related to the permeability of the porous medium.

The impact of the Hartmann number and the magnetic field orientation is shown in **Figure IV.10 (a-b)**. **Figure IV.10a** illustrates the effect of Hartmann number at ψ=0°. With rising Hartmann number, the maximum velocity drops and flattens. Whereas the velocity gradient near the duct walls grows as Lorentz forces strengthen, slowing the hybrid nanofluid's motion.

In **Figure IV.10b**, for ψ=90°, the axial velocity profiles are similar regardless of Hartmann numbers, suggesting that Lorentz forces do not alter nanofluid movement. When the magnetic field occurs in the axial direction, Lorentz forces act as a resistive force, slowing down the nanofluid movement. Whereas, there is no influence when the magnetic field acting perpendicular to the fluid flow.

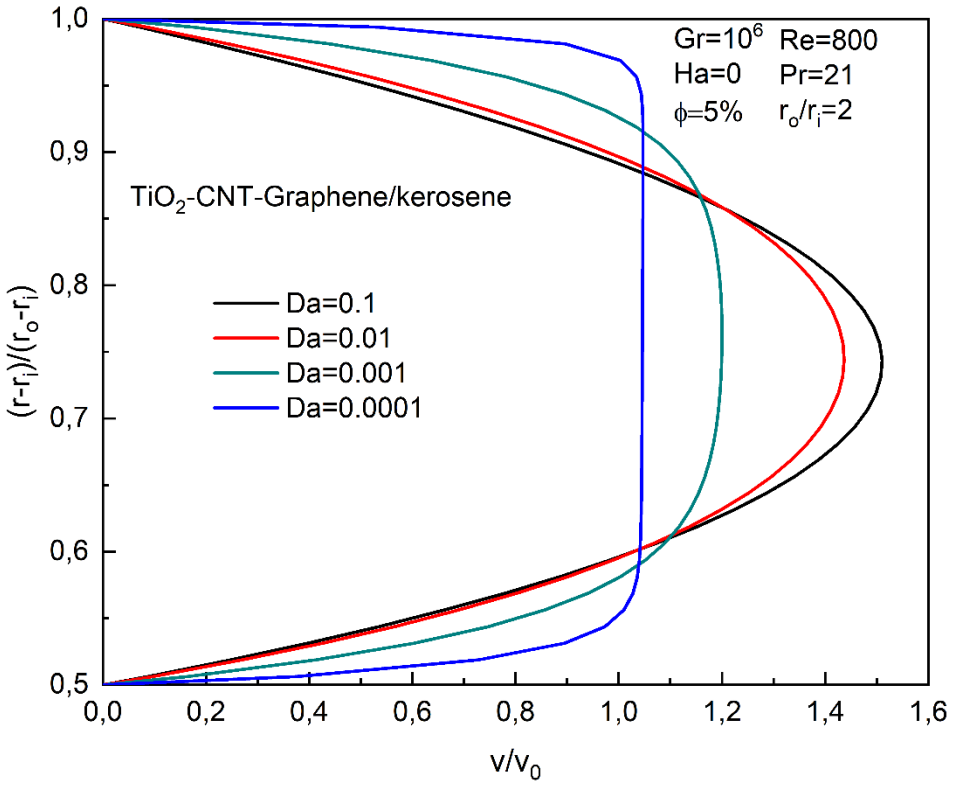

Figure IV. 9. Non dimensional axial velocity ratio along the radial direction for different Darcy numbers and Ha=0 by utilizing (TiO_2-CNT-Graphene/kerosene).

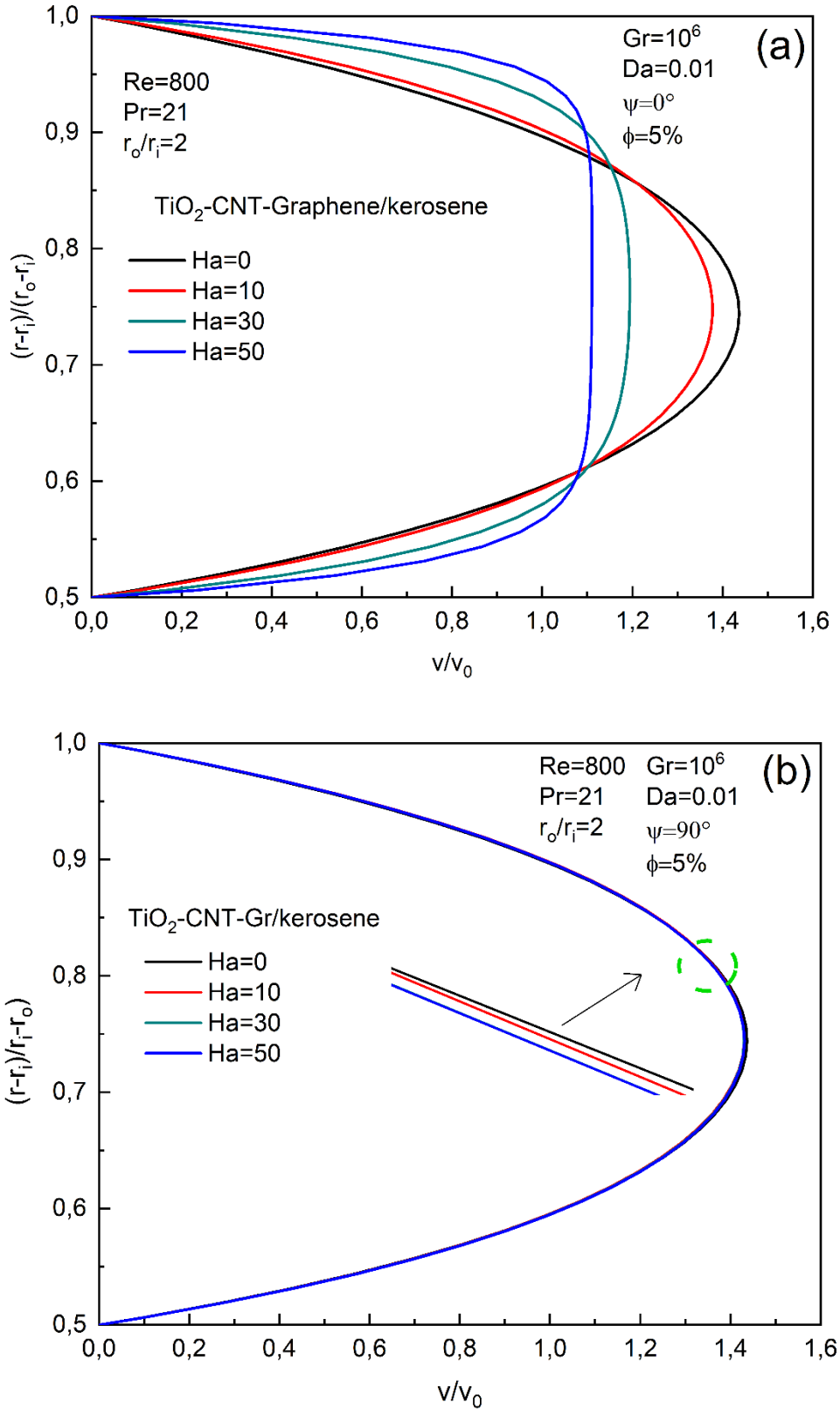

Figure IV. 10. Non-dimensional velocity ratio along the radial direction for different Hartmann numbers at Da=0.01 using (TiO_2-CNT/kerosene): a ψ=0°, b ψ=90°.

IV.2.2 Thermal field

Figures IV.11 and **IV.12** show 3D isotherm contours for various Hartmann and Darcy numbers using the three hybrid nanofluids examined. **Figure IV.11** depicts the influence of Darcy number at the absence of the magnetic field. At lower Darcy numbers, temperature contours form concentric rings with radial and axial stratification. This phenomenon is caused by restricted permeability, which causes temperature to decrease from the heated outer cylinder to the adiabatic inner cylinder while increasing from the inlet to the duct exit. As the Darcy number increases, the temperature contours become increasingly distorted, indicating the effect of buoyancy force. The porous media becomes more permeable, allowing the hot hybrid nanofluid in proximity to the heated wall to rise up. Furthermore, the TiO_2,Graphene/kerosene binary hybrid nanofluid has more distorted temperature contours than the other hybrid nanofluids. This discrepancy is related to the thermal conductivity of platelet-shaped graphene nanoparticles versus cylindrical CNT nanoparticles.

Figure IV.12 shows the effect of Hartmann number at Da=0.01 and $\psi=0°$. As Hartmann number increases, the highest temperature decreases regardless the hybrid nanofluids examined, showing that the magnetic field controls and suppresses the buoyancy-driven flow that causes natural convection. The binary hybrid nanofluid TiO_2,CNT/kerosene, with its elongated cylindrical nanoparticle, had lower natural convection. Regardless of the Darcy and Hartmann numbers, the highest temperature was at the outlet near the outer wall: ($z^*=98.33$, $\theta=0$, and $r^*=0.99$).

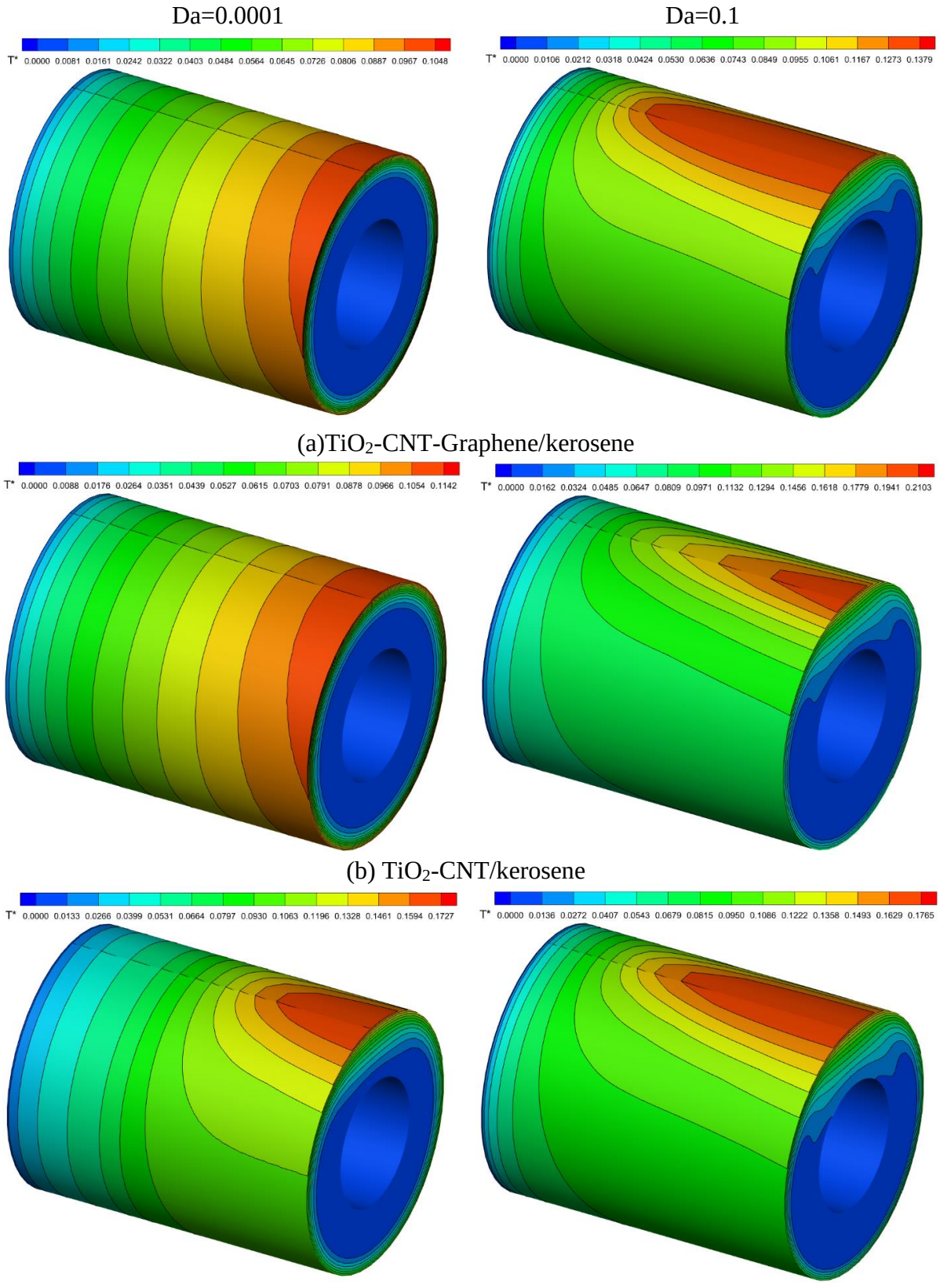

Figure IV. 11. 3D temperature contours for various Da numbers at Ha=0: (a) TiO_2,CNT,Graphene/kerosene, (b) TiO_2,CNT/kerosene, (c) TiO_2,Graphene/kerosene.

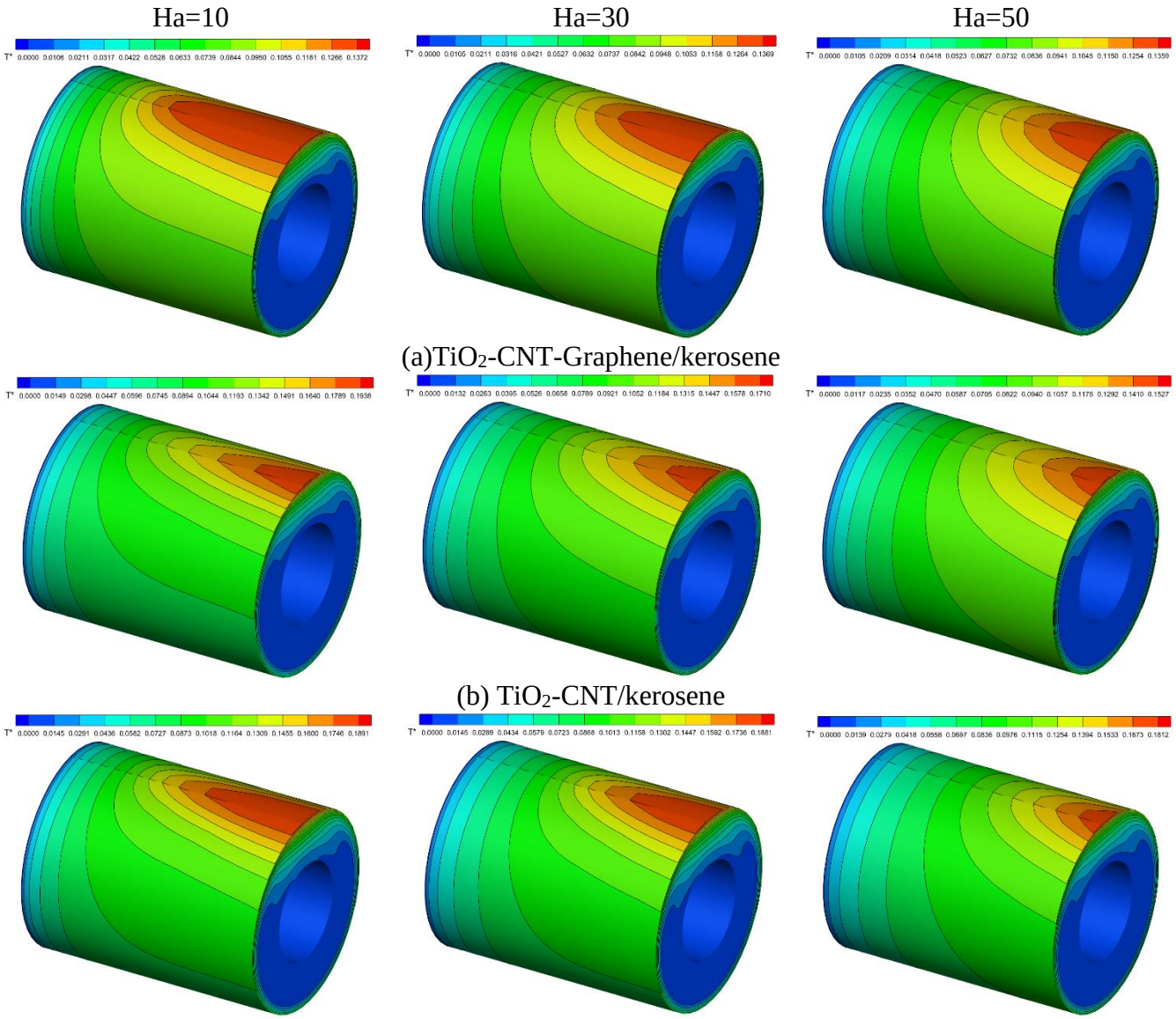

Figure IV. 12. 3D isotherm contours versus Ha numbers at Da=0.01, and ψ=0°: (a) TiO_2,CNT,Graphene/kerosene, (b) TiO_2,CNT/kerosene, and (c) TiO_2, Graphene/kerosene.

Figure IV.13 presents the 3D isotherm contours for different Hartmann numbers at ψ =90° with (TiO_2,CNT,Graphene/ kerosene) ternary hybrid nanofluid. The graph shows that if the magnetic field is perpendicular to the fluid motion, the temperature contours remain essentially consistent, with no notable variations as the Hartmann number increases. In this scenario, we can conclude that the magnetic field has no significant impact on the buoyancy force.

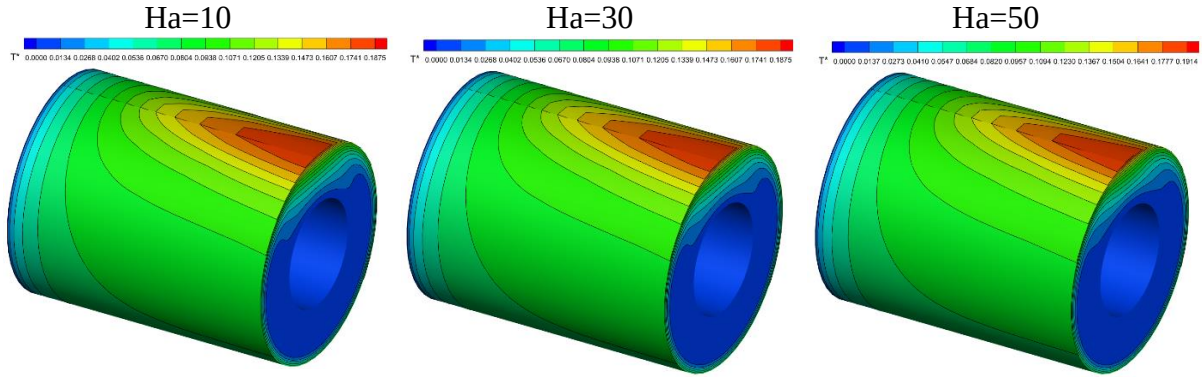

Figure IV. 13. 3D isotherm contours for various Ha numbers at ψ=90°, and Da=0.01, using (TiO_2-CNT-Graphene/kerosene).

IV.2.3 Secondary flow

Secondary flow is a phenomenon that generates fluid motion perpendicular to the main flow direction. **Figure IV.14** shows the development of the secondary flow along the annular duct in three different positions using (TiO_2-CNT/water) binary hybrid nanofluid with Ha=0, Da=0, and ϕ=5%. The secondary flow is in the form of two counter-rotating cells. The cells near the outer wall move upwards while the cells near the inner wall move downwards. As shown in **Figure IV.14**, at a position very close to the inlet z^*=7 the secondary flow is very weak because the hybrid nanofluid enter at a constant temperature, following this zone the secondary flow intensifies until z^*= 33 where the buoyancy forces start to affect the flow. After this zone the strength of the secondary flow decreases until the outlet of the duct because of the temperature stratification. The secondary flow is induced by the buoyancy force, which arises from a temperature difference between the hybrid nanofluid and the pipe walls. This difference of temperature create a density gradient that cause the flow motion. The strength of the buoyancy force can greatly impact the intensity and pattern of the secondary flow, in order to quantify its influences, **Figure IV.15** shows the effect of Grashof number on the secondary flow for 5% volume concentration at the duct's outlet. Grashof number is defined as the ratio of buoyancy force to viscous force. As shown in this Figure, with increasing Grashof number the secondary flow intensifies and become stronger.

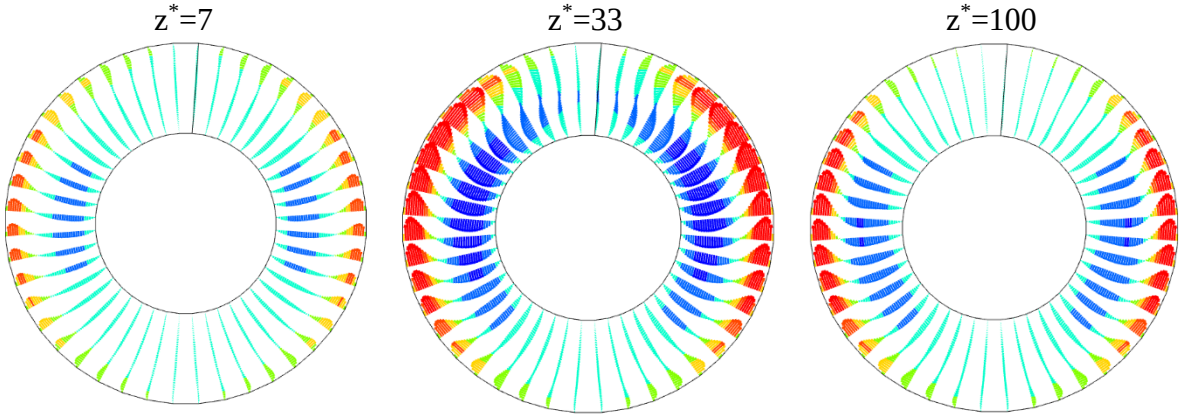

Figure IV. 14. Development of secondary flow along the annulus duct for Gr=2.5 x 10^6, Ha=0, Da=0, and ϕ=5%.

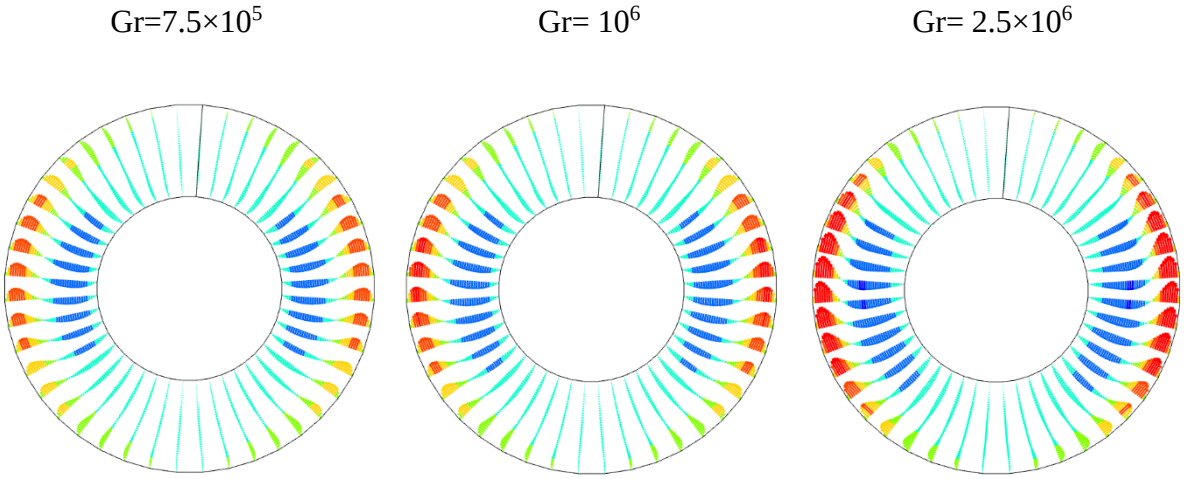

Figure IV. 15. Secondary flow at the outlet of the annular duct for different Gr numbers at Da=0.01, Ha=0, and ϕ=5%.

The secondary flow may be influenced by different parameter such as Darcy number, Hartmann number, and magnetic field orientation. **Figure IV.16** show the effect of Darcy number on the secondary flow at the outlet of the duct. The secondary flow is very weak for low Darcy number because viscous force are dominant which interrupt their motion, while with increasing Darcy number the secondary flow become strong. **Figure IV.17 (a-b)** present the impact of Hartmann number and the magnetic field orientation. As shown in this Figure, there was no significant impact of Hartmann number on the secondary flow for both magnetic field orientations (ψ=0° and ψ=90°).

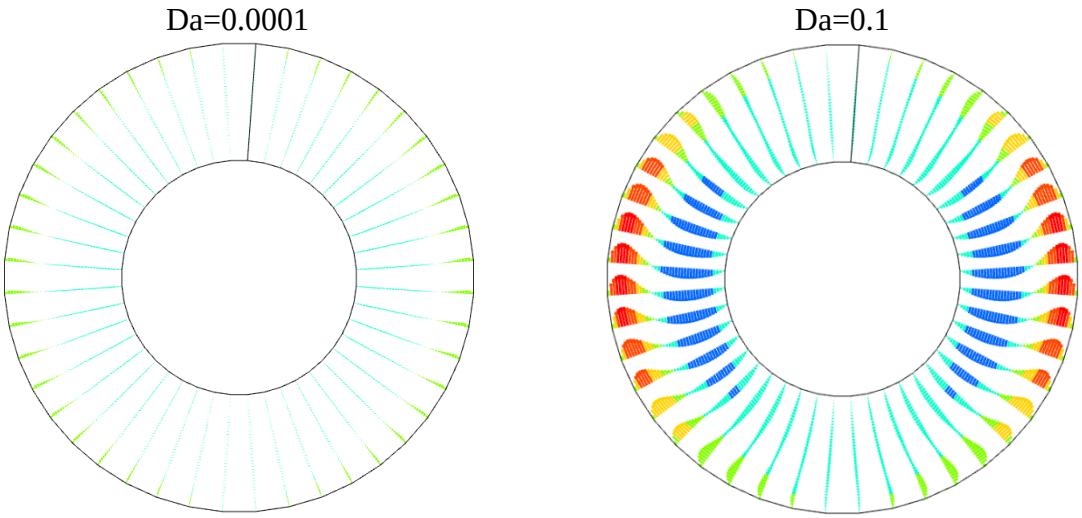

Figure IV. 16. Secondary flow at the outlet of the annular duct for different Darcy numbers at $Gr=10^6$, Ha=0, and ϕ=5%.

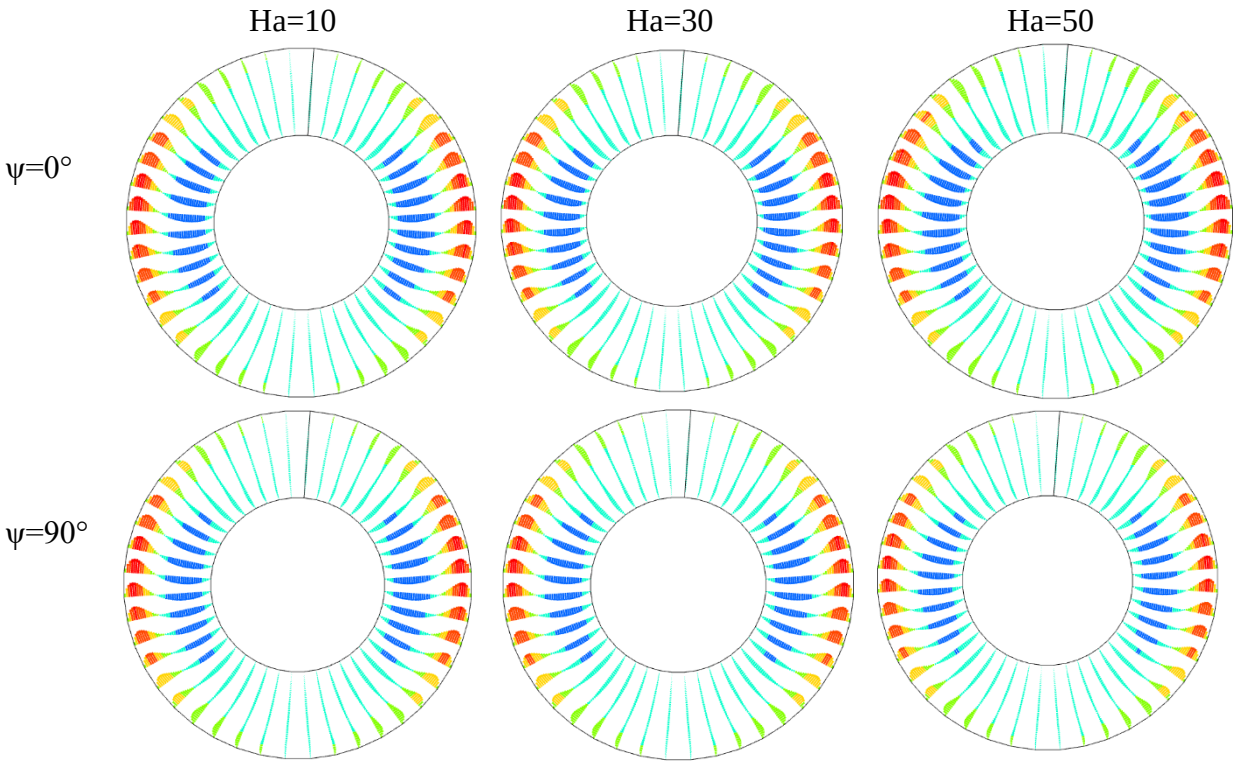

Figure IV. 17. Secondary flow at the outlet of the annular duct for different Ha number and magnetic field inclination at Gr=106, Da=0.01, and ϕ=5%.

IV.2.4 Nusselt number

Figure IV.18 (a, b, and c) display the average Nusselt number versus Darcy and Hartmann numbers. In **Figure IV.18a**, the average Nusselt number is plotted against Darcy number at the absence of the magnetic field by utilizing the three hybrid nanofluids examined. Raising Darcy number from 10^{-4} to 10^{-1} reduces the average Nusselt number by 24%, 23%, and 21% using using TiO_2,CNT,Graphene/kerosene, TiO_2,CNT/kerosene, and TiO_2,Graphene/kerosene respectively. In **Figure IV.18b** the Nusselt number is plotted against Hartmann number at Da=0.01 and ψ=0°, it is clearly shown that increasing Hartmann number boosts the average Nusselt number by 15%, 16.5%, and 15.2% using TiO_2,CNT,Graphene/kerosene, TiO_2,CNT/kerosene, and TiO_2,Graphene/kerosene, respectively. For low Darcy number or high Hartmann number, the velocity decreases in the center of the annulus pipe. Consequently, due to continuity, the velocity boosts in proximity to the outer heated wall, as shown in **Figures IV.9** and **IV.10**. This rise in velocity near the wall boosts convective heat transfer across the fluid and the heated pipe.

Figure IV.18c displays the impact of Hartmann number at ψ=90°. As displayed, there is no remarkable change in Nusselt number while changing the Hartmann number. Moreover, independent of Hartmann or Darcy number changes, the (TiO_2,CNT,Graphene/kerosene) ternary hybrid nanofluid surpasses the binary hybrid nanofluids because it has the maximum thermal conductivity, which improves heat transfer.

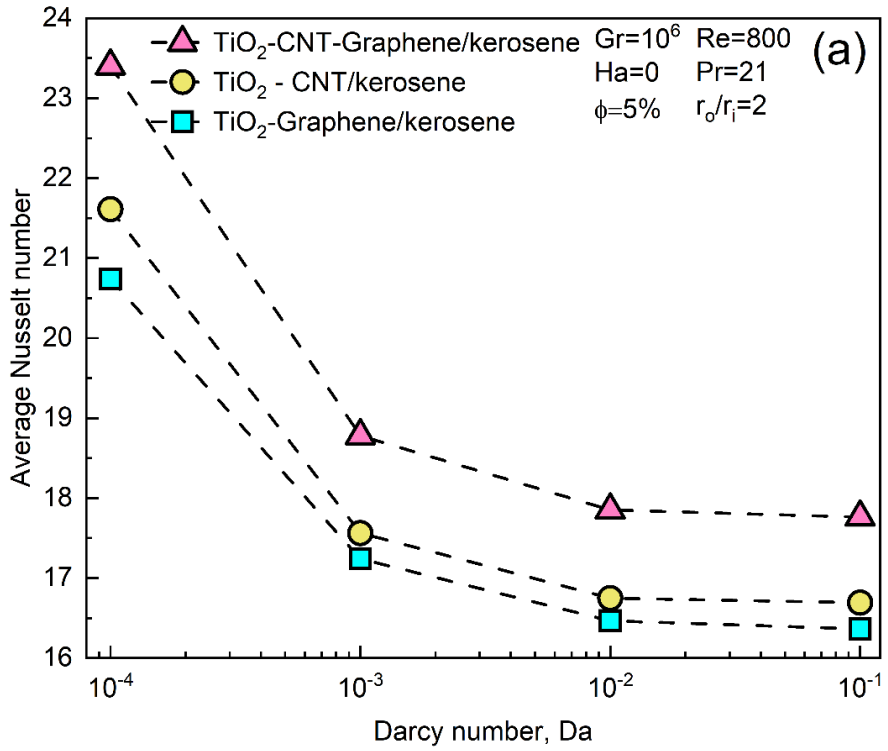
TiO2-CNT-Graphene/kerosene
TiO2 - CNT/kerosene
TiO2-Graphene/kerosene
Gr=10^6 Re=800
Ha=0 Pr=21
ϕ=5% ro/ri=2
(a)
Average Nusselt number
Darcy number, Da

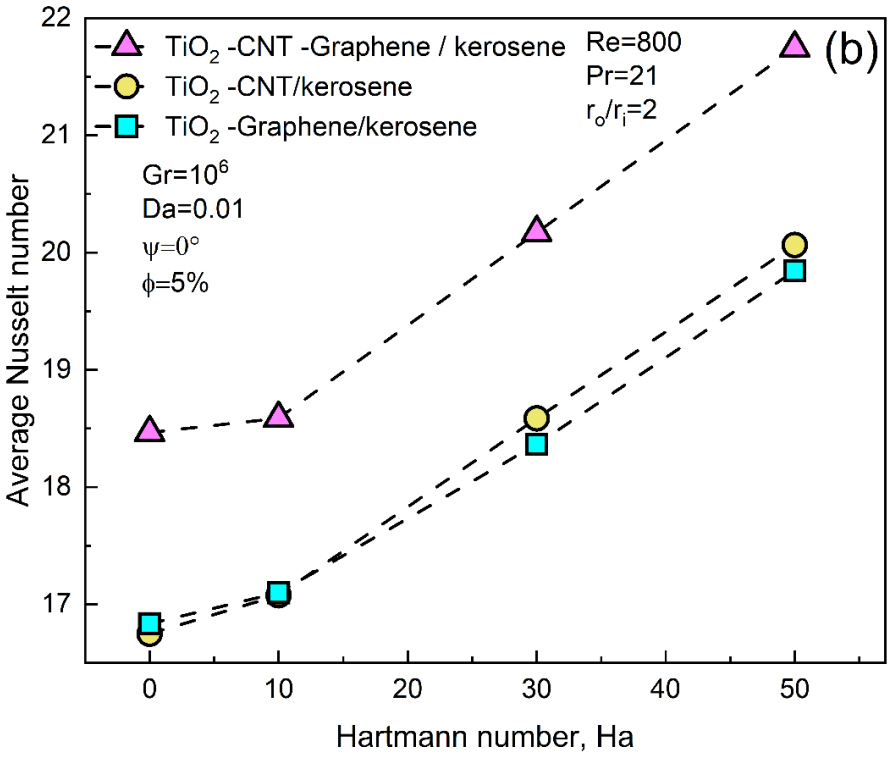
TiO2 -CNT -Graphene / kerosene
TiO2 -CNT/kerosene
TiO2 -Graphene/kerosene
Re=800
Pr=21
ro/ri=2
Gr=10^6
Da=0.01
ψ=0°
ϕ=5%
(b)
Average Nusselt number
Hartmann number, Ha

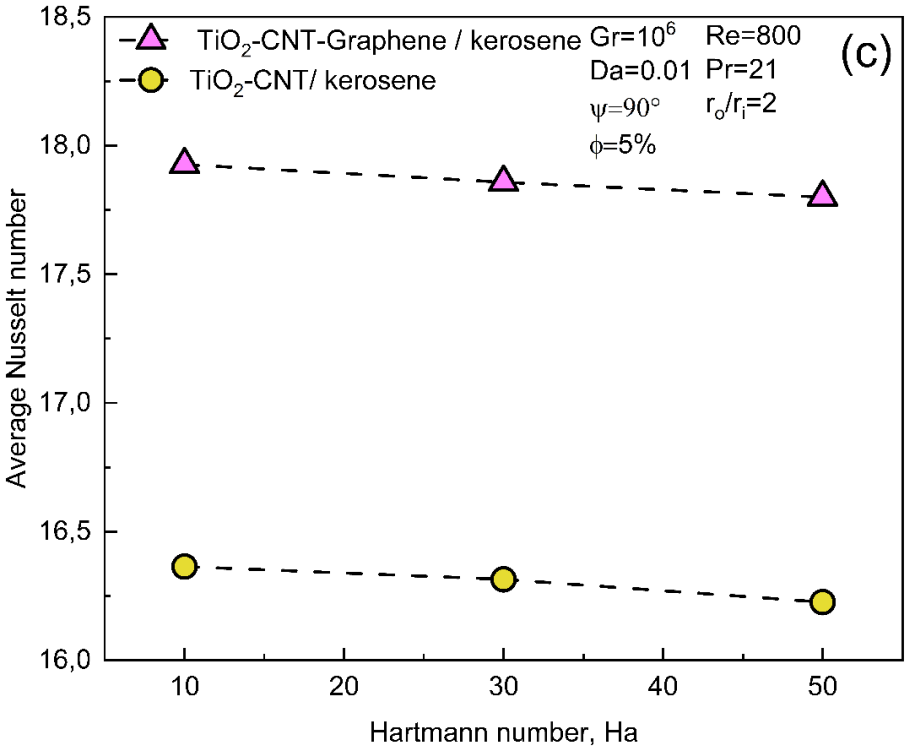

Figure IV. 18. Average Nusselt number for different: (a) Da number, (b) Ha number at ψ=0°, (c) Ha number at ψ=90°.

IV.2.5 Skin friction coefficient

The average skin friction coefficient is a dimensionless measure that varies with flow conditions. It is directly proportional to the fluid's viscosity and shear stress and inversely proportional to the fluid's velocity and density. **Figures IV.19a** and **IV.19b** show the average skin friction coefficient along the outer wall for different Darcy and Hartmann numbers.

Figure IV.19a indicates that the average skin friction is higher at a low Darcy number for all tested hybrid nanofluids. This means that when the flow is obstructed by obstacles or porous materials, the friction between the fluid and the surface increases. Conversely, the average skin friction coefficient decreases as the Darcy number rises, indicating less friction in less obstructed flows.

From **Figure IV.19b**, the average skin friction coefficient increases with a higher Hartmann number regardless the hybrid nanofluids examined. This increase is due to an enhanced velocity gradient near the outer wall, which raises shear stress. Comparing the examined hybrid nanofluids in **Figures IV.19a** and **IV.19b**, the skin friction coefficients for TiO_2-CNT-Graphene/kerosene ternary hybrid nanofluid and TiO_2-Graphene/kerosene binary hybrid

nanofluid are approximately the same regardless of the Darcy and Hartmann numbers. In contrast, the skin friction coefficient of TiO_2-CNT/kerosene binary hybrid nanofluid is significantly higher at a low Darcy number ($Da=10^{-4}$) compared to the other hybrid nanofluids. This is due to the elongated shape of CNT nanoparticles, which leads to a pronounced increase in the skin friction coefficient in more restricted flows. However, as the Darcy number increases, indicating less obstructed flow, the influence of CNT nanoparticles on viscosity becomes less significant.

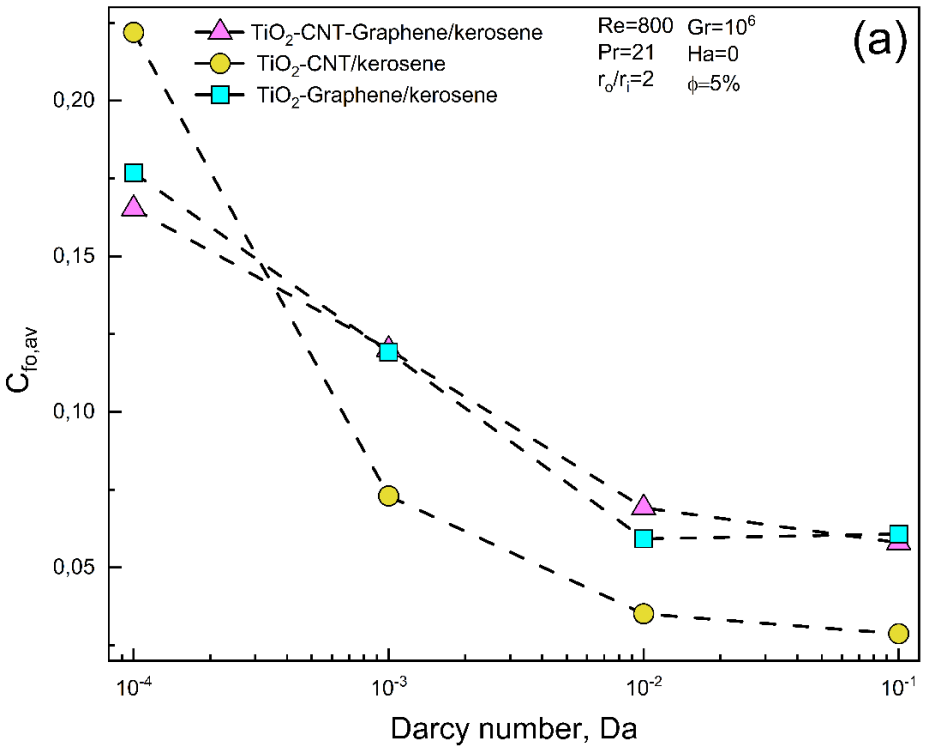

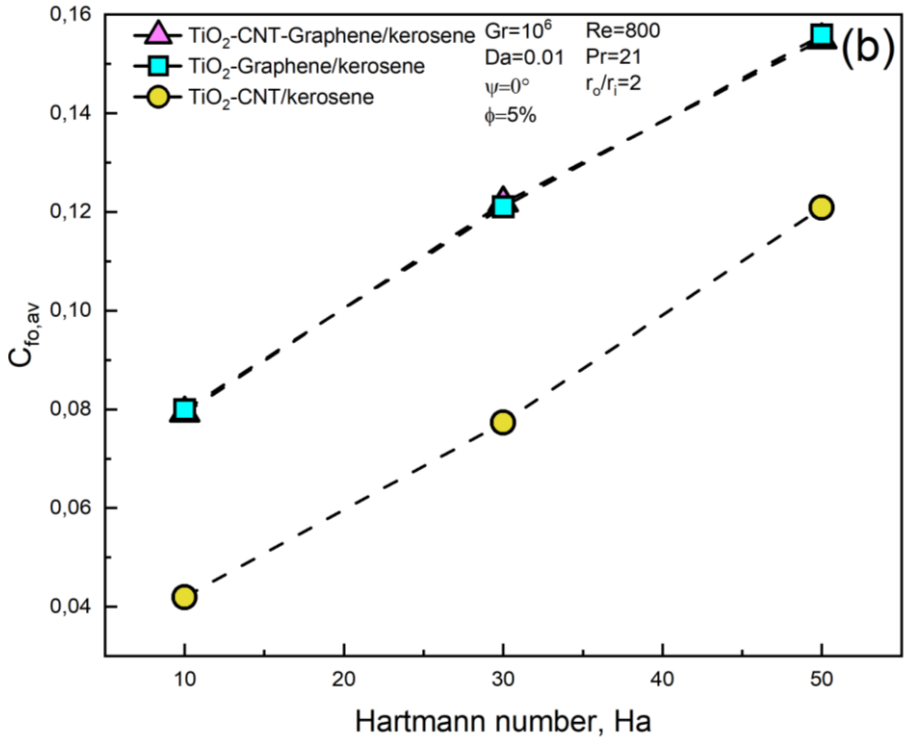

Figure IV. 19. Average skin friction coefficient for various: (a) Da number at Ha=0, (b) Ha number at Da=0.01, and ψ=0°.

IV.2.6. Pressure drop

Understanding the relationship between pressure drop and both Hartmann and Darcy numbers is a crucial step in maximizing fluid system efficiency.

Figures IV.20 (a-b) give the pressure drop versus Darcy and Hartmann numbers at ψ=0° for the three hybrid nanofluids examined. From **Figure IV.20a**, the pressure drop declines by 98.99% for all the hybrid nanofluids as the Darcy number increases, due to reduced flow resistance at higher Darcy numbers. Additionally, there is no significant difference in pressure drop regardless the hybrid nanofluids types.

Conversely, **Figure IV.20b** demonstrates that increasing the Hartmann number raises the pressure drop regardless all the hybrid nanofluids, attributed to the Lorentz force, which slows down fluid motion, thereby increasing resistance and resulting in a higher pressure drop. The highest pressure drop was observed with the TiO_2-CNT/kerosene binary hybrid nanofluid at Ha=50, due to the form of CNT nanoparticles significantly affecting the nanofluid's viscosity. Elongated nanoparticles, such as cylindrical ones, create higher viscosity compared to other shapes, leading to increased resistance to fluid flow. Consequently, the TiO_2-CNT binary hybrid

nanofluid exhibits a 1.12 times higher pressure drop than the TiO_2-Graphene binary hybrid nanofluid.

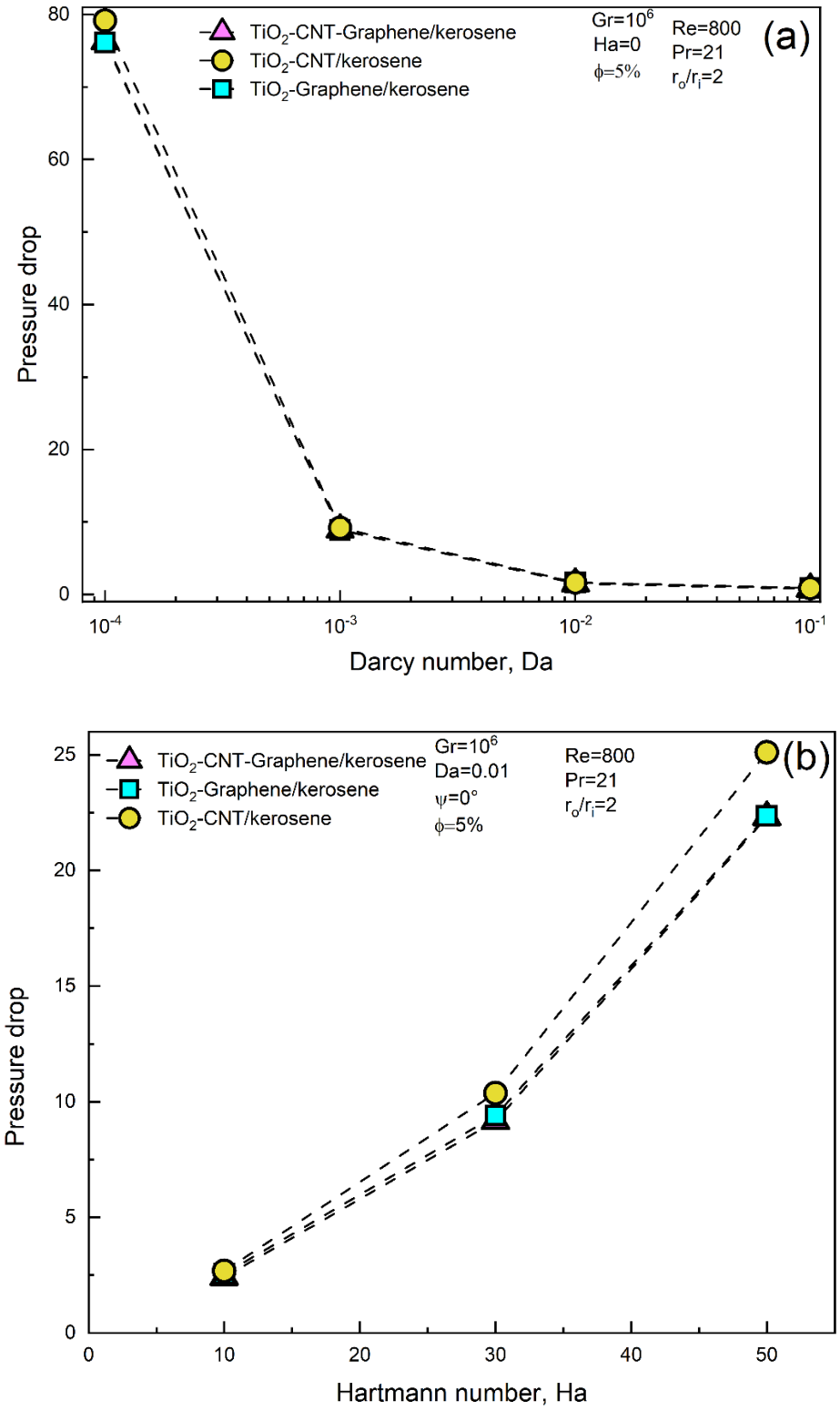

Figure IV. 20. Pressure drop for various: (a) Dar number at Ha=0, (b) Ha number at Da=0.01, and ψ=0°.

IV.2.7. Entropy generation

Entropy generation is an important concept in engineering since it reveals inefficiencies and irreversibilities within diverse systems. **Figures IV.21-IV.22** depict the entropy generation and the Bejan number as a function of Darcy and Hartmann numbers for distinct hybrid nanofluids. **Figure IV.21a** shows that thermal entropy generation increases with Da number by 26%, 13.7%, and 30% using TiO_2-CNT-Graphene/kerosene, TiO_2-Graphene/kerosene, and TiO_2-CNT/kerosene, respectively. Higher Darcy numbers enhance the medium's ability to conduct heat, leading to more significant thermal gradients and higher thermal entropy generation. Among the hybrid nanofluids examined, the TiO_2-Graphene/kerosene exhibits the highest thermal entropy generation, followed by TiO_2-CNT/kerosene and TiO_2-CNT-Graphene/kerosene, respectively. Graphene's exceptional thermal conductivity significantly enhances the heat transfer capabilities of the base fluid (kerosene). The two-dimensional structure of Graphene provides a large surface area for heat transfer, leading to more efficient thermal energy distribution and higher thermal entropy production.

Conversely, **Figure IV.21b** indicates that frictional entropy decreases with Darcy number regardless all the examined hybrid nanofluids. The existence of porous media rises the energy dissipation; when the Darcy number is low, flow resistance rises, resulting in an increased in frictional entropy generation.

Figure IV.21c displays the Bejan number versus Da number. The Bejan number, which represents the ratio of thermal entropy generation to the total entropy generation, As the Darcy number increases, the Bejan number rises regardless all the hybrid nanofluids examined.

In contrast, the Hartmann number has an inverse influence on entropy generation. **Figures IV.22(a-c)** reveal that thermal entropy generation decreases with an increasing Hartmann number, while frictional and magnetic entropy increase regardless all the hybrid nanofluids examined. Thermal entropy reduce by 11.8%, 14.8%, and 13.18% using TiO_2,CNT Graphene/kerosene, TiO_2, CNT/kerosene, and TiO_2, Graphene/kerosene, respectively. Similarly, the frictional entropy increases by 28.7%, 28.5%, and 25.8% using (TiO_2, CNT, Graphene/kerosene), (TiO_2, CNT/kerosene), and (TiO_2, Graphene/kerosene), respectively. The increase in magnetic entropy is approximately 94% among all examined hybrid nanofluids. As the Hartmann number rises, the thermal gradient declines, and flow resistance increases. Additionally, the ternary hybrid nanofluid shows the lowest thermal entropy compared to the

binary hybrid nanofluids, while there is no significant difference in frictional and magnetic entropy between the ternary and binary hybrid nanofluids. **Figure IV.22d** illustrates that with an increasing Hartmann number, the Bejan number decreases.

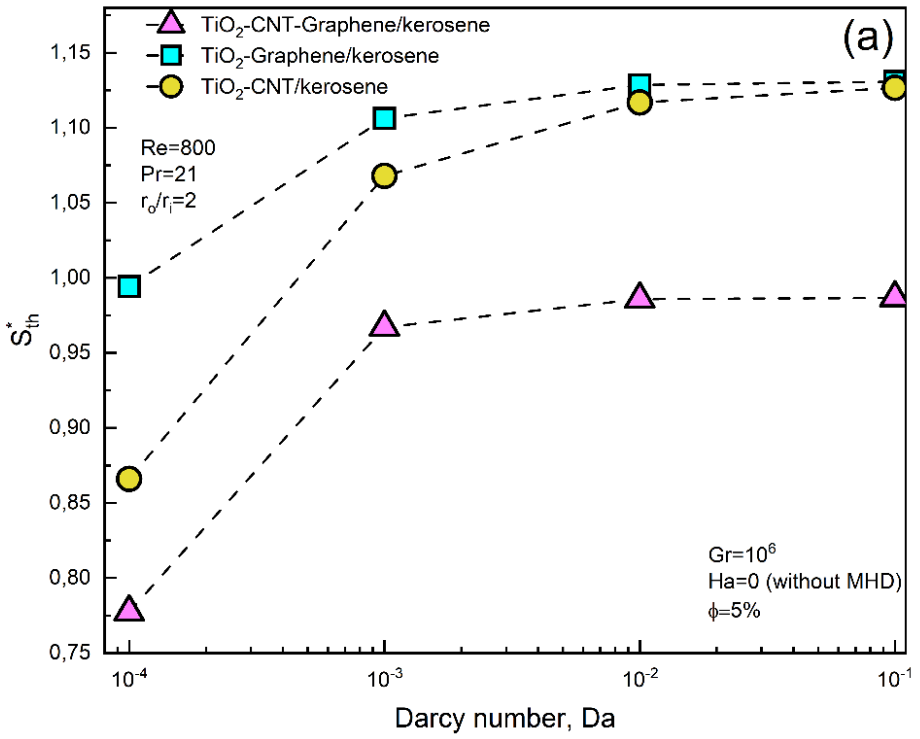

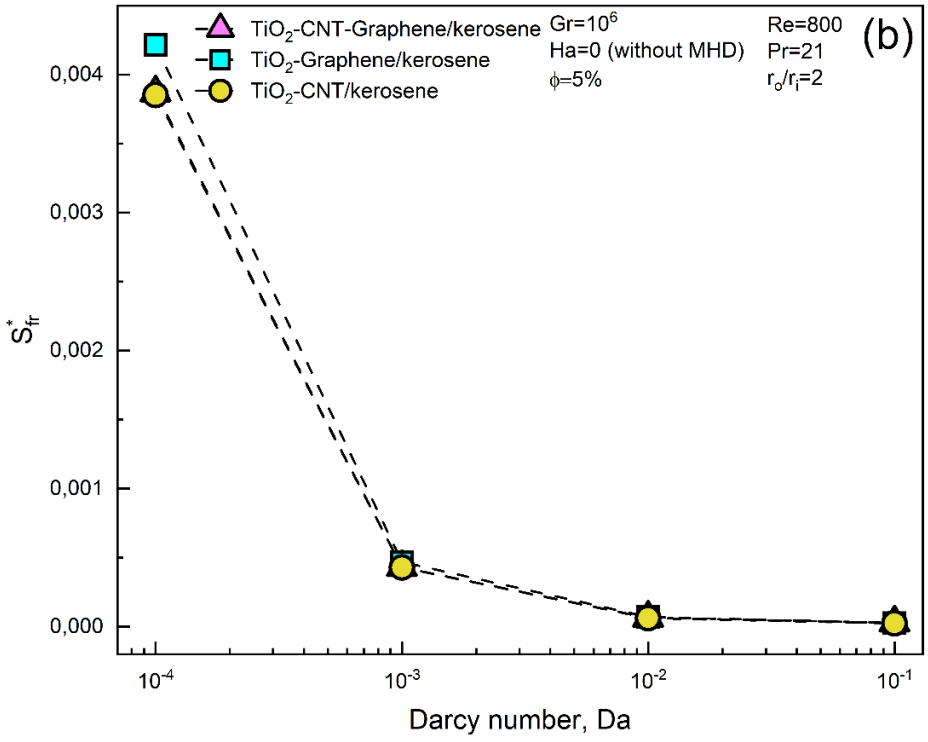

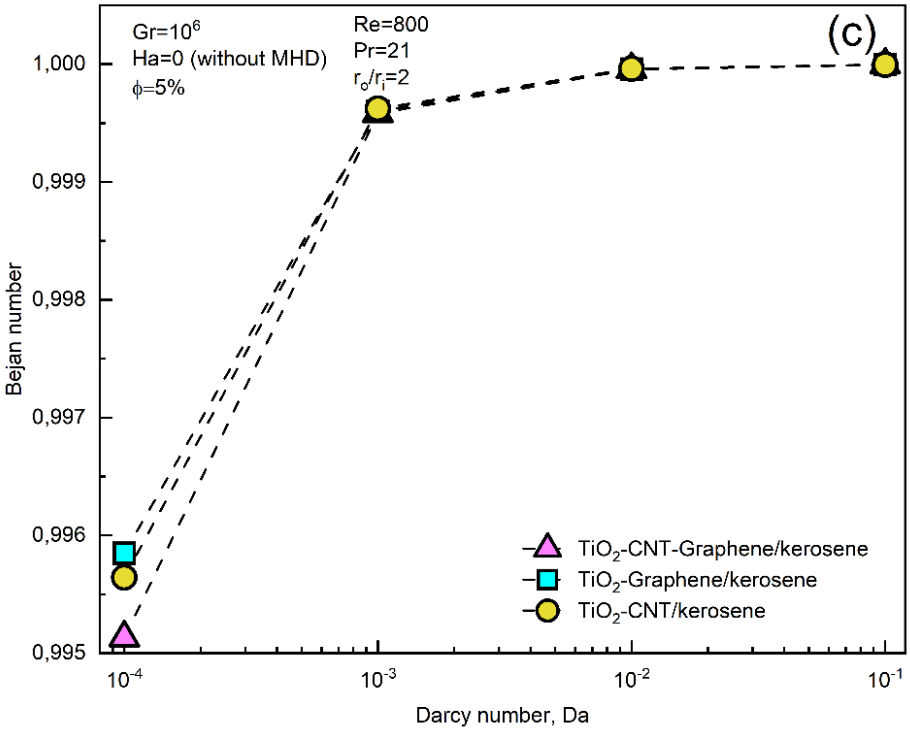

Figure IV. 21. Entropy generation for various Darcy number at Ha=0: (a) thermal entropy, (b) frictional entropy, (c) Bejan number.

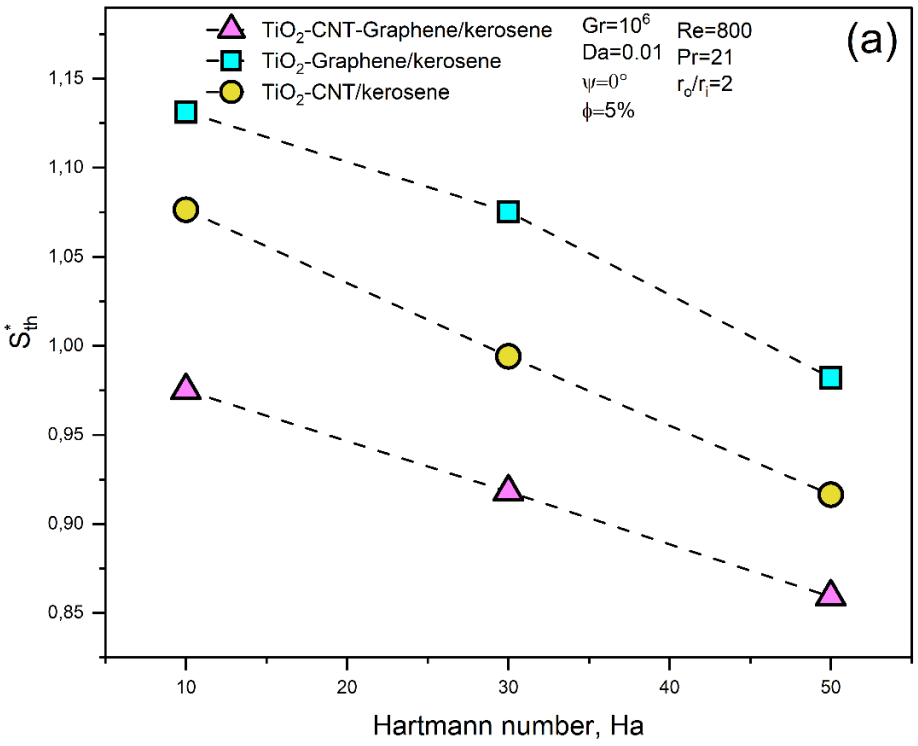
TiO2-CNT-Graphene/kerosene
TiO2-Graphene/kerosene
TiO2-CNT/kerosene
Gr=10^6
Da=0.01
ψ=0°
ϕ=5%
Re=800
Pr=21
ro/ri=2
(a)
S*th
1,15
1,10
1,05
1,00
0,95
0,90
0,85
10
20
30
40
50
Hartmann number, Ha

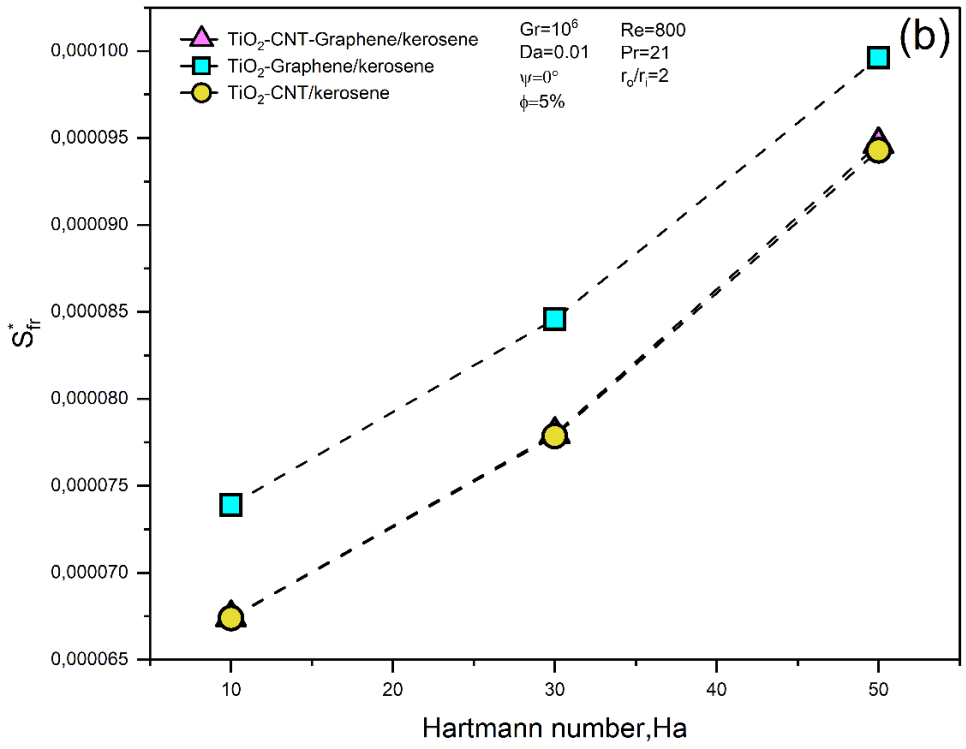
TiO2-CNT-Graphene/kerosene
TiO2-Graphene/kerosene
TiO2-CNT/kerosene
Gr=10^6
Da=0.01
ψ=0°
ϕ=5%
Re=800
Pr=21
ro/ri=2
(b)
S*fr
0,000100
0,000095
0,000090
0,000085
0,000080
0,000075
0,000070
0,000065
10
20
30
40
50
Hartmann number,Ha

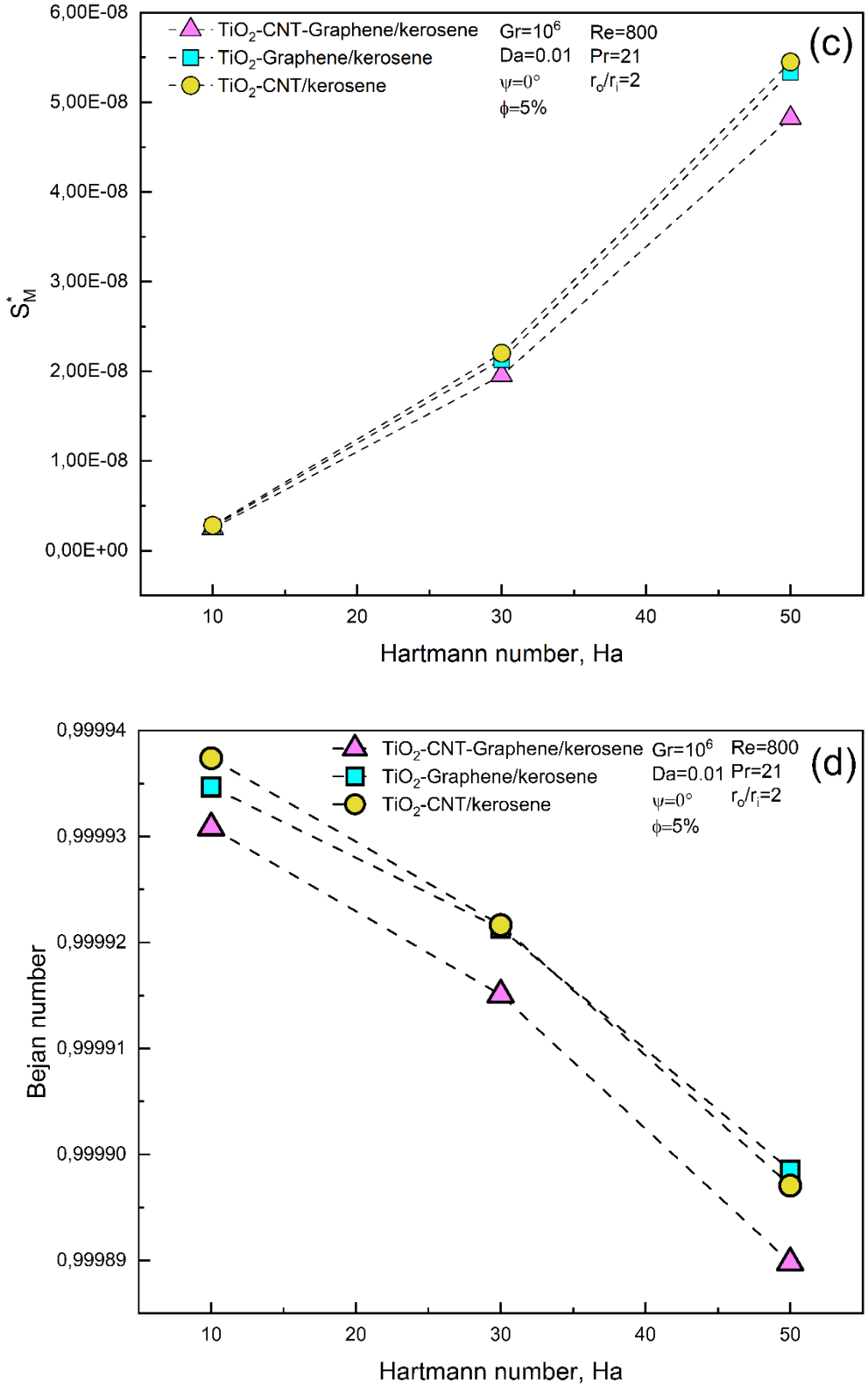

Figure IV. 22. Entropy generation for various Hartmann number at Da=0.01 and ψ =0°: (a) Thermal entropy, (b) Frictional entropy, (c) Magnetic entropy, (d) Bejan number.

IV.3 Second application

In this investigation, forced convection and entropy generation of two different binary hybrid nanofluids and a ternary hybrid nanofluid through a porous wavy annulus duct are explored, considering the impact of the non-uniform magnetic field imposed at the outer wall for different cases of position and joule heating. The binary hybrid nanofluids based on titanium contain various nanoparticle shapes dispersed in conventional water fluid. The first binary hybrid nanofluid contains nanoparticles of TiO_2 and CNT with spherical and cylindrical shapes, respectively. The second binary hybrid nanofluid contains TiO_2 and Graphene with spherical and platelet shapes, respectively. Both binary hybrid nanofluids are 75% TiO_2 nanoparticles and 25% for each CNT and Graphene. Ternary hybrid nanofluid includes TiO_2, CNT, and Graphene nanoparticles in a ratio of 50% TiO_2 and 25% for each CNT and Graphene. The analysis was conducted for distinct wave's amplitude A (0.1, 0.2, 0.3), wavelengths L (1.256, 2.452, 5.026), and Hartmann numbers ($0 \leq Ha \leq 50$) at a fixed volume concentration ϕ=5%, Darcy number Da=0.01 and Reynolds number Re=800. The present section examines the effect of these parameters on the magneto-hydrothermal field. In addition, the average Nusselt number, pressure drop, average skin friction coefficient, and entropy generation are explored.

IV.3.1 Hydrodynamic field

The dimensionless axial velocity contours for two distinct wavy annulus channel configurations have been tested for control parameters using ternary hybrid nanofluids case (TiO_2-CNT-Graphene/water): Reynolds number, Re=800, Darcy number, Da=0.01, without Hartmann number, Ha=0, dimensionless wavelength, L=2.452, dimensionless amplitude, A=0.2 and volume fraction ϕ=5%. **Figure IV.23** shows the dimensionless axial velocity distribution in a cross-section located at the exit of the annulus channel. The dimensionless axial velocity contours are concentric circles with the maximum dimensionless velocity observed in the middle between the inner and outer cylinder for both cases. This result is confirmed by Benkhedda et al. [57] for the case of forced convection laminar flow through the cylindrical annulus space. Moreover, the results show that the maximum axial velocity of a wavy annulus duct ($v^*_{max} = 1.491$) is higher than that of a straight annulus channel ($v^*_{max} = 1.383$). This suggests that the wavy configuration improves the fluid flow characteristics, as seen by the increase in axial velocity through the annulus channel.

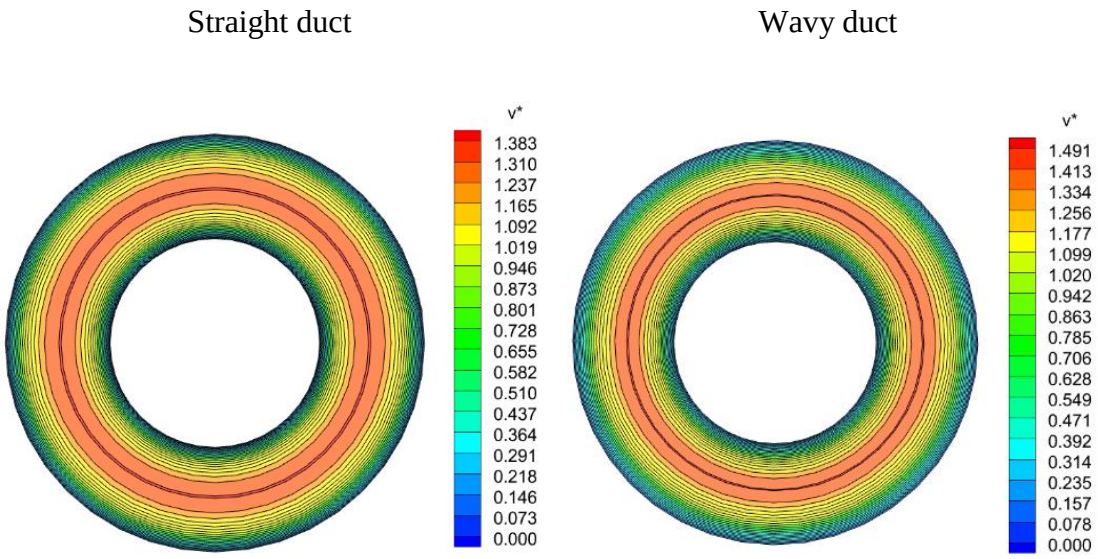

Figure IV. 23. Axial velocity contours using (TiO_2-CNT-Graphene/water) at Re=800, Da=0.01, and ϕ=5 for (a) straight duct, and (b) wavy duct.

Figure IV.24 presents the axial velocity contours in a cross-section (r, θ) for two binary hybrid nanofluids (TiO_2-CNT/water), (TiO_2-Graphene/water) and ternary hybrid nanofluid (TiO_2-CNT-Graphene/water) at the outlet of the annulus for different dimensionless amplitude wave A (0.1, 0.2 and 0.3) using control parameters such as dimensionless wavelength, L=2.452, Re=800, Da=0.01, without magnetic field (Ha=0), and at ϕ=5%. The first observation for all hybrid nanofluids is that the dimensionless axial velocity contours are concentric circles, with the maximum velocity in the middle between the inner and outer cylinders. Moreover, the dimensionless axial velocity increases with increasing dimensionless amplitude, for example, in the case of the binary hybrid nanofluid TiO_2-CNT /water, $v^*_{max} = (1.445\ , 1.508 \text{ and } 1.578)$ for dimensionless amplitude A=0.1, 0.2 and 0.3, respectively. On the other hand, for the same dimensionless amplitude A=0.3, a comparison of the axial velocity shows that the higher value of the dimensionless velocity is obtained when using the binary hybrid nanofluid (TiO_2-CNT/water) is ($v^*_{max} = 1.576$) followed by binary hybrid nanofluid (TiO_2-Graphene/water) is ($v^*_{max} = 1.566$), and ternary hybrid nanofluid (TiO_2-CNT-Graphene/water) is ($v^*_{max} = 1.445$). In general, increasing the dimensionless amplitude leads to easier flow through the annular passage, which leads to an increase in dimensionless axial velocity.

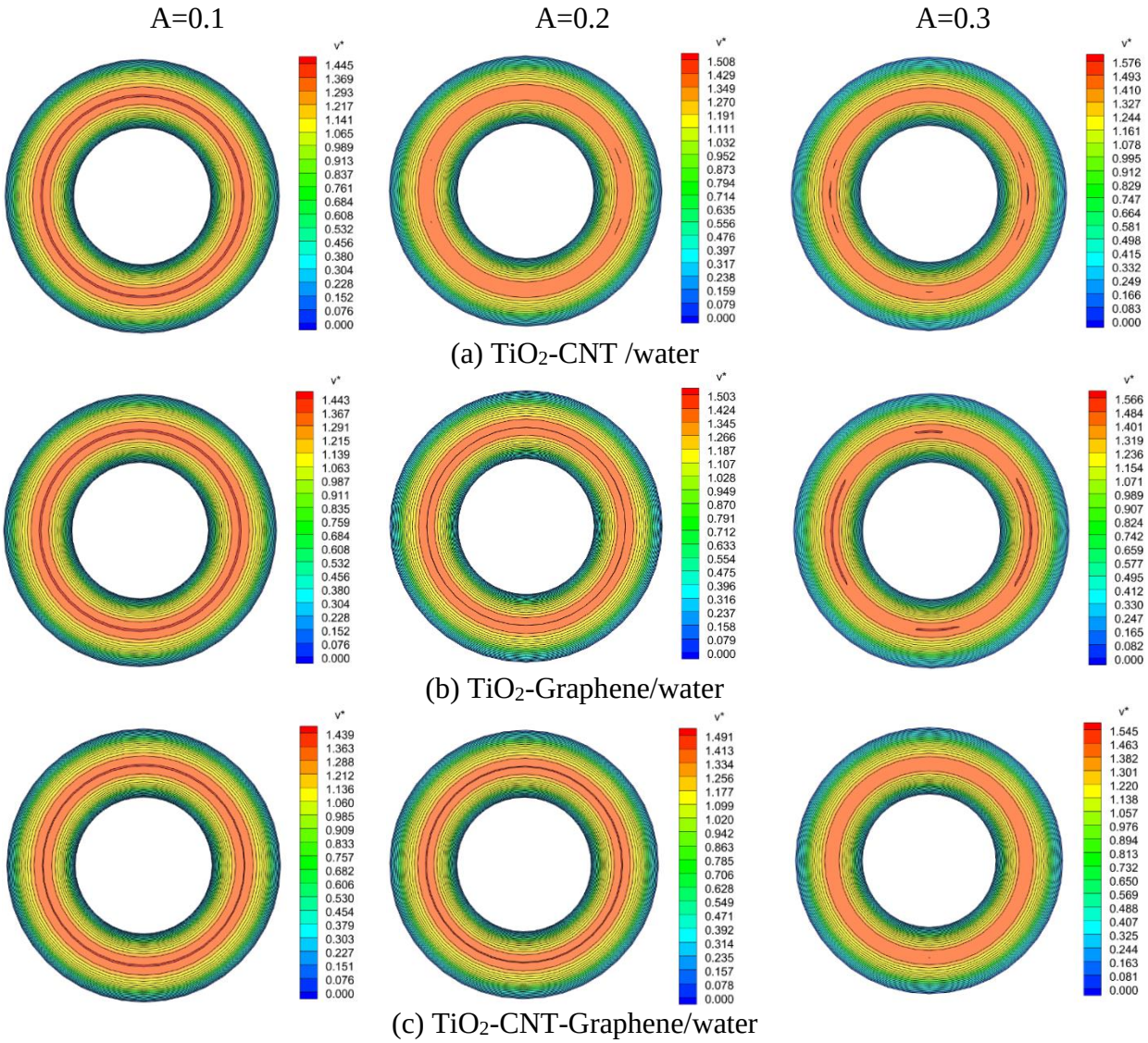

Figure IV. 24. Axial velocity contours for different amplitude at Re=800, Da=0.01, L=2.452, and ϕ=5%: (a) TiO_2-CNT/water, (b) TiO_2-Graphene/water, and (c) TiO_2-CNT-Graphene/water.

Figure IV.25 illustrates the axial velocity distribution for ternary hybrid nanofluid (TiO_2-CNT-Graphene/water) in the longitudinal section represented by the (r,z) plane for the three amplitudes A (0.1, 0.2 and 0.3) and the same dimensionless wavelength of the annulus channel L=2.452. The results show that the axial velocity distribution along the wavy annulus is nearly identical for the three amplitude cases. On the other hand, the forced flow of the hybrid nanofluid has a maximum axial velocity in four regions, which are located near the convex walls of the inner wavy cylinder and symmetrical concerning a horizontal plane that includes the axis of the annulus channel. Furthermore, the increase in axial velocity is caused by the narrowing of the annulus, as the axial velocity is proportional to the amplitude of the wavy

annulus, which indicates that the annulus's undulating shape influences the fluid particles' acceleration. Specifically, fluid particles are more likely to be accelerated near the wave crests closer to the convex walls. As a result, regions adjacent to these convex walls experience higher velocities than other duct parts. The maximum velocities for the three amplitudes A=0.1, A=0.2 and A=0.3 are respectively, $v^*_{max} = 1.626$, $v^*_{max} = 1.943$ and $v^*_{max} = 2.384$.

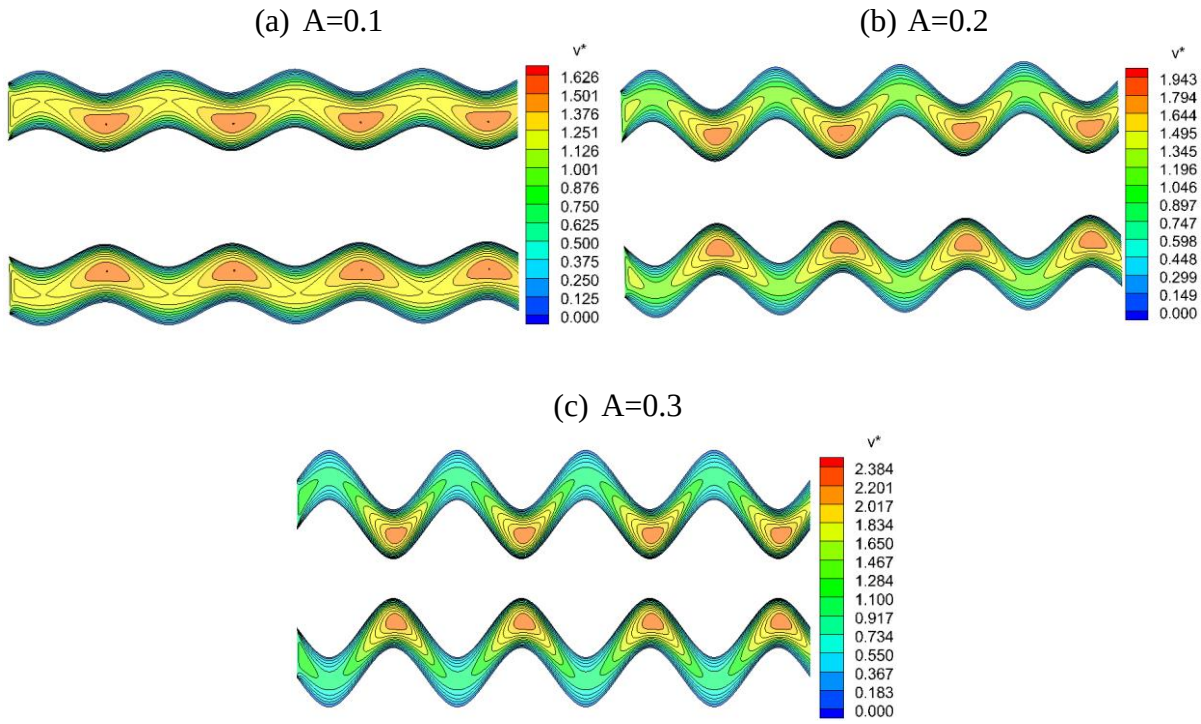

Figure IV. 25. Axial velocity contours using (TiO_2-CNT-Graphene/water) for different amplitude wave at Re=800, Da=0.01, L=2.452, and ϕ=5%: (a) A=0.1, (b) A=0.2, and (c) A=0.3.

Figure IV.26 compares the axial velocity for two wavelengths, L=5.026 and L=1.256, using a ternary hybrid nanofluid (TiO_2-CNT-Graphene/water). In the case of wavelength L=1.256, the maximum axial velocity is located in eight regions adjacent to each other near the adiabatic inner wavy cylinder rather than the outer heated wavy cylinder. Conversely, for the wavelength L=5.026, only two regions with maximum velocity are formed. The maximum velocities for two wavelengths, L=5.026 and L=1.256 are respectively, $v^*_{max} = 1.951$ and $v^*_{max} = 1.908$. It can be concluded that the increasing the wavelength leads to an increase in the axial velocity.

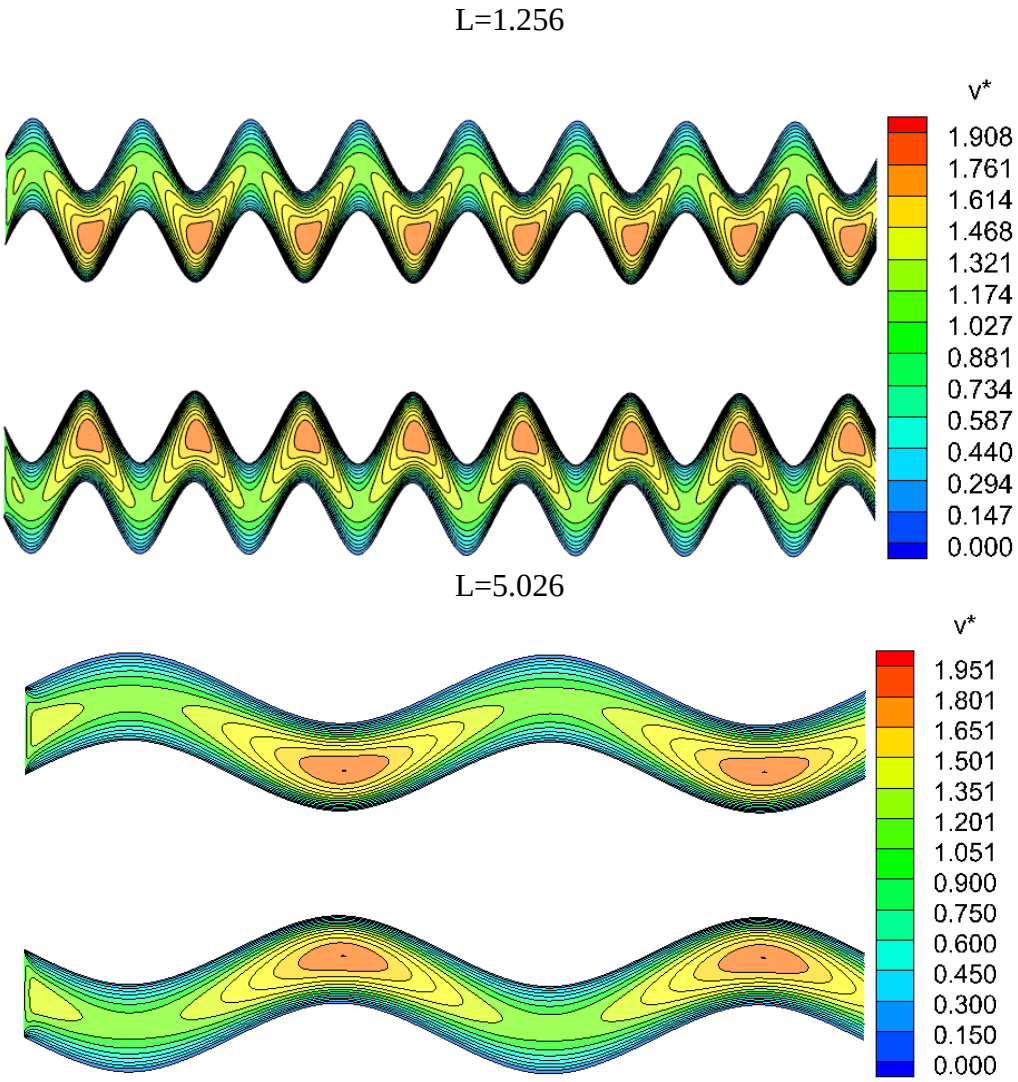

Figure IV. 26. Axial velocity contours for two different wavelengths using (TiO_2-CNT-Graphene/water) ternary hybrid nanofluid at Re=800, Da=0.01, A=0.2, and ϕ=5%.

Figure IV.27 presents the dimensionless axial velocity contours at the outlet of the wavy annulus for different hybrid nanofluids: ternary (TiO_2-CNT-Graphene/water), binary (TiO_2-CNT/water), and binary (TiO_2-Graphene/water) for various Hartmann numbers. The Figure shows that for a low Hartman number (Ha=10), the distribution of axial velocity contours appears symmetrical to the horizontal plane, with two cells in the middle containing the maximum velocity, one in the top part and the other in the bottom part of the annulus. Both cells are located in the same radius between the two wavy cylinders. For both Hartmann numbers 50 and 30, the axial velocity has similar distributions to those of the Hartmann number Ha = 10 in that it forms two symmetrical cells with respect to a horizontal plane passing through the cylinder axis, with a small difference corresponding to a radial displacement of the

maximum velocity while maintaining the angular position with respect to the vertical plane of the annulus as it partially approaches the insulated inner cylinder and moves away from the heated outer cylinder. The reason for this movement is the significant effect of the magnetic field on axial velocity as its intensity increases. The location of the maximum of the axial velocity for the three Hartmann numbers is: Ha=10 (r*=0.725, top θ =0 and bottom π/2), Ha=30 (r*=0.65, top θ =0 and bottom π/2) and Ha=50 (r*=0.6, top θ =0 and bottom π/2). Finally, we can conclude that in higher Hartman numbers, the maximum axial velocity approaches the thermally insulated inner cylinder and moves away from the heated outer cylinder.

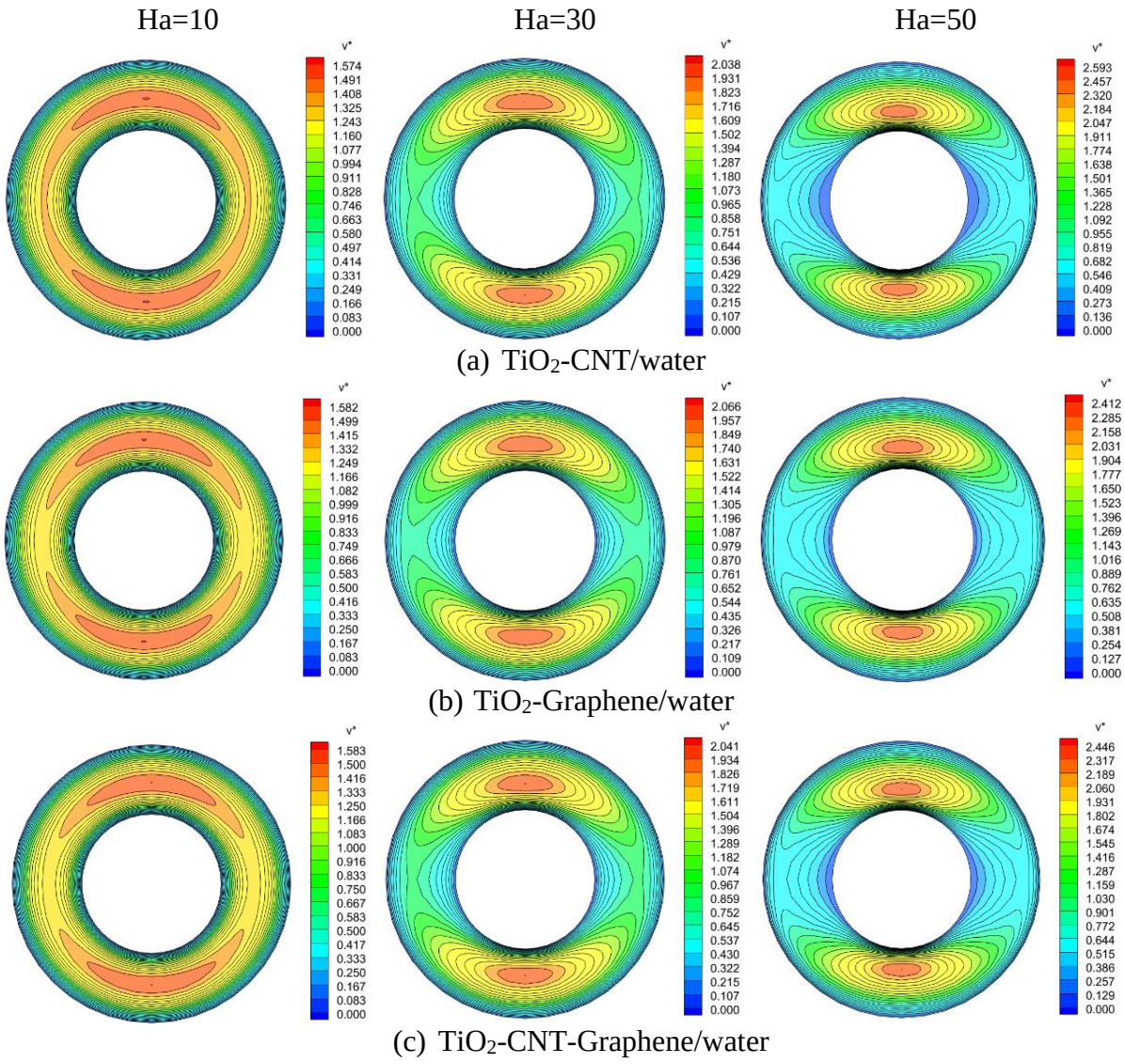

Figure IV. 27. Effect of Hartmann number on axial velocity contours at the duct's outlet for: (a) TiO_2-CNT/water, (b) TiO_2-Graphene/water, and (c) TiO_2-CNT-Graphene/water.

Figure IV.28 represents the effect of the partial magnetic field on the axial velocity contours for different scenarios and different Hartmann numbers. The results are taken using the ternary hybrid nanofluid at Da=0.01, L=2.452, A=0.2, and ϕ=5%. At low Hartmann number, the velocity contours remain qualitatively and quantitatively similar across all partial magnetic field scenarios. As the Hartmann number increases up to Ha=50, a relatively large decrease in velocity is observed in the region where the magnetic field is applied. This decrease is particularly significant in the first and second scenarios but less pronounced in the third scenario. Moreover, the distribution of axial velocity depends on the location of the magnetic field. This provides an indication of the areas in which we wish to decelerate the flow of the hybrid nanofluid through the magnetic field's effect.

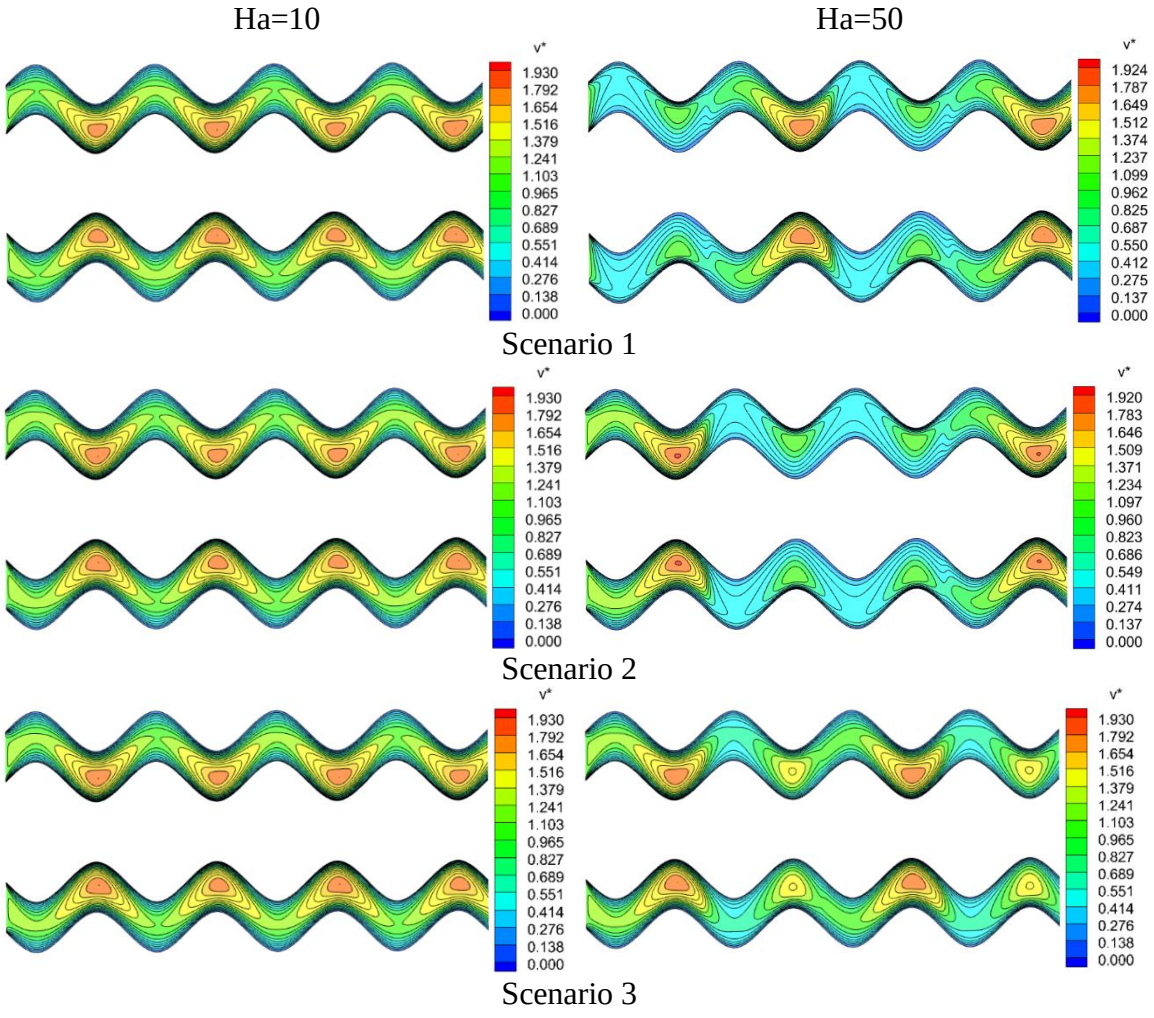

Figure IV. 28. Effect of different partial magnetic field scenarios on axial velocity contours at (r,z) plane.

IV.3.2 Thermal field

Figure IV.29 illustrate the comparison of 3D isotherms profile using ternary hybrid nanofluid (TiO_2-CNT-Graphene/water) for two cases, a straight annulus channel and a wavy annulus channel. The results are taken with Re=800, Da=0.01, Ha=0, ϕ=5%, and (L=2.452, A=0.2). It can be seen that at the outlet of the annulus channel, the dimensionless temperature of the straight annulus is higher than the wavy annulus channel.

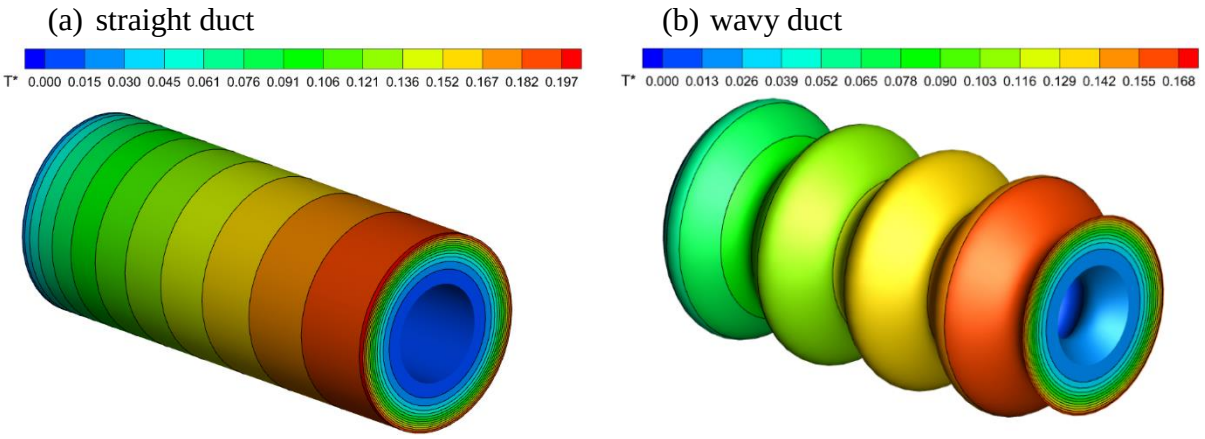

Figure IV. 29. 3D isotherms contours using (TiO_2-CNT-Graphene/water) at Re=800, Da=0.01, and ϕ=5%: (a) straight duct, (b) wavy duct.

Figure IV.30 compares the 3D isotherms profile for ternary hybrid nanofluid (TiO_2-CNT-Graphene/water) and two binary nanofluids: (TiO_2-CNT/water) and (TiO_2-Graphene/water), for two cases of wave amplitudes A=0.1 and A=0.3. The results are taken with Re=800, Da=0.01, L=2.452, Ha=0, and ϕ=5%. The temperature profile of the three hybrid nanofluids for both amplitudes A=0.1 and A=0.3 presents a concentric circular shape structure that exhibits radial and axial stratification. An interesting observation is that the maximum temperature decreases as the wave amplitude increases. This phenomenon is attributed to the intensified fluid flow motion associated with larger wave amplitudes, leading to reduced viscous dissipation and, subsequently, lower wall temperatures. Moreover, the comparison between different hybrid nanofluids shows that the maximum temperature was achieved using TiO_2-CNT/water followed by TiO_2-Graphene/water and TiO_2-CNT-Graphene/water, respectively.

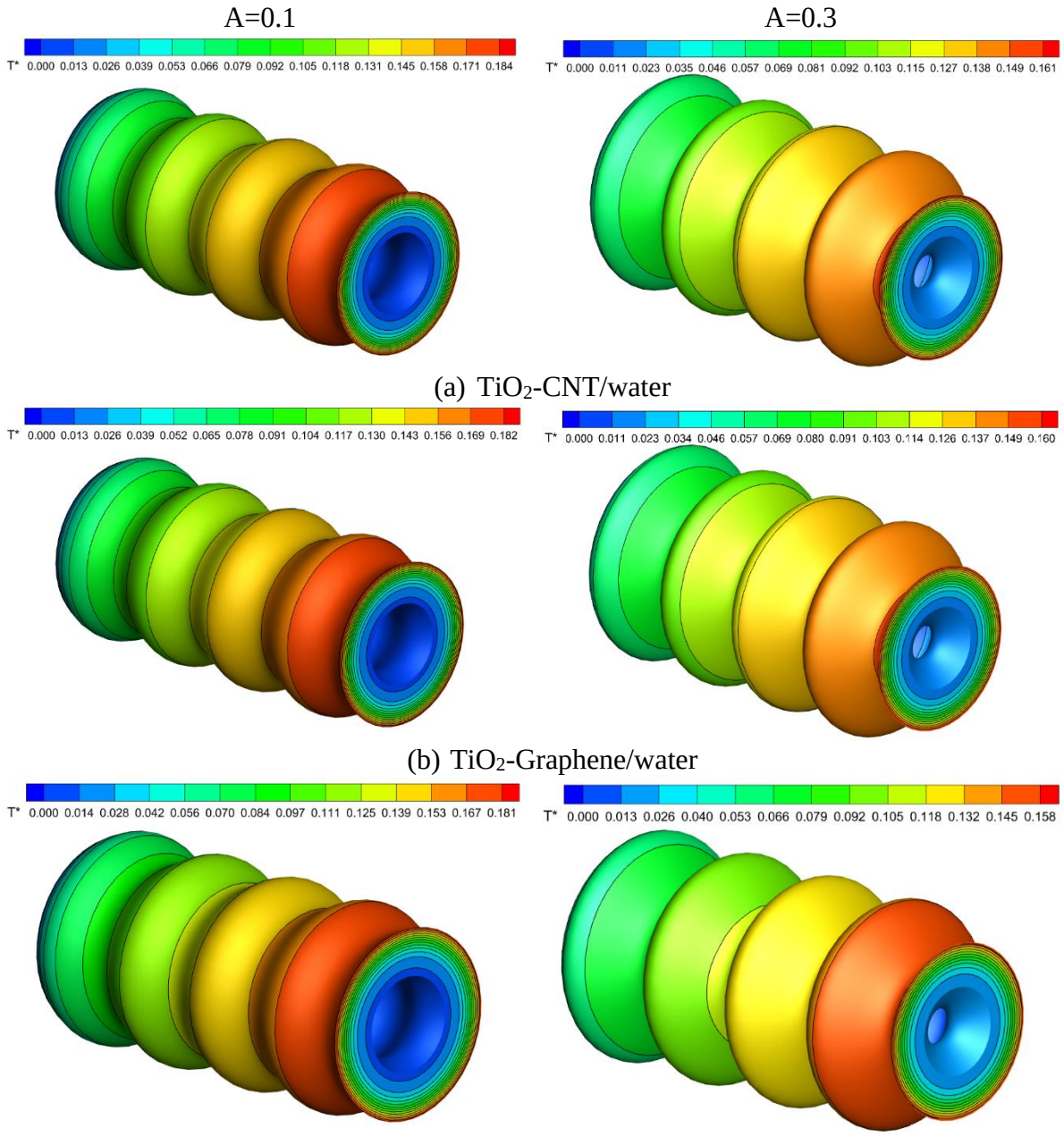

Figure IV. 30. 3D isotherms contours for different amplitude at Re=800, Da=0.01, L=2.452, and ϕ=5%: (a) TiO_2-CNT/water, (b) TiO_2-Graphene/water, and (c) TiO_2-CNT-Graphene/water.

The comparison of the ternary hybrid nanofluid (TiO_2-CNT-Graphene/water) for two wavelengths L=1.256 and L=5.026 are shown in **Figure IV.31**, at Re=800, Da=0.01, A=0.2, and ϕ=5%. From the figure, it can be seen that wavelength has no significant effect on the temperature distribution.

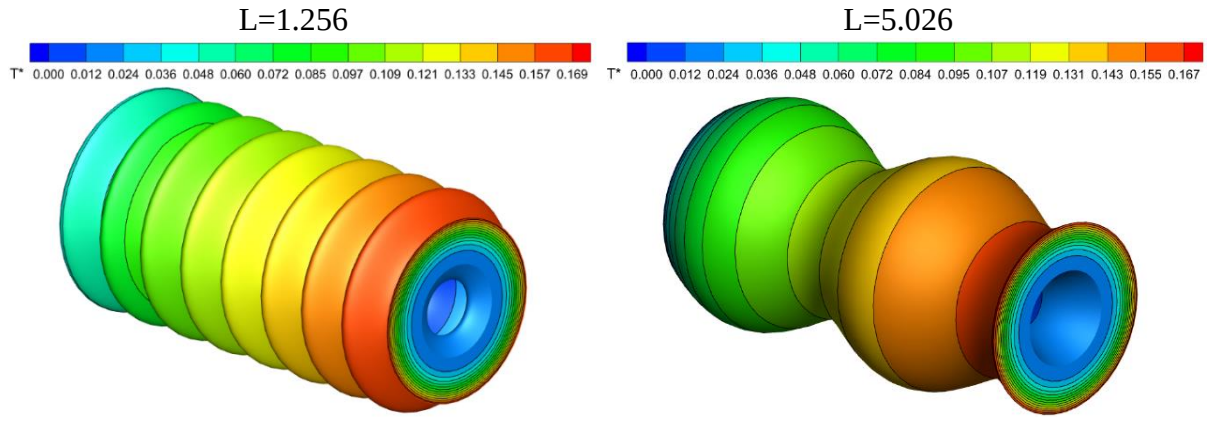

Figure IV. 31. 3D isotherms contours using (TiO_2-CNT-Graphene/water) for different wavelengths at Re=800, Da=0.01, A=0.2, and ϕ=5%.

Figure IV.32 shows the 3D isotherms profile using different hybrid nanofluids: (TiO_2-CNT-Graphene/water) ternary hybrid nanofluid, (TiO_2-CNT /water), and (TiO_2-Graphene/water) binary hybrid nanofluids subjected to a full magnetic field for different Hartmann numbers, Ha (10, 30 and 50) using the following parameters, Da=0.01, L=2.452, A=0.2, and ϕ=5%. The first observation shows that at a low Hartmann number (Ha = 10), the temperature distribution appears in the form of concentric circles, indicating radial and axial stratification. An angular deformation is observed near to the outlet of the annulus wavy channel. In addition, this deformation becomes increasingly important with the increase in the Hartman numbers from Ha=30 to Ha=50, the maximum temperature moving towards two positions: the right and left sides of the outer heated cylinder of the annulus channel. Generally, the temperature within the fluid domain decreases due to the effect of Lorentz force, except for the maximum temperature, which increases with higher Hartmann numbers. This can be attributed to the Joule heating effect, which is more significant in these regions. For the case of binary hybrid nanofluid (TiO_2-CNT/water), for example the dimensionless temperature for three Hartmann number are $T^* = 0.172$, $T^* = 0.181$, and $T^* = 0.189$ for Hartmann number Ha=10, 30 and 50, respectively. Also, for the same Hartmann number Ha=50, the dimensionless temperature is higher using, TiO_2-CNT/water $T^* = 0.189$, TiO_2-Graphene/water $T^* = 0.187$ and TiO_2-CNT-Graphene/water $T^* = 0.181$.

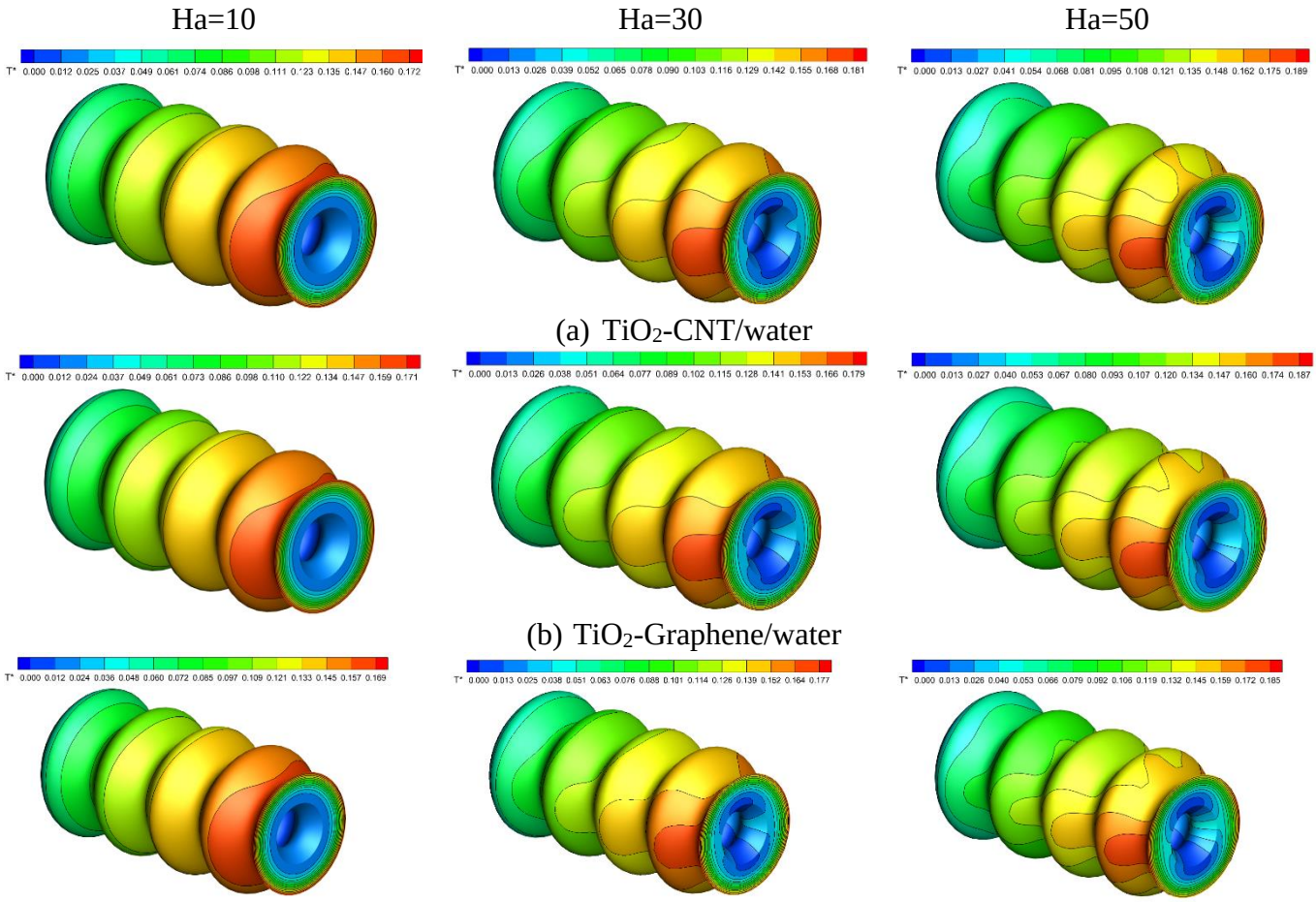

Figure IV. 32. Hartmann number effect on temperature contours for different hybrid nanofluids.

Figure IV.32 presents 3D isotherms contours using ternary hybrid nanofluid by applying partial magnetic field at 3 different scenarios and for the smallest Ha=10 and largest Hartmann number Ha=50. For all the partial magnetic field scenarios tested, the same behavior as the full magnetic field scenario is observed. Moreover, the temperature decreases with increasing Hartmann number, except the maximum temperature which increases. The maximum temperature is located at the heated outer wavy cylinder near the outlet of the annulus wavy channel in two opposite sections in the right and left side. The comparison between the different partial magnetic field scenarios (see **Figure IV.33**) and the full magnetic field case (see **Figure IV.32**), for a low Hartmann number (Ha=10), the isotherms profiles are qualitatively and quantitatively the same distribution. Furthermore, the increase of the Hartmann number to Ha=50, obvious distortion of the distribution occurs of the concentric circles in all the cases start in the zone

where the magnetic field is applied. In addition, another important observation is that the temperature variation in the third scenario is not significant compared to the other scenarios.

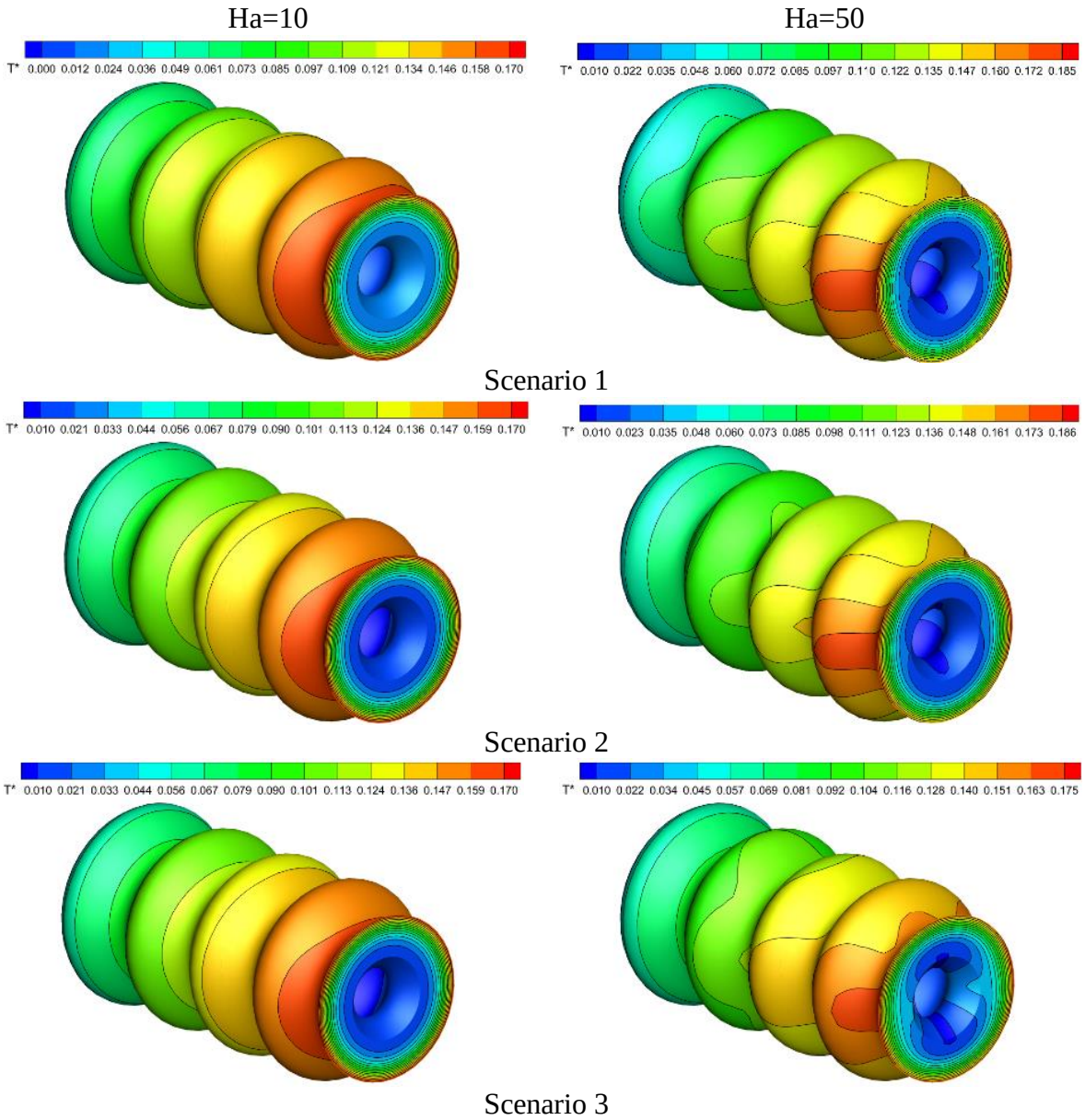

Figure IV. 33. The effect of different partial magnetic field scenarios on temperature contours using ternary hybrid nanofluid.

IV.3.3 Nusselt number

Figure IV.34 (a-b) illustrate the effect of amplitude and wavelength on heat transfer in terms of average Nusselt number using two binary hybrid nanofluids and ternary hybrid nanofluid at fixed wavelength L=2.452 (**Figure IV.34a**), and at fixed wave amplitude A=0.2 (**Figure IV.34b**). The results are taken at Re=800, Da=0.01, Ha=0, and ϕ=5%. Form **Figure IV34a**, it can be seen, that the average Nusselt number increases with increasing the wave amplitude, and

the high average Nusselt number obtained using ternary hybrid nanofluid TiO_2-CNT-Graphene/water, followed by binary nanofluid TiO_2-Graphene/water) and in last place the binary nanofluid TiO_2-CNT/water. The increase in wave amplitude from 0.1 to 0.3 results in improved average Nusselt numbers by 19.5%, 19.4%, and 19.3% using TiO_2-CNT-Graphene/water, TiO_2-Graphene/water, and TiO_2-CNT/water, respectively. This is due to the thermal conductivity which plays an essential factor on the heat transfer within the hybrid nanofluids, this is justified by the existence of two nanoparticles of very high thermal conductivity represented respectively by the two nanoparticles Gr and CNT and a nanoparticle TiO_2 of very low thermal conductivity compared to them. Additionally, heat transfer is improved by using wavy annulus channel that have larger wave amplitudes.

Figure IV.34b shows the average Nusselt number as a function of wavelength, we notice a weak decrease in the Nusselt number with increasing wavelength. The relative average Nusselt number is constant with increasing wavelength for the two binary hybrid nanofluids TiO_2-Graphene/water and TiO_2-CNT/water, but for the ternary hybrid nanofluid TiO_2-CNT-Graphene/water there is a difference where the Nusselt number is relatively high at wavelength L=1.256 and then decreases and stabilizes at wavelengths L=2.452 and L=5.026. The increase in wavelength from 1.256 to 5.026 results in a decrease in average Nusselt number of 1.2%, 0.22% and 0.18% with TiO_2-CNT-Graphene/water, followed by TiO_2-Graphene/water and TiO_2-CNT/water, respectively. In addition, the ternary hybrid nanofluid TiO_2-CNT-Graphene/water gives the highest average Nusselt number values for both variations wave amplitude and wavelength, followed by the TiO_2-Graphene/water and TiO_2-CNT/water binary hybrid nanofluids, respectively. This implies that the ternary hybrid nanofluid offers superior thermal performance.

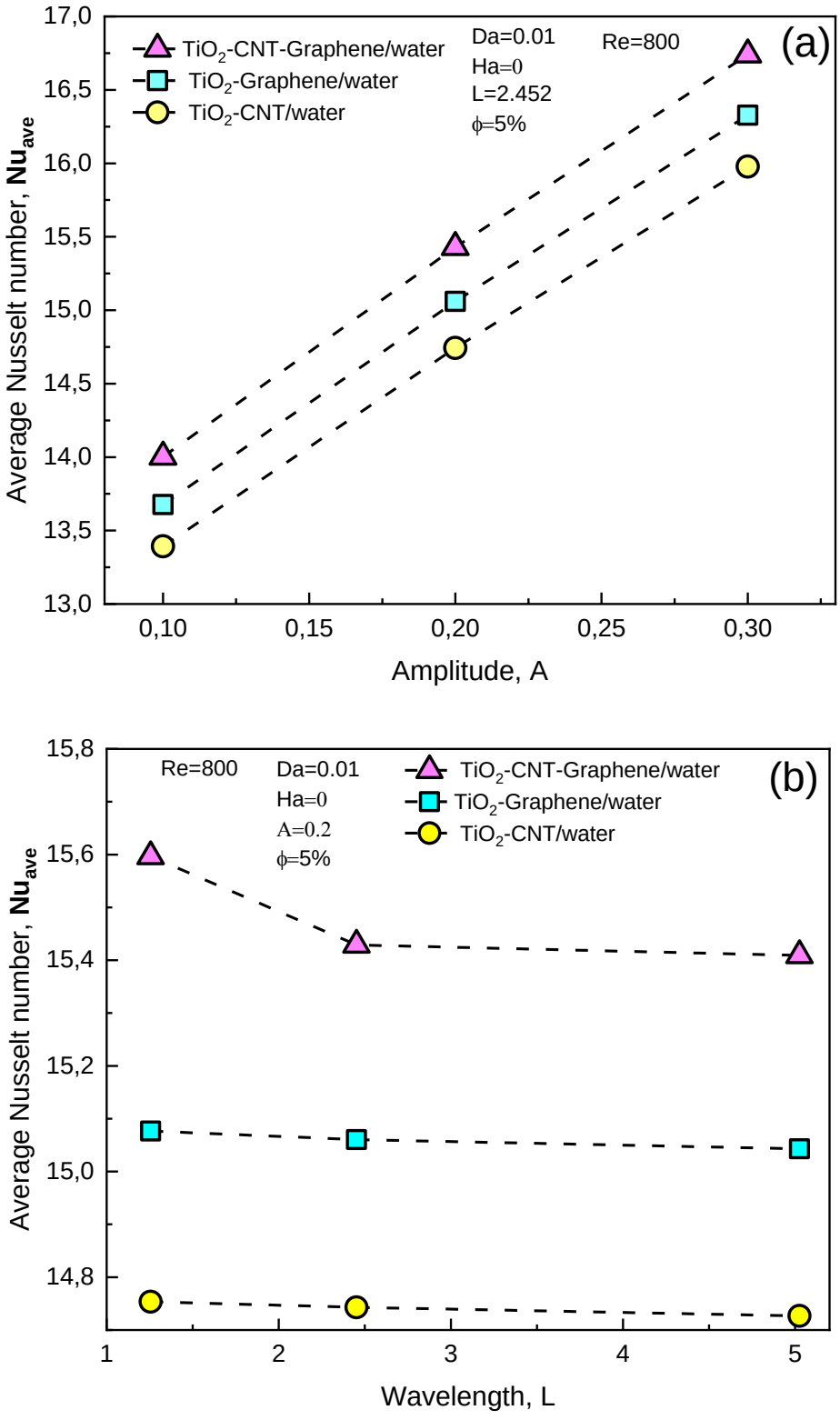

Figure IV. 34. Average Nusselt number using three different hybrid nanofluids for (a) effect of wave amplitude, (b) effect of wavelength.

Figure IV.35a displays the average Nusselt number of hybrid nanofluids for different Hartmann numbers corresponds to the full magnetic field applied to the outer wavy cylinder of

the annulus channel taking amplitude A=0.2, wavelength L=2.452, and volume fraction ϕ=5%. It can be seen that, the increasing of Hartmann number, the average Nusselt number increase for all hybrid nanofluids tested. The higher values are achieved using (TiO_2-CNT-Graphene/water) ternary hybrid nanofluid, followed by (TiO_2-Graphene/water), and (TiO_2-CNT/water) binary hybrid nanofluids, respectively. The application of the magnetic field represented by the Hartmann number is a key factor in optimizing heat transfer through the corrugated ring channels found in many thermal systems.

Figure IV.35b shows the average Nusselt number versus Hartmann number for four scenarios, the full magnetic field (FMF) and partial magnetic field (PMF) using a ternary hybrid nanofluid(TiO_2-CNT-Graphene/water). The first observation is that the number of Nusselt increases as the number of Hartmann increases for all scenarios. However, in the case of low Hartmann number 10, we observe that the Nusselt number takes the same value for all the examined scenarios FMF and PMF with a slight variation among them. In addition to that, for the highest Hartmann number Ha=50, the highest Nusselt number is achieved using full magnetic field scenario (FMF), followed by partial magnetic field (PMF) scenario 1, scenario 2, and scenario 3, respectively.

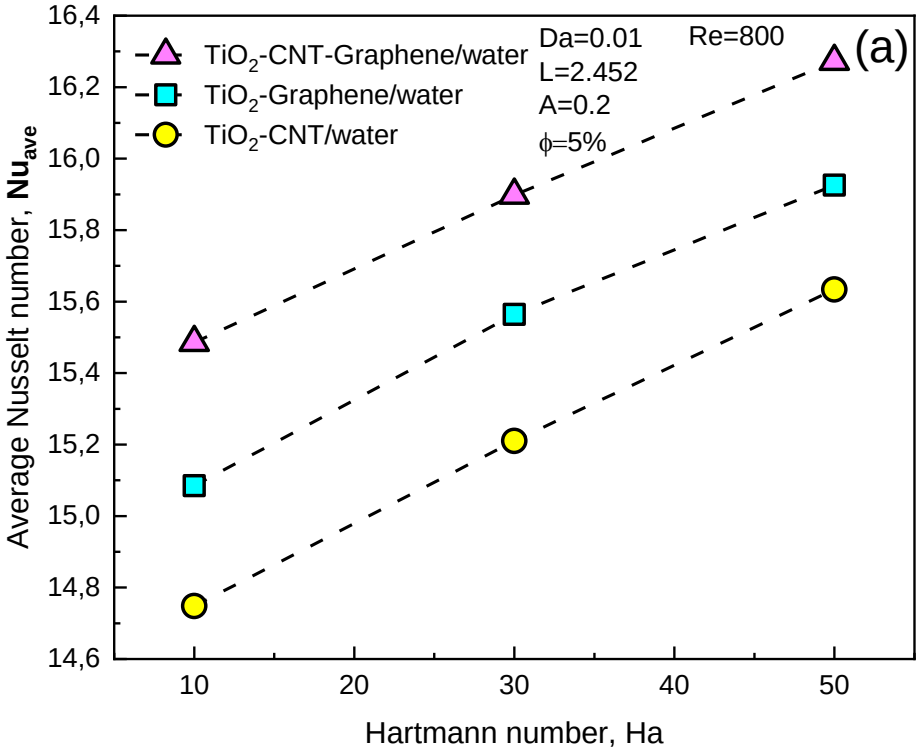

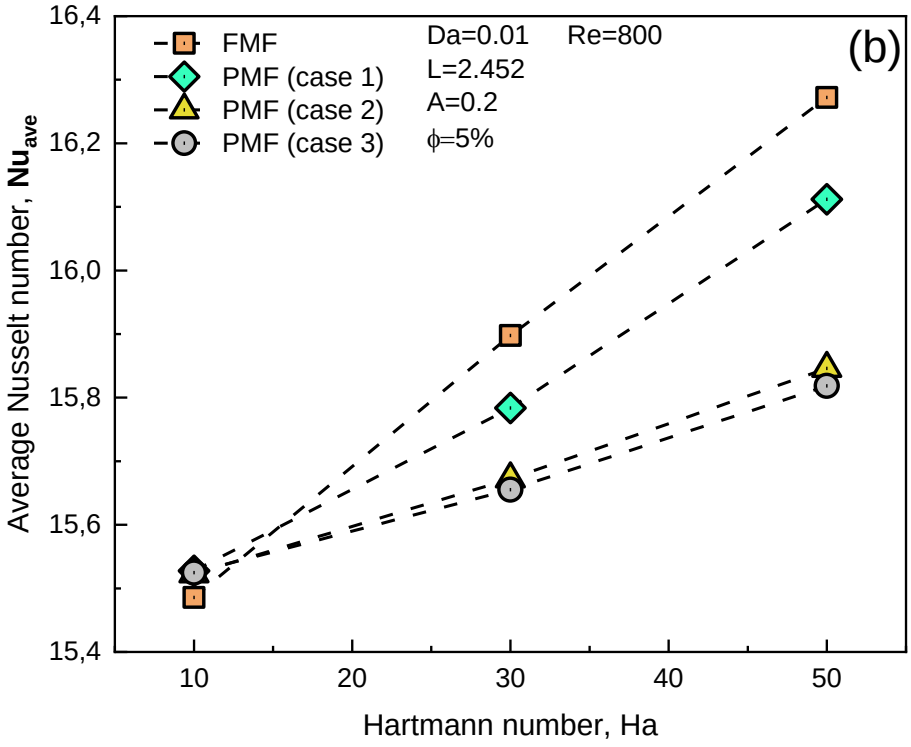

Figure IV. 35. Average Nusselt number versus Hartmann number (a) for different hybrid nanofluid using full magnetic field, (b) comparison of full and partial magnetic field scenarios.

IV.3.4 Skin friction coefficient

Reminder, the skin friction coefficient is caused by the dynamic viscosity of hybrid nanofluids and is developed as the hybrid nanofluids moves on the surface of a body. Note that viscosity is influenced by several factors, the most important of which is the shape of the nanoparticles such as spherical, cylindrical, platelet ....etc. **Figure IV.36a** show the variation of the average skin friction coefficient for three hybrid nanofluids along the inner wall of outer wavy cylinder versus the wave's amplitude. The results show that the average coefficient of skin friction increases with increasing amplitude. This phenomenon is attributed to heightened interaction between the fluid and the annulus channel walls, particularly near the convex parts where increased maximum velocity leads to higher velocity gradients near the walls, resulting in elevated shear stresses. Comparison between three types of hybrid nanofluids tested, it is apparent that the (TiO_2-CNT-Graphene/water) ternary hybrid nanofluid has the highest values regardless the wave's amplitude, followed by (TiO_2-Graphene/water), and (TiO_2-CNT/water) binary hybrid nanofluids, respectively.

Figure IV.36b shows the variation in the average friction coefficient for different wavelengths from 1.256 to 5.026. It can be seen that the average coefficient of skin friction remains constant for all the wavelengths tested. Therefore, it can be concluded that the wavelength has no effect on the skin friction coefficient.

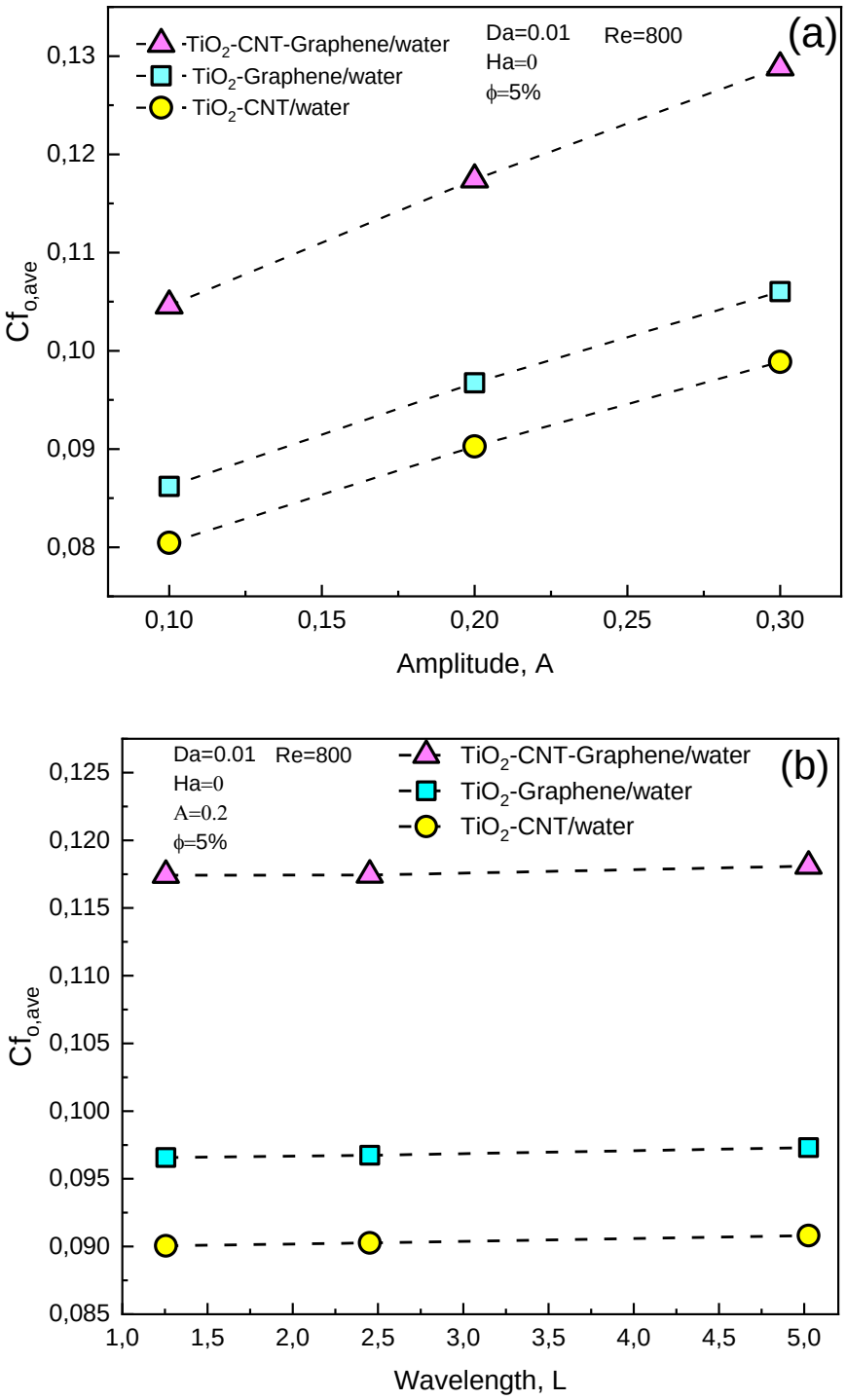

Figure IV. 36. Average skin friction coefficient using three different hybrid nanofluids for (a) wave amplitude, (b) wavelength.

In **Figure IV.37a**, it is clear that the average skin friction coefficient increases as the Hartmann number increases is due to the amplification of the Lorentz force. These forces lead to an increase in the shear stress exerted on the outer wall of the annulus channel. Consequently, the skin friction coefficient, which quantifies the frictional force experienced by the fluid flowing over a surface, increases as a result of the enhanced resistance encountered. The (TiO_2-CNT-Graphene/water) ternary hybrid nanofluid exhibits the highest values, followed by (TiO_2-Graphene/water), and (TiO_2-CNT/water) binary hybrid nanofluids respectively. Figure IV.37b presents the average skin friction coefficient versus Hartmann number for both full magnetic field (FMF), and partial magnetic field (PMF) cases using (TiO_2-CNT-Graphene/water) ternary hybrid nanofluid. The average skin friction coefficient increases as the Hartmann number increases for all the studied cases. The full magnetic field shows a much higher average skin friction coefficient compared to the partial magnetic field cases, which show almost identical results.

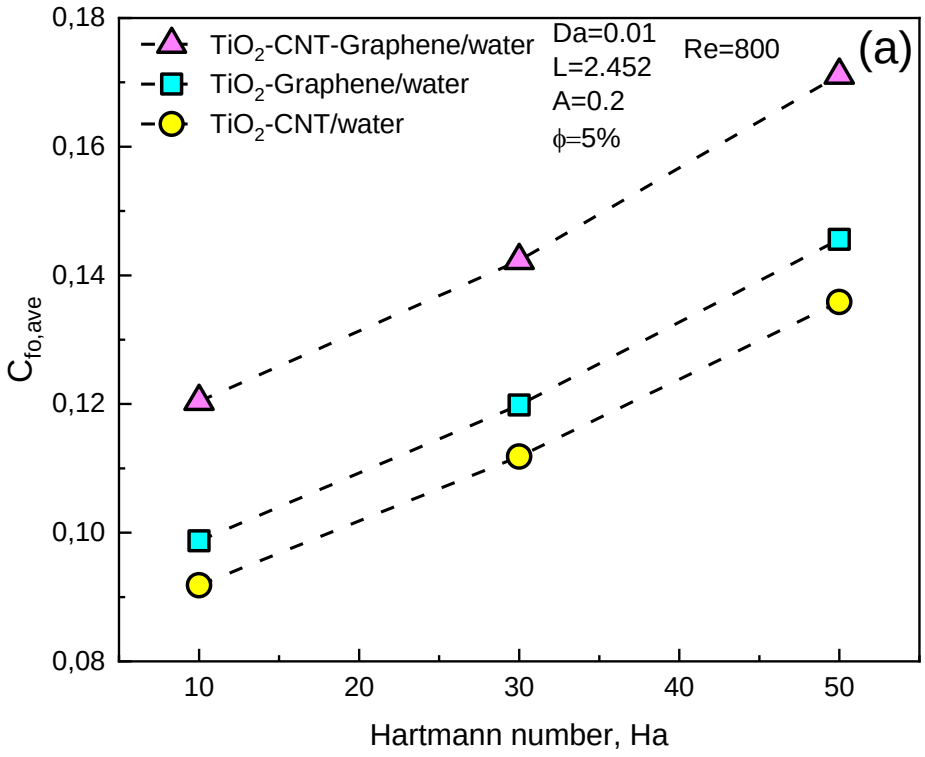

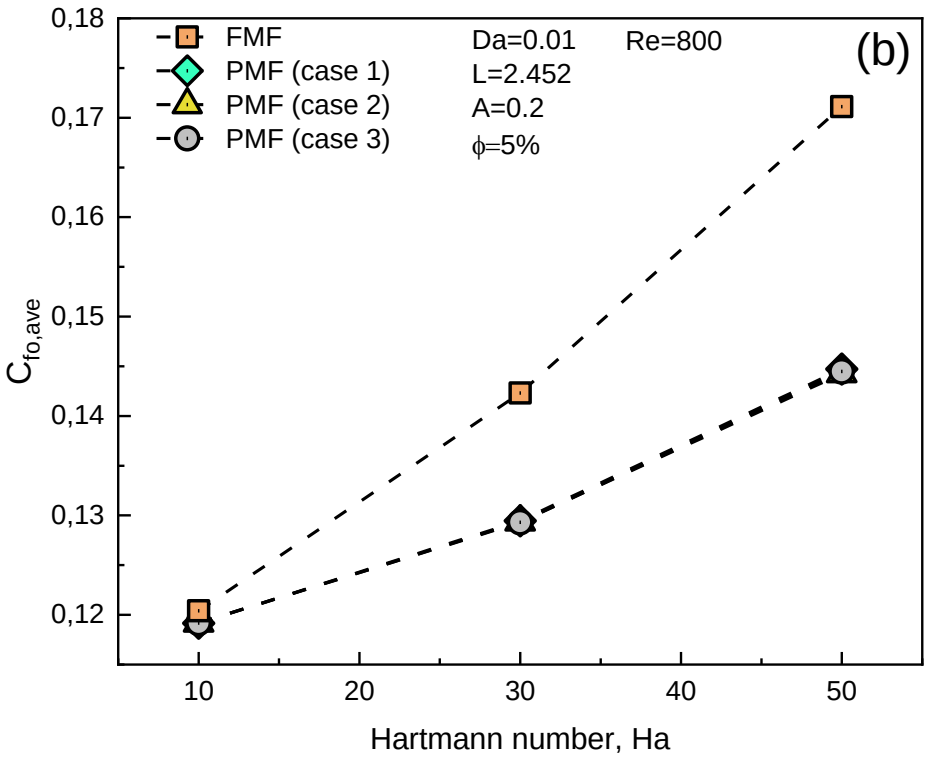

Figure IV. 37. Average skin friction coefficient versus Hartmann number (a) for different hybrid nanofluid using full magnetic field, (b) comparison of full and partial magnetic field scenarios.

IV.3.5. Pressure drop

Figure IV.38a demonstrate the variation of pressure drop concerning the wave's amplitude for three hybrid nanofluids studied. The results indicate that the pressure drop increases with increasing wave amplitude for all the hybrid nanofluids. Independently of amplitude, the TiO_2-CNT-Graphene/water ternary hybrid nanofluid shows the highest pressure drop, followed by the TiO_2-Graphene/water and TiO_2-CNT/water binary hybrid nanofluids, respectively. The ternary hybrid nanofluid, with its unique composition, exhibit higher viscosity and, consequently, higher pressure drop values compared to the both binary hybrid nanofluids.

Figure IV.38b demonstrate the variation of pressure drop concerning the wavelengths for three hybrid nanofluids studied. The obtained results showed that the pressure drop starts with a relatively high value with the wavelength of 1.256, then its value decreases with increasing wavelength, noting a relative stability in the pressure drop between the wavelength values 2.452 to 5.026.

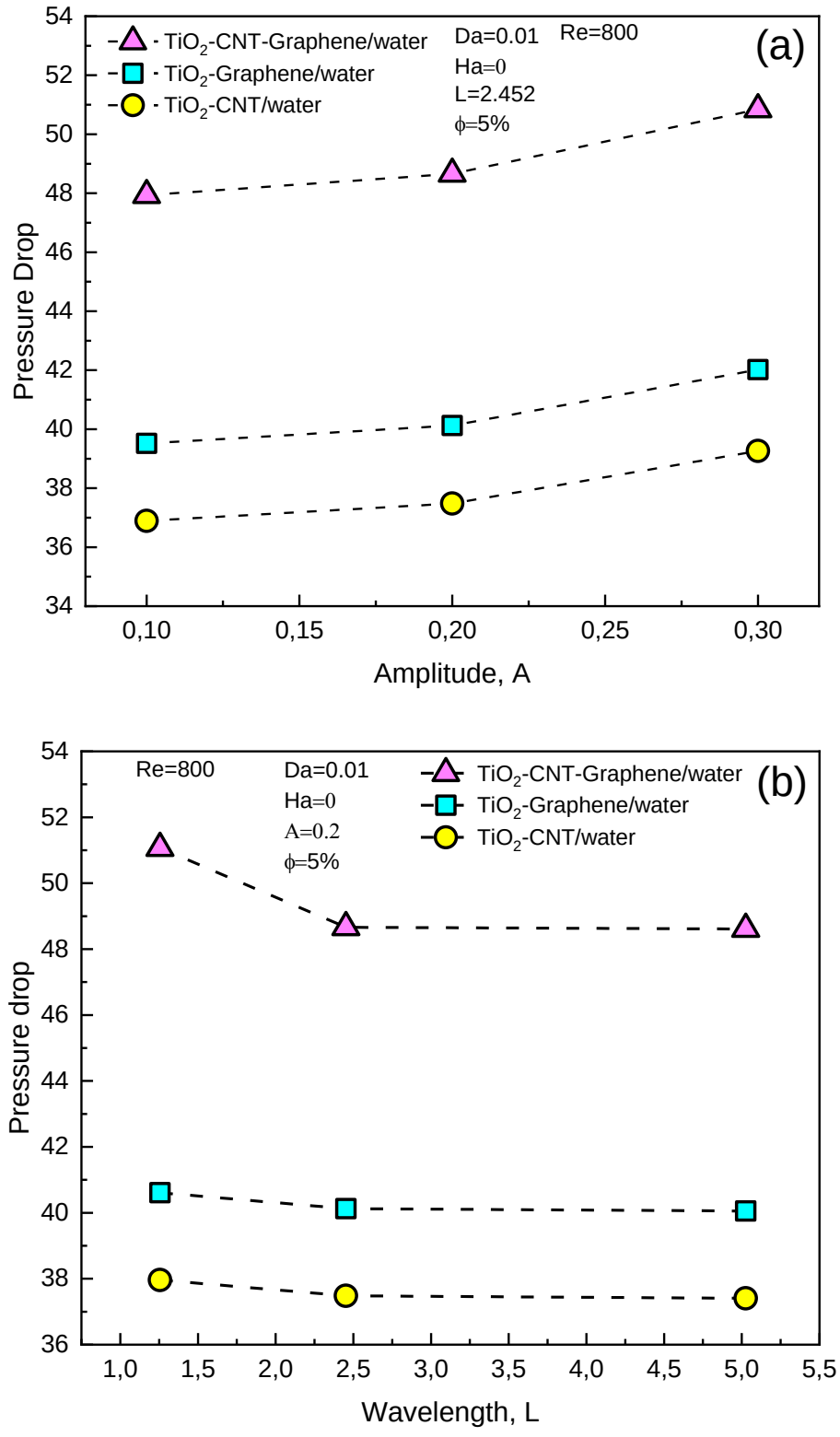

Figure IV. 38. Pressure drop using three different hybrid nanofluids for (a) effect of wave amplitude, (b) effect of wavelength.

Figure IV.39a, show the pressure drop versus Hartmann number for three hybrid nanofluids. The pressure drop increase with increasing Hartmann number for all the hybrid nanofluids

tested. This observed phenomenon is due to the Lorentz force, which is opposed to the movement of the hybrid nanofluid, resulting in increased resistance and, consequently, a higher pressure drop appearing. Furthermore, among the hybrid nanofluids examined, the (TiO_2-CNT-Graphene/water) ternary hybrid nanofluid displays the highest pressure drop, while the binary hybrid nanofluids (TiO_2-Graphene/water, and TiO_2-CNT/water) exhibit similar pressure drop values. For Ha=50, the (TiO_2-CNT-Graphene/water) ternary hybrid nanofluid gives a 1.09 times higher pressure drop than both (TiO_2-Graphene/water) and (TiO_2-CNT/water) binary hybrid nanofluids. **Figure IV.39b** presents the pressure drop versus Hartmann number for both full and partial magnetic field cases using ternary hybrid nanofluid (TiO_2-CNT-Graphene/water). At low Hartmann number (Ha=10), the pressure drop are approximately similar across all the cases. Furthermore, with increasing Hartmann number (Ha=30, and 50), the pressure drop increase for all the cases, indicating an intensified flow resistance attributed to elevated magnetic field strengths. However, an exception is observed at Ha=50 with partial magnetic field (case 3), where the pressure drop remains constant at the value observed at Ha=30. Moreover, a comparative analysis reveals that the full magnetic field configuration gives the highest pressure drop values. Afterwards, the case 2 of partial magnetic field (PMF) shows the highest pressure drop, followed by case 1 and case 3, respectively.

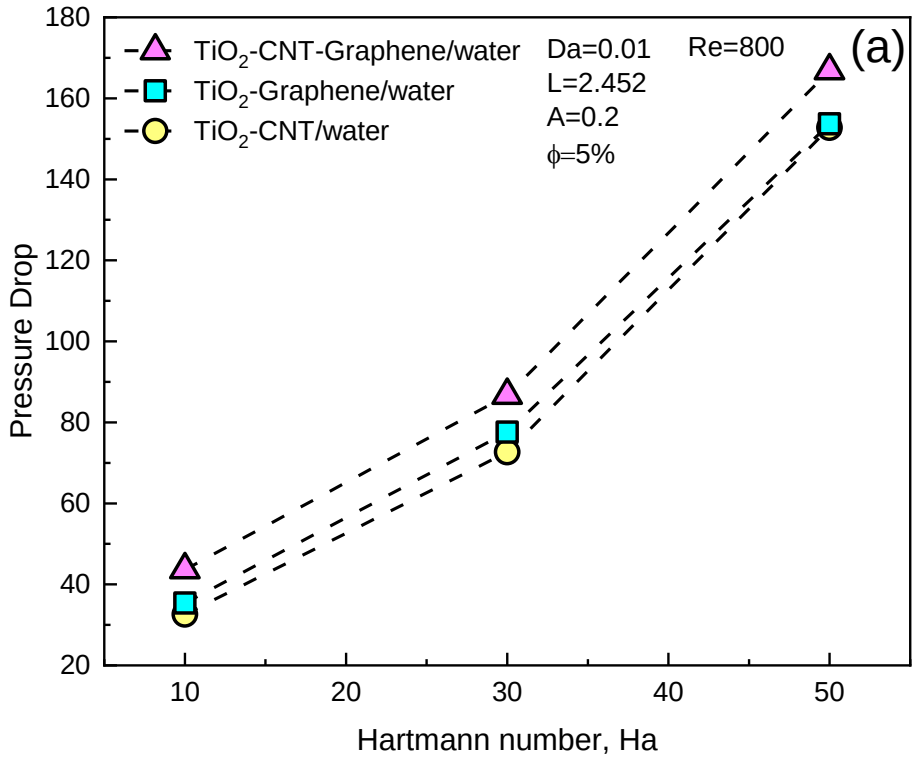

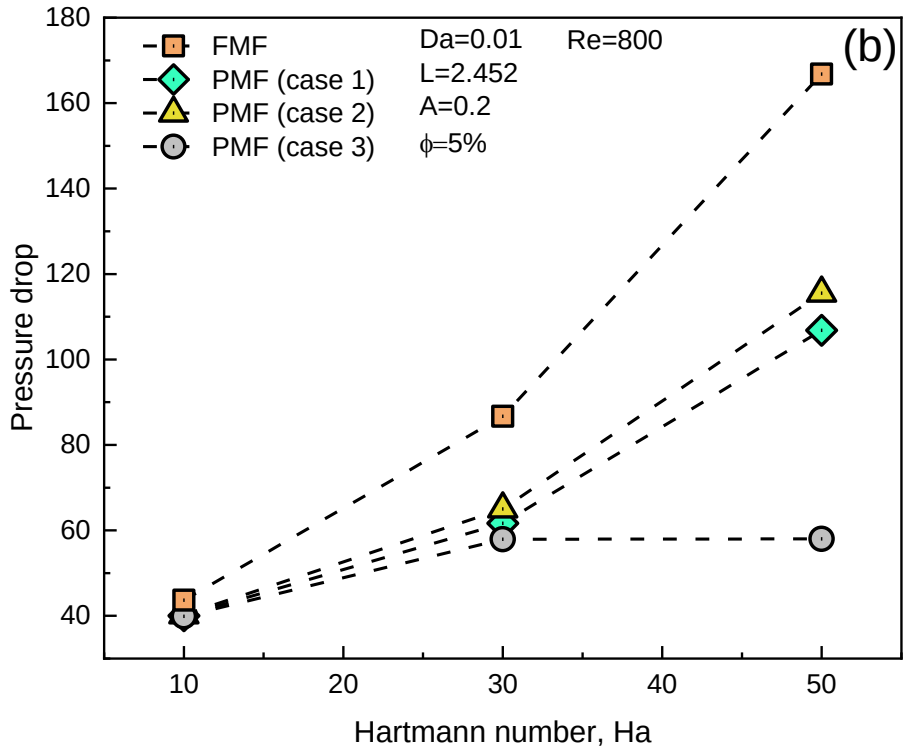

Figure IV. 39. Pressure drop versus Hartmann number (a) for different hybrid nanofluid using full magnetic field, (b) comparison of full and partial magnetic field scenarios.

IV.3.6. Entropy generation

Reminder, entropy generation refers to the production of entropy within a system due to irreversible processes such as heat transfer, fluid friction, and magnetic field. **Figure IV.40 (a-b)** displays the entropy generation for three different hybrid nanofluids and for different amplitude waves. An increase in wave amplitude causes a decrease in thermal entropy and friction entropy because higher amplitude waves for an annulus channel tend to provide better heat transfer and reduce fluid friction than lower amplitude waves. **Figure IV.40c** displays the variation of the Bejan number for different wave amplitudes. It can be seen that the Bejan number increases with increasing the amplitude wave; this indicates that the heat transfer is the dominant source of entropy generation.

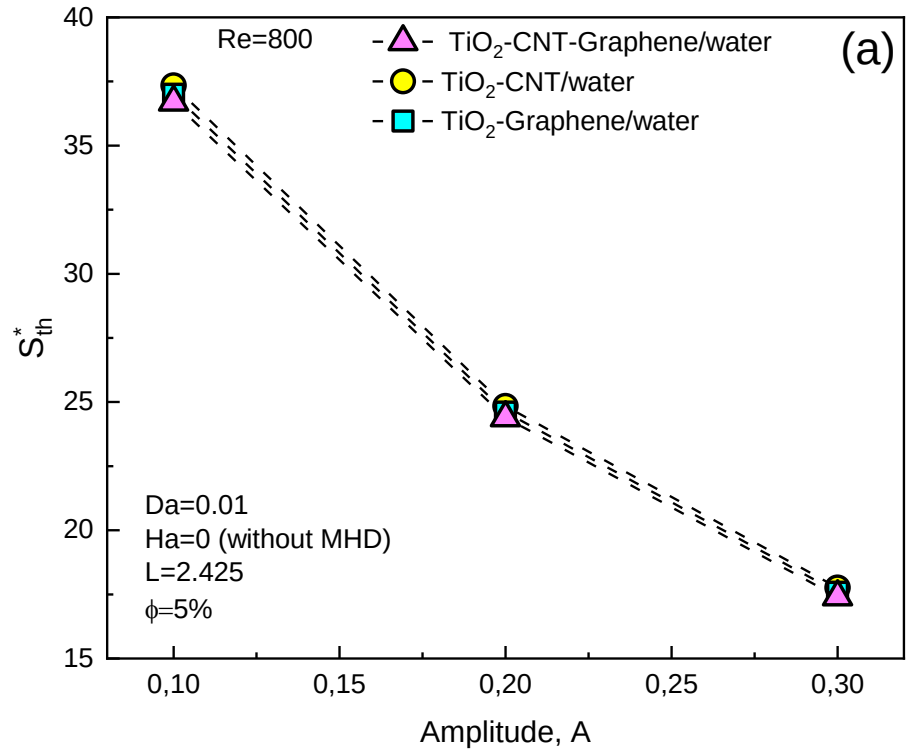
Re=800
TiO2-CNT-Graphene/water
TiO2-CNT/water
TiO2-Graphene/water
(a)
Da=0.01
Ha=0 (without MHD)
L=2.425
ϕ=5%
S*th
Amplitude, A
40
35
30
25
20
15
0,10
0,15
0,20
0,25
0,30

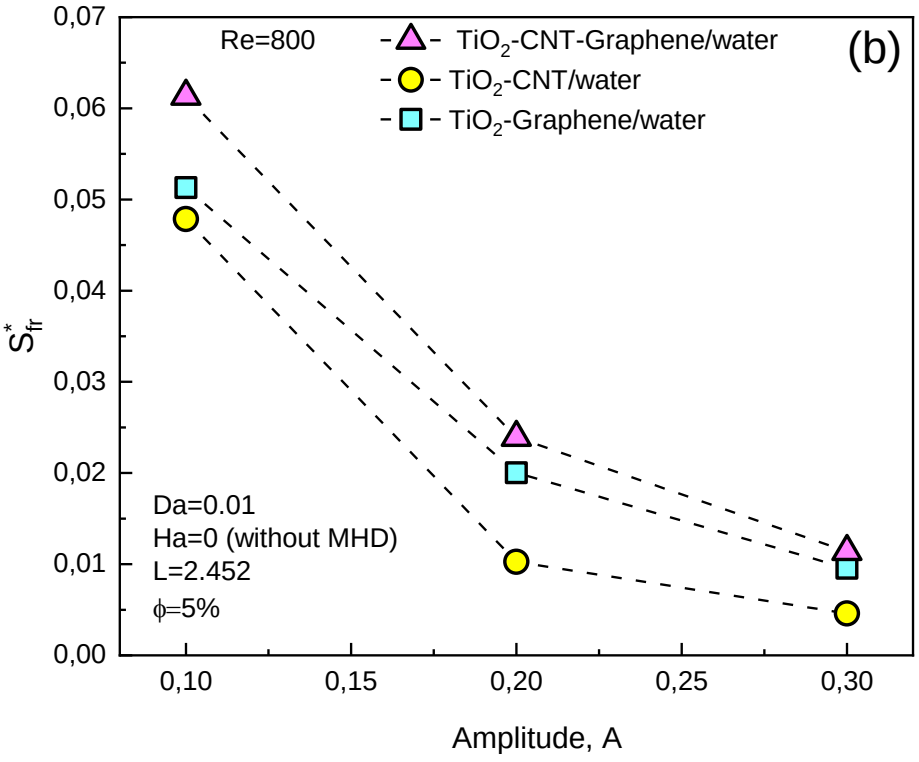
Re=800
TiO2-CNT-Graphene/water
TiO2-CNT/water
TiO2-Graphene/water
(b)
Da=0.01
Ha=0 (without MHD)
L=2.452
ϕ=5%
S*fr
Amplitude, A
0,07
0,06
0,05
0,04
0,03
0,02
0,01
0,00
0,10
0,15
0,20
0,25
0,30

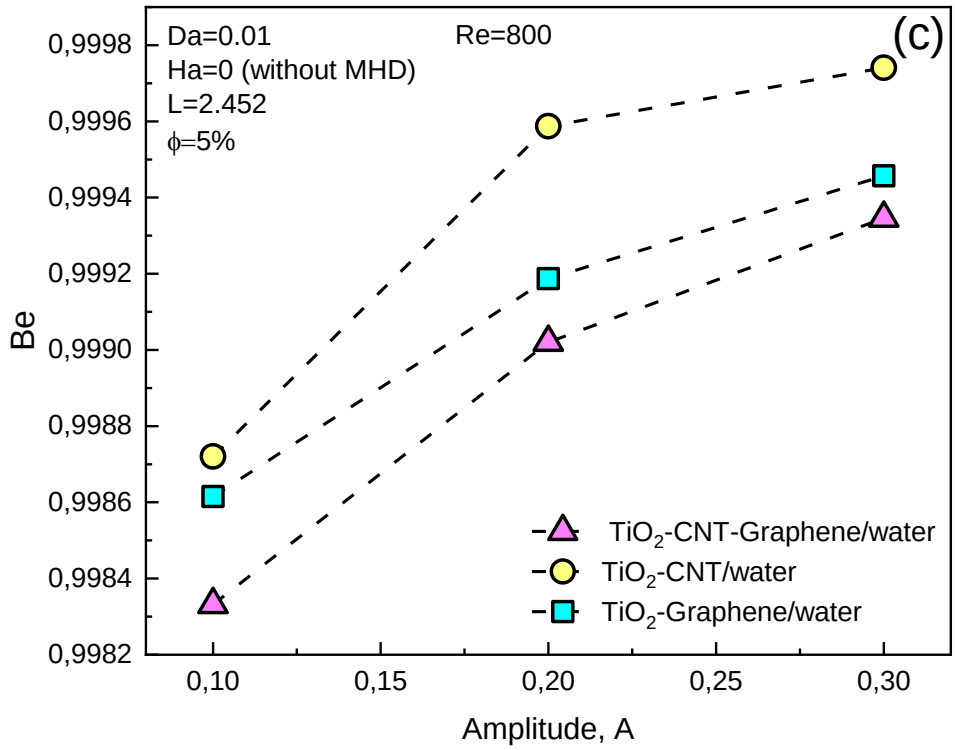

Figure IV. 40. Entropy generation and Bejan number for different hybrid nanofluids and wave amplitude at L=2.452.

Figure IV.41 (a-c) illustrates the entropy generation and Bejan number for three hybrid nanofluids and different wavelengths. It can be seen that as the wavelengths increase, a slight decrease in thermal entropy is observed. In contrast, there is no remarkable variation in frictional entropy and Bejan number for all the hybrid nanofluids tested. This indicates that the relative importance of heat transfer and viscous dissipation in the entropy generation do not change significantly with wavelength.

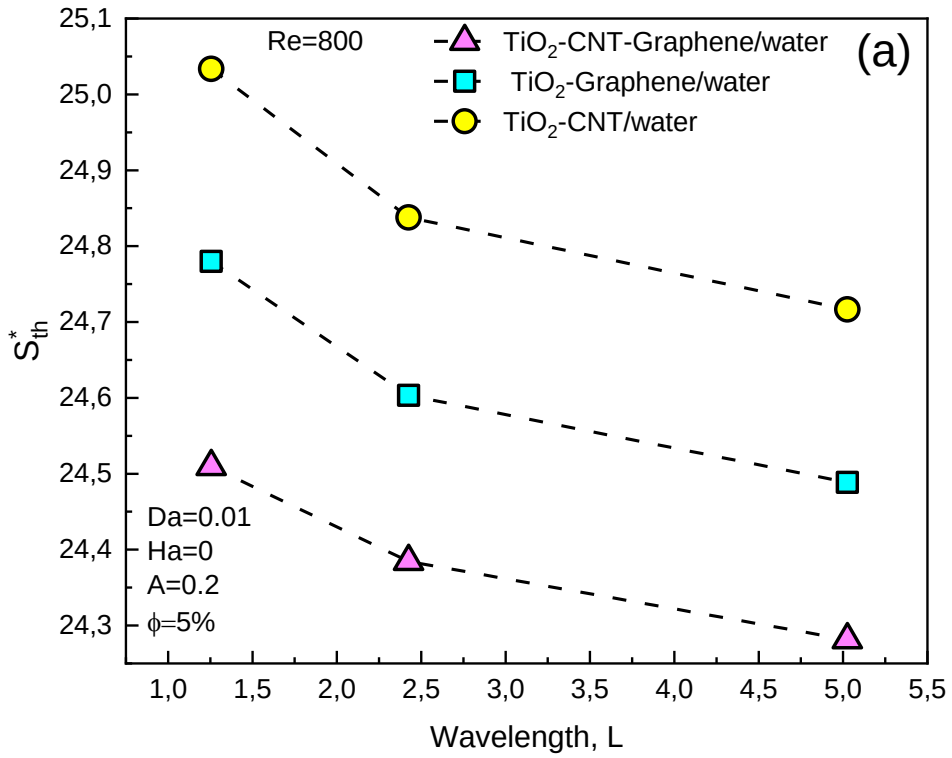
Re=800
TiO2-CNT-Graphene/water
TiO2-Graphene/water
TiO2-CNT/water
(a)
Da=0.01
Ha=0
A=0.2
ϕ=5%
S*th
Wavelength, L

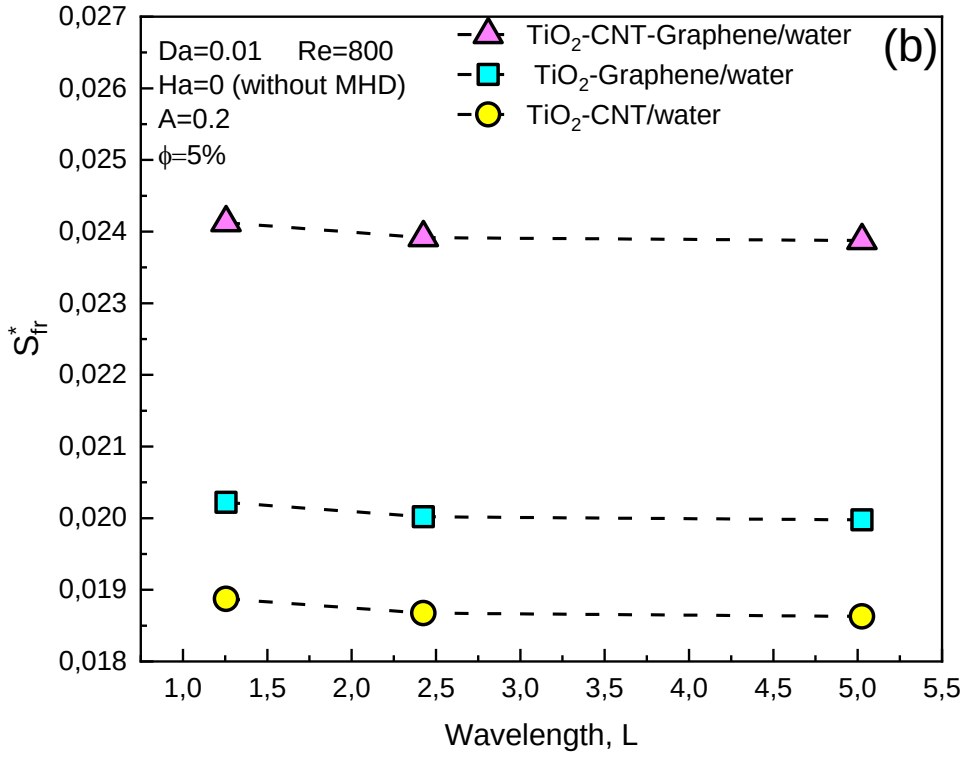
Da=0.01 Re=800
Ha=0 (without MHD)
A=0.2
ϕ=5%
TiO2-CNT-Graphene/water
TiO2-Graphene/water
TiO2-CNT/water
(b)
S*fr
Wavelength, L

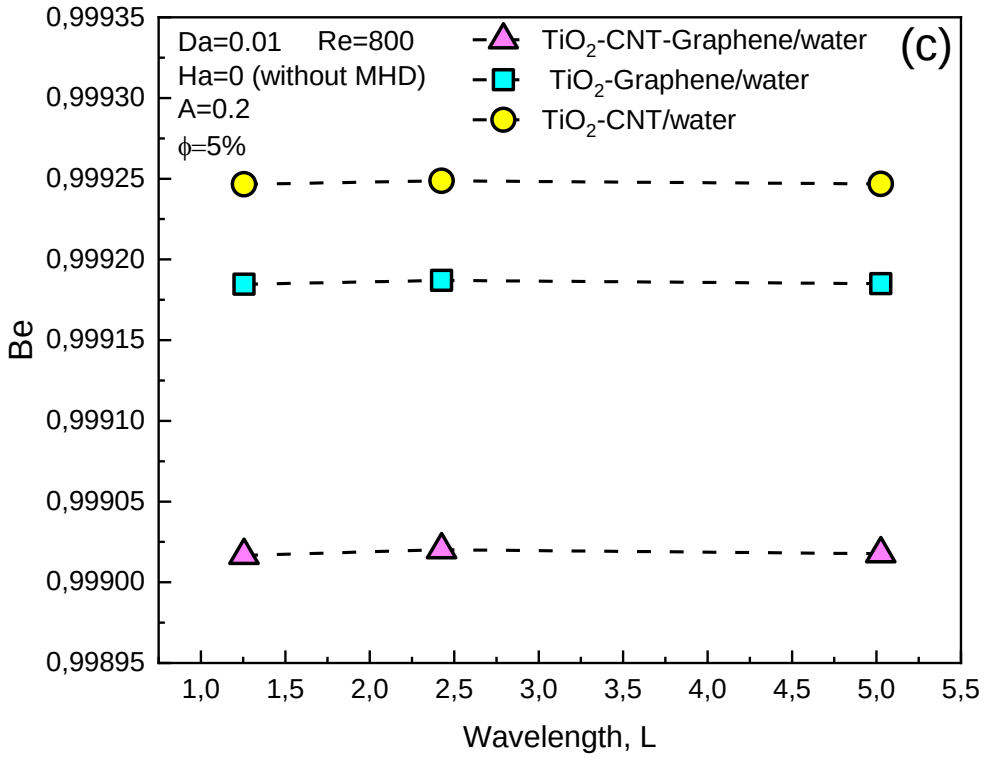

Figure IV. 41. Entropy generation and Bejan number for different hybrid nanofluids and wavelengths at A=0.2.

Figure IV.42 (a-d) shows the variation of entropy generation and Bejan number for different Hartmann numbers. It can be seen that, for all hybrid nanofluids, the thermal entropy reduces with increasing Hartmann number due to the reduced thermal gradient. Simultaneously, as demonstrated earlier, frictional entropy increases due to the increased resistance induced by the stronger magnetic field, leading to decreased velocity. Magnetic entropy consistently increases with rising Hartmann numbers across all tested hybrid nanofluids, with no significant variations observed between them. Furthermore, the Bejan number decreases with increasing Hartmann number for all hybrid nanofluids examined, indicating an enhancement in heat transfer efficiency. This suggests that heat transfer becomes more efficient in the system as the magnetic field strength increases. The (TiO_2-CNT-Graphene/water) ternary hybrid nanofluid presents lower thermal entropy and higher frictional entropy, attributed to its unique combination of nanoparticles with varying shapes and materials.

Figure IV.43 (a-c) displays the variation of thermal, frictional, and magnetic entropy with Hartmann number for different scenarios of magnetic field imposed on the wavy outer cylinder wall of the annulus channel. Thermal entropy decreases with increasing Hartmann number for all magnetic field (FMF) and (PMF) scenarios, except for the third scenario of partial magnetic

field where it decreases until Ha=30; after this point, it remains constant until Ha=50. Moreover, full magnetic field have the lowest values of thermal entropy. An important magnetic field reduces velocity, and the flow of hybrid nanofluids becomes more ordered, reducing thermal entropy. The third scenario is the lowest compared to the other scenarios because applying a magnetic field in a zone close to the outlet of the wavy annulus has no significant influence than applying the magnetic field in the middle or near the entrance of the wavy annulus. Contrary to thermal entropy, frictional entropy increases with increasing Hartmann number. This is because the magnetic field induces a Lorentz force that opposes the hybrid nanofluids flow and forces the fluid to dissipate more energy. Magnetic field entropy increases with rising Hartmann number for full and partial magnetic field scenarios, and there is no remarkable difference between all the cases. **Figure IV.43d** represents Bejan number variation with Hartmann number and different partial magnetic field scenarios; it can be observed that Bejan number reduces with decreasing Hartmann number for all magnetic field scenarios. There is no remarkable difference between the scenarios at Hartmann number (Ha=10 and 30). At the same time, at Ha=50, the full magnetic field has the smallest Bejan number, and the third case of the partial magnetic field has the highest Bejan number. This can be attributed to a stronger magnetic field suppressing convection, which is the main source of irreversibility in a flow. As a result, the Bejan number will decrease with the increase in the Hartmann number.

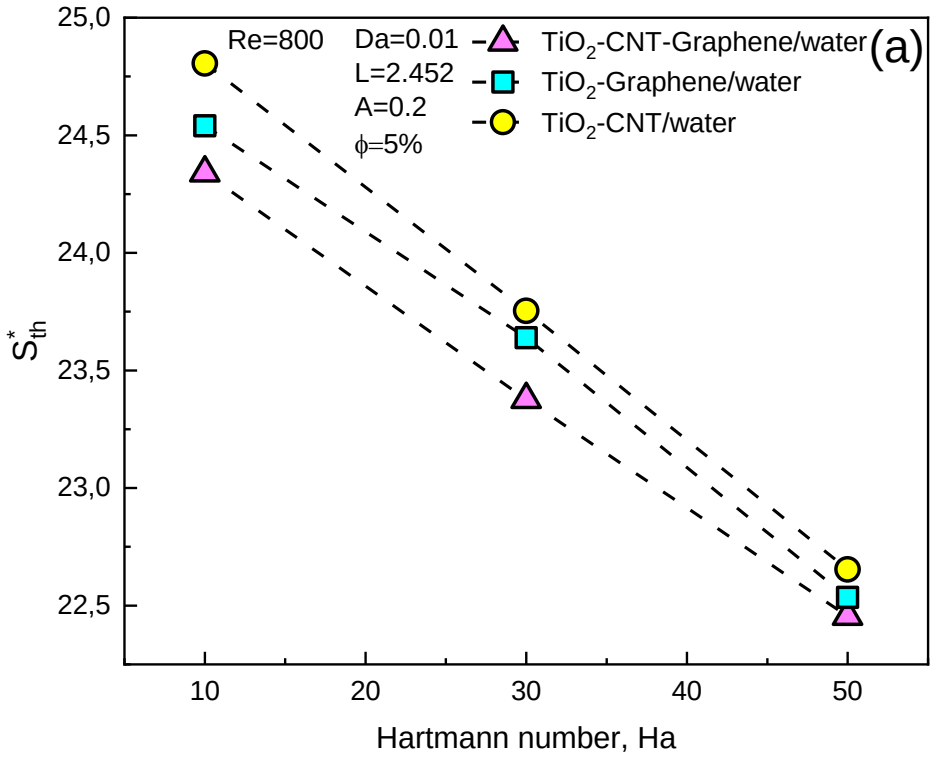
Re=800
Da=0.01
L=2.452
A=0.2
ϕ=5%
TiO2-CNT-Graphene/water
TiO2-Graphene/water
TiO2-CNT/water
(a)
25,0
24,5
24,0
23,5
23,0
22,5
S*th
10
20
30
40
50
Hartmann number, Ha

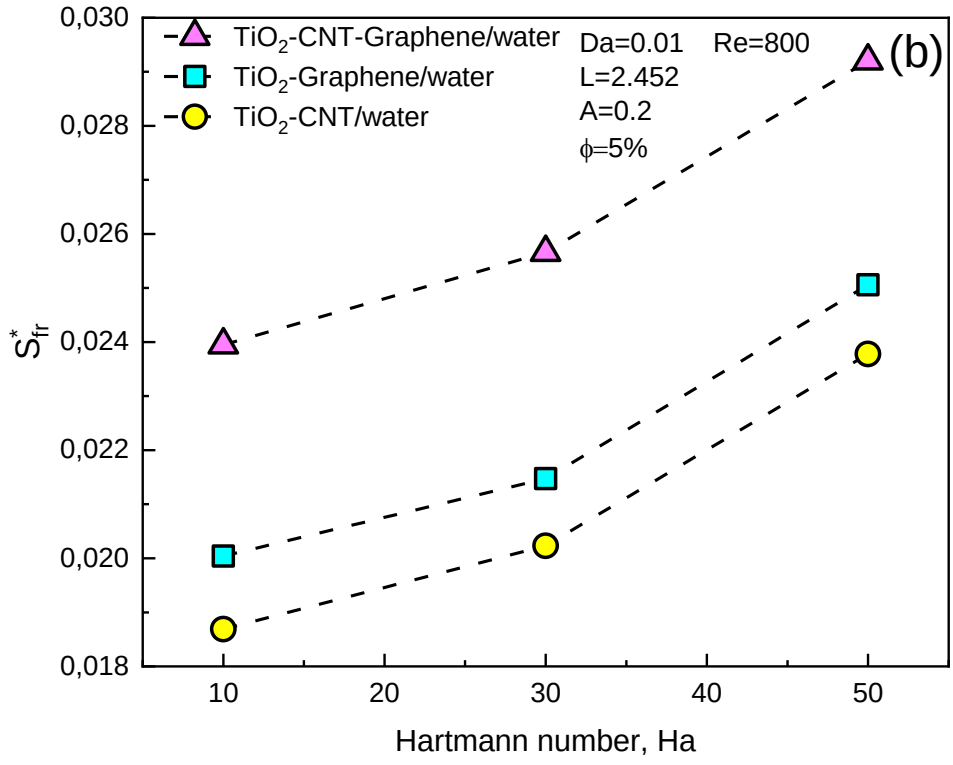
TiO2-CNT-Graphene/water
TiO2-Graphene/water
TiO2-CNT/water
Da=0.01
L=2.452
A=0.2
ϕ=5%
Re=800
(b)
0,030
0,028
0,026
0,024
0,022
0,020
0,018
S*fr
10
20
30
40
50
Hartmann number, Ha

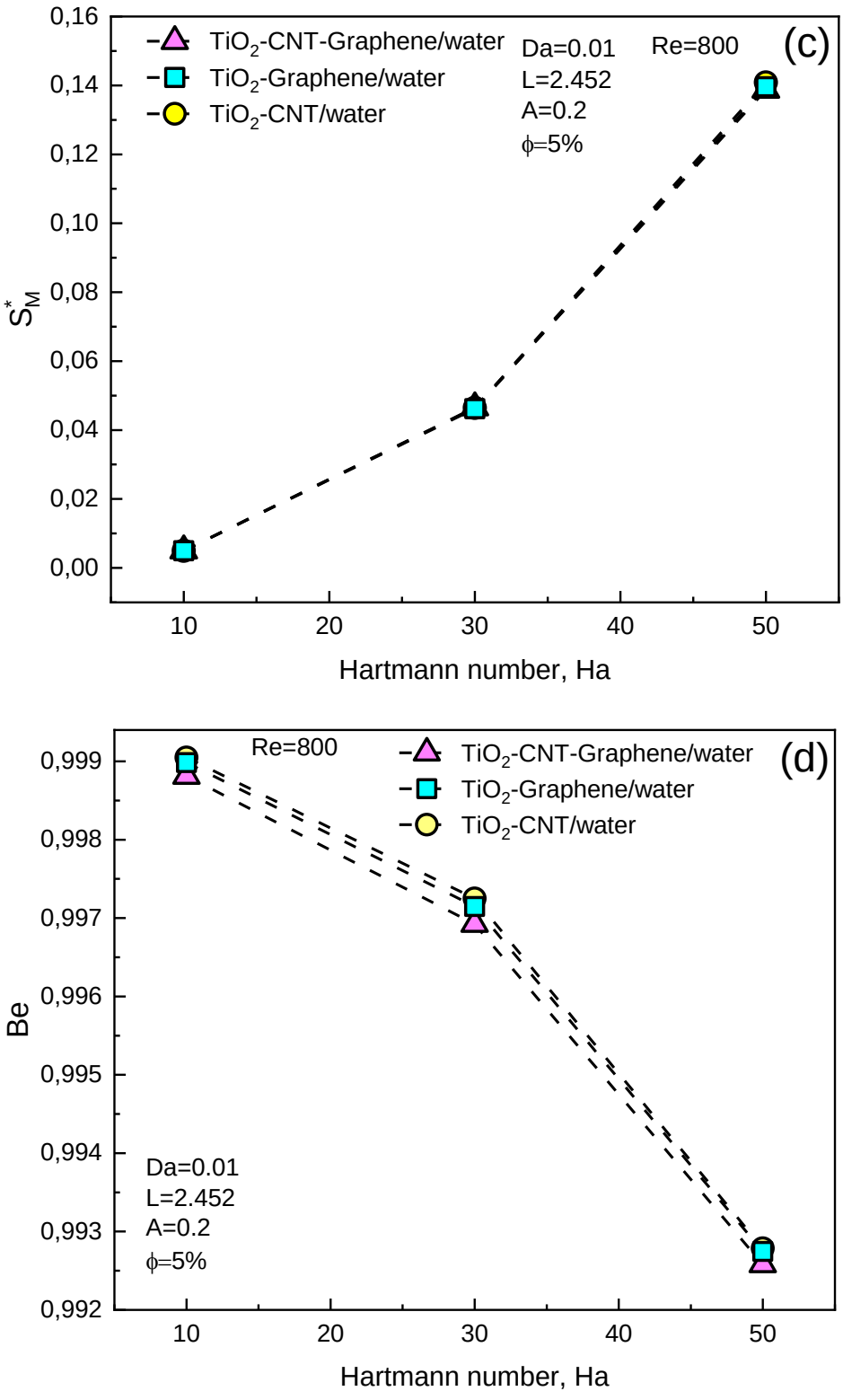

Figure IV. 42. Entropy generation and Bejan number for different hybrid nanofluids and Hartmann number using full magnetic field.

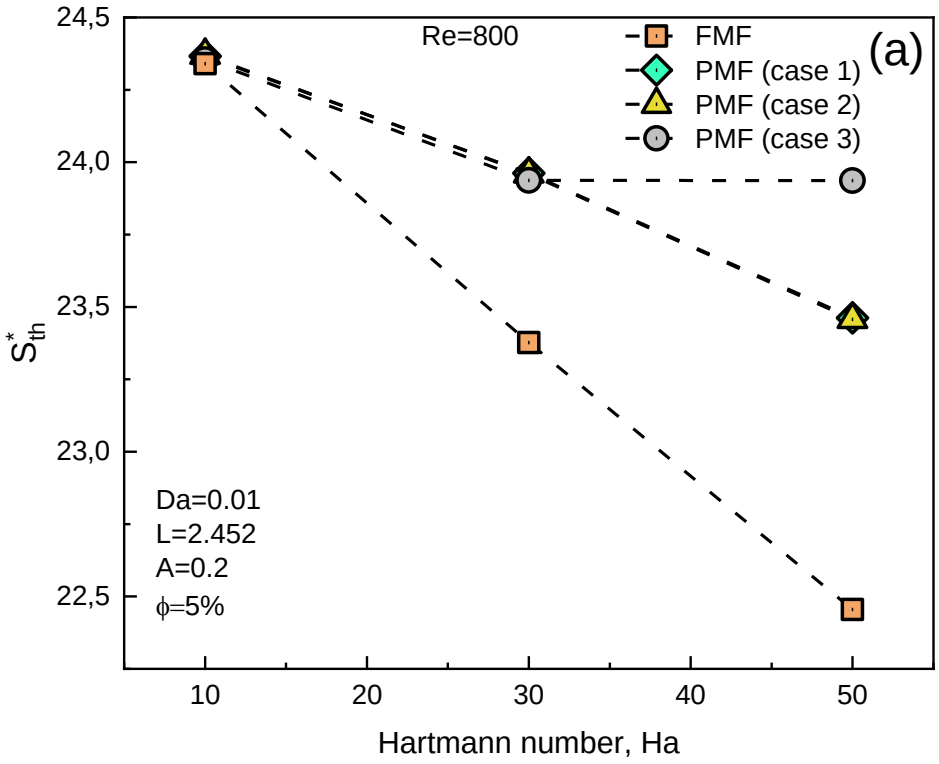
Re=800
FMF
PMF (case 1)
PMF (case 2)
PMF (case 3)
(a)
Da=0.01
L=2.452
A=0.2
ϕ=5%
S^*_{th}
24,5
24,0
23,5
23,0
22,5
10
20
30
40
50
Hartmann number, Ha

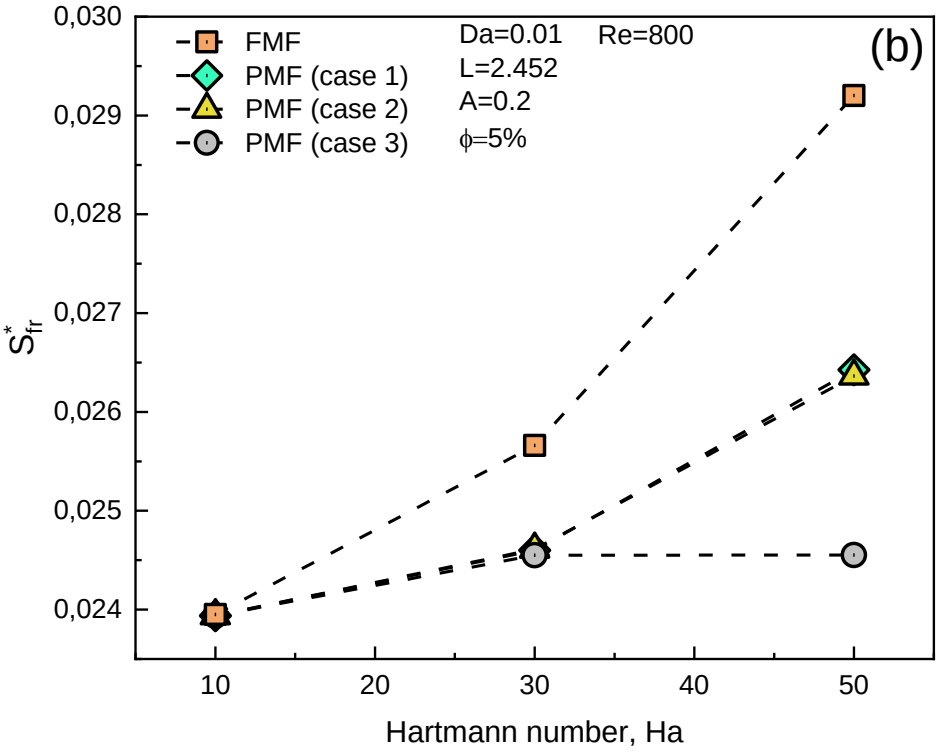
FMF
PMF (case 1)
PMF (case 2)
PMF (case 3)
Da=0.01
L=2.452
A=0.2
ϕ=5%
Re=800
(b)
S^*_{fr}
0,030
0,029
0,028
0,027
0,026
0,025
0,024
10
20
30
40
50
Hartmann number, Ha

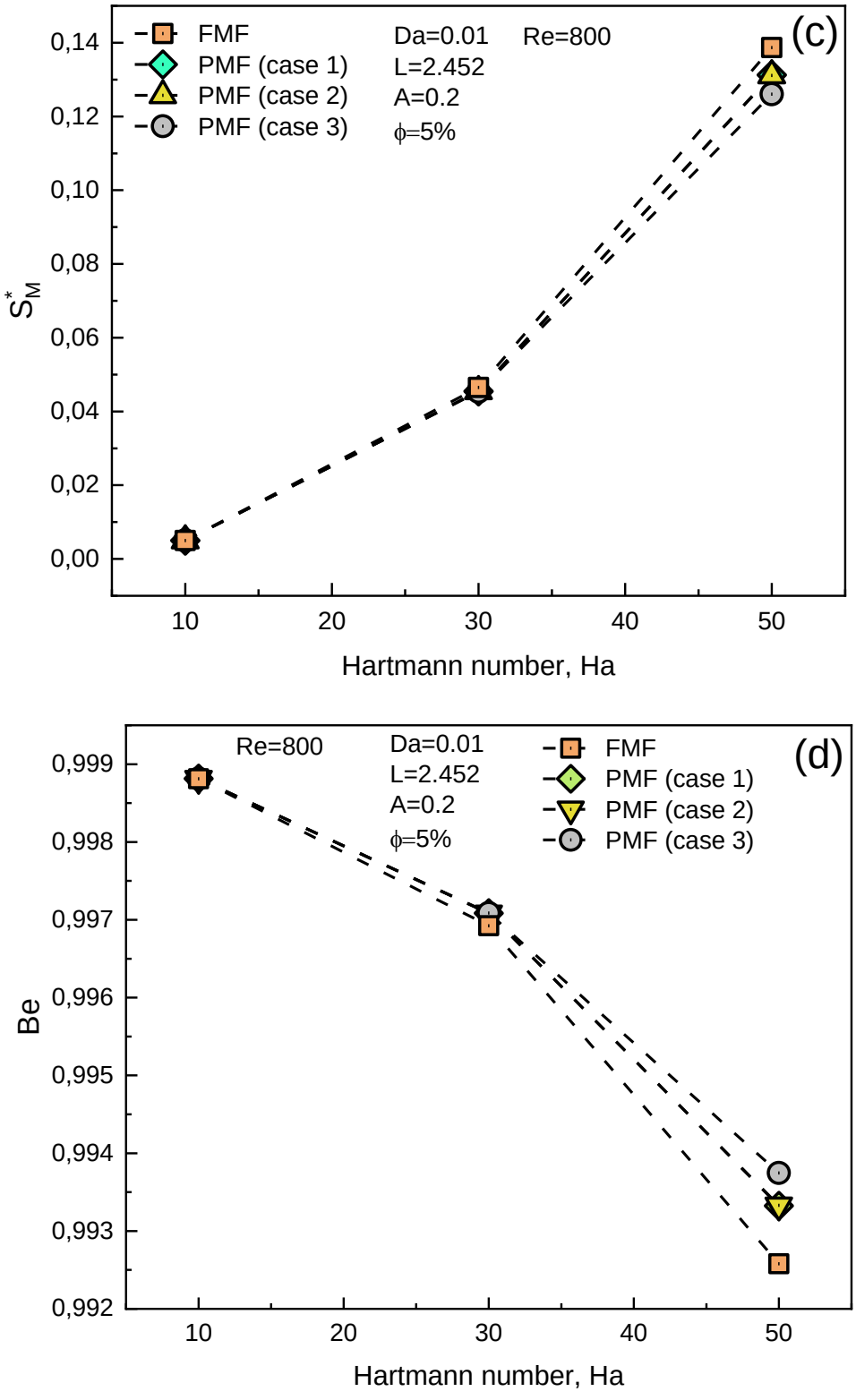

Figure IV. 43. Entropy generation and Bejan number for different Hartmann number and different magnetic field scenarios using Ternary hybrid nanofluid at A=0.2, and L=2.452.

General conclusion

This thesis presents a comprehensive numerical study on laminar convective heat transfer using binary and ternary hybrid nanofluids in the presence of porous media and magnetic fields. The primary objective was to investigate the hydrothermal performance of binary and ternary hybrid nanofluids in two distinct applications: mixed convection and forced convection, within different geometrical configurations and magnetic field conditions.

In the first application, a detailed three-dimensional analysis of mixed convection and entropy generation was conducted using binary and ternary hybrid nanofluids within a straight annulus duct. The study employed FORTRAN code to simulate the behavior of kerosene-based suspensions containing TiO_2, CNT, and Graphene nanoparticles. The major findings of this study include:

- The flow experiences a significant delay at low Darcy numbers, and when the magnetic field is applied horizontally and aligned with the flow.
- Buoyancy forces are minimal at low Darcy numbers but become prominent at higher values, significantly altering temperature distribution and flow characteristics.
- The average Nusselt number increases with the Hartmann number and decreases with the Darcy number, indicating improved heat transfer with stronger magnetic fields.
- A substantial increase in the average Nusselt number was observed with the addition of a magnetic field, particularly for the ternary hybrid nanofluid.
- The pressure drop decreases with increasing Darcy number and increases with rising Hartmann number.
- Skin friction coefficients and entropy generation are significantly influenced by Hartmann number and Darcy number,

The second application focused on forced convection heat transfer and entropy generation using hybrid nanofluids in a wavy annulus duct. This study utilized Ansys-Fluent software to simulate water-based suspensions of TiO_2, CNT, and Graphene nanoparticles. Major conclusions from this investigation include:

- Increasing the wave amplitude of the duct leads to a significant enhancement in the Nusselt number, indicating better heat transfer performance.
- Both pressure drop and skin friction coefficient increase with higher wave amplitude and Hartmann number, while the wavelength has minimal impact.

- The full magnetic field scenario achieved the highest Nusselt number at a higher Hartmann number, demonstrating the efficacy of magnetic fields in improving heat transfer.
- Thermal and frictional entropy generation decreases with higher wave amplitudes, while the Hartmann number has a more complex effect, decreasing thermal entropy but increasing frictional entropy due to viscous dissipation caused by the Lorentz force.
- The Bejan number decreases with increasing Hartmann number, reflecting reduced irreversibility and enhanced thermal performance in stronger magnetic fields.

The results demonstrate that the strategic use of binary and ternary hybrid nanofluids, along with the application of magnetic fields, can significantly improve heat transfer efficiency and manage entropy generation in various flow configurations

Perspectives and future research

Future studies building on the present work can be formulated as follows:

- Plan an experimental study on hybrid nanofluids to determine our correlations of thermal conductivity and dynamic viscosity as a function of temperature.
- Investigate the effects of different geometrical configurations of the annular duct. This includes varying the inner and outer radii and introducing additional geometric complexities.
- Explore the use of ferrofluids and examine the impact of magnetic fields on heat transfer and fluid flow characteristics.
- Extend the current numerical model to simulate multiphase flows within the annular duct.
- Explore the integration of the studied thermal systems with renewable energy sources, such as solar or geothermal energy.

References

[1] J.C. Maxwell, Electricity and Magnetism Clarendon Press, Ed Oxf. UK (1873).

[2] S.U. Choi, J.A. Eastman, Enhancing thermal conductivity of fluids with nanoparticles, Argonne National Lab.(ANL), Argonne, IL (United States), 1995.

[3] M. Benkhedda, Étude Numérique des Écoulements Thermoconvectifs d'un Nanofluide à travers un Espace Cylindrique Annulaire muni d'Ailettes, Université Frères Mentouri Constantine 1, 2018.

[4] M. Chandrasekar, S. Suresh, A. Chandra Bose, Experimental investigations and theoretical determination of thermal conductivity and viscosity of Al2O3/water nanofluid, Exp. Therm. Fluid Sci. 34 (2010) 210–216. https://doi.org/10.1016/j.expthermflusci.2009.10.022.

[5] N. Gupta, S.M. Gupta, S.K. Sharma, Synthesis, characterization and dispersion stability of water-based Cu–CNT hybrid nanofluid without surfactant, Microfluid. Nanofluidics 25 (2021) 14. https://doi.org/10.1007/s10404-021-02421-2.

[6] Z. Said, N.K. Cakmak, P. Sharma, L.S. Sundar, A. Inayat, O. Keklikcioglu, C. Li, Synthesis, stability, density, viscosity of ethylene glycol-based ternary hybrid nanofluids: Experimental investigations and model -prediction using modern machine learning techniques, Powder Technol. 400 (2022) 117190. https://doi.org/10.1016/j.powtec.2022.117190.

[7] R. Ekiciler, K. Arslan, O. Turgut, B. Kurşun, Effect of hybrid nanofluid on heat transfer performance of parabolic trough solar collector receiver, J. Therm. Anal. Calorim. 143 (2021) 1637–1654. https://doi.org/10.1007/s10973-020-09717-5.

[8] V. Selvaraj, H. Krishnan, Synthesis of graphene encased alumina and its application as nanofluid for cooling of heat-generating electronic devices, Powder Technol. 363 (2020) 665–675. https://doi.org/10.1016/j.powtec.2020.01.050.

[9] F. Abbas, H.M. Ali, M. Shaban, M.M. Janjua, T.R. Shah, M.H. Doranehgard, M. Ahmadlouydarab, F. Farukh, Towards convective heat transfer optimization in aluminum tube automotive radiators: Potential assessment of novel Fe2O3-TiO2/water hybrid nanofluid, J. Taiwan Inst. Chem. Eng. 124 (2021) 424–436. https://doi.org/10.1016/j.jtice.2021.02.002.

[10] R.R. Sahoo, Thermo-hydraulic characteristics of radiator with various shape nanoparticle-based ternary hybrid nanofluid, Powder Technol. 370 (2020) 19–28. https://doi.org/10.1016/j.powtec.2020.05.013.

[11] Z.A. Alrowaili, M. Ezzeldien, N.M. Shaaalan, E. Hussein, M.A. Sharafeldin, Investigation of the effect of hybrid CuO-Cu/water nanofluid on the solar thermal energy storage system, J. Energy Storage 50 (2022) 104675. https://doi.org/10.1016/j.est.2022.104675.

[12] B.C. Pak, Y.I. Cho, Hydrodynamic and Heat Transfer Study of Dispersed Fluids with Submicron Metallic Oxide Particles, Exp. Heat Transf. 11 (1998) 151–170. https://doi.org/10.1080/08916159808946559.

[13] B. Takabi, S. Salehi, Augmentation of the Heat Transfer Performance of a Sinusoidal Corrugated Enclosure by Employing Hybrid Nanofluid, Adv. Mech. Eng. 6 (2014). https://doi.org/10.1155/2014/147059.

[14]K. Khanafer, K. Vafai, A critical synthesis of thermophysical characteristics of nanofluids, Int. J. Heat Mass Transf. 54 (2011) 4410–4428. https://doi.org/10.1016/j.ijheatmasstransfer.2011.04.048.

[15]E.V. Timofeeva, J.L. Routbort, D. Singh, Particle shape effects on thermophysical properties of alumina nanofluids, J. Appl. Phys. 106 (2009) 014304. https://doi.org/10.1063/1.3155999.

[16]J.C. Maxwell, A treatise on electricity and magnetism, Clarendon press, 1873.

[17]R.L. Hamilton, O. Crosser, Thermal Conductivity of Heterogeneous Two-Component Systems, Ind. Eng. Chem. Fundam. 1 (1962) 187–191.

[18]J. Koo, C. Kleinstreur, Impact analysis of nanoparticle motion mechanisms on the thermal conductivity of nanofluids, Int. Commun. Heat Mass Transf. 32 (2005) 1111–1118. https://doi.org/10.1016/j.icheatmasstransfer.2005.05.014.

[19]R. Motallebzadeh, S. Hajizadeh, M.R. Ghasemi, Numerical Study of Laminar Mixed Convection Heat Transfer of a Nanofluid in a Concentric Annular Tube Using Two-Phase Mixture Model, Int. J. Aerosp. Mech. Eng. 8 (2014) 568–575.

[20]M. Benkhedda, T. Boufendi, S. Touahri, Laminar mixed convective heat transfer enhancement by using Ag-TiO2-water hybrid Nanofluid in a heated horizontal annulus, Heat Mass Transf. 54 (2018) 2799–2814. https://doi.org/10.1007/s00231-018-2302-x.

[21]B. Takabi, A. Gheitaghy, P. Tazraei, Hybrid Water-Based Suspension of Al2O3 and Cu Nanoparticles on Laminar Convection Effectiveness, J. Thermophys. Heat Transf. 30 (2016) 1–10. https://doi.org/10.2514/1.T4756.

[22]R.K. SHAH, A.L. London, Laminar Flow Forced Convection Heat Transfer and Flow Friction in Straight and Curved Ducts--A Summary of Analytical Solutions, Stanford University, 1972.

[23]M. Benkhedda, T. Boufendi, T. Tayebi, A.J. Chamkha, Convective heat transfer performance of hybrid nanofluid in a horizontal pipe considering nanoparticles shapes effect, J. Therm. Anal. Calorim. 140 (2020) 411–425. https://doi.org/10.1007/s10973-019-08836-y.

[24]M. Benkhedda, F. Bensouici, T. Boufendi, Parametric Study of Nanoparticles Effects on Convective Heat Transfer of Nanofluids in a Heated Horizontal Annulus, J. Nano Res. 70 (2021) 81–100. https://doi.org/10.4028/www.scientific.net/JNanoR.70.81.

[25]Badr Ali Bzya Albeshri, Nazrul Islam, Ahmad Yahya Bokhary, Amjad Ali Pasha, Hydrodynamic Analysis of Laminar Mixed Convective Flow of Ag-TiO2-Water Hybrid Nanofluid in a Horizontal Annulus, CFD Lett. 13 (2021) 45–57. https://doi.org/10.37934/cfdl.13.7.4557.

[26]A. Abedini, S. Emadoddin, T. Armaghani, Numerical analysis of mixed convection of different nanofluids in concentric annulus, Int. J. Numer. Methods Heat Fluid Flow 29 (2019) 1506–1525. https://doi.org/10.1108/HFF-06-2018-0337.

[27]A. Rezaei Gorjaei, M. Soltani, M. Bahiraei, F. M. Kashkooli, CFD simulation of nanofluid forced convection inside a three-dimensional annulus by two-phase mixture approach: Heat transfer and entropy generation analyses, Int. J. Mech. Sci. 146–147 (2018) 396–404. https://doi.org/10.1016/j.ijmecsci.2018.08.002.

[28]S. Mirmasoumi, A. Behzadmehr, Numerical study of laminar mixed convection of a nanofluid in a horizontal tube using two-phase mixture model, Appl. Therm. Eng. 28 (2008) 717–727. https://doi.org/10.1016/j.applthermaleng.2007.06.019.

[29]Y. Sheikhnejad, R. Hosseini, M. Saffar Avval, Experimental study on heat transfer enhancement of laminar ferrofluid flow in horizontal tube partially filled porous media under fixed parallel magnet bars, J. Magn. Magn. Mater. 424 (2017) 16–25. https://doi.org/10.1016/j.jmmm.2016.09.098.

[30]M. Bahiraei, A.R. Gorjaei, A. Shahidian, Investigating heat transfer and entropy generation for mixed convection of CuO–water nanofluid in an inclined annulus, J. Mol. Liq. 248 (2017) 36–47. https://doi.org/10.1016/j.molliq.2017.10.025.

[31]H. Aminfar, M. Mohammadpourfard, Y. Narmani Kahnamouei, A 3D numerical simulation of mixed convection of a magnetic nanofluid in the presence of non-uniform magnetic field in a vertical tube using two phase mixture model, J. Magn. Magn. Mater. 323 (2011) 1963–1972. https://doi.org/10.1016/j.jmmm.2011.02.039.

[32]A. Alsaedi, K. Muhammad, T. Hayat, Numerical study of MHD hybrid nanofluid flow between two coaxial cylinders, Alex. Eng. J. 61 (2022) 8355–8362. https://doi.org/10.1016/j.aej.2022.01.067.

[33]P. Barnoon, D. Toghraie, F. Eslami, B. Mehmandoust, Entropy generation analysis of different nanofluid flows in the space between two concentric horizontal pipes in the presence of magnetic field: Single-phase and two-phase approaches, Comput. Math. Appl. 77 (2019) 662–692.

[34]M. Goharkhah, M. Esmaeili, M. Ashjaee, Numerical Simulation and Optimization of Forced Convection Heat Transfer of Magnetic Nanofluid in a Channel in the Presence of a Non-Uniform Magnetic Field, 11 (2018) 9.

[35]A.A. Servati V., K. Javaherdeh, H.R. Ashorynejad, Magnetic field effects on force convection flow of a nanofluid in a channel partially filled with porous media using Lattice Boltzmann Method, Adv. Powder Technol. 25 (2014) 666–675. https://doi.org/10.1016/j.apt.2013.10.012.

[36]S. Mohsenian, S. Gouran, S.E. Ghasemi, Evaluation of weighted residual methods for thermal radiation on nanofluid flow between two tubes in presence of magnetic field, Case Stud. Therm. Eng. 32 (2022) 101867. https://doi.org/10.1016/j.csite.2022.101867.

[37]N. Hatami, A. Kazemnejad Banari, A. Malekzadeh, A.R. Pouranfard, The effect of magnetic field on nanofluids heat transfer through a uniformly heated horizontal tube, Phys. Lett. A 381 (2017) 510–515. https://doi.org/10.1016/j.physleta.2016.12.017.

[38]X. Liu, D. Toghraie, M. Hekmatifar, O.A. Akbari, A. Karimipour, M. Afrand, Numerical investigation of nanofluid laminar forced convection heat transfer between two horizontal concentric cylinders in the presence of porous medium, J. Therm. Anal. Calorim. 141 (2020) 2095–2108. https://doi.org/10.1007/s10973-020-09406-3.

[39]H. Moghadasi, E. Aminian, H. Saffari, M. Mahjoorghani, A. Emamifar, Numerical analysis on laminar forced convection improvement of hybrid nanofluid within a U-bend pipe in porous media, Int. J. Mech. Sci. 179 (2020) 105659. https://doi.org/10.1016/j.ijmecsci.2020.105659.

[40]M. Siavashi, H.R.T. Bahrami, E. Aminian, H. Saffari, Numerical analysis on forced convection enhancement in an annulus using porous ribs and nanoparticle addition to base fluid, (2019) 10.

[41]H.R. Talesh Bahrami, H. Safikhani, Heat transfer enhancement inside an eccentric cylinder with an inner rotating wall using porous media: a numerical study, J. Therm. Anal. Calorim. 141 (2020) 1905–1917. https://doi.org/10.1007/s10973-020-09532-y.

[42]A. Shahabi Nejad, M. Fallah Barzoki, M. Rahmani, A. Kasaeian, A. Hajinezhad, Simulation of the heat transfer performance of Al2O3–Cu/water binary nanofluid in a homogenous copper metal foam, J. Therm. Anal. Calorim. (2022). https://doi.org/10.1007/s10973-022-11487-1.

[43]S. Kuharat, O.A. Bég, Computational Fluid Dynamics Simulation of a Nanofluid-Based Annular Solar Collector with Different Metallic Nano-Particles, 3 (2019) 24.

[44]Y. Peng, A numerical simulation for magnetohydrodynamic nanofluid flow and heat transfer in rotating horizontal annulus with thermal radiation, RSC Adv. (2019) 13.

[45]S. Aberkane, M. Ihdene, M. Moderres, G. Abderrahmane, Effect of Magnetic Field on the Heat and Mass Transfer in a Rotating Horizontal Annulus, 2014.

[46]A.F. Al-Alawy, A Numerical Analysis of Cu–Engine Oil Nanofluid Forced Convection in Annular Tubes, 6 (2017) 10.

[47]S. Majid, J. Mohammad, Optimal selection of annulus radius ratio to enhance heat transfer with minimum entropy generation in developing laminar forced convection of water-Al2O3 nanofluid flow, J. Cent. South Univ. 24 (2017) 1850–1865. https://doi.org/10.1007/s11771-017-3593-7.

[48]A. Shahsavar, M. Moradi, M. Bahiraei, Heat transfer and entropy generation optimization for flow of a non-Newtonian hybrid nanofluid containing coated CNT/Fe 3 O 4 nanoparticles in a concentric annulus, J. Taiwan Inst. Chem. Eng. 84 (2018) 28–40. https://doi.org/10.1016/j.jtice.2017.12.029.

[49]N. Acharya, K. Das, P. Kumar Kundu, Ramification of variable thickness on MHD TiO2 and Ag nanofluid flow over a slendering stretching sheet using NDM, Eur. Phys. J. Plus 131 (2016) 303. https://doi.org/10.1140/epjp/i2016-16303-4.

[50]K. Zitouni, L. Aidaoui, Y. Lasbet, T. Tayebi, Entropy Generation-Based Analysis of Laminar Magneto-Convection in Different Cross-Section Channel Filled with Ferrofluid and Subjected to Partial and Full Magnetic Fields, J. Nanofluids 12 (2023) 1275–1297.

[51]S.V. Patankar, Numerical Heat Transfer and Fluid Flow, McGraw-Hill, New York, 1980, n.d.

[52]D. Kim, Y. Kwon, Y. Cho, C. Li, S. Cheong, Y. Hwang, J. Lee, D. Hong, S. Moon, Convective heat transfer characteristics of nanofluids under laminar and turbulent flow conditions, Curr. Appl. Phys. 9 (2009) e119–e123. https://doi.org/10.1016/j.cap.2008.12.047.

[53]J. Bayat, A.H. Nikseresht, Investigation of the different base fluid effects on the nanofluids heat transfer and pressure drop, Heat Mass Transf. 47 (2011) 1089–1099. https://doi.org/10.1007/s00231-011-0773-0.

[54]B. Takabi, A. Gheitaghy, P. Tazraei, Hybrid Water-Based Suspension of Al2O3 and Cu Nanoparticles on Laminar Convection Effectiveness, J. Thermophys. Heat Transf. 30 (2016) 1–10. https://doi.org/10.2514/1.T4756.

[55]B.I. Pavel, A.A. Mohamad, An experimental and numerical study on heat transfer enhancement for gas heat exchangers fitted with porous media, Int. J. Heat Mass Transf. 47 (2004) 4939–4952. https://doi.org/10.1016/j.ijheatmasstransfer.2004.06.014.

[56]E. Aminian, H. Moghadasi, H. Saffari, Magnetic field effects on forced convection flow of a hybrid nanofluid in a cylinder filled with porous media: a numerical study, J. Therm. Anal. Calorim. 141 (2020) 2019–2031. https://doi.org/10.1007/s10973-020-09257-y.

[57]M. Benkhedda, T. Tayebi, A.J. Chamkha, Toward the thermohydrodynamic behavior of a nanofluid containing C-MWCNTs flowing through a 3D annulus channel under constant imposed heat flux, Heat Transf. 51 (2022) 2524–2545. https://doi.org/10.1002/htj.22411.

Abstract

This thesis presents a comprehensive numerical study on the laminar convective heat transfer of hybrid nanofluids between two horizontal concentric cylinders filled with porous media under uniform heating. The study investigates two distinct applications: laminar mixed convection through a straight annulus duct exposed to a full magnetic field at different inclination angles and laminar forced convection through a wavy annulus duct exposed to both full and partial magnetic fields across various scenarios considering joule heating. The primary focus is on understanding the magneto-hydrothermal flow behavior of binary and ternary hybrid nanofluids. The hybrid nanofluids are composed of different materials and shapes of nanoparticles, spherical, cylindrical, and platelet with different mixture ratio dispersed in water or kerosene. The Finite volume method was employed to solve the system of equations using single phase approach. The simulation explores the effects of multiple parameters including Hartmann number, magnetic field inclination angle, Darcy number, Grashof number, amplitude wave, and wavelength at fixed Reynolds number and volume fraction. The results indicate that the ternary hybrid nanofluid exhibits the highest Nusselt number compared to binary compositions under similar conditions. It was observed that increasing the Darcy number reduces the heat transfer rate. Moreover, the influence of magnetic fields, characterized by the Hartmann number, shows that higher values enhance the Nusselt number, indicating improved heat transfer efficiency due to enhanced magnetic field-induced suppression of convection. Additionally, variations in wave amplitude also contribute positively to heat transfer enhancement, while changes in wavelength showed no significant impact.

Keywords: Annulus, Duct, Joule heating, Laminar convection, Magnetic field, Porous media, Ternary hybrid nanofluid, Wavy.

الملخص

تقدم هذه الأطروحة دراسة عددية شاملة حول الانتقال الحراري الصفحي للسوائل النانوية الهجينة بين أسطوانتين أفقيتين متحدتي المركز مملوءتين بوسائط مسامية تحت تسخين موحد. وتبحث الدراسة في تطبيقين مختلفين: الحمل الحراري الصفحي المختلط من خلال قناة حلقية مستقيمة معرضة لمجال مغناطيسي كامل بزوايا ميل مختلفة، والحمل الحراري القسري الصفحي من خلال قناة حلقية متموجة معرضة لمجالات مغناطيسية كاملة وجزئية عبر سيناريوهات مختلفة مع اعتبار التسخين بالجول. ينصب التركيز الأساسي على فهم سلوك التدفق المغناطيسي-الحراري للسوائل النانوية الهجينة الثنائية والثلاثية. تتألف الموائع النانوية الهجينة من مواد وأشكال مختلفة من الجسيمات النانوية، كروية وأسطوانية وصفيحية مع نسب خليط مختلفة مشتتة في الماء أو الكيروسين. استُخدمت طريقة الحجم المحدود لحل نظام المعادلات باستخدام نموذج الطور الواحد. تستكشف المحاكاة تأثيرات معاملات متعددة بما في ذلك رقم هارتمان، وزاوية ميل المجال المغناطيسي، ورقم دارسي، ورقم غراشوف، وسعة الموجة، والطول الموجي عند رقم رينولدز ثابت وتركيز الحجم. تشير النتائج إلى أن المائع النانوي الهجين الثلاثي يُظهر أعلى رقم نوسيلت مقارنةً بالتركيبات الثنائية في ظروف مماثلة. ولوحظ أن زيادة عدد دارسي يقلل من معدل انتقال الحرارة. ويبين تأثير المجالات المغناطيسية، التي تتميز برقم هارتمان، أن القيم الأعلى تحسّن رقم نوسيلت، مما يشير إلى تحسين كفاءة نقل الحرارة بسبب تحسين كبح الحمل الحراري الناجم عن المجال المغناطيسي. بالإضافة إلى ذلك، تساهم الاختلافات في سعة الموجة أيضًا بشكل إيجابي في تعزيز نقل الحرارة، في حين لم تُظهر التغيرات في الطول الموجي أي تأثير كبير.

الكلمات المفتاحية: الحمل الحراري الصفحي، السائل النانوي الهجين الثلاثي، المجال المغناطيسي، الأوساط المسامية، تسخين الجول، التموج، الحلقة، القناة.

Résumé

Cette thèse présente une étude numérique sur le transfert de chaleur par convection laminaire de nanofluides hybrides entre deux cylindres concentriques horizontaux remplis d'un milieu poreux sous chauffage uniforme. L'étude porte sur deux applications distinctes : la convection mixte laminaire à travers un conduit annulaire droit exposé à un champ magnétique uniforme à différents angles d'inclinaison et la convection forcée laminaire à travers un conduit annulaire ondulé exposé à des champs magnétiques uniforme et partiels à travers différents scénarios prenant en compte l'effet joule. L'objectif principal est de comprendre le comportement de l'écoulement magnéto-hydrothermique des nanofluides hybrides binaires et ternaires. Les nanofluides hybrides sont composés de différents matériaux et formes de nanoparticules, sphériques, cylindriques et en plaquettes avec différents rapports de mélange dispersés dans l'eau ou le kérosène. La méthode des volumes finis a été employée pour résoudre le système d'équations en utilisant une approche monophasique. La simulation explore les effets de multiples paramètres, le nombre de Hartmann, l'angle d'inclinaison du champ magnétique, le nombre de Darcy, le nombre de Grashof, l'amplitude de l'onde et la longueur d'onde à un nombre de Reynolds et une fraction de volume fixes. Les résultats indiquent que le nanofluide hybride ternaire présente le nombre de Nusselt le plus élevé par rapport aux compositions binaires dans des conditions similaires. Il a été observé que l'augmentation du nombre de Darcy réduit le taux de transfert de chaleur. En outre, l'influence des champs magnétiques, caractérisée par le nombre de Hartmann, montre que des valeurs plus élevées augmentent le nombre de Nusselt, ce qui indique une amélioration de l'efficacité du transfert de chaleur en raison de la suppression de la convection induite par le champ magnétique. En outre, les variations de l'amplitude des ondes contribuent également à l'amélioration du transfert de chaleur, tandis que les variations de la longueur d'onde n'ont pas d'impact significatif.

Mots clé : Convection laminaire, Nanofluide hybride ternaire, Champ magnétique, Milieu poreux, Effet joule, Ondulation, Anneau, Conduit.